

NORTHWESTERN UNIVERSITY

Engineering Scalable Microenvironments to Enhance *Ex Vivo* Megakaryocyte Production
and Platelet Release

A DISSERTATION

SUBMITTED TO THE GRADUATE SCHOOL
IN PARTIAL FULFILLMENT OF THE REQUIREMENTS

for the degree

DOCTOR OF PHILOSOPHY

Field of Chemical Engineering

By

Andres Martinez

EVANSTON, ILLINOIS

JUNE 2019

© Copyright by Andres Martinez 2019

All Rights Reserved

ABSTRACT

Engineering Scalable Microenvironments to Enhance *Ex Vivo* Megakaryocyte Production and Platelet Release

Andres Martinez

Currently, platelet transfusions, possessing profound clinical importance in the clotting of blood and healing of wounds, are entirely derived from human volunteer donors. This approach is limited by a 5-day shelf life, the potential risk of contamination, and differences in donor/recipient immunology. *In vivo*, platelets are formed when bone marrow megakaryocytes (Mks) extend long, cytoplasmic projections, called proplatelets (proPLTs), into the sinusoids where shear forces accelerate proPLT elongation and release platelets into circulation. Additionally, platelet formation can occur from trapped Mks in the lung capillary bed. Developing a clinically relevant *ex vivo* platelet production process is limited by (1) expansion and differentiation of hematopoietic stem and progenitor cells (HSPCs) into Mks and (2) generation of platelet-like-particles (PLPs) from mature Mks. We and others have made progress in addressing these challenges yet major limitations remain to deliver a donor-independent process for *ex vivo* platelet production.

In the first part of this work, we aimed to further understand *ex vivo* PLP production from Mks through the engineering of novel microfluidic bioreactors that mimic *in vivo* physiological conditions in the bone marrow and lung. Leveraging computational fluid dynamics (CFD) modeling to help guide and understand the hydrodynamics of the systems,

we developed uniform-shear-rate bioreactors (USRBs) that permit real-time visualization of the proPLT formation process and the rapid-release of individual PLPs, which has been observed *in vivo*, but not previously reported for platelet bioreactors. We showed that modulating shear forces and flow patterns had an immediate and significant impact on PLP generation. By identifying particularly effective operating conditions within a physiologically relevant environment, these USRB bioreactors provide a useful tool for the study and analysis of proPLT/PLP formation to further our understanding of PLP release.

Critical advancements are needed to improve scalability and increase Mk culture productivity. In the second part of this work, we evaluated Mk production from mobilized peripheral blood CD34⁺ cells cultured on a commercially available gas-permeable silicone rubber membrane, which provides efficient gas exchange. This technology has been used to accelerate the expansion of other cell types, such as T-cells, for cell-based therapies and demonstrated scalability. Additionally, we investigated the use of fed-batch media dilution schemes since this cell-culture technique was shown to be beneficial for HSPC expansion. Our new culture process improved Mk yields by over two-fold while retaining Mk potential to make proPLTs and generate PLPs.

Finally, we aimed to improve PLP potential through pharmacological inhibition of the Rho GTPases: RhoA, Cdc42 and Rac1. These targets are regulators of the actin cytoskeleton and have been implicated in the polyploidization and proPLT formation of Mks. Our goal in this study was to enhance ploidy levels and proPLT formation thus increasing PLP yields but

overall, we saw limited improvements. The results further underline the lack of understanding driving Mk maturation and PLP generation and highlight the need of more Mk mechanistic studies of the pathways that regulate the fate of late-stage Mks.

Acknowledgements

I am very grateful to many people who have supported me in many ways during graduate school. To my advisor, Professor Bill Miller, I consider myself extremely fortunate to have joined your lab. Your vast experience in industry and academia was a great fit with my career trajectory and interests. Thank you for your personal and scientific mentorship throughout my time in your lab. I can honestly say that I am a better person, writer, thinker and scientist because of your investment. I'd like to also thank my committee members, Professor Mike Jewett, Professor Josh Leonard and Professor Sadie Wignall for your thoughtful contributions to my time at Northwestern. I'd like to also thank Professor Wes Burghardt for his helpful discussion on computational fluid dynamics topics of my research and Dr. Marc Horner from ANSYS for guiding me through the initial phases of my computational projects.

To the lab members that I got to share this experience with, I share my research and success with all of you. Thanks to Mark Duncan, Joe Magura and Richard McMahon for taking time to introducing me to the world of microfluidics. To Teresa DeLuca, who taught me all the cell culture skills I needed to be successful, I am appreciative of your patient demeanor and friendly spirit and wish you the best. I'm very thankful for spending most of my time in lab with Ellesse Bess. We are not only lab mates but very close friends who have shared some trying times in lab, yet she still finds ways to make me laugh. To Jia Wu, our discussion and conversations about science and life were always a favorite part of my day. Thanks to Master's students Damien and Afra for leading the effort of our microfluidic projects, I hope you learned from me as much as I learned from you. Thanks to the various undergraduate

students I've had the pleasure to work with and sharpen my mentorship skills, Kathleen, Vasil and Conner. I hope to cross paths with all of you in the future. I'd like to extend my thanks to the ChBE department and staff. You all have made this experience much enjoyable.

To friends from the department, Adam Ponedal, Weston Kightlinger and Casey Whitford, thank you for all your laughs, support and friendship outside of lab. Taking first place on trivia competitions and exploring the best areas of Chicago are highlights of my time at Northwestern. I'd like to especially thank Rob Brydon for becoming a true and dear friend of mine. This experience wouldn't have been the same without you and I will miss seeing you often but hope our paths brings us back together. To my friends from Chicago, Taba and Sally, thanks for introducing me to board games as these relaxing nights were a nice break from the sometimes-chaotic life in lab. To my dear friends from far away, Jordan and Christine, thanks for remaining close in spirit.

Finally, I need to thank my family for their loving support these last years. My parents, Flora and Xavier, for instilling in me the desire to be a life-long learner and to be a good person. And most importantly to my husband, Juan. When I told you almost 6 years ago I wanted to go back to graduate school, you didn't ask why, you just said Yes. We left our friends and jobs in Indianapolis and I am very appreciative of you for taking this adventure with me. Thanks for making sure I had dinner every day even if it meant eating in the office late at night with me. These last years were stressful and you were the calm-soul that reminded me of why I was here and kept me grounded and focused.

Table of Contents

CHAPTER 1. Introduction and Background	20
1.1. Clinical significance of platelet transfusions	20
1.2. Hematopoiesis, megakaryopoiesis, and platelet release	20
1.3. Current state of <i>ex vivo</i> Mk and platelet-like-particle (PLP) production	23
1.4. Rho GTPases regulate the cytoskeleton and impact Mk maturation and proPLTs	24
1.5. Goals for this work	27
CHAPTER 2. Using computational fluid dynamics (CFD) to design and characterize an improved microfluidic platelet bioreactor with uniform-shear rates	29
2.1 Introduction	29
2.2 Materials and methods	32
2.2.1 CFD modeling	32
2.2.1.1 Methodology for Nakagawa et al.[82]	36
2.2.1.2 Methodology for Thon et al. [50]	38
2.2.1.3 Methodology for uniform-shear rate bioreactor (USRB-7μm)	40
2.2.3 Bioreactor fabrication	43
2.3. Results	44
2.3.1 CFD modeling of shear rates within slit bioreactors	44
2.3.2 CFD-Driven design and assessment of a uniform-shear-rate bioreactor	49
2.3.3 Understanding shear forces in the presence of cell blockages	53
2.4 Discussion	56
2.5 Acknowledgements	58
CHAPTER 3. A uniform-shear rate microfluidic bioreactor for real-time study of proplatelet formation and rapidly-released platelets	59
3.1 Introduction	59
3.2 Materials and methods	60
3.2.1 CFD modeling	60
3.2.3 Cell culture	62
3.2.4 Bioreactor fabrication	63
3.2.5 Bioreactor effluent preparation	63

3.2.6 Confocal microscopy	64
3.2.7 Flow cytometry preparation of bioreactor effluent	64
3.2.8 Bioreactor perfusion with Mks	65
3.2.9 Video analysis	66
3.2.10 Statistical analysis	66
3.3 Results.....	67
3.3.1 Uniform-shear rate bioreactor promotes proPLT and rapid platelet-like-particle (PLP) generation from Mks	67
3.3.2 Evaluating PLP-release kinetics under different flow conditions	70
3.3.3 Characterization of PLPs collected from USRB-7 μ m	79
3.3.4 CFD analysis of changes to the outer channel flow rate	84
3.4 Discussion	93
3.5 Acknowledgements	97
CHAPTER 4: Engineering improved and scaled-up microfluidic platelet bioreactors	98
4.1 Introduction	98
4.2 Material and methods	99
4.2.1 CFD modeling – USRB-5 μ m	99
4.2.2 CFD modeling – Lung-USRB	100
4.2.3 Cell culture – Cord Blood Mks	103
4.2.4 Cell culture – mPB Mks	104
4.2.5 Bioreactor fabrication	105
4.2.6 Bioreactor perfusion with Mks – USRB-7 μ m and USRB-5 μ m	106
4.2.7 Bioreactor perfusion with Mks – Lung-USRB	106
4.2.8 Video analysis	107
4.2.9 Bioreactor effluent preparation	108
4.2.10 Flow cytometry preparation of bioreactor effluent	108
4.2.11 Confocal microscopy	109
4.3 Results.....	110
4.3.1 Cord-blood derived Mks can be trapped in USRB-7 μ m.....	110

4.3.2 New USRB-5 μ m retains a uniform shear rate environment	112
4.3.4 CB-Mks are productive in the USRB-5 μ m.....	117
4.3.5 Designing a scaled-up lung-inspired USRB device	119
4.3.6 CFD analysis of Lung-USRB: velocity, shear rate and pressure drop	123
4.3.7 Evaluating single-pass experiments in Lung-USRB with mPB and CB-Mks	131
4.3.8 Recirculation of CB and mPB-Mks through the Lung-USRB	136
4.4 Discussion	142
4.5 Acknowledgements	145
CHAPTER 5: Enabling large-scale ex vivo production of megakaryocytes from CD34⁺ cells using gas-permeable surfaces	146
5.1 Introduction	146
5.2 Materials and methods.....	148
5.2.1 Cell culture	149
5.2.2 Initial screening of high cell-surface-density experiments.....	151
5.2.3 Initial screening of low cell-surface-density experiments and media dilutions	154
5.2.4 Restricted oxygen and soft-surface studies in G-Rex	157
5.2.5 Platelet-like-particle (PLP) preparation and collection	157
5.2.6 Flow cytometry.....	158
5.2.7 Mk ploidy analysis	158
5.2.8 PLP flow cytometry	158
5.2.9 proPLT and PLP immunofluorescence microscopy.....	159
5.2.10 Aggregation flow chamber assay	159
5.2.11 Bioreactor fabrication	160
5.2.12 Bioreactor perfusion with Mks in USRB-7 μ m.....	161
5.2.13 Statistical analysis	162
5.3 Results.....	162
5.3.1 Initial cell-surface screening studies in G-Rex.....	162
5.3.2 Cell-surface density of 40 x 10 ³ cells/cm ² in G-rex improves total nucleated cell (TNC) and Mk production	165

5.3.3 G-Rex cells retain CD34 longer	169
5.3.4 G-Rex conditions have lower %high-ploidy and higher numbers of 2N and 4N Mks	172
5.3.5 G-Rex-grown Mks are capable of making proPLTs and PLPs.....	178
5.3.6 Increased Mk production is driven by media retention and an increase in Mk progenitors at higher G-Rex densities	182
5.4 Discussion	198
5.5 Acknowledgements.....	205
CHAPTER 6: Evaluating culture methods of increasing PLP production via pharmacological inhibition of Rho GTPases	206
6.1 Introduction	206
6.2 Material and methods	207
6.2.1 Cell culture	207
6.2.2 Flow cytometric analysis of Mk viability	209
6.2.3 Flow cytometric analysis of MK apoptosis	209
6.2.4 Mk ploidy analysis	209
6.2.5 Quantification of proPLT forming Mks	210
6.2.6 Bioreactor fabrication	210
6.2.7 Bioreactor perfusion with Mks.....	211
6.2.8 Bioreactor effluent preparation.....	211
6.2.9 Platelet-like-particle (PLP) preparation and collection from orbital shaker	212
6.2.10 Flow Cytometry Preparation of PLPs from orbital shaker and bioreactor	212
6.2.11 proPLT and PLP immunofluorescence microscopy.....	213
6.2.12 Statistical Analysis	213
6.3. Results.....	214
6.3.1 Screening inhibitor concentrations and assessing viability and apoptosis	214
6.3.2 proPLT formation is dependent on Rac1 but not Cdc42 or RhoA	219
6.3.3 Evaluating reversibility of Rac1 inhibition on proPLT formation	222
6.3.4 Inhibition of Rac1, Cdc42 or RhoA does not significantly impact ploidy levels in Mks	223

6.3.5 Combined inhibition of Rac1 and Cdc42 increases ploidy of Mks but with reduced proPLT formation.....	225
6.3.6 Evaluating platelet-like-particle generation from inhibited conditions	230
6.4. Discussion.....	237
6.5 Acknowledgements.....	241
CHAPTER 7: Conclusions and recommendations	242
7.1 CHAPTERS 2-4: Microfluidic bioreactors to study proPLT and PLP formation	242
7.2 CHAPTER 5: Improving megakaryocyte yields with G-Rex surfaces and fed-batch dilutions.....	244
7.3 CHAPTER 6: Increasing ploidy, proPLTs and PLPs by targeting cytoskeletal signaling pathways of Rho GTPases.....	246
7.4 Towards a scalable <i>ex vivo</i> Mk and PLP production process	248
References	250

List of Figures

Figure 1.1 Megakaryocyte and platelet generation <i>in vivo</i>	21
Figure 1.2 Overview of Rho GTPases regulation on the cytoskeleton.....	26
Figure 1.3 Overview of the goals for this work.....	28
Figure 2.1 Shear rates of published platelet bioreactors.....	31
Figure 2.2 Methodology behind the CFD simulations.....	35
Figure 2.3 CFD analysis for Nakagawa et al. bioreactor.....	37
Figure 2.4 CFD analysis for Thon et al. bioreactor.....	39
Figure 2.5 Schematic of the new uniform-shear rate bioreactor (USRB-7 μ m).....	41
Figure 2.6 CFD analysis for uniform-shear rate bioreactor (USRB-7 μ m).....	41
Figure 2.7 Individual slit shear stress range for uniform-shear rate bioreactor (USRB-7 μ m).....	42
Figure 2.8 CFD analysis of the published slit bioreactors.....	45
Figure 2.9 Individual slit shear stress range for the Nakagawa et al. bioreactor.....	47
Figure 2.10 Individual slit shear stress range for the Thon et al. bioreactor.....	48
Figure 2.11 Design concept of USRB-7 μ m and experimental set up.....	50
Figure 2.12 Qualitative validation of USRB-7 μ m flow profiles.....	51
Figure 2.13 Shear rate analysis of cell-free USRB-7 μ m.....	52
Figure 2.14 Shear analysis using 20- μ m spheres near the slits (2- μ m gap size upstream of posts).....	54
Figure 2.15 Modeling cell blockage of USRB-7 μ m slits	55
Figure 3.1 Shear-driven proPLT formation in USRB-7 μ m.....	68

Figure 3.2 Shear-driven rapid PLP release in USRB-7 μ m.....	69
Figure 3.3 PLP-release kinetics in USRB-7 μ m	71
Figure 3.4 Counting PLPs on proPLTs.....	72
Figure 3.5 Additional PLP-release kinetics in USRB-7 μ m.....	73
Figure 3.6 Pressure drop from CFD modeling of USRB-7 μ m.....	74
Figure 3.7 Number of PLP releases or active slits based on system changes.....	75
Figure 3.8 PLP release kinetics in USRB-7 μ m with no outer channel flow.....	77
Figure 3.9 Distributions of PLP release kinetics in USRB-7 μ m.....	78
Figure 3.10 Characterization of recovered PLPs from effluent.....	80
Figure 3.11 Bioreactor derived PLPs and pre-released particle analysis.....	81
Figure 3.12 Expired blood platelets in the bioreactor compared to PLPs released from Mks.....	83
Figure 3.13 Shear rate analysis of USRB-7 μ m with no outer channel flow.....	86
Figure 3.14 CFD analysis across slits along the x-axis and center height ($z = 20 \mu\text{m}$) of USRB-7 μ m.....	87
Figure 3.15 Average CFD outputs across the slits along the x-axis.....	88
Figure 3.16 Streamline observations under different outside channel flow rates.....	89
Figure 3.17 CFD streamlines overlaid on images from Mk experiments.....	90
Figure 3.18 Difference of flow structures depicted with velocity vectors.....	91
Figure 4.1 Mesh settings for uniform-shear rate bioreactor, USRB-5 μ m.....	100
Figure 4.2 Mesh settings for Lung-USRB.....	102
Figure 4.3 Cord blood-derived (CB) E8 VPA+ Mks in USRB-7 μ m.....	111

Figure 4.4 Individual slit shear stress range for uniform-shear rate bioreactor, USRB-5 μ m.....	113
Figure 4.5 Shear rate analysis and streamlines of cell-free USRB-5 μ m.....	114
Figure 4.6 Average CFD outputs across the slits along the x-axis of USRB-5 μ m.....	116
Figure 4.7 Evaluating Mk activity in USRB-5 μ m from different CB culture conditions..	118
Figure 4.8 Schematic of Lung-USRB.....	120
Figure 4.9 Design and dimensions of Lung-USRB.....	121
Figure 4.10 Fabricated Lung-USRB.....	122
Figure 4.11 Velocity analysis in Lung-USRB at $z = 20 \mu\text{m}$	126
Figure 4.12 Wall shear rate analysis in Lung-USRB.....	128
Figure 4.13 Pressure drop analysis in Lung-USRB at $z = 20 \mu\text{m}$	130
Figure 4.14 mPB-Mks generate proPLTs and PLPs in Lung-USRB.....	132
Figure 4.15 Effluent analysis of mPB-Mks from Lung-USRB at 10 $\mu\text{L}/\text{min}$	133
Figure 4.16 Effluent analysis of a non-selected CB culture from Lung-USRB at 10 $\mu\text{L}/\text{min}$	135
Figure 4.17 Recirculating a non-selected CB culture at 40 $\mu\text{L}/\text{min}$ in Lung-USRB.....	138
Figure 4.18 Effluent analysis of mPB-Mks after recirculation at 100 $\mu\text{L}/\text{min}$ in Lung-USRB.....	139
Figure 4.19 mPB-Mks recirculating through Lung-USRB at 200 $\mu\text{L}/\text{min}$	140
Figure 4.20 Effluent analysis of mPB-Mks after recirculation at 200 $\mu\text{L}/\text{min}$ in Lung-USRB.....	141
Figure 5.1 Megakaryocyte (Mk) production protocol.....	148

Figure 5.2 Preliminary screening of high surface densities in G-Rex.....	152
Figure 5.3 Screening lower surface densities in G-Rex.....	155
Figure 5.4 G-Rex at seeding density of 40×10^3 cells/cm ² (G40D) and dilutions improve overall culture productivity.....	167
Figure 5.5 CD41 ⁺ cell production of G-Rex at seeding density of 40×10^3 cells/cm ² and dilutions.....	168
Figure 5.6 G-Rex cells retain CD34 longer and exhibit increased CD34 ⁺ CD41 ⁺ cell production.....	170
Figure 5.7 G-Rex cells have lower numbers of CD34 ⁺ CD41 ⁺ cells.....	171
Figure 5.8 G-Rex with media dilutions have lower %high-ploidy but greater total Mk DNA.....	173
Figure 5.9 Ploidy distributions of G-Rex at seeding density of 40×10^3 cells/cm ² and dilutions between Days 11 and 13.....	175
Figure 5.10 G-Rex at seeding density of 40×10^3 cells/cm ² yield greater numbers of 2N, 4N and high-ploidy Mks.....	176
Figure 5.11 G-Rex Mks form proPLTs and generate PLPs.....	179
Figure 5.12 G-Rex PLP generation estimates from orbital shaker on Day 13.....	180
Figure 5.13 Analysis of proPLT and PLP generation from G40D-Mks in bioreactor.....	181
Figure 5.14 Experimental layout for variables that may affect Mk expansion in G-Rex and diluted conditions.....	182
Figure 5.15 Factors contributing to expansion in G-Rex cultures.....	184
Figure 5.16 Time profiles for conditions shown in Figure 5.15.....	186

Figure 5.17. High G-Rex surface densities have greater CD34 retention.....	187
Figure 5.18 Cells kept in G-rex until Day 7 (G40DL) vs. Day 5 (G40D) retain CD34 longer.....	188
Figure 5.19 Factors contributing to greater % Viability in G-Rex and diluted cultures.....	189
Figure 5.20 Late media exchange and IL-3 removal reduce Mk expansion.....	191
Figure 5.21 Removing G-Rex media or IL-3 late in culture diminishes culture productivity.....	193
Figure 5.22 proPLTs from various G-Rex 40 conditions.....	195
Figure 5.23 G40D and G40D-x9 PLP generation estimates from orbital shaker on Day 13.....	196
Figure 5.24 G40D and G40D-x9 PLP activation analysis.....	197
Figure 5.25 Proposed model of how G-Rex and media dilutions enhance Mk production from mPB CD34 ⁺ cells.....	201
Figure 6.1 Screening GTPase inhibitor concentrations seeded on Day 9.....	216
Figure 6.2 Inhibition of Cdc42 with ML141 impacts DAPI uptake.....	218
Figure 6.3 Analysis of proplatelet formation of inhibitor conditions.....	220
Figure 6.4 Analysis of proplatelet formation of washed Rac1 inhibitor conditions.....	222
Figure 6.5 Ploidy analysis of inhibitor conditions.....	224
Figure 6.6 Dual inhibition of Rac1 and Cdc42 increased Mk ploidy.....	227
Figure 6.7 Analysis of inhibition of Arp2/3 on Mks.....	229
Figure 6.8 Analysis of proPLT and PLP generation from inhibitor conditions in bioreactor.....	231

Figure 6.9 Analysis of PLPs collected from inhibitor conditions from bioreactor.....	232
Figure 6.10 Confocal analysis of collected PLPs from inhibitor conditions from bioreactor.....	233
Figure 6.11 Analysis of PLPs collected from inhibitor conditions from orbital shaker...	235
Figure 6.12 PLPs collected from inhibited Arp2/3 and RhoA conditions from orbital shaker.....	236
Figure 7.1 Restarting Mk productivity in stagnated environments in Lung-USRB.....	243
Figure 7.2 Towards a scalable <i>ex vivo</i> Mk and PLP production process.....	249

List of Tables

Table 2.1 Operation and details of slit platelet bioreactors.....	34
Table 2.2 Viscosity measurements conducted with a Cannon-Fenkse viscometer.....	35
Table 5.1 Experimental set-up for high cell-surface-density conditions in G-Rex.....	153
Table 5.2 Experimental set-up for low cell-surface-density and media dilution conditions.....	156
Table 5.3 Results for screening of high surface densities in G-Rex.....	163
Table 5.4 Results from screening lower surface densities in G-Rex and media dilutions.....	164
Table 5.5 Example calculations for total Mk DNA produced per input CD34 ⁺ cell for five separate mPB donors.....	177

CHAPTER 1. Introduction and Background

1.1. Clinical significance of platelet transfusions

More than 2 million platelet units are transfused each year in the US alone to treat patients with low platelet counts (thrombocytopenia) or defective platelets.[1-4] Platelets are small anucleate discoids (2–3 μm) responsible for thrombosis and hemostasis.[5] Patients who suffer from thrombocytopenia often do so due to chemotherapy side effects or bone marrow failures leading to myelodysplastic syndromes or leukemia.[6] Currently, platelet transfusions are entirely dependent on volunteer donors through apheresis or from the buffy coats of 4-8 whole blood donations. Hospitals are dependent on a steady supply of platelet donors. Disruptions of this supply together with a 5-day shelf-life of platelets can result in critical shortages.[7] In addition, because platelets require room temperature storage to maintain activity, there is significant risk of bacterial contamination developing prior to transfusion.[8] A current Good Manufacturing Practices (cGMP) process for platelet production from megakaryocytes (Mks) would allow for better control and characterization of transfusion units. This new process could transition the supply from fluctuating donors to a steady *in vitro* process. Finally, culture-derived platelet production can reduce the risk of immunogenic reactions by avoiding the need to pool from multiple donors.[7,9] As such, there is great interest in generating platelets *ex vivo* for transfusions.[10-13]

1.2. Hematopoiesis, megakaryopoiesis, and platelet release

Platelet formation begins in the bone marrow, starting with pluripotent hematopoietic stem and progenitor cells (HSPCs). These cells undergo differentiation to create different mature

blood cells, such as megakaryocytes (Mks). Throughout the Mk differentiation process, cells migrate from the osteoblastic niche to the vascular niche (**Figure 1.1**). There is also a gradient of oxygen tension – with hypoxic conditions near the bone and higher O₂ concentrations at the vasculature [14,15]. HSPCs are commonly identified by the CD34 surface marker. HSPCs acquire CD41, a marker for early commitment to Mk lineage, and lose the CD34 marker. Over time, CD42b is gained by maturing Mks. These mature Mks and the platelets they produce can be then be identified by CD41⁺CD42b⁺ surface markers.

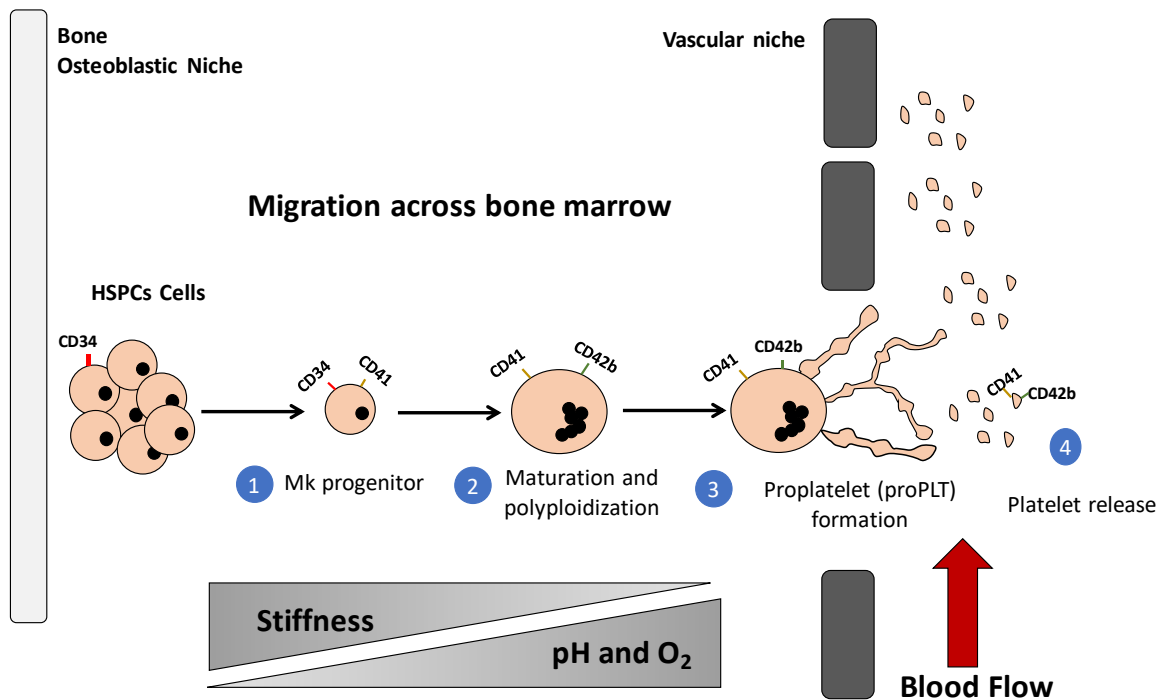


Figure 1.1 Mk and platelet generation *in vivo*. Mks are derived from HSPCs and undergo a unique maturation process and polyploidization. Finally, Mks extend proPLTs into the bone marrow sinusoids where shear forces from the blood fragment of proPLTs into platelets.

Mks go through various cycles of endomitosis (polyploidization), without cytokinesis, to give rise to high ploidy Mks.[16] *In vivo*, human Mks with ploidy as high as 128N and a modal ploidy of 16N have been observed.[17] It has been noted that higher ploidy cells likely generate more platelets.[18] *In vitro*, the instances of Mks achieving ploidy of >16N are low but the use of small molecules to promote polyploidization has led to higher ploidy levels.[19,20] Additionally, Mks generate and accumulate large amounts of intracellular membrane, forming a structure known as the demarcation membrane system (DMS). The DMS is believed to serve as a future source of membrane when platelets are released with higher ploidy Mks generating more DMS.[21,22]

At the end of maturation, Mks will undergo extensive cytoskeletal rearrangements to create proplatelets (proPLTs), which are precursors to platelets. In the bone marrow, Mks directionally extend proPLTs into the blood sinuses where shear forces elongate and fragment proPLTs into platelets. Based on intravital microscopy studies, shear stress in the bone marrow sinusoids (1.3 – 4.1 dynes/cm²) aids in shedding proPLTs from Mks.[23] High shear stress in the lung capillary bed can also process Mks into platelets[24-27], showing that a wide range of shear stresses could be used for *in vitro* platelet production. Mks also experience trans-endothelial gradients that may regulate proPLT formation. For example, the chemoattractant stromal derived factor-1 α (SDF-1 α) drives Mk migration towards the bone marrow sinusoids.[28] Sphingosine-1-phosphate (S1P), found in the blood, binds to the S1P receptor on Mks and can induce directional platelet release.[29] A second model by which Mks make platelets observes a rapid fragmentation process that releases platelets

without the propPLT formation step.[12,30] Transmission electron micrographs have shown that distinct platelet territories exist within mature Mks and fragmentation of the Mk cytoplasm would release the platelets.[31,32] Intravital microscopy studies of mice bone marrow showed Mks rapidly releasing platelets from the cytoplasm into blood vessels in response to acute platelet needs.[33]

1.3. Current state of *ex vivo* Mk and platelet-like-particle (PLP) production

The ability to generate large numbers of Mks from CD34⁺ hematopoietic stem and progenitor cells (HSPCs) has improved, now up to 1 – 100 Mks produced per input CD34⁺. [34] Media conditions and cytokine combinations are continuously being optimized to increase Mk numbers. Culture processes also increase the pH and pO₂ during culture to shift cells from a proliferative, progenitor state to the maturation stage.[35,36] Elevated temperature has also been shown to be beneficial for Mk maturation.[37,38] Mks can be derived from either umbilical cord blood (CB) or mobilized peripheral blood (mPB) HSPCs.[39-42] Also, iPSC were used to generate Mk cell lines to produce functional platelets.[43] HSPC expansion has been studied in 2D static cultures, perfusion chambers, stirred tank bioreactors, and fixed bed reactors.[44,45] Besides the 2D static cultures, the other technologies have not been evaluated specifically for Mk production. Recently, a rotary cell culture system (RCCS) that keeps cells in a continuous free falling 3D environment was used to enhance the expansion of CD34⁺ cells into PLP-producing Mks.[46] The RCCS generated higher number of CD41⁺CD42b⁺ Mks, higher ploidy Mks, and higher yield and population of CD41⁺CD42b⁺ PLPs compared to static controls.

Despite the increasing numbers of Mks produced *in vitro*, the number of Mks making proPLTs is ~10 – 20% and the number of PLPs generated per Mk remains low. *In vivo* estimates of platelet production are >1000 platelets per Mk [24]; in comparison, *in vitro* studies report <100 PLPs per Mk.[34,47] This low efficiency prevents the generation of clinically relevant numbers of platelets. Many groups, including the Miller Lab, are investigating the use of bioreactors to study and enhance *ex vivo* platelet release from mature Mks. These systems, largely microfluidic-based, have incorporated different aspects of the bone marrow niche, such as stiffness, binding proteins of the extra cellular matrix (ECM), and the presence of shear forces[48-50]. The collected PLPs from these systems have shown functionality *in vitro*. Recently, turbulence has been identified as another key environmental parameter that promotes *ex vivo* PLP production.[51] In the final step of the process, the separation of released PLPs from Mks is essential to generate a purified product of only PLPs. The Miller Lab previously showed that to separate Mks from PLPs, a commercially available spinning membrane filtration process could be used.[52] A membrane with pore sizes of 4 μm was able to obtain a clean PLP fraction that retained functionality.

1.4. Rho GTPases regulate the cytoskeleton and impact Mk maturation and proPLTs

The cytoskeleton plays a key role in the maturation of Mks by allowing them to generate proPLTs and platelets. The cytoskeleton is composed of intermediate filaments, actin fibers and tubulin assembled into microtubules. Pharmacological inhibition of actin and tubulin polymers have elucidated their importance in Mk maturation and proPLT formation. Cytochalasin B reduced actin polymerization but it did not prevent proPLT formation,

though proPLT branching was reduced.[53] Mks produced thick proPLTs and fewer extensions in the presence of taxol, a microtubule stabilizing drug.[53] Nocodazole prevented microtubule polymerization but studies showed proPLT elongation did not appear to depend on microtubule polymerization.[54] Instead, dynein-dependent microtubule sliding drives proPLT elongation and inhibition of dynein motors reduced proPLT formation in static and flow conditions.[55]

One important group of proteins that regulate the actin cytoskeleton are RhoA, Cdc42 and Rac1 GTPases (**Figure 1.2**). The activity of these Rho GTPases has been shown to impact Mk ploidy and proPLT formation.[56] RhoA is associated with stress fiber formations, focal adhesions, and regulation of actomyosin contraction.[57] RhoA activity has a negative impact on proPLT formation due to stress fibers and focal adhesion formations.[58] Inhibition of ROCK, a downstream effector of RhoA, increased proPLT formation.[59] Another RhoA effector, mDia1, was also implicated as a negative regulator of proPLT formation through its actin polymerization role and its impact on microtubule stability. Co-inhibition or knockout of mDia1 and ROCK showed an additive increase in proPLT formation.[60] RhoA is associated in the late cytokinesis step for cell division and reduced RhoA activity leads to higher ploidy Mks.[61] Mice lacking RhoA had lower number of Mks but achieved a higher modal ploidy.[62]

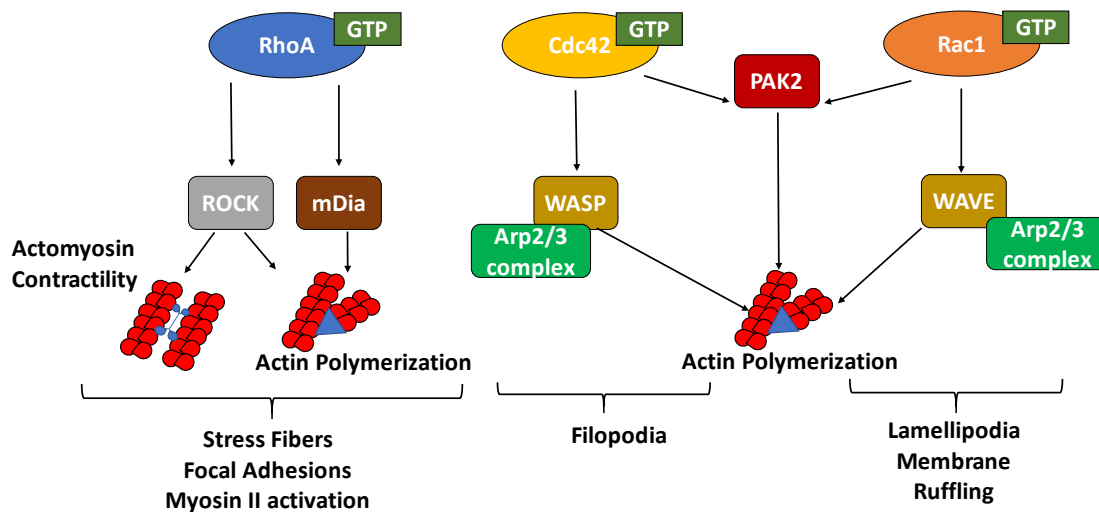


Figure 1.2 Overview of Rho GTPases regulation on the cytoskeleton. Figure summarizes key effectors and outcomes of the pathways for RhoA, Cdc42 and Rac1.

Cdc42 activity has been linked to filopodia (finger-like projections) formation in cells[63] and it is thought that the protrusion forces that Cdc42 regulates drives proPLT formation. One of Cdc42's effectors is the Wiskott-Aldrich Syndrome Protein (WASP) which functions as an actin nucleator in conjunction with the Arp2/3 complex.[64] Conditional knockout studies of Cdc42 in mouse Mks revealed mild thrombocytopenia, reduced DMS and reduction of proPLTs *in vitro*.[65] Yet, platelets from these studies were still able to normally spread on fibrinogen in the presence of thrombin.

Rac1 localizes to the leading edge of a cell and it is associated with the formation of lamellipodia (membrane protrusions).[66] Rac1 interacts with WAVE (a WASP family Verprolin-homologous protein) to drive actin nucleation and polymerization through

interaction with the Arp2/3 complex.[67,68] Conditional knockout of Rac1 in mice showed Mks with normal DMS, proPLTs formation comparable to the wild type, and no impact to blood platelet counts.[65] However, these platelets were not able to form lamellopodia or spread on fibrinogen after thrombin addition.[65,69] Several studies on different cell lines have shown that Rac1 is required for cell division and cells with dominant negative Rac1 can attain a higher DNA content.[70-73] A conditional knockout of Pak2 (effector of Rac1 and Cdc42) led to higher ploidy Mks but decreased proPLT formation, along with reduced DMS.[74] Double conditional knockouts of Rac1 and Cdc42 in mice showed severe thrombocytopenia, reduced DMS, near loss of proPLT formation, no impact to ploidy, abnormal platelet morphology, and reduced functionality of platelets.[65] These studies show the importance of Rac1 and Cdc42, and their potential impact to Mk maturation, proPLTs and ploidy.

1.5. Goals for this work

In this work (**Figure 1.3**), we aimed to improve our understanding of in vitro PLP production from Mks and develop culture processes to improve Mk and PLP yields by:

1) *Engineering microfluidic bioreactor systems to study and enhance proplatelet (proPLT) and PLP formation (Chapters 2-4)*. Recent studies have demonstrated the utility of shear forces to enhance platelet release from cultured Mks. We performed computational fluid dynamics (CFD) analysis of several published platelet microbioreactor systems to design improved microfluidic systems to study PLP generation.

2) Evaluate scalable technologies for use in HSPCs expansion into mature Mks (Chapter 5).

Developing cell-culture technologies will enable ex vivo and donor-independent platelet production. However, critical advancements are needed to improve scalability and increase Mk culture productivity. To address these needs, we evaluated Mk production from mobilized peripheral blood CD34⁺ cells cultured on a commercially available gas-permeable silicone rubber membrane, which provides efficient gas exchange, and investigated the use of fed-batch media dilution schemes.

3) Use Rho GTPase inhibitors for RhoA, Rac1 and Cdc42 to optimize proPLT formation and increase PLP yields (Chapter 6). These GTPases regulate the actin cytoskeleton and have been linked to Mk maturation and proPLT formation.[75] The impact of the inhibition will be studied in static and shear conditions from microfluidic systems designed in Chapter 2.

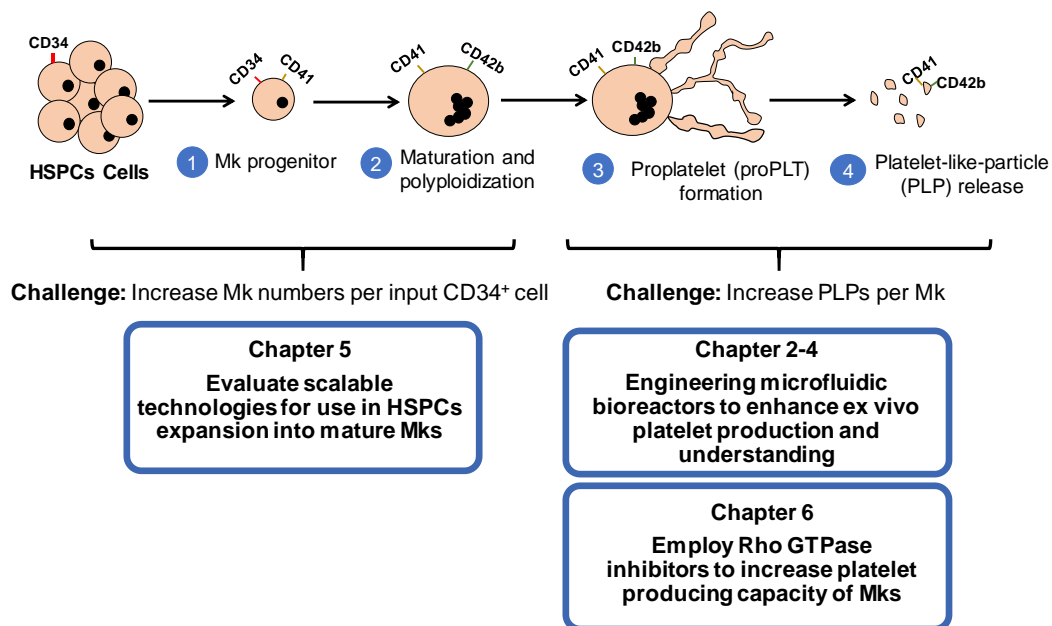


Figure 1.3 Overview of the goals for this work.

CHAPTER 2. Using computational fluid dynamics (CFD) to design and characterize an improved microfluidic platelet bioreactor with uniform-shear rates

This chapter is part of a published study[76]:

- Martinez AF, McMahon RD, Horner M, Miller WM. A uniform-shear rate microfluidic bioreactor for real-time study of proplatelet formation and rapidly-released platelets. *Biotechnology Progress*. 2017;33(6):1614-1629.

2.1 Introduction

A major challenge in the development of platelet bioreactors is that much remains unknown about the *ex vivo* initiation and regulation of proPLT formation, as well as how to maximize PLP release. The importance of shear forces has led many groups, including the Miller Lab, to investigate the use of bioreactors to study proplatelet (proPLT) formation and enhance platelet-like-particle (PLP) release from mature megakaryocytes (Mks) (**Figure 2.1**).[77] Parallel-plate flow reactors (PPFRs) are the simplest bioreactors that have been used to study proPLT/PLP formation from adhered Mks under high (1800 s^{-1})[78] and low (400 s^{-1}) shear rates.[79] However, it is difficult to carry out long-term analysis of individual Mks due to transient adhesions as Mks roll over the PPFR surface. Blin et al. improved on open-channel PPFRs by introducing an array of vWF (Von Willebrand factor)-coated columns in bioreactors.[48] The anchoring of Mks to columns, at a shear rate of 5000 s^{-1} , allowed longer Mk retention for analysis and study of the proPLT formation step. Complex niche bioreactors occupy the other end of the bioreactor spectrum. For example, a 3D silk-based

porous microtube surrounded by a silk sponge reproduced the structure of a blood sinus and the bone marrow niche.[49,80] Using a shear rate of 60 s^{-1} , the system reproduced PLP production in a physiologically relevant environment, but real-time visualization was challenging. Therefore, insight into the factors that regulate proPLT formation and PLP release could be limited since immediate changes to the proPLT formation process cannot be analyzed. Similar limitations in real-time visualizations are present for the Avanzi et al. porous membrane system through which Mks extended proPLTs into a lower chamber with shear rates of $30 - 70 \text{ s}^{-1}$. [81]

In contrast, slit bioreactors, which use small features to create $< 10\text{-}\mu\text{m}$ openings that mimic gaps or fenestrations in endothelial cells lining sinuses in the bone marrow, offer the advantage of in situ study and analysis of proPLT and PLP formation that is difficult in the other types of bioreactors. Nakagawa et al.[82] used a $4\text{-}\mu\text{m}$ slit bioreactor with unspecified shear rates and Thon et al.[50] introduced a $2\text{-}\mu\text{m}$ slit bioreactor with a shear rate of 500 s^{-1} . Although the PDMS-based fabrication of these slit bioreactors facilitate the opportunity to visualize the proPLT formation process in real-time, the flow patterns and shear rates within current systems have not been fully characterized. Developing an understanding of the bioreactor flow environment is important since non-uniformity in the flow patterns would lead to Mks experiencing different shear rates depending on slit location.

We applied computational fluid dynamics (CFD) to assess the flow environment of published slit bioreactors and showed that they generate largely non-uniform environments that could expose Mks to different shear rates based on locations. We then used those results

to develop an improved slit bioreactor with a well-characterized flow environment and uniform shear profiles across all the 7- μm slits (USRB-7 μm). In the USRB-7 μm , we performed simulations with cells present at the slits and complete blockages of slits to understand changes to the flow environment. Future work focused on introducing Mks into the USRB-7 μm and assessing proPLT and PLP generation (see Chapter 3).

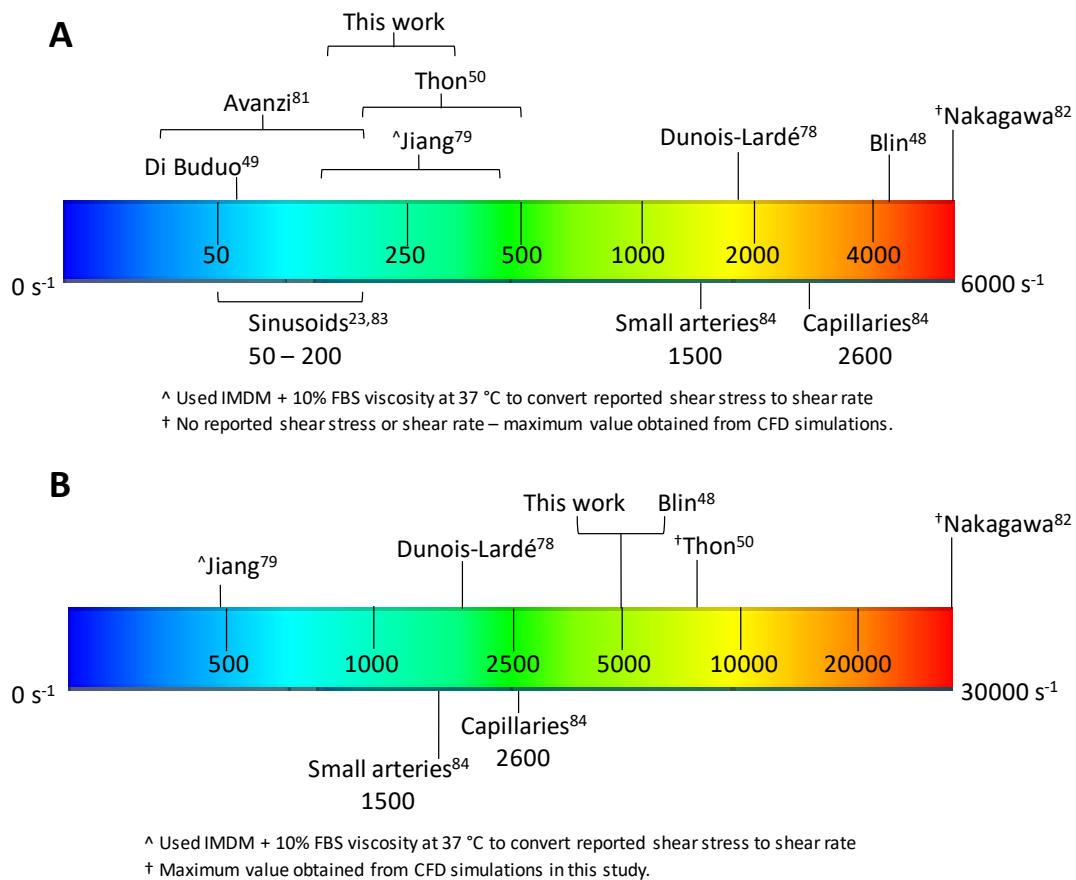


Figure 2.1 Shear rates of published platelet bioreactors. (A) Shear rate range that proPLTs experience within published bioreactor systems and this work. (B) Maximum shear rates that Mk bodies would experience within cell-free published bioreactor systems. The

maps show the wide spectrum of shear rates that have been studied in bioreactors, as well as *in vivo* values for bone marrow sinusoids[83] and the lung[84].

2.2 Materials and methods

Unless otherwise specified, all reagents were obtained from Sigma-Aldrich (St. Louis, MO), and cytokines from Peprotech (Rocky Hill, NJ).

2.2.1 CFD modeling

A summary of platelet slit bioreactors published to date is provided in **Table 1**. A description of the system and operation, as well as key dimensions, is given for each bioreactor. The slit bioreactor simulations were carried out using ANSYS version 16.1 (Canonsburg, PA) that includes the computational fluid dynamics solver FLUENT. The 3D models were created in Autodesk Inventor Professional software 2015 (San Rafael, CA). The files were converted to Parasolid binary text in Inventor and then imported into ANSYS Design Modeler. A mesh was then created for each system, in which the geometry is discretized into small volumes (elements) where the CFD calculates an approximate solution to the discretized form of the governing equations. The mesh for each individual system was optimized to yield a converging solution that is mesh-independent. The acceptance criteria used was a change in the predicted CFD velocity of no more than 5% from the previous converged solution. Boundary conditions were no-slip at the walls, constant inlet velocity, and default gauge pressure of 0 Pa at the outlet. The velocity input into each system was determined from the

volumetric flow rate and the dimensions specified by the authors. FLUENT was used to solve the steady-state form of the Navier-Stokes Equation (**Eq. 2.1**) for an incompressible Newtonian fluid subjected to the specified flow conditions. The convergence tolerance for all simulations, which is the normalized residual for each degree of freedom, was set to 10^{-3} . The overall methodology is shown in **Figure 2.2**.

$$\rho (\vec{v} \cdot \vec{\nabla} \vec{v}) = -\vec{\nabla} P + \mu \vec{\nabla}^2 \vec{v} \quad \text{Eq. 2.1}$$

$$\rho = \text{density} \left[\frac{\text{kg}}{\text{m}^3} \right], v = \text{velocity} \left[\frac{\text{m}}{\text{s}} \right], \mu = \text{viscosity} [\text{Pa} \cdot \text{s}], P = \text{pressure} [\text{Pa}]$$

Overall, the flow rates and designs lead to laminar flow conditions inside the bioreactors, such that viscous forces dominate inertial forces. Thus, the viscosity of the media used for perfusion through the systems and the operating temperature have a substantial impact on the expected shear forces within the bioreactors. **Table 2** shows our viscosity measurements for different media at 37°C. The measured fluid viscosity was used in the simulations.

All simulations for the systems were run with the following computer and software settings:

Computer Specs: Dell Precision T1700, Intel® Core™ i7-4790 CPU @ 3.60GHz, 32GB RAM, 64-bit, Windows 10 Pro

FLUENT Settings:

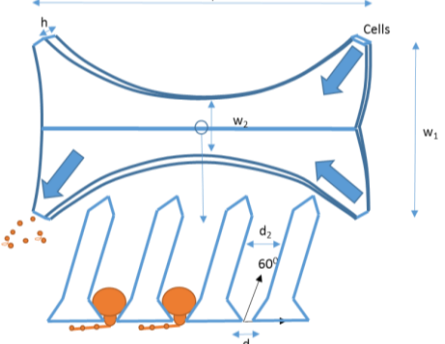
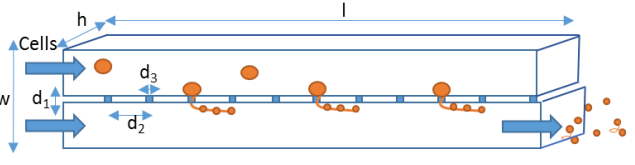
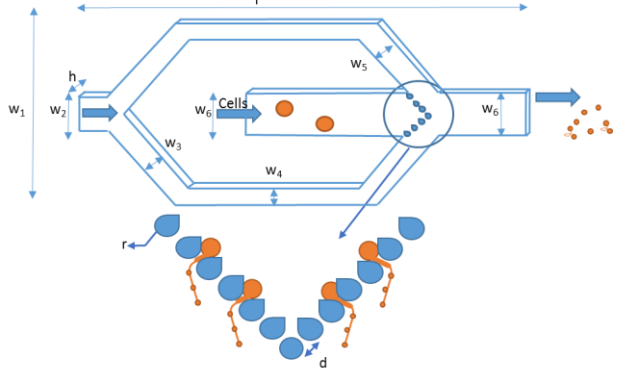
Solver: 3D, double-precision, pressure-based, parallel (8 processors)

Time: steady-state

Pressure-Velocity Coupling Scheme: Simple

Discretization: Second-order upwinding

Table 2.1 Operation and details of slit platelet bioreactors

Ref	System Operation	Key Dimensions	Process Flow Diagram
[82]	Dual-flow system made with glass bottom and PDMS chamber. Mks are captured into channels that have slit openings. One flow pushes the Mks into the slits and a second flow creates shear on the proPLTs through the slits. The slit flows are at a 60° angle.	$h = 50 \mu\text{m}$ $w_1 = 13 \text{ mm}$ $w_2 = 3.8 \text{ mm}$ $l = 25 \text{ mm}$ $d_1 = 4 \mu\text{m}$ $d_2 = 12 \mu\text{m}$	
[50]	Dual-flow system made with glass bottom and PDMS chamber. Mks are introduced into the upper chamber where Mks occupy a series of slits. A second flow on the bottom chamber creates shear on the proPLTs extended through the slits.	$h = 30 \mu\text{m}$ $w = 130 \mu\text{m}$ $l = 1.305 \text{ mm}$ $d_1 = 10 \mu\text{m}$ $d_2 = 90 \mu\text{m}$ $d_3 = 2 \mu\text{m}$	
This work	Dual-flow system made with glass bottom and PDMS chamber. Mks are introduced into the center channel, at the end of which a series of posts captures Mks at slits. A second flow splits into two flows that then converge at 90° at the outer surface of the posts to create shear on the extended proPLTs.	$h = 40 \mu\text{m}$ $w_1 = 3.5 \text{ mm}$ $w_2 = 0.707 \text{ mm}$ $w_3 = 0.5 \text{ mm}$ $w_4 = 0.354 \text{ mm}$ $w_5 = 0.5 \text{ mm}$ $w_6 = 0.9 \text{ mm}$ $l = 12 \text{ mm}$ $r = 30 \mu\text{m}$ $d = 7 \mu\text{m}$	

PDMS – Polydimethylsiloxane

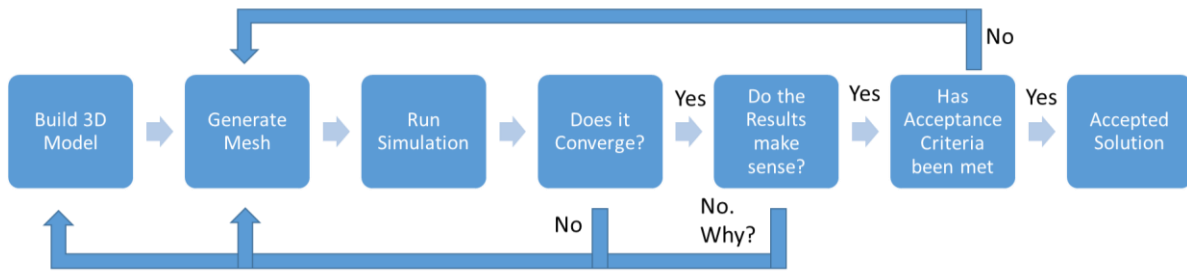


Figure 2.2 Methodology behind the CFD simulations.

Table 2.2 Viscosity measurements conducted with a Cannon-Fenkse viscometer.

	IMDM	IMDM + 20% BIT	IMDM + 10% FBS
Viscosity dynes-s/cm ²	0.0082 +/- 0.00008	0.0088 +/- 0.00005	0.0083 +/- 0.00005
System Used	Nakagawa et al.	This work	--

Thon et al. provided their own media measurement of 0.012 dynes-s/cm². [50]

2.2.1.1 Methodology for Nakagawa et al.[82]

First, the minimum element size was specified for the entire geometry. Next, the geometry was subdivided into two parts: Body and Slits. Using this approach, the 4- μm slits could be assigned a specific element size that could sufficiently resolve these small regions. The top and bottom chambers (Body) were assigned identical element sizes. The element size for the slits matched the minimum element size for the entire geometry. The mesh was further refined by reducing the slit's element size as part of the mesh-independence study. This approach avoids creating an excessive number of elements in the body region that are not needed, while resolving additional detail in the slit region. The final mesh-independent system and mesh settings are shown in **Figure 2.3A**. This bioreactor system contains a primary flow that pushes Mks into the 4- μm slits and a second flow that shears off proPLTs from Mks. Both flow rates are 16.7 $\mu\text{L}/\text{min}$, which corresponds to an inlet velocity of 5.85 cm/s. Velocity analysis of the Nakagawa et al. system focused on the flow patterns in the slits as well as the net flow along the length of the reactor (**Figure 2.3B**).

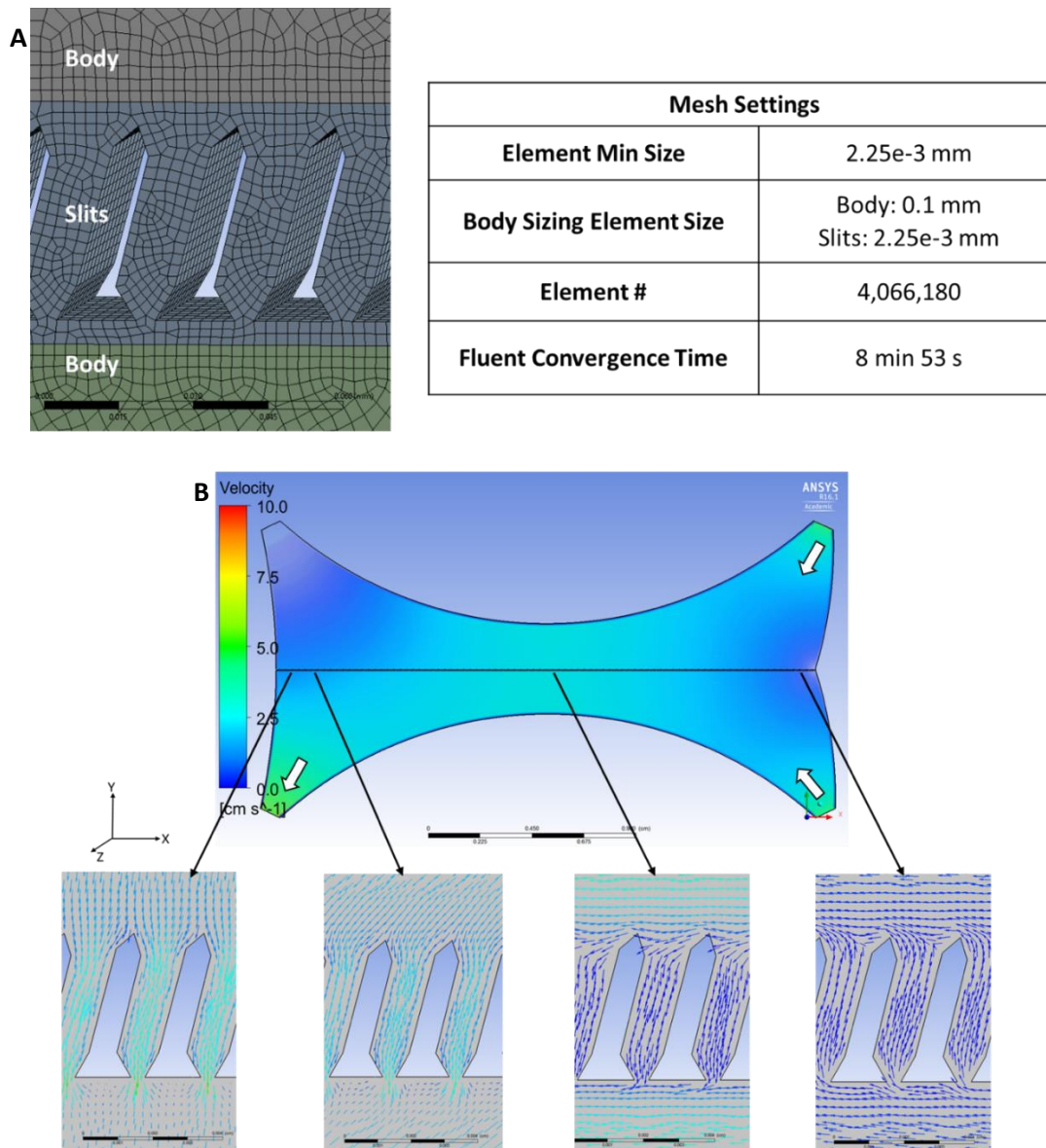


Figure 2.3 CFD analysis for Nakagawa et al. bioreactor. (A) Mesh settings used to generate the displayed mesh. The geometry has been slightly rotated to show the depth and elements across the slits. (B) Velocity profile of the reactor with insets of specific regions in the system. Inlet flow rate = $16.7 \mu\text{L}/\text{min}$ for each channel. White arrows indicate direction of flow.

2.2.1.2 Methodology for Thon et al. [50]

Similar to the approach mentioned for Nakagawa et al., the distribution of the elements in the computational mesh for the Thon et al. system was refined in the region of the slits and coarser in the parallel flow channels. The mesh was further refined by sequentially reducing the element size in the slits. The final mesh-independent system and mesh settings are shown in **Figure 2.4A**. The 2- μm slits connect parallel channels where the inlet flow rate for each channel was set to 6.25 $\mu\text{L}/\text{h}$ (total combined inlet flow rate 12.5 $\mu\text{L}/\text{h}$) corresponding to an inlet velocity per channel of 0.965 cm/s. Velocity analysis of the Thon et al. system focused on the slits and along the length of the reactor (**Figure 2.4B**).

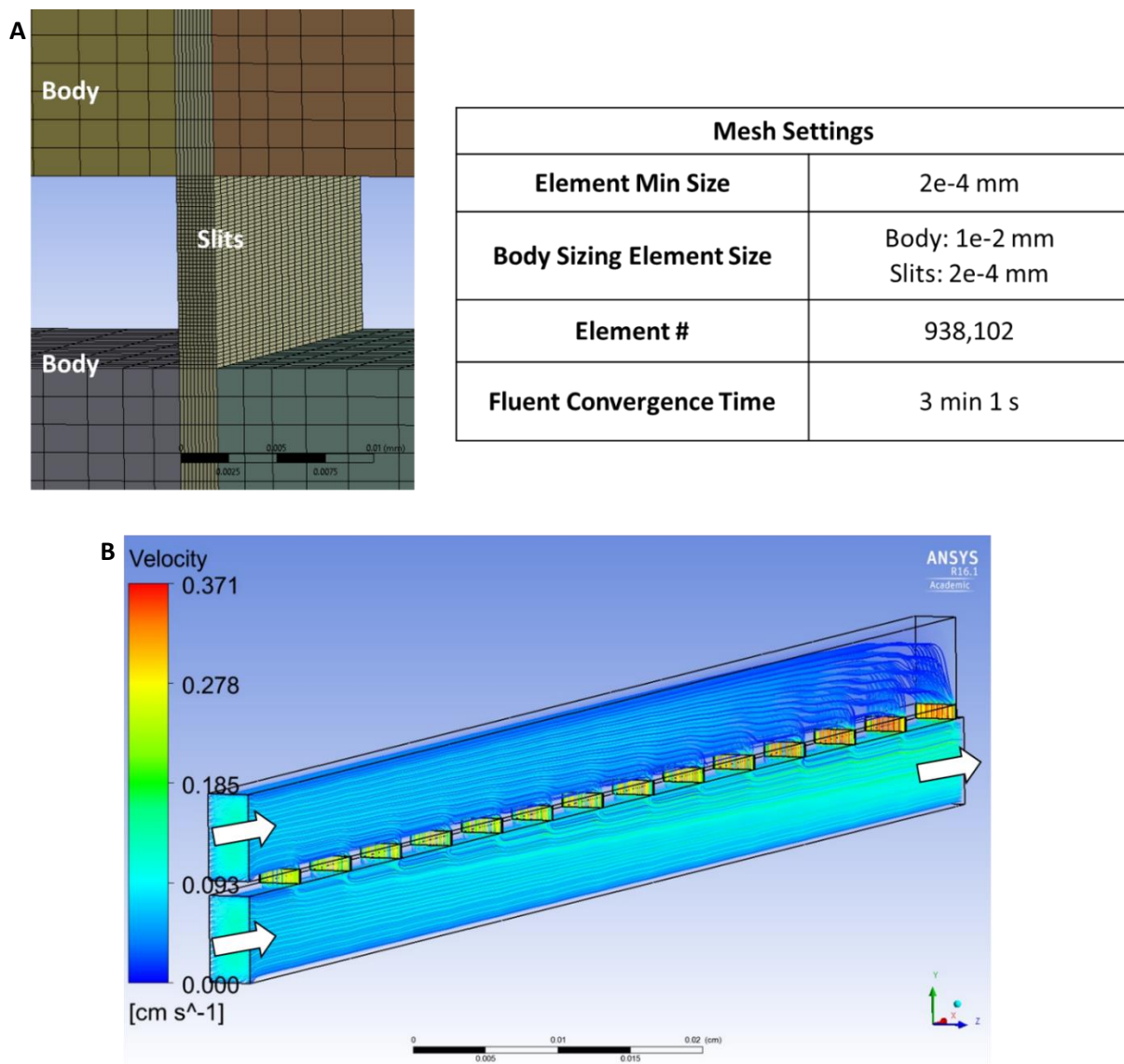


Figure 2.4 CFD analysis for Thon et al. bioreactor. (A) Mesh settings used to generate the displayed mesh. The geometry has been slightly rotated to show the depth and elements across the slits. (B) Velocity profile of the bioreactor. Combined inlet flow rate = 12.5 $\mu\text{L/hr}$. White arrows indicate direction of flow.

2.2.1.3 Methodology for uniform-shear rate bioreactor (USRB-7 μ m)

Initially, the whole system, as shown in **Figure 2.5A** was cropped to only focus on the slit region, see **Figure 2.5B**. This approach minimized the number of elements needed to analyze the system since the cropped-out regions are simple straight channels and allowed for refinement to occur mainly in the slit region. Unlike the method presented for Nakagawa et al. and Thon et al., the bioreactor was not separated into regions – Body and Slits. Rather, the proximity method in the ANSYS meshing software was used to increase the mesh resolution in the slits. The proximity method can be used to set the minimum number of element layers within gaps, e.g., slits in the bioreactor. Thus, the slits, separated by columns, can be further refined. The minimum element size and proximity size can be specified. The minimum number of element layers (number of cells across gap) further subdivides the mesh in tight regions. The number of cells across each gap was increased along with a reduction in the minimum element size, to further refine the mesh. The final mesh-independent system and mesh settings are shown in **Figure 2.6A**.

The bioreactor system contains a primary flow down the center channel that pushes Mks into the 7- μ m slits and an outer channel flow that shears off proPLTs from Mks. The center channel flow rate and the combined outer channel flow rate are both 1.5 μ L/min. Since the geometry was cropped, the input velocity of the center channel is set to 0.0694 cm/s (V_1 in **Figure 2.5B**) and the outer channel to 0.0625 cm/s (V_2 in **Figure 2.5B**). The velocity analysis of the USRB-7 μ m focused around the slits (**Figure 2.6B**). The range of shear

stresses across the slits is shown in **Figure 2.7**. Only half of the slits are presented since there is symmetry across the reactor and the other slits would have similar shear stress ranges.

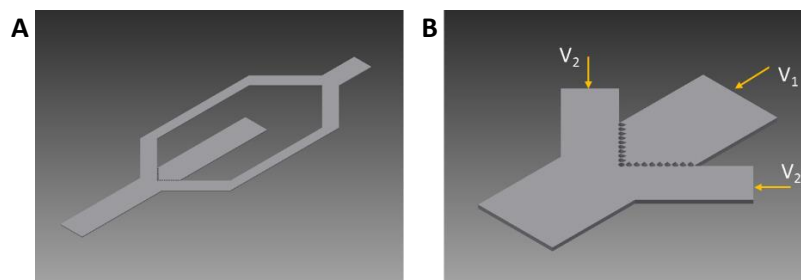


Figure 2.5 Schematic of the new uniform-shear rate bioreactor (USRB-7 μ m). Entire bioreactor (A) and cropped region in the center to isolate the slit area (B).

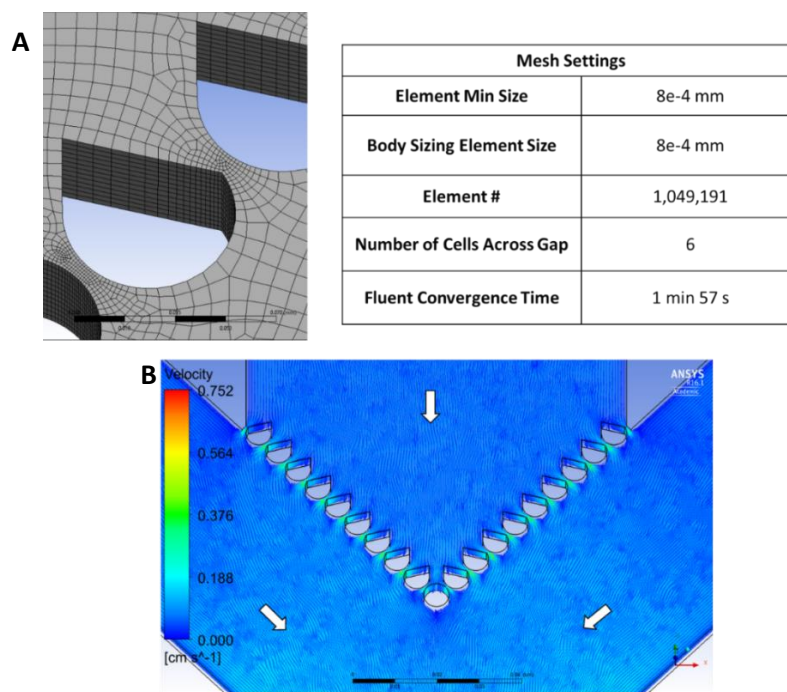


Figure 2.6 CFD analysis for uniform-shear rate bioreactor (USRB-7 μ m). (A) Mesh settings used to generate the displayed mesh. The geometry has been slightly rotated to show the depth and elements across the slits. (B) Velocity profile of the reactor. Center channel

inlet flow rate = $1.5 \mu\text{L}/\text{min}$ and outer channels inlet flow rate = $0.75 \mu\text{L}/\text{min}$ each. White arrows indicate direction of flow.

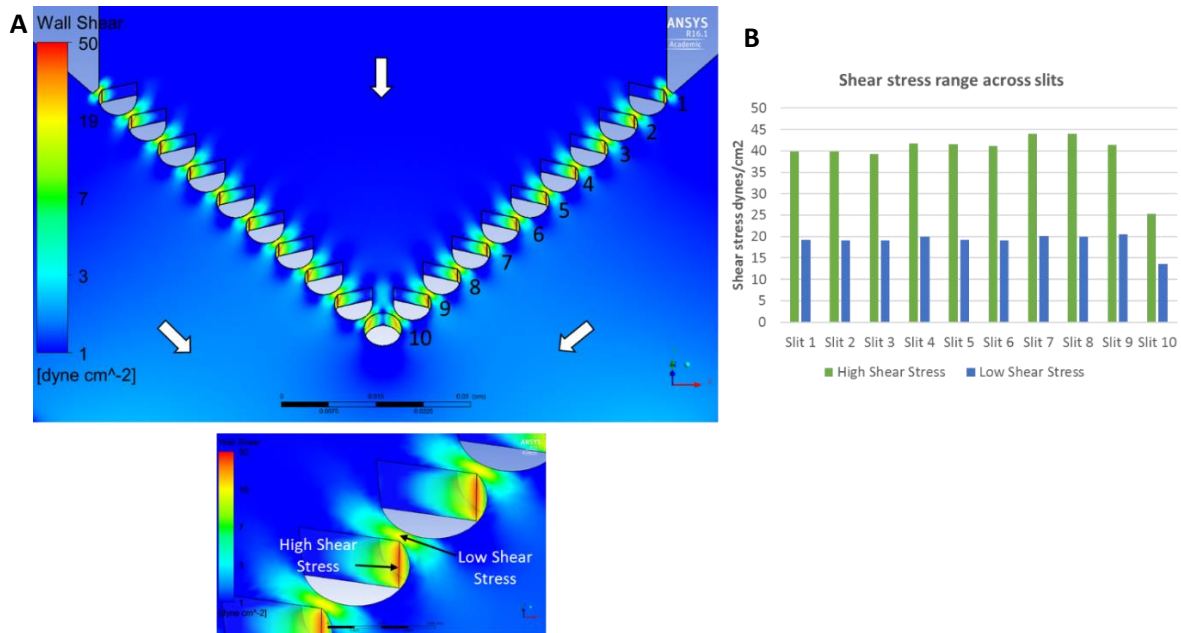


Figure 2.7 Individual slit shear stress range for uniform-shear rate bioreactor (USRB- $7\mu\text{m}$). (A) Shear stress profile for the reactor. Numbers represent slits. Inset shows the area of the slit that was designated high or low shear. (B) Range of shear stress values for all the slits. Center channel inlet flow rate = $1.5 \mu\text{L}/\text{min}$ and outer channels inlet flow rate = $0.75 \mu\text{L}/\text{min}$ each. Log-scale. White arrows indicate direction of flow

2.2.3 Bioreactor fabrication

A 2D design of the bioreactor was created in AutoCAD 2014 (San Rafael, CA) and then printed onto a chrome mask (Front Range Photomask, Palmer Lake, CO). A silicon wafer (WRS Materials, San Jose, CA) was spin-coated with SU8-2035 photoresist (MicroChem Corp, Westborough, MA) at 4000 RPM for 30 s to achieve a photoresist height of 40 μm . The wafer was soft-baked at 65°C for 3 min and then hard-baked at 95°C for 6 min. Afterwards, the wafer was exposed to UV light for 17 s using a Karl Suss MA6 Mask Aligner (SUSS MicroTec, Garching, Germany). The exposed resist was then baked at 95°C for 6 min. Finally, the resist was developed using SU8 developer solution (MicroChem) for 2 min and dried with a nitrogen gun. The dry wafer was silanized overnight (5 μL of 1H,1H,2H,2H-perfluorooctyltrichlorosilane; Alfa Aesar, Ward Hill, MA) in a vacuum chamber. Next, a 1:10 curing agent to polydimethyl siloxane (PDMS) solution (Slygard 184 Kit; Electron Microscopy Sciences, Hatfield, PA) was poured over the wafer to cast a mold that was placed in an oven at 65°C overnight. The PDMS mold was then cut, holes for inlets and outlets created with a 2-mm punch, and the PDMS plasma-bonded (Model BD-20; Electro-Technic Products, INC, Chicago, IL) to an ethanol-cleaned premium plain glass slide (25 x 75 x 1 mm; VWR, Radnor, PA).

2.3. Results

2.3.1 CFD modeling of shear rates within slit bioreactors

We used CFD to evaluate the flow and shear conditions within several slit bioreactors (**Table 1**). CFD analysis of the Nakagawa bioreactor (**Figure 2.3**), which uses 4- μm slits,[82] predicts slit shear rate that ranges from 400 s^{-1} near the inlet to 30,000 s^{-1} near the outlet (**Figure 2.8A**). The calculated shear rate on proPLT extensions in the lower chamber ranges from 200 s^{-1} near the inlet up to 6000 s^{-1} near the outlet (**Figure 2.8A**). Additionally, simulations predict a net flow from the lower chamber into the upper chamber near the bioreactor inlets (**Figure 2.3B**). Based on this CFD analysis, the flow and shear environment varies significantly across the bioreactor (**Figures 2.8A, 2.3B, Figure 2.9**).

Thon et al. analyzed their 2- μm slit reactor using CFD.[50] We also provide a CFD analysis of their system (**Figure 2.4**). Consistent with Thon et al., our simulations showed that the shear rate in the slits increases from the inlet towards the outlet of the bioreactor. The calculated shear rate in the open slits ranges from 5000 s^{-1} at the inlet to 7500 s^{-1} at the outlet (**Figure 2.8B**). Our calculated shear rate below the slits, along the lower channel wall, ranges from 250 s^{-1} near the inlet to 500 s^{-1} at the outlet (**Figure 2.8B**), similar to that reported by Thon et al.[50] This reactor provides a more uniform shear profile compared to that of Nakagawa et al. However, there is still an increase in slit-shear rates towards the bioreactor outlet (**Figures 2.8B, Figure 2.10**).

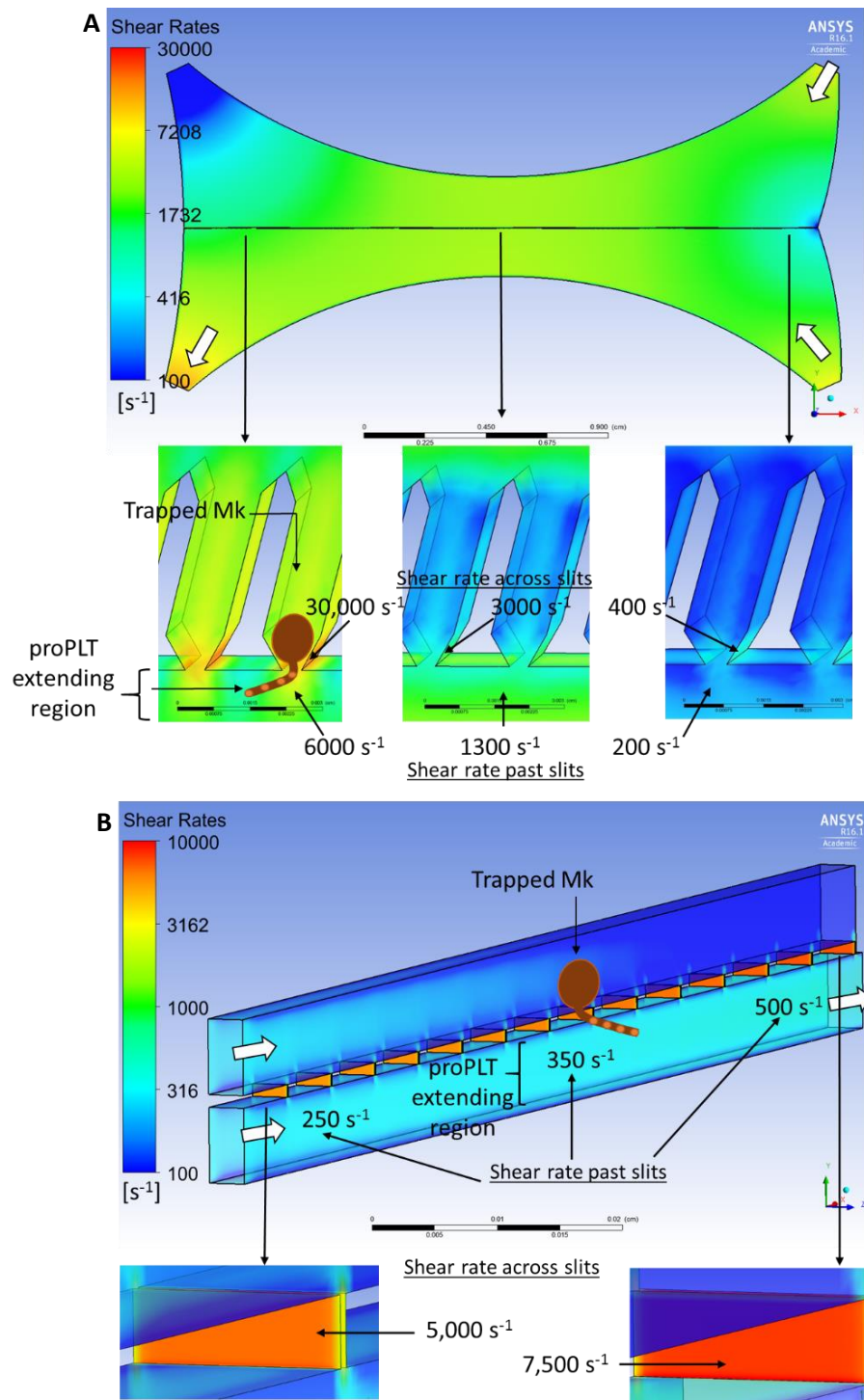


Figure 2.8 CFD analysis of the published slit bioreactors. (A) Shear profile of Nakagawa et al. system.[82] Inlet flow rates = 16.7 $\mu\text{L}/\text{min}$. (B) Shear rates in the Thon et al.

system.[50] Inlet flow rate for each channel was set to $6.25 \mu\text{L}/\text{h}$ (total combined inlet flow rate $12.5 \mu\text{L}/\text{h}$). White arrows indicate the flow direction. Insets of both systems are shown for details around the slit channels that Mks occupy (insets rotated to show all the channel walls).

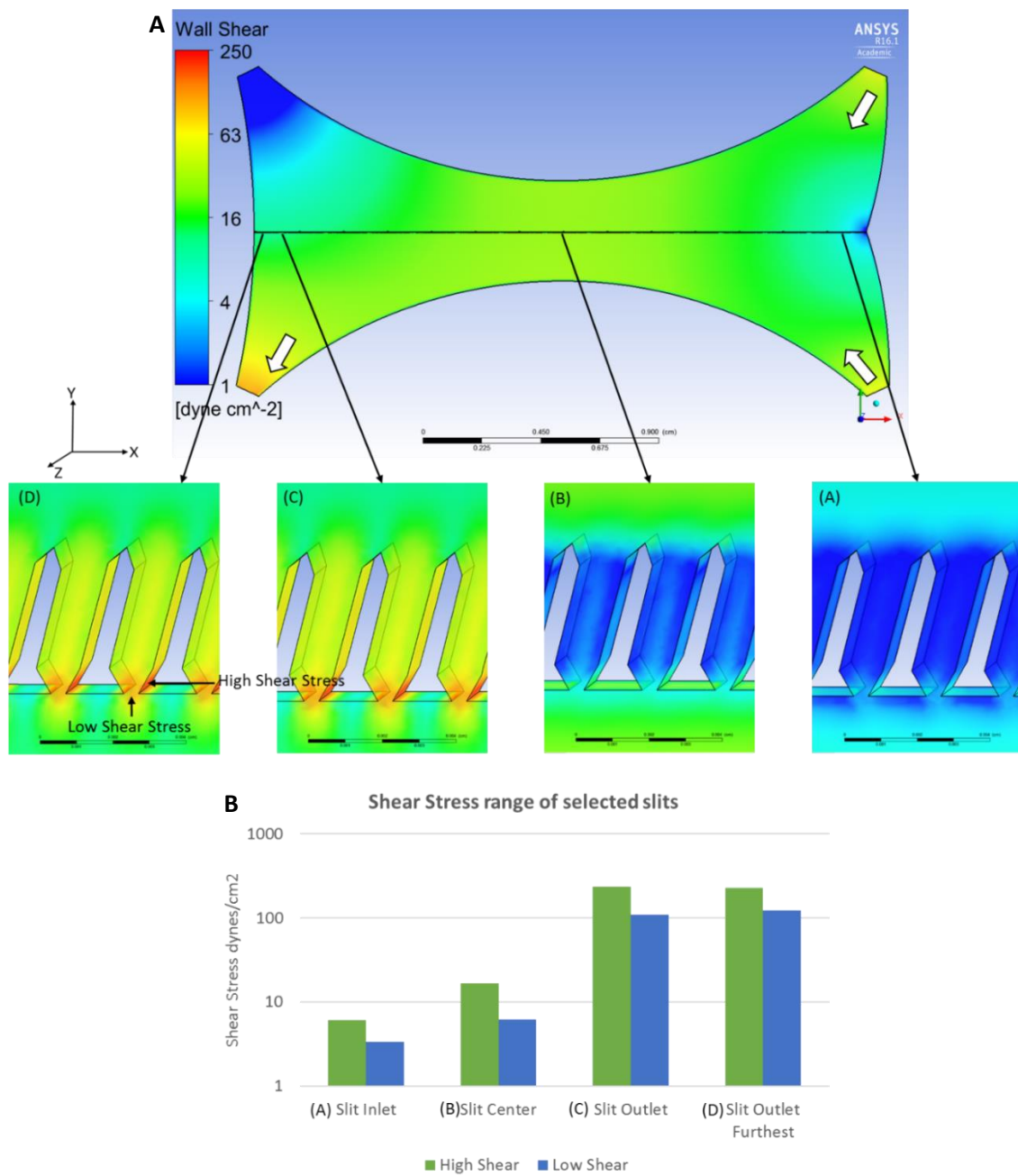


Figure 2.9 Individual slit shear stress range for the Nakagawa et al. bioreactor. (A) Shear stress profile for the reactor. Inset shows the area of the slit that was designated high or low shear. (B) Range of shear stress values for selected slits. Inlet flow rate = 16.7 $\mu\text{L}/\text{min}$ for each channel. White arrows indicate direction of flow.

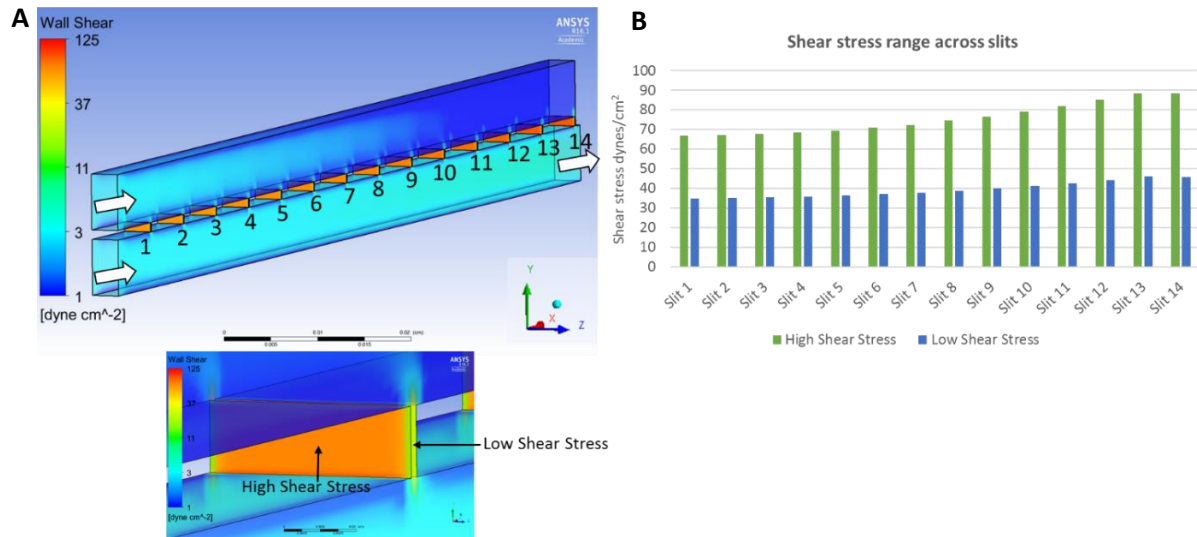


Figure 2.10. Individual slit shear stress range for the Thon et al. bioreactor. (A) Shear stress profile for the reactor. Numbers represent all the slits. Inset shows the area of the slit that was designated high or low shear. **(B)** Range of shear stress values for all the slits. Inlet flow rate = 12.5 $\mu\text{L/hr}$. White arrows indicate direction of flow.

2.3.2 CFD-Driven design and assessment of a uniform-shear-rate bioreactor

A thorough CFD analysis was conducted on potential new slit bioreactor designs to avoid the CFD-predicted non-uniform flow and shear profiles of current slit bioreactors. In our optimized bioreactor system, Mks enter a center channel where a V-shaped array of twenty 7- μm slits separates the Mks from outside flows converging at 90° (**Figures 2.5, 2.6, 2.11**). The slit dimension was chosen to retain mature Mks – usually $>20 \mu\text{m}$ – and to prevent large pressure drops and flow stagnation. The height of the bioreactor was chosen to be $40 \mu\text{m}$, similar to blood sinusoid dimensions.[83] To experimentally visualize and confirm flow patterns in the system, 1- μm fluorescent beads were used to map the streamlines of the cell-free system, and showed good agreement with the CFD streamlines (**Figure 2.12**). Uniform shear profiles across and downstream of the slits were confirmed through CFD simulations of the cell-free system. For center channel and combined outer channel flow rates of $1.5 \mu\text{L}/\text{min}$ each, the 7- μm slits have a maximum calculated shear rate of 5000 s^{-1} , except for a maximum shear rate of 2800 s^{-1} for the two slits at the end of the V where the flow in the outer channels converges (**Figure 2.7, 2.13A and B**). ProPLTs extending through the slits would experience a shear rate range from $100\text{-}200 \text{ s}^{-1}$ (past the slits in the open channel) (**Figure 2.13A and B**). Increasing the combined outer channel flow rate to $5 \mu\text{L}/\text{min}$ did not affect the shear rate through the slits (maximum remained 5000 s^{-1}), but the shear rate that would be experienced by proPLTs increased to $250\text{-}350 \text{ s}^{-1}$ (**Figure 2.13C, D**). Therefore, the USRB-7 μm allows Mks trapped at the slits and extending proPLTs to experience similar shear rates regardless of location within the bioreactor.

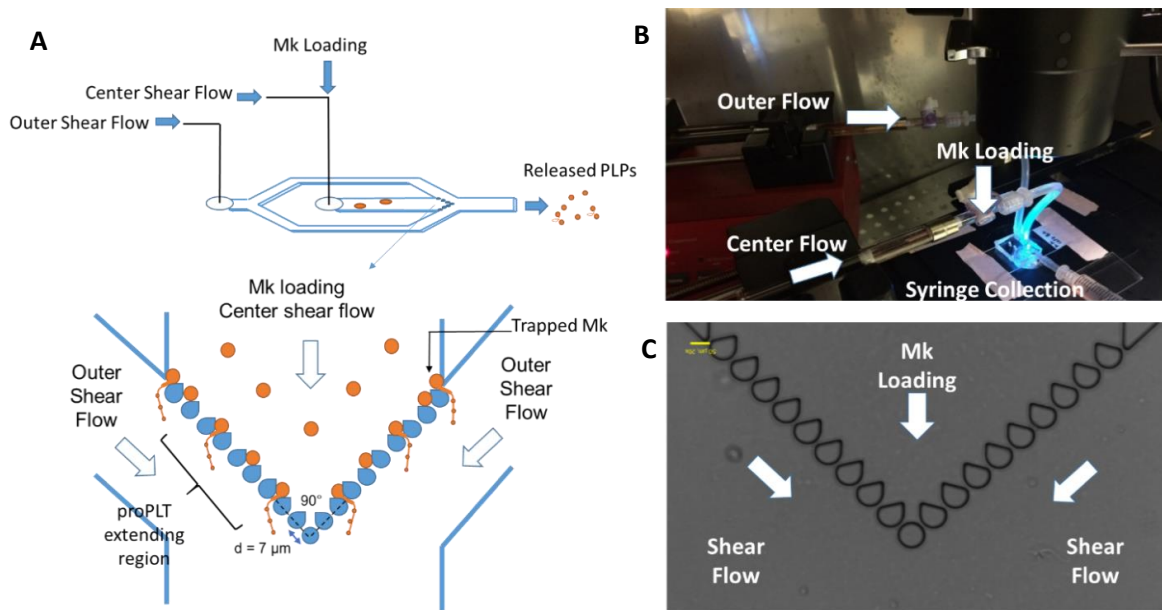


Figure 2.11 Design concept of USRB-7µm and experimental set up. (A) The newly designed system uses an array of 7-µm slits to capture Mks. Outside flows converge at the slits to apply shear forces on extending proPLTs. (B) Two syringe pumps are used for the bioreactor operation, allowing for independent flow rate changes to the center and outer channels. The bioreactor is positioned over a microscope equipped with real-time imaging in brightfield and green fluorescence. The entire system is placed inside an incubator at 37°C, 20% O₂, and 5% CO₂. (C) Cell-free fabricated bioreactor. Scale bar = 50 µm.

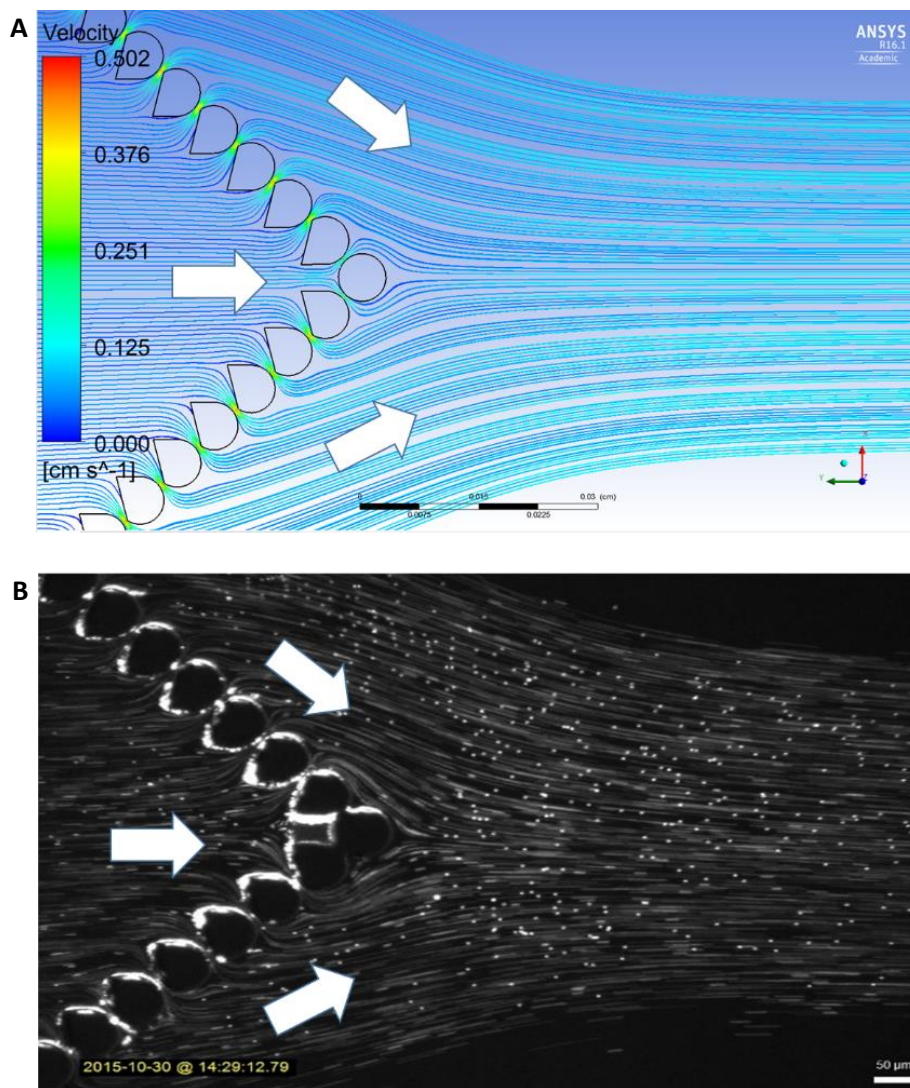


Figure 2.12 Qualitative validation of USRB-7 μm flow profiles. Comparison of streamline plots from the (A) CFD simulations and (B) experimental flow visualizations using 1- μm fluorescent beads. The flow rate is 1 $\mu\text{L}/\text{min}$ in the center channel and in the combined outer channels. White arrows indicate the flow direction. Scale bar = 50 μm .

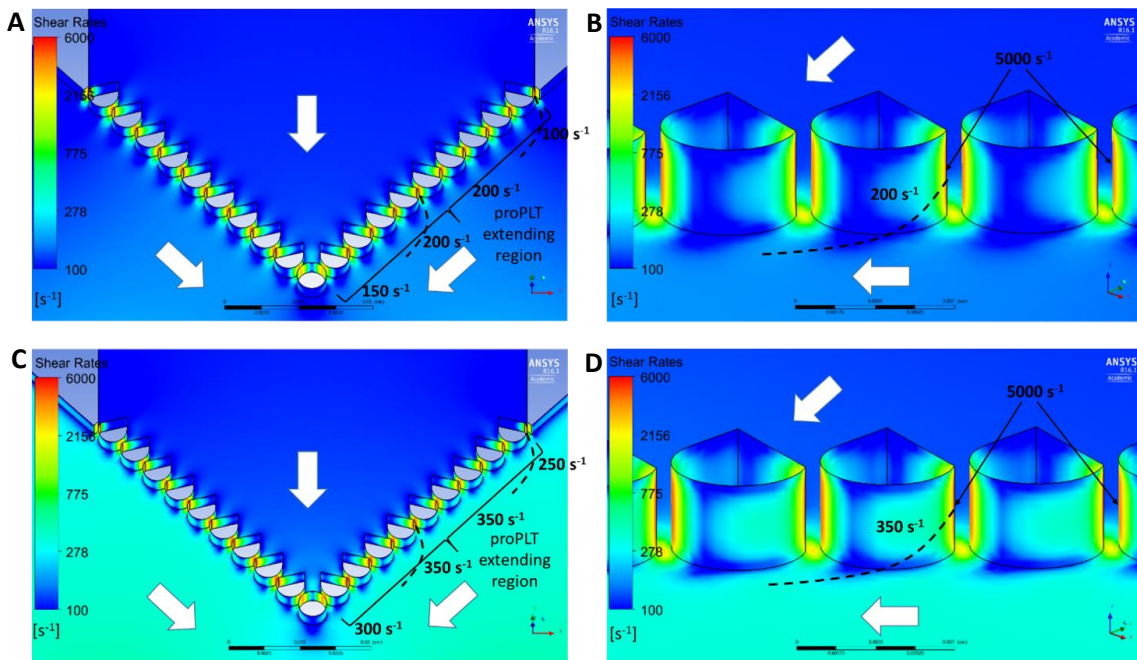


Figure 2.13 Shear rate analysis of cell-free USRB-7µm. Shear rates in the entire slit region (A) and close-up view of individual slits (B) for 1.5 µL/min flow rates in the center and combined outer channels. Shear rates through the entire region (C) and details for individual slits (D) for a flow rate of 1.5 µL/min in the center channel with 5 µL/min in the combined outer channels. White arrows indicate the general flow direction. Estimated shear rates on proPLTs (dashed lines) are within 100 µm from the slits.

2.3.3 Understanding shear forces in the presence of cell blockages

Cell-blockage scenarios for the slits were simulated using CFD, with a center channel flow rate of 1.5 $\mu\text{L}/\text{min}$ and a combined outer channel flow rate of 5 $\mu\text{L}/\text{min}$. First, 20- μm sized spheres were modeled just upstream of slits (i.e., partial blockage). The simulations predict that these cells would experience a shear rate of 1500-3000 s^{-1} (**Figure 2.14**). Second, the system was modeled with only 2 open slits by completely blocking the remaining 18 slits. ProPLTs extending past the slits are expected to experience a shear rate of 100-900 s^{-1} (**Figure 2.15A**). The shear rate is the highest (900 s^{-1}) near the 2 open slits where the velocity is the highest (**Figure 2.15A, B**). The lowest shear rate (100 s^{-1}) occurs upstream of the open slits where it appears that the flow from the open slit is re-directing the outside flow away from the slits (**Figure 2.15A, B**). Finally, similarity between the simulation streamlines and experimental streamlines was confirmed using cells and 1- μm fluorescent beads (**Figure 2.15B vs 2.15C**). Thus, CFD can help understand the flow profile, as well as estimate the shear rates, in the USRB-7 μm when Mks are trapped at the slits.

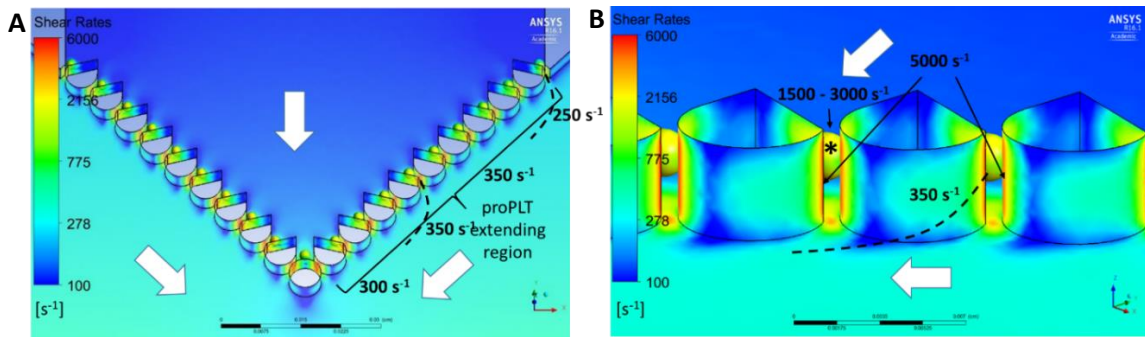


Figure 2.14 Shear analysis using 20- μm spheres near the slits (2- μm gap size upstream of posts). Center of spheres are placed at the center of the bioreactor height ($z = 20 \mu\text{m}$). Shear rates through the entire region (A) and details for individual slits (B) for a flow rate of 1.5 $\mu\text{L}/\text{min}$ in the center channel with 5 $\mu\text{L}/\text{min}$ in the combined outer channels. White arrows indicate the flow direction. Estimated shear rates on cells designated by (*). Estimated shear rates on proPLTs (dashed lines) are within 100 μm from the slits.

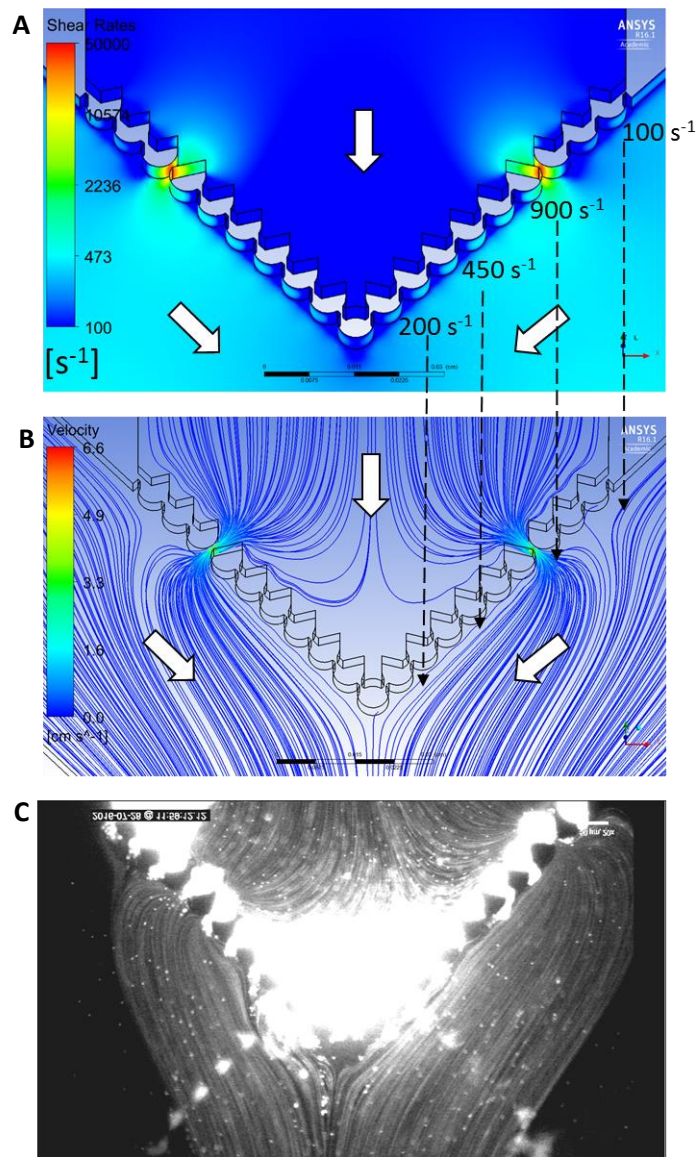


Figure 2.15 Modeling cell blockage of USRB-7 μ m slits. (A) Shear rates after blocking all but 2 of the slits. (B) Velocity streamlines of a system with 2 open slits. (C) Visualization of the system dynamics with fluorescent beads and Calcein-stained cells. Simulation and experimental flow rates were 1.5 μ L/min in the center channel with a combined flow of 5 μ L/min in the outer channels. White arrows indicate the flow direction. Estimated shear rates on proPLTs are within 100 μ m from the slits. Scale bar = 50 μ m.

2.4 Discussion

CFD modeling has been used to analyze numerous biotechnology processes[85], as well as microfluidic-based systems.[86] Using CFD to guide platelet bioreactor design, analyze forces on Mks, and examine bioreactor performance could greatly advance the design of platelet bioreactors – for which CFD has been minimally applied to-date. In this study, we used CFD to evaluate published slit bioreactors and develop a USRB-7 μ m design with improved flow and shear uniformity. The 4- μ m slit bioreactor introduced by Nakagawa et al. had no specified shear rates.[82] Therefore, we proceeded to evaluate the Nakagawa et al. system with CFD. Shear rates on proPLTs (along the length of the bioreactor) were within the sinusoids range (200 s^{-1}) and above physiological rates (6000 s^{-1}), depending on the location. However, the shear rate within the 4- μ m slits where Mks would be trapped had a much higher range of 400 – 30,000 s^{-1} . The substantial non-uniformity of shear rates along the bioreactor length might make it difficult to study proPLT/PLP formation real-time since Mks at different regions of the bioreactor would experience substantially different microenvironments.

The 2- μ m slit bioreactor developed by Thon et al. had a narrower range of shear rates than Nakagawa et al.[50] The authors used CFD to analyze their system and reported a shear rate of \sim 500 s^{-1} . Our CFD outputs showed that, along the length of the bioreactor, proPLTs would experience shear rates from 250-500 s^{-1} , confirming the author's findings, and that the slit shear rates ranged from 5000-7500 s^{-1} . Additionally, Thon et al. provided real-time visualization of the proPLT formation process. However, the shear rates within the slits

showed a steady increase along the bioreactor so that Mks trapped at various slits would be exposed to different shear rates.

CFD analysis of the Nakagawa et al. and Thon et al. systems suggests the shear rate across slits increased along the bioreactor from the inlet to the outlet. This can be attributed to the design of the systems in which two parallel-like flows are separated by slits and where the top flow (pushing on the Mks) is re-directed into the lower channel at the end of the bioreactor length (**Table 1**). To avoid generating this increase of shear rates across the slits, our new design instead converged the two outer flows at a 90° V-shaped region. This arrangement allowed the center channel flow to push whole-Mk bodies into the 7- μm slits with similar maximum shear rates of 5000 s^{-1} . The outer flow converges at the slits and exerts nearly uniform shear rates ($250\text{-}350\text{ s}^{-1}$) on extending proPLTs. Mks exiting the bone marrow sinusoids can be trapped in the vascular bed of the lung where high shear forces are exerted on the whole-cell body and on proPLTs[26,27], thus, we also aimed to utilize high shear forces on Mk bodies and physiological shear on the proPLTs. We extended our CFD analysis to include cell-blockages within the slits and confirmed the flow patterns experimentally to understand behavior of an occupied bioreactor and to estimate anticipated shear rates on proPLTs ($100\text{-}900\text{ s}^{-1}$). Next, USB-7 μm studies with Mks will increase understanding of proPLT/ PLP formation and reveal important variables and operating parameters through which *ex vivo* platelet production can be increased.

2.5 Acknowledgements

This research was supported by NSF grant CBET-1265029. Andres Martinez was supported in part by NIH Predoctoral Training Grant T32 GM008449. This work used the Micro/Nano Fabrication Facility (NUFAB) at Northwestern University. The CFD software was provided through an ANSYS Academic Partnership. We thank Dr. Marc Horner from ANSYS for valuable CFD help and Mark Duncan for initiating microfluidic bioreactor work in the lab.

CHAPTER 3. A uniform-shear rate microfluidic bioreactor for real-time study of proplatelet formation and rapidly-released platelets

This chapter is part of a published study[76]:

- Martinez AF, McMahon RD, Horner M, Miller WM. A uniform-shear rate microfluidic bioreactor for real-time study of proplatelet formation and rapidly-released platelets. *Biotechnology Progress*. 2017;33(6):1614-1629.

3.1 Introduction

Stimulating a high percentage of megakaryocytes (Mks) to undergo platelet release *ex vivo* remains a major challenge. Recent studies have demonstrated the utility of shear forces to enhance platelet release from cultured Mks. We applied computational fluid dynamics (CFD) to assess the flow environment of published slit bioreactors and used those results to develop an improved slit bioreactor with a well-characterized flow environment and uniform shear profiles across all the 7- μm slits (see Chapter 2). This uniform-shear-rate bioreactor (USRB-7 μm) allows for the real-time visualization of proplatelet (proPLT) formation. Furthermore, the environment within the USRB-7 μm promotes the rapid release of individual PLPs from Mks, which has been reported *in vivo* in mice [33], but not reported in previously published slit bioreactors that have used mouse-derived or human-derived Mks.[50,82]

We showed that modulating shear forces and flow patterns had an immediate and significant impact on PLP generation. Surprisingly, using a single flow instead of dual flows led to an unexpected 6-fold increase in PLP production. Computational fluid dynamics (CFD) modeling was then used to further understand the associated changes in the flow environment. By identifying particularly effective operating conditions within a physiologically relevant environment, the USRB-7 μ m, coupled with CFD, will be a useful tool for the study and analysis of proPLT/PLP formation that will further understanding of how to increase *ex vivo* platelet release.

3.2 Materials and methods

Unless otherwise specified, all reagents were obtained from Sigma-Aldrich (St. Louis, MO), and cytokines from Peprotech (Rocky Hill, NJ). Antibodies for flow cytometry analysis from BD Biosciences. LSR II (BD Biosciences, San Jose, CA) flow cytometer was used to collect data and analysis was done using FlowJo v.10 (FlowJo LLC, Ashland, OR).

3.2.1 CFD modeling

The USRB-7 μ m simulations were carried out using ANSYS version 16.1 (Canonsburg, PA) that includes the computational fluid dynamics solver FLUENT. The 3D models were created in Autodesk Inventor Professional software 2015 (San Rafael, CA). The files were converted to Parasolid binary text in Inventor and then imported into ANSYS Design Modeler. A mesh was created in which the geometry is discretized into small volumes (elements) where the CFD calculates an approximate solution to the discretized form of the

governing equations. The mesh was optimized to yield a converging solution that is mesh-independent. The proximity method in the ANSYS meshing software was used to increase the mesh resolution in the slits. The proximity method can be used to set the minimum number of element layers within gaps, e.g., slits in the bioreactor. Thus, the slits, separated by columns, can be further refined. The minimum element size and proximity size can be specified. The minimum number of element layers (number of cells across gap) further subdivides the mesh in tight regions. The number of cells across each gap was increased along with a reduction in the minimum element size, to further refine the mesh. The final mesh settings were element minimum size of 8×10^{-4} mm, element numbers of 1,049,191 and number of cells across gap was 6.

The acceptance criteria used was a change in the predicted CFD velocity of no more than 5% from the previous converged solution. Boundary conditions were no-slip at the walls, constant inlet velocity, and default gauge pressure of 0 Pa at the outlet. FLUENT was used to solve the steady-state form of the Navier-Stokes Equation (see Chapter 2, **Eq. 2.1**) for an incompressible Newtonian fluid subjected to the specified flow conditions. The convergence tolerance for all simulations, which is the normalized residual for each degree of freedom, was set to 10^{-3} . All simulations for the systems were run with the following computer and software settings:

Computer Specs: Dell Precision T1700, Intel® Core™ i7-4790 CPU @ 3.60GHz, 32GB RAM, 64-bit, Windows 10 Pro

FLUENT Settings:

Solver: 3D, double-precision, pressure-based, parallel (8 processors)

Time: steady-state

Pressure-Velocity Coupling Scheme: Simple

Discretization: Second-order upwinding

3.2.3 Cell culture

Previously frozen mobilized peripheral blood (mPB) CD34⁺ cells from the Fred Hutchinson Cancer Research Center (Seattle, WA) with Northwestern University Institutional Review Board approval were grown in 78% IMDM (Gibco, Carlsbad, CA), 20% BIT 9500 Serum Substitute (STEMCELL, Vancouver, BC, Canada), 1% Glutamax (Gibco), 1 µg/mL low-density lipoproteins (Calbiochem, Whitehouse Station, NJ), 100 U/mL Pen/Strep, 100 ng/mL TPO, 100 ng/mL SCF, 10 ng/mL IL-6, 10 ng/mL IL-11 and 2.5 ng/mL IL-3 (R&D Systems, Inc., Minneapolis, MN). Cells were maintained between 100,000 to 400,000 cells/mL at 37°C, 5% CO₂, and 5% O₂ for 5 days (Panasonic incubator MCO-170M, Wood Dale, IL). On day 5, the cytokines were replaced with 100 ng/mL TPO, 100 ng/mL SCF, 10 ng/mL IL-9, 10 ng/mL IL-11 and 10 ng/mL IL-3. Cells were maintained at a density of 250,000 to 500,000 cells/mL and kept at 37°C, 5% CO₂, and 20% O₂ until day 7. On day 7, cells were selected using anti-CD61-conjugated magnetic microbeads (Miltenyi Biotech Inc, San Diego, CA) and then cultured in medium with 100 ng/mL TPO, 100 ng/mL SCF and 6.25 mM nicotinamide thereafter. The cells were maintained at a density between 250,000 to 500,000 cells/mL and kept at 37°C, 5% CO₂, and 20% O₂.

3.2.4 Bioreactor fabrication

A 2D design of the bioreactor was created in AutoCAD 2014 (San Rafael, CA) and then printed onto a chrome mask (Front Range Photomask, Palmer Lake, CO). A silicon wafer (WRS Materials, San Jose, CA) was spin-coated with SU8-2035 photoresist (MicroChem Corp, Westborough, MA) at 4000 RPM for 30 s to achieve a photoresist height of 40 μm . The wafer was soft-baked at 65°C for 3 min and then hard-baked at 95°C for 6 min. Afterwards, the wafer was exposed to UV light for 17 s using a Karl Suss MA6 Mask Aligner (SUSS MicroTec, Garching, Germany). The exposed resist was then baked at 95°C for 6 min. Finally, the resist was developed using SU8 developer solution (MicroChem) for 2 min and dried with a nitrogen gun. The dry wafer was silanized overnight (5 μL of 1H,1H,2H,2H-perfluorooctyltrichlorosilane; Alfa Aesar, Ward Hill, MA) in a vacuum chamber. Next, a 1:10 curing agent to polydimethyl siloxane (PDMS) solution (Slygard 184 Kit; Electron Microscopy Sciences, Hatfield, PA) was poured over the wafer to cast a mold that was placed in an oven at 65°C overnight. The PDMS mold was then cut, holes for inlets and outlets created with a 2-mm punch, and the PDMS plasma-bonded (Model BD-20; Electro-Technic Products, INC, Chicago, IL) to an ethanol-cleaned premium plain glass slide (25 x 75 x 1 mm; VWR, Radnor, PA).

3.2.5 Bioreactor effluent preparation

Effluent collected was spun once at 2200 g for 20 min to pellet Mks and PLPs. The pellet was then resuspended in HEPES/Tyrode's (HT) buffer (10 mM HEPES, 137 mM NaCl, 2.8 mM KCl, 1 mM MgCl₂, 12 mM NaHCO₃, 0.4 mM Na₂HPO₄, 0.35% BSA, 5.5 mM glucose,

pH 7.4) and allowed to rest for 20 min at room temperature. 2 mM CaCl₂ was added to the suspension 5 min before use in assays.

3.2.6 Confocal microscopy

Effluent collected from the bioreactor was analyzed via immunofluorescence. 8-well chamber glass slides (125658, Lab NunTek II, Thermo Scientific, Waltham, MA) were coated with fibrinogen (Innovative Research, Novi, MI) at 60 µg/mL in PBS or 1% BSA in PBS. The effluent suspension was added to each well and allowed to rest at 37°C for 20 min and then 3 U/mL of thrombin was added to one of the wells coated with fibrinogen, and incubated for 30min at 37°C, 5% CO₂. The chamber slide was washed once with warm PBS with Ca²⁺ and Mg²⁺ and then fixed with 3.7% paraformaldehyde and permeabilized with 0.3% Triton X-100 before sequentially staining with 5 µg/mL mouse anti-beta-tubulin primary antibody (5656321, BD Biosciences), and 1 µg/mL of Alexa Fluor 488-conjugated goat anti-mouse secondary antibody (A11001, Thermo Scientific). After removing unbound secondary antibody, wells were incubated with TRITC-phalloidin, washed, and then stained with DAPI (Invitrogen, Carlsbad, CA) to identify Mk bodies from anucleate proplatelets and platelet-like-particles (PLPs). Slides were imaged with a 63x oil objective on a Leica DMI6000 Spinning Disc Confocal Microscope (Leica, Wetzlar, Germany).

3.2.7 Flow cytometry preparation of bioreactor effluent

Effluent from the bioreactor was analyzed for surface markers using the following antibodies: CD41-APC (559777), CD42b-PE (555473), CD62P-BV421 (564038). Effluent

suspension was aliquoted into 0.65-mL polypropylene tubes, respective antibodies added, and thrombin at 3 U/mL was added to activate PLPs. Samples were incubated for 15 min at room temperature (RT). Samples were run on a LSRII Flow Cytometer (BD Biosciences). Prior to perfusion through the bioreactor, Mks were stained with live stain Calcein AM so viable PLPs in the effluent also carried this live stain. Calcein⁺ PLP events were identified. Expression of markers on PLPs was compared to an unactivated (no thrombin), stained sample.

3.2.8 Bioreactor perfusion with Mks

The USRB-7 μ m was positioned on a Lumascope microscope v500 (Etaluma Inc., Carlsbad, CA) placed inside an incubator (Thermo Scientific, Waltham, MA) maintained at 37°C and 5% CO₂. Separate syringe pumps (NE-300, New Era Pump Systems Inc., Farmingdale, NY) were used for each flow channel. A 5-mL glass syringe (81520, Hamilton Company, Reno, NV) was used for the outer channels and a 2.5-mL glass syringe (81420, Hamilton) was used for the center channel. Media (78% IMDM (Gibco, Carlsbad, CA), 20% BIT 9500 Serum Substitute (STEMCELL, Vancouver, BC, Canada), 1% Glutamax (Gibco), 1 μ g/mL low-density lipoproteins (Calbiochem, Whitehouse Station, NJ), 100 U/mL Pen/Strep) without cytokines was perfused throughout the bioreactor for 30 min at 6.5 μ L/min prior to Mk introduction. On day 10, 11, or 12 of Mk culture, Mks at density of 50,000/mL were stained for 15 min with 1 μ M Calcein AM at 37°C. After the 30-min media perfusion, 25,000 Mks (a sufficient number to observe the system dynamics and how often they might repeat and under what conditions, without clogging the slits) were microinjected into the tubing

upstream from the reactor. No Mks were present within the syringes. A video was recorded of each bioreactor for 1-2 hrs.

3.2.9 Video analysis

Videos (6 frames-per-second) were recorded for each experimental run using the Lumascope v500, equipped with High Sensitivity Monochrome CMOS Sensor camera, using a 20x or 40x objective. Each video was analyzed for every 5-min time interval for the duration of an experiment. One half of the bioreactor (10 slits) was analyzed at one time throughout 5-min time intervals for the entire video recorded. This process was repeated on the other half of the reactor. The data from each half of the reactor was then combined for each 5-min time interval. During each interval, only proPLTs and PLPs that originated from trapped Mks the slits were counted. Additionally, for some videos, pre-released particles flowing into and out of the slits were counted separately. Mks can give rise to particles without shear and these could be present in the suspension that was microinjected into the system. To increase accuracy, the videos were played at a slower speed during times of high PLP release activity. The 5-min interval was selected because it allowed us to effectively analyze and understand the dynamics of the process. Pre-staining Mks with Calcein AM allowed the Mks trapped in the reactor, as well as proPLTs/PLPs, to be clearly observed.

3.2.10 Statistical analysis

JMP Pro 11 (SAS Institute Inc., Cary, NC) was used to generate histograms, distributions, and standard errors of mean (SEM) of the video analysis data for released proPLTs/PLPs.

3.3 Results

3.3.1 Uniform-shear rate bioreactor promotes proPLT and rapid platelet-like-particle (PLP) generation from Mks

After design and fabrication of the USRB-7 μ m (Chapter 2, **Figure 2.11**), and validation of the flow patterns (Chapter 2, **Figure 2.12** and **Figure 2.15C**), the capability of the system to promote proPLT formation from mobilized peripheral blood (mPB)-derived Mks was assessed. Experiments showed that, depending on the size of the trapped Mks, 1-3 cells can occupy a slit. Importantly, the shear environment within the USRB-7 μ m could stimulate proPLT formation from trapped Mks (**Figure 3.1**). Mks were stained with Calcein to allow clearer visualization of the proPLT formation process (**Figure 3.1A**). Trapped Mks within the slits extruded their bodies and elongated into the characteristic proPLTs with beads-on-a-string morphology (**Figure 3.1B**, **Video 1**). Interestingly, the USRB-7 μ m microenvironment also promoted trapped Mks to release individual PLPs directly from their bodies. Some Mks, immediately after slit capture, rapidly released dozens of PLPs within seconds (**Figure 3.2**, **Video 2**).

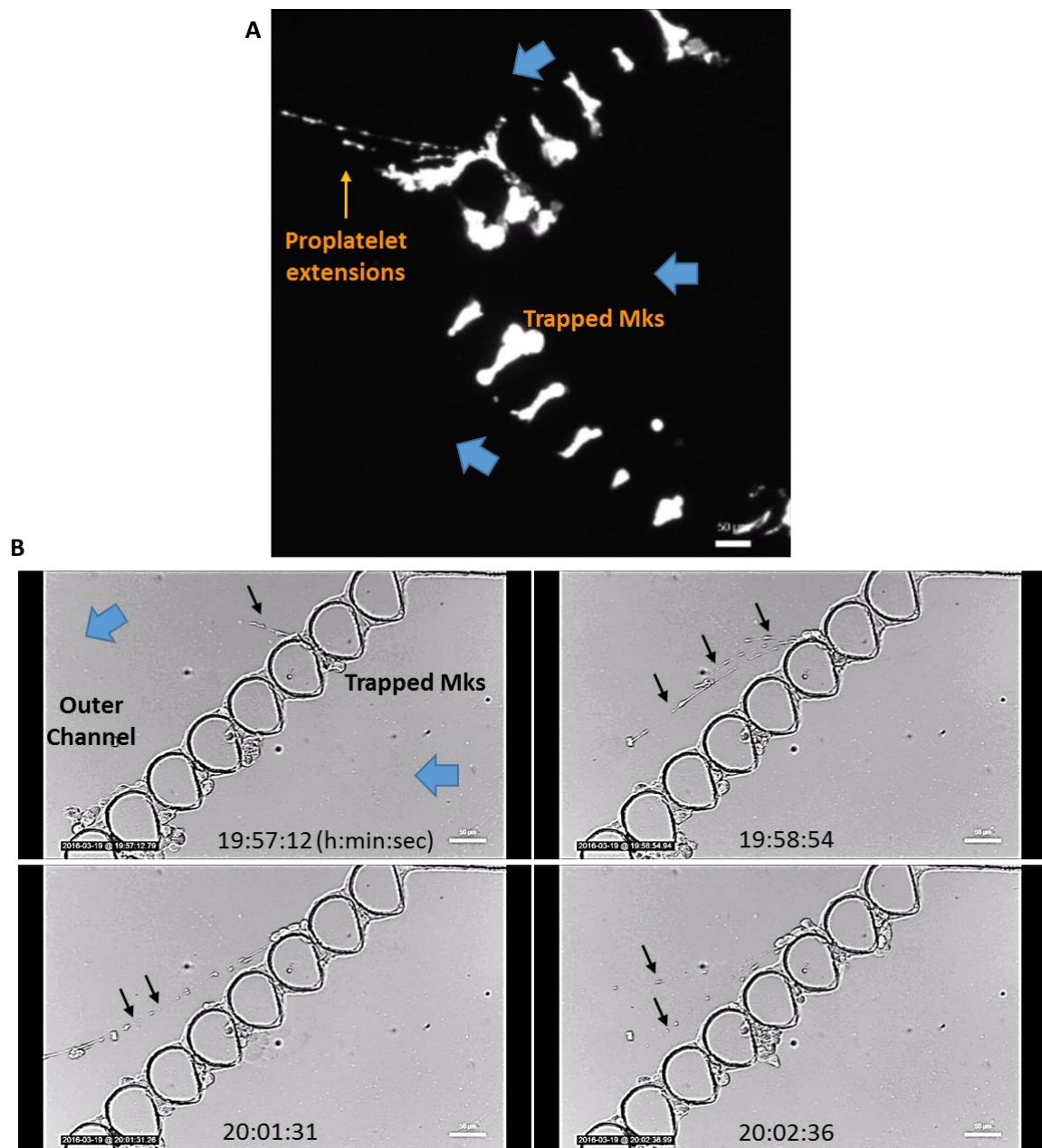


Figure 3.1 Shear-driven proPLT formation in USRB-7 μ m. (A) Green fluorescence observation of Calcein-labeled Mks with proPLT formation. (B) Brightfield time-lapse images of cells trapped in a slit and exposed to shear. The center channel flow elongates Mks through the slits. Flow in the outer channels applies shear on the extensions further

elongating them leading to fragmentation after several minutes. Black arrows indicate proPLTs. Scale bars = 50 μm . Flow rate of 1.5 $\mu\text{L}/\text{min}$ in the center channel with 5 $\mu\text{L}/\text{min}$ in the combined outer channels. Blue arrows show direction of flow.

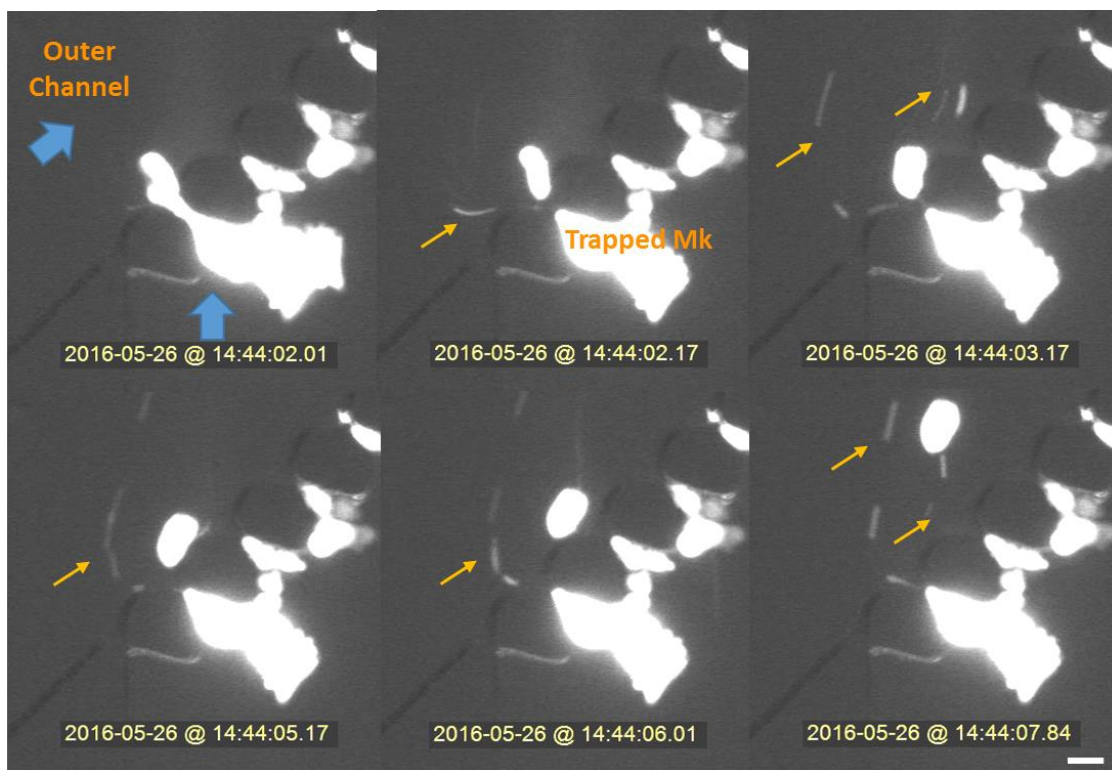


Figure 3.2 Shear-driven rapid PLP release in USRB-7 μm . Time-lapse images of trapped Mks in a slit, rapidly releasing many individual PLPs in seconds. Time units: h:min:s. Orange arrows point to individual PLPs. Scale bar = 35 μm . Blue arrows show direction of flow. Flow rate of 1.5 $\mu\text{L}/\text{min}$ in the center channel with 5 $\mu\text{L}/\text{min}$ in the combined outer channels.

3.3.2 Evaluating PLP-release kinetics under different flow conditions

We analyzed the kinetics of the USRB-7 μ m to identify conditions that change Mk behavior by counting the number of Calcein-stained PLPs that originate from Mks trapped at the slits per 5-min time interval across individual experimental runs (**Figure 3.3**). The number of PLPs-on-a string that were observed on proPLTs were also counted as released PLPs (**Figure 3.4**) and we estimated that ~30% of PLPs released were from proPLTs. We observed that, when an incoming Mk blocked the flow of an open slit, proPLT/PLP formation and the number of slits making PLPs greatly increased within the bioreactor (**Figure 3.3A – green arrows, Video 3**). The blockage most likely increased the pressure drop across the slits, thus, trapped Mks were exposed to an immediate higher pressure and shear that increased their productivity. This observation led us to hypothesize that introducing a step-increase in the center channel flow rate may mimic the effects of cell-blockage. Indeed, similar responses after multiple step-increases in flow rate were observed during five separate experimental runs (**Figure 3.3B, Figure 3.5A**). The calculated CFD pressure drop across the slits increased continuously as more slits were occupied, especially when few slits remained open (**Figure 3.6A**). Further, increasing the flow rate of the system with a constant number of open slits increased the calculated CFD pressure drop across the slits in a linear manner (**Figure 3.6B**). The experimental observations and CFD analysis support our hypothesis that a pressure drop increase by a blockage event or flow rate change could increase Mk productivity, as both types of changes increased the immediate number of PLPs released by ~3-fold and the number of active slits by 30-50% (**Figure 3.7**).

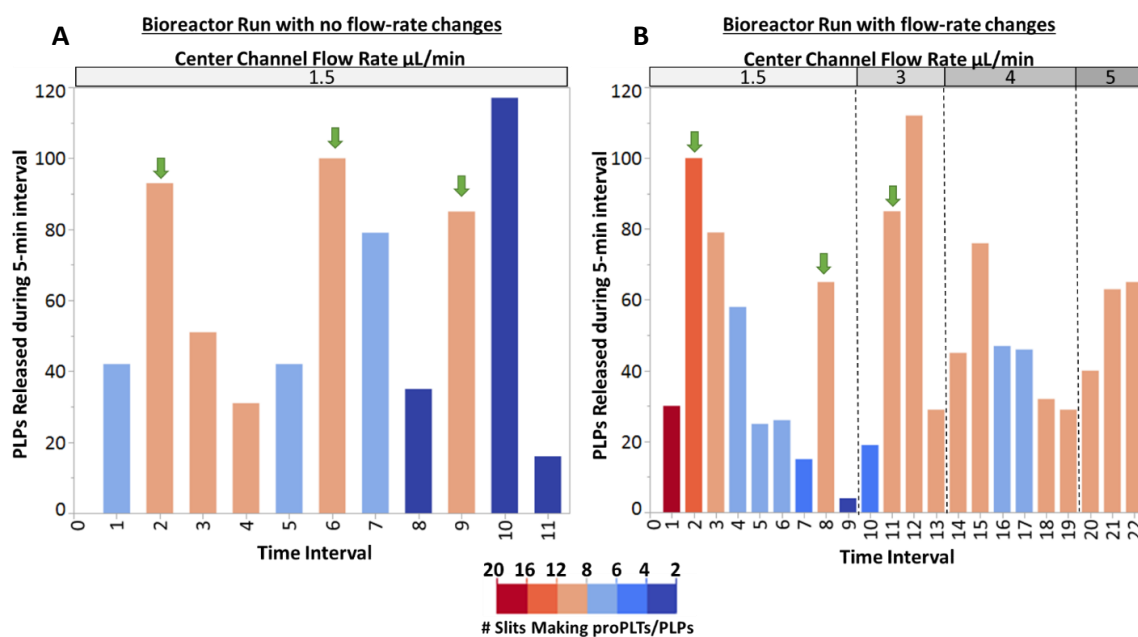


Figure 3.3 PLP-release kinetics in USRB-7 μm . (A) Number of PLPs released per 5-min time interval during a bioreactor run with constant center channel flow rate (indicated above plot) and three significant cell blockages of open slits during that time interval denoted by green arrows. (B) Number of PLPs released per 5-min time interval during a bioreactor run with three center channel flow rate increases (dashed lines - indicated above plot) and three significant cell blockages of open slits denoted by green arrow. For (A) and (B), combined outer channels flow rate = 5 $\mu\text{L}/\text{min}$. Color legend in (A) and (B) depicts the number of slits making PLPs during each 5-min time interval.

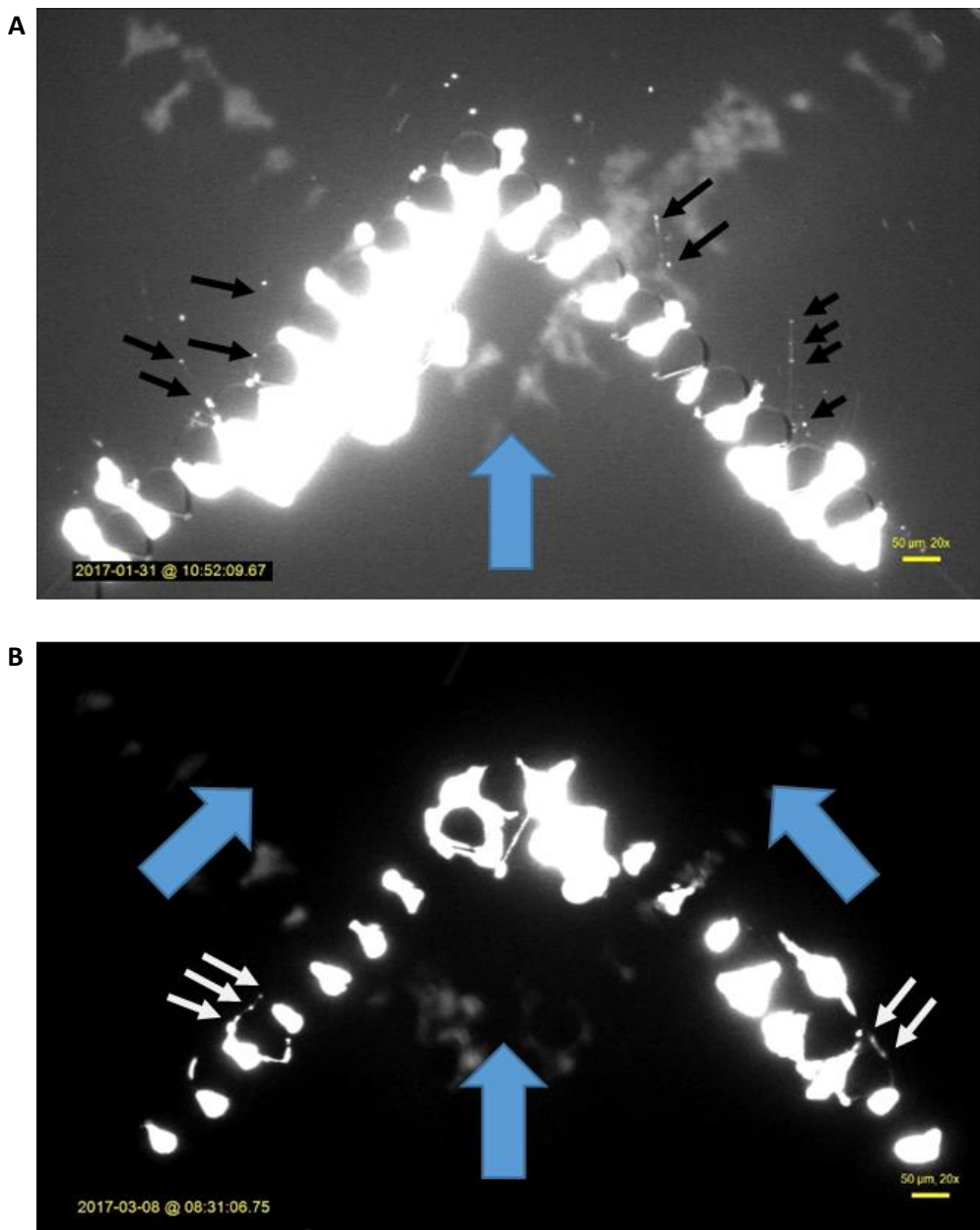


Figure 3.4 Counting PLPs on proPLTs. (A) Images of Calcein-stained Mks extending proPLTs; black arrows indicate the PLPs that were counted on these proPLTs (0 $\mu\text{L}/\text{min}$ outer channel combined flow rate). (B) Images of Calcein-stained Mks extending proPLTs; white arrows indicate the PLPs that were counted on these proPLTs (5 $\mu\text{L}/\text{min}$ outer channel combined flow rate). Blue arrows indicate the flow direction.

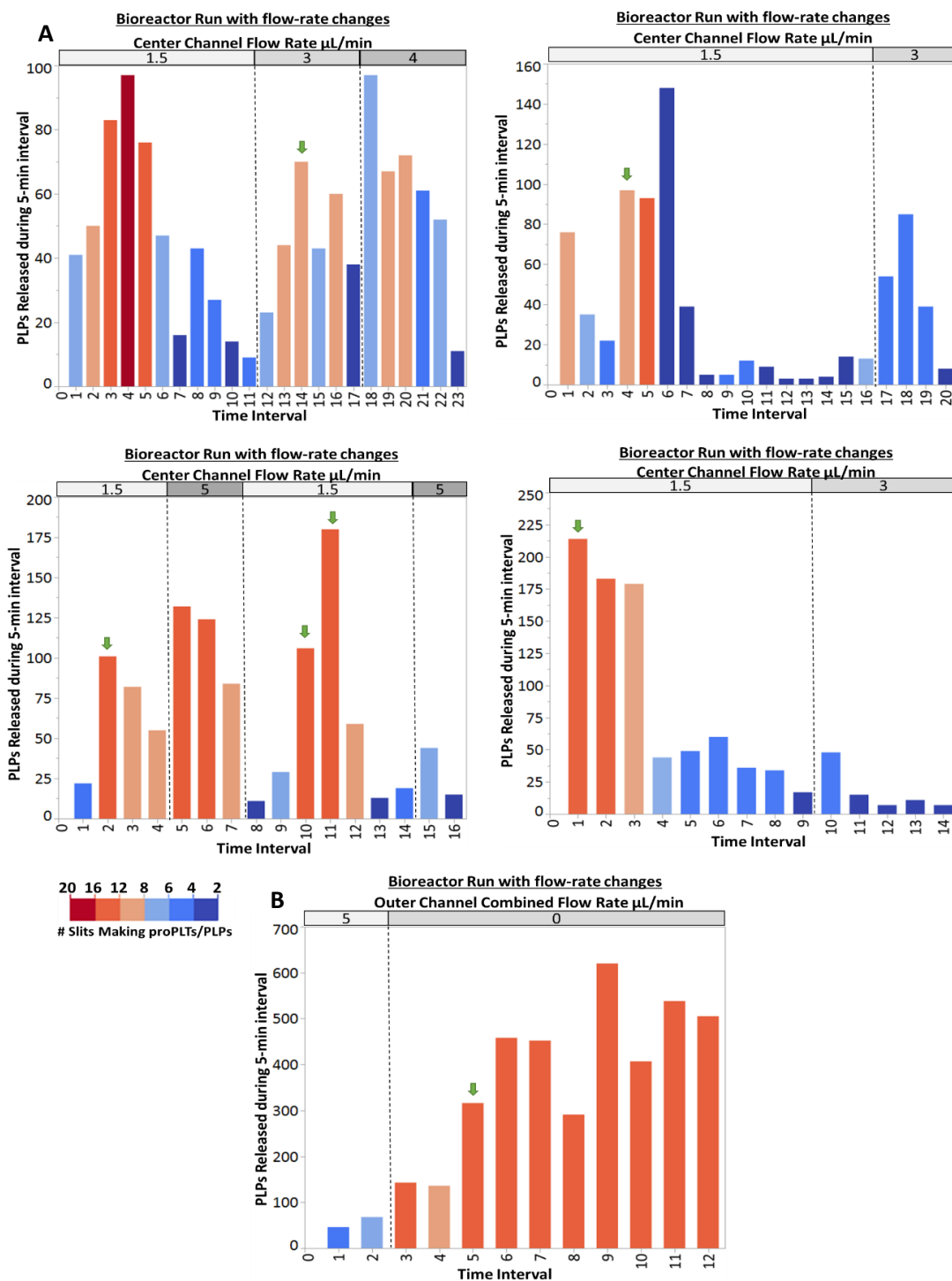


Figure 3.5 Additional PLP-release kinetics in USBR-7 μm . (A) Profile of PLPs released per 5-min time interval within bioreactors with center channel flow rate changes and

observed cell blockages denoted by green arrow. (B) Profile of PLPs released per 5-min time interval within a bioreactor outer combined channel flow rate change and observed cell blockage denoted by green arrow. For (A), combined outer channel flow rate = 5 $\mu\text{L}/\text{min}$. For (B), center channel flow rate = 1.5 $\mu\text{L}/\text{min}$ Color legend in (A) and (B) depicts the number of slits making PLPs per 5-min time interval.

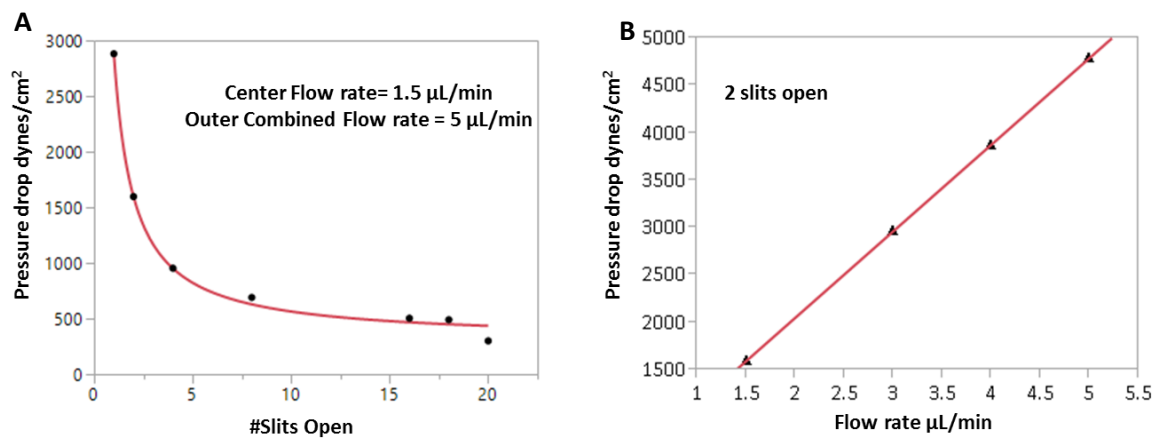


Figure 3.6 Pressure drop from CFD modeling of USRB-7 μm . (A) Pressure drop values across the reactor from CFD simulations of completely blocking slits within a cell-free bioreactor with a flow rate of 1.5 $\mu\text{L}/\text{min}$ in the center channel and a combined outer channels flow rate of 5 $\mu\text{L}/\text{min}$ (line fitted to $1/\#\text{Slits Open}$). (B) For a system with 2 open slits, pressure drop values from CFD simulations for different flow rates in the center channel with a constant combined flow rate of 5 $\mu\text{L}/\text{min}$ in the outer channels (fitted to a straight line).

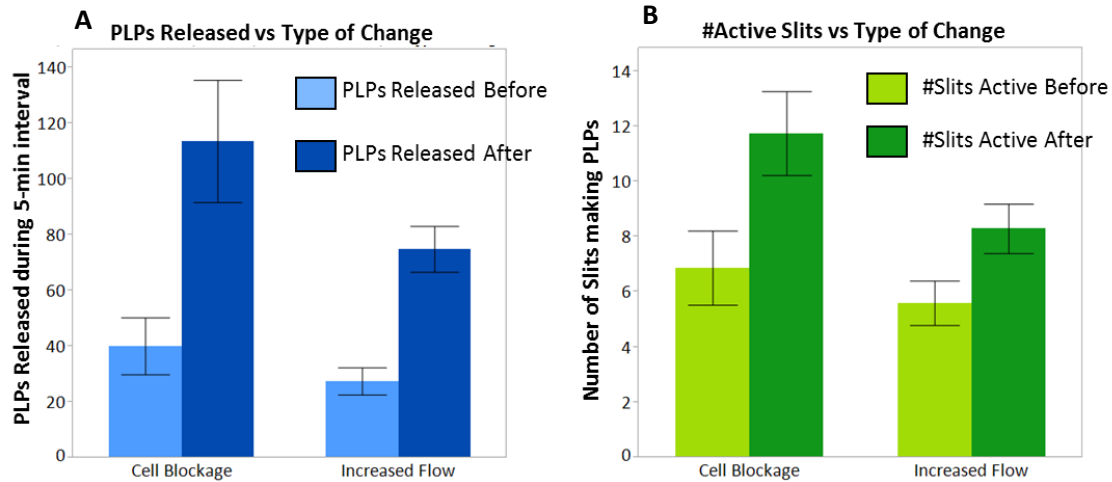


Figure 3.7 Number of PLP releases or active slits based on system changes. (A) Number of PLPs released in the 5-min time interval before or during a cell blockage event or a center channel flow rate increase. (B) Number of slits making PLPs in the 5-min time interval before and during a cell blockage event or a center channel flow rate increase. Combined outer channels flow rate maintained at 5 $\mu\text{L}/\text{min}$. (A) and (B) represents 8 bioreactors runs across 3 different Mk cultures. Error bars $\pm\text{SEM}$.

While trying to remove a small bubble from the outer channel during an experiment, we inadvertently stopped the flow of the outer channels. To our surprise, when the outer channel flow was completely stopped, the rate of proPLT and PLP release dramatically increased (**Figure 3.8 vs. Figure 3.3, Figure 3.5B**). The outer channel flow-rate is intended to impose shear forces on the extending proPLTs, so it is also a key parameter of the system. Yet, we discovered that turning off the outer channel flow rate dramatically changed the Mk behavior and greatly increased PLP release (**Video 4**). Further, we could still observe an increase in productivity when an incoming Mk blocked the flow of an open slit (**Figure 3.8A – green arrows**) or by introducing a step-increase in flow rate in the center channel (**Figure 3.8B**), similar to that seen when the outside flow was maintained at 5 $\mu\text{L}/\text{min}$ (**Figure 3.3**). Under this new operating condition, upon capture, some Mks continued to rapidly release dozens of PLPs within seconds (**Video 5**).

We compared bioreactor runs using outer channel combined flow rates of 5 $\mu\text{L}/\text{min}$ (9 bioreactor runs across 3 different Mk cultures) and 0 $\mu\text{L}/\text{min}$ (4 bioreactor runs across 2 different Mk cultures) (**Figure 3.9**). The average number of open slits was 2 for 5 $\mu\text{L}/\text{min}$ and 1 for 0 $\mu\text{L}/\text{min}$ combined outer channel flow rates (**Figure 3.9A**). On average, 40% of the occupied slits were actively making proPLTs/PLPs under the 5 $\mu\text{L}/\text{min}$ outer flow condition, whereas 61% were active when operating at 0 $\mu\text{L}/\text{min}$ outer flow condition (**Figure 3.9B**). The number of PLPs released per 5-min time interval had a mean of 55 and followed an exponential decay curve for the 5 $\mu\text{L}/\text{min}$ outer flow condition, while there was

a 6-fold higher mean of 351 PLPs released with a log-normal distribution for 0 $\mu\text{L}/\text{min}$ (Figure 3.9C). Thus, unexpectedly, an outer channel flow rate of 0 $\mu\text{L}/\text{min}$ greatly increased PLP production compared to 5 $\mu\text{L}/\text{min}$. An interesting observation from both environments is that the productivity increase from a blockage event (green arrow) could carry over into the next interval if the blockage occurred near the end of that interval (Figure 3.3A – intervals 9 to 10, Figure 3.3B – intervals 11 to 12, Figure 3.8B – intervals 13 to 14, and Figure 3.5B – intervals 5 to 6).

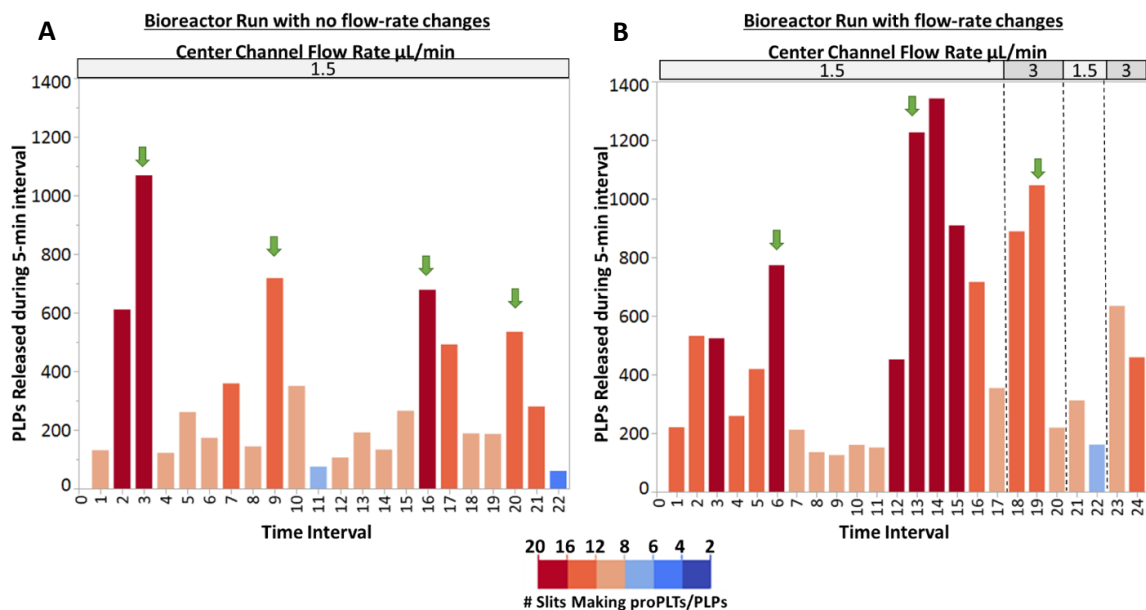


Figure 3.8 PLP release kinetics in USRB-7 μm with no outer channel flow. (A) Number of PLPs released per 5-min time interval during a bioreactor run with no center channel flow rate changes (indicated above plot) and four significant cell blockages of open slits denoted by green arrow. (B) Number of PLPs released per 5-min time interval during a bioreactor run with two center channel flow rate changes (dashed lines - indicated above plot) and three significant cell blockages of open slits denoted by green arrow. For (A) and (B), combined

outer channels flow rate = 0 $\mu\text{L}/\text{min}$. Color legend in (A) and (B) depicts the number of slits making PLPs during each 5-min time interval.

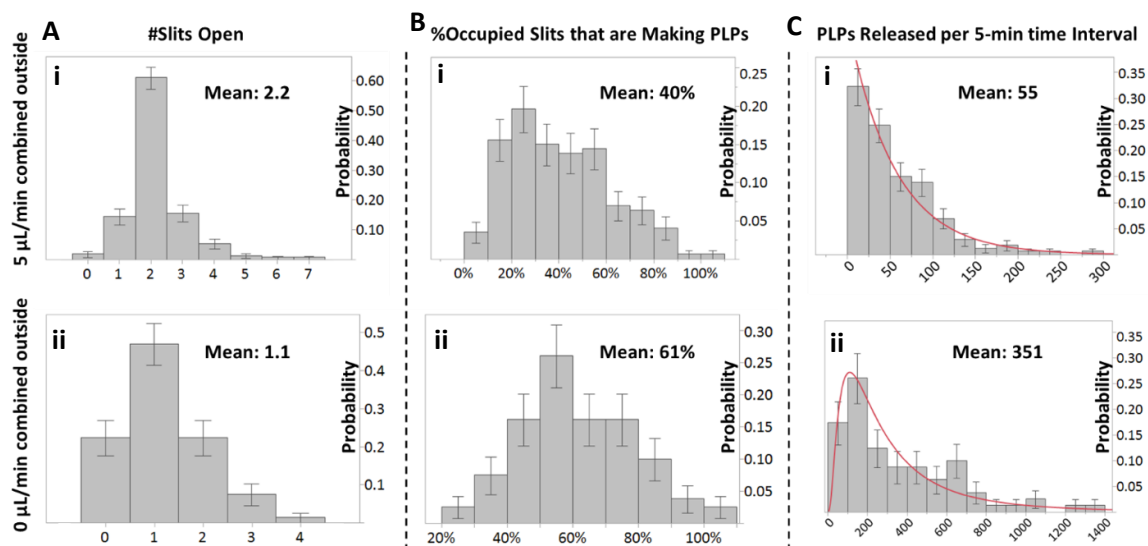


Figure 3.9 Distributions of PLP release kinetics in USRB-7 μm . (A) Number of slits open per 5-min time interval for (i) 5 $\mu\text{L}/\text{min}$ and (ii) 0 $\mu\text{L}/\text{min}$ combined outside channel flow rate. (B) %Occupied slits that were making PLPs per 5-min time interval for (i) 5 $\mu\text{L}/\text{min}$ and (ii) 0 $\mu\text{L}/\text{min}$ outside flow rate. (C) PLPs released per 5-min time interval for (i) 5 $\mu\text{L}/\text{min}$ (exponential fit) and (ii) 0 $\mu\text{L}/\text{min}$ (log-normal fit) outside flow rate. Error bars indicate $\pm\text{SEM}$.

3.3.3 Characterization of PLPs collected from USRB-7 μ m

It is important to demonstrate that the PLPs produced exhibit functional activity. Due to the higher productivity, we analyzed the effluent of three bioreactors operated with an outer channel combined flow rate of 0 μ L/min. Calcein⁺ PLPs were ~67% CD41⁺CD42b⁺ (**Figure 3.10A**). Functional activity of CD41⁺CD42b⁺ PLPs was evaluated via expression of CD62P – a transmembrane glycoprotein that is translocated by granules to the surface of platelets after activation – both before (**Figure 3.10Bi**) and after adding thrombin (**Figure 3.10Bii**) to activate the PLPs. The average percentage of CD62P⁺ PLPs increased from ~20 to ~70% after thrombin addition (**Figure 3.10Biii**). Confocal analysis of PLPs on fibrinogen revealed a characteristic tubulin ring in the absence of thrombin and highly spread PLPs in the presence of thrombin (**Figure 3.10C**), which is similar to the behavior of fresh platelets.[42]

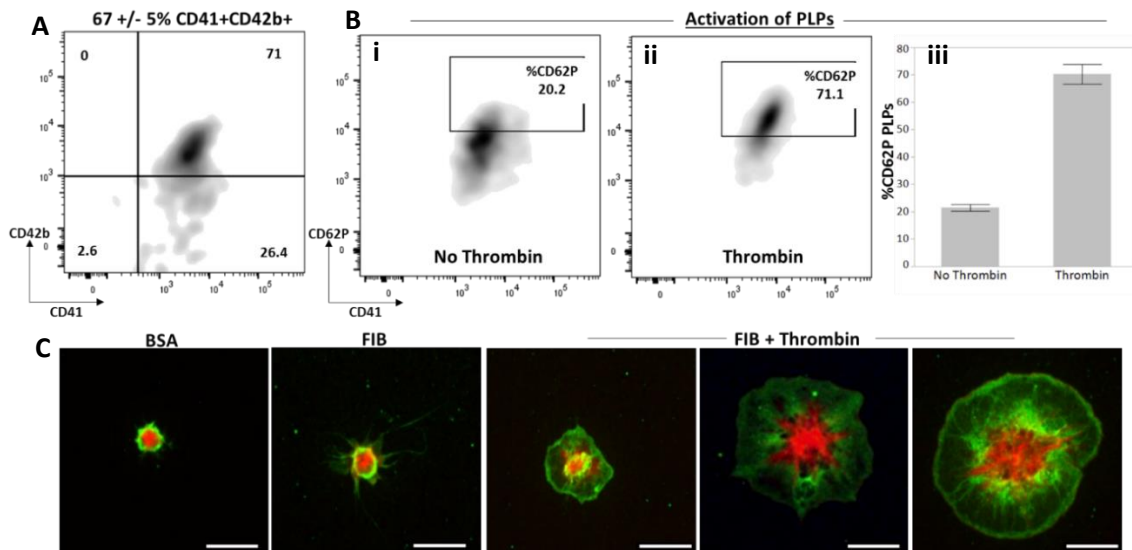


Figure 3.10 Characterization of recovered PLPs from effluent. (A) CD41 and CD42b expression of Calcein⁺ PLPs. (B) Representative plots of activation of recovered CD41⁺CD42b⁺ PLPs in the absence (i) or presence (ii) of thrombin and (iii) summary of %CD62P⁺ PLPs for 3 bioreactor experiments from two Mk cultures with different donors. (C) Recovered PLPs adhere to BSA and fibrinogen (FIB) with a characteristic tubulin ring and spread extensively after activation with thrombin. (green – beta tubulin, red- actin, blue – DNA). Scale bar = 10 μ m. Bioreactor conditions: 1.5 μ L/min center channel and 0 μ L/min outer combined flow rate.

The effluent most likely contained a combination of pre-released particles (present in the Mk suspension introduced into the system) and PLPs generated at the slits. We analyzed the videos using the counting strategy described earlier to determine the rate at which pre-released Calcein-stained particles entered and exited the slits. The mean rate was 125 per 5-min time interval (**Figure 3.11A**), which is higher than the mean rate of PLP generation for a combined outer channel flow rate of 5 $\mu\text{L}/\text{min}$ (55), but less than half than the mean rate for a combined outer channel flow rate of 0 $\mu\text{L}/\text{min}$ (351). By counting flow-through and newly produced PLPs in the same experiment, we estimated that $\sim 76\%$ of Calcein-stained PLPs were generated by the slits in the reactors with no flow in the outer channels (**Figure 3.11B**). Therefore, the Calcein⁺ PLPs characterized in the effluent were largely generated by Mks trapped at the slits.

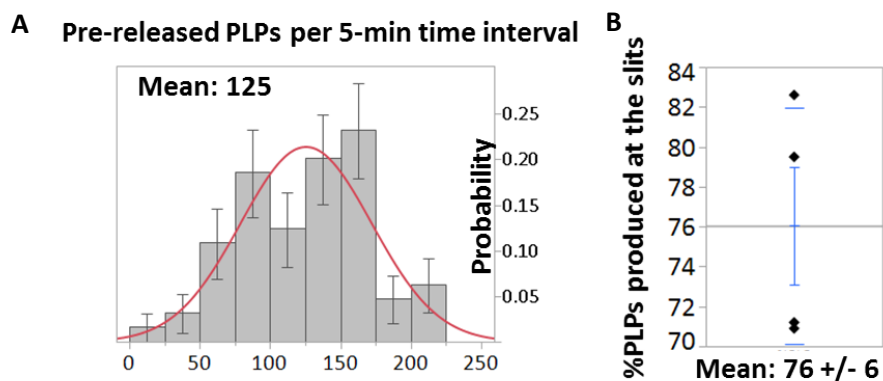


Figure 3.11 Bioreactor derived PLPs and pre-released particle analysis. (A) Pre-released PLPs per 5-min time interval (normal fit). Error bars indicate $\pm\text{SEM}$. (B) Estimated percentage of PLPs that were generated from trapped Mks at the slits. (A) and (B) represents

4 bioreactors runs across 2 different Mk cultures Center channel flow rate = 1.5 $\mu\text{L}/\text{min}$ and combined outer channel flow rate = 0 $\mu\text{L}/\text{min}$.

Finally, to verify our PLP counting process, we introduced expired blood platelets, stained with Calcein, into a cell-free bioreactor. During a 30-min perfusion, platelets were counted per 5-min time interval for outer channel combined flow rates of 5 $\mu\text{L}/\text{min}$ or 0 $\mu\text{L}/\text{min}$ (**Figure 3.12A**). The number of platelets counted per time interval was about the same for either condition, as expected, since platelets would only enter via the center channel. Additionally, we provide images of expired platelets flowing through the USRB-7 μm (**Figure 3.12B**) to compare them to the PLPs released from trapped Mks to further support our count strategy (**Figure 3.12C**).

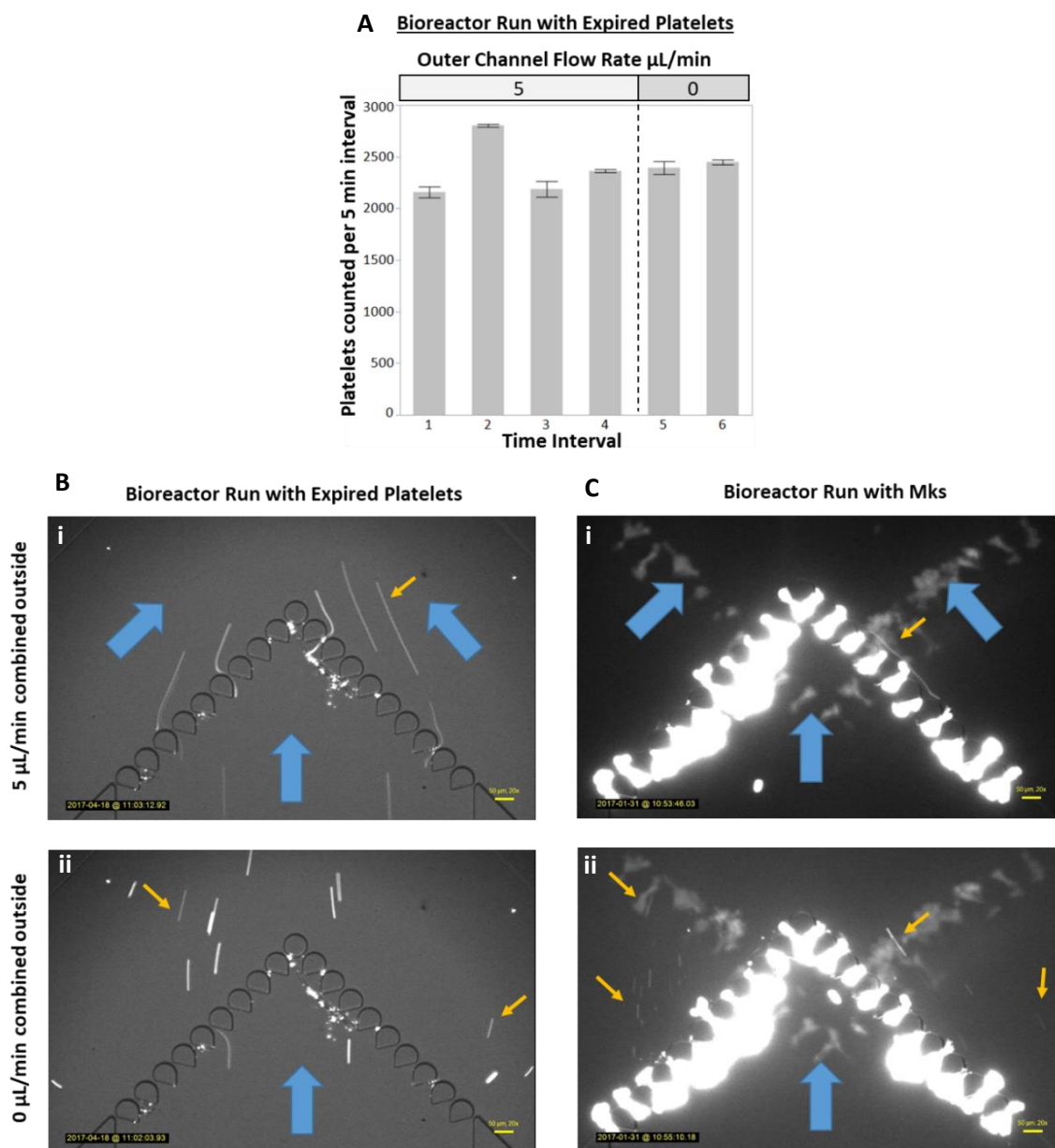


Figure 3.12 Expired blood platelets in the bioreactor compared to PLPs released from Mks. (A) Profile of expired platelets per 5-min time interval within a bioreactor (counted three times). Error bars indicate $\pm\text{SEM}$. (B) Images of Calcein-stained platelets flowing through bioreactor with either (i) $5 \mu\text{L}/\text{min}$ or (ii) $0 \mu\text{L}/\text{min}$ combined outer channel flow rate. (C) Images of Mks releasing PLPs from the slits with either (i) $5 \mu\text{L}/\text{min}$ and (ii) 0

$\mu\text{L}/\text{min}$ combined outer channel flow rate. For (A-C), the center channel flow rate was maintained at $1.5 \mu\text{L}/\text{min}$. Blue arrows indicate the flow direction. Yellow arrows indicate platelets or PLPs.

3.3.4 CFD analysis of changes to the outer channel flow rate

CFD was used to evaluate what environmental factors could explain the differences in Mk behavior at $5 \mu\text{L}/\text{min}$ vs. $0 \mu\text{L}/\text{min}$ flow rates in the outer channels, while keeping the center channel flow rate constant at $1.5 \mu\text{L}/\text{min}$. Wall shear rate, pressure, velocity, strain rate, and the structure of the flow patterns were the primary factors of interest. Simulations with the outer flow rate of $0 \mu\text{L}/\text{min}$ did not show changes to the wall shear rates within the slits of the bioreactor (**Figure 3.13 vs. Figure 2.13**). Next, we focused on CFD-predicted pressure and velocity profiles across the slits at the center height of the bioreactor, $z = 20 \mu\text{m}$ (**Figure 3.14A**). The average CFD pressure drop across the slits was similar for the two outer channel flow rate conditions, but at $5 \mu\text{L}/\text{min}$ the variability between slits was greater (**Figure 3.14B, Figure 3.15A**). The outside flow likely imparts some back pressure in the center channel flow, evident by the higher relative pressures shown in **Figure 3.15A**. Stopping the outside flow potentially reduced the pressure downstream of the slits and may allow Mks to release more PLPs. The velocity profile across the slits is also more variable when the combined outside channel flow rate is $5 \mu\text{L}/\text{min}$ vs. $0 \mu\text{L}/\text{min}$, but the average velocity profiles were similar (**Figure 3.14C, D Figure 3.15B**).

Next, we examined the strain rate (rate of deformation) within the bioreactor slits. Strain rates represent extensional flow that is created due to a velocity gradient in the direction of flow. The CFD outputs of our bioreactor showed an increase in velocity along the slits, due to the hyperbolic-like-converging region (**Figure 3.15B**). In CFD, the strain rate can be easily extracted from the velocity gradient tensor output as dV_x/dx . Plotting the average strain rate across the slits did not show any large differences for combined outer channel flow rates of 5 $\mu\text{L}/\text{min}$ or 0 $\mu\text{L}/\text{min}$ (**Figure 3.15C**). The maximum strain rates predicted are 336 s^{-1} for 5 $\mu\text{L}/\text{min}$ and 346 s^{-1} for 0 $\mu\text{L}/\text{min}$ outside combined flow rate. Based on this analysis, though there were no differences in the strain rates, we can observe extensional flow conditions within our slits.

Finally, we assessed the structure of the flow patterns using the CFD streamlines, as well as 1- μm fluorescent beads to map the experimental streamlines. There is strong agreement between the predicted and experimental streamlines under the two different outside flow conditions (**Figure 3.16**). The flow patterns are very different at the two flow rates. For the 5 $\mu\text{L}/\text{min}$ combined outer channel flow rate, the streamlines are compressed towards the center of the reactor along the posts (**Figure 3.16A, B**). On the other hand, with no outer channel flow, the streamlines are not compressed, but rather expand downstream of the slits (**Figure 3.16C, D**). Furthermore, overlaying images from Mk experiments with the CFD streamlines demonstrates how the flow structure influences the behavior of the Mks (**Figure 3.17**). This is further supported by the observation of switching the flow from 5 $\mu\text{L}/\text{min}$ to 0 $\mu\text{L}/\text{min}$ shown in **Video 4**. Also, the velocity vectors past the slits show that the flows

through individual slits seem to interact with each other when the outside flow is at 5 $\mu\text{L}/\text{min}$, whereas a more isolated slit environment is generated with no outside flow (**Figure 3.18A vs. Figure 3.18B**).

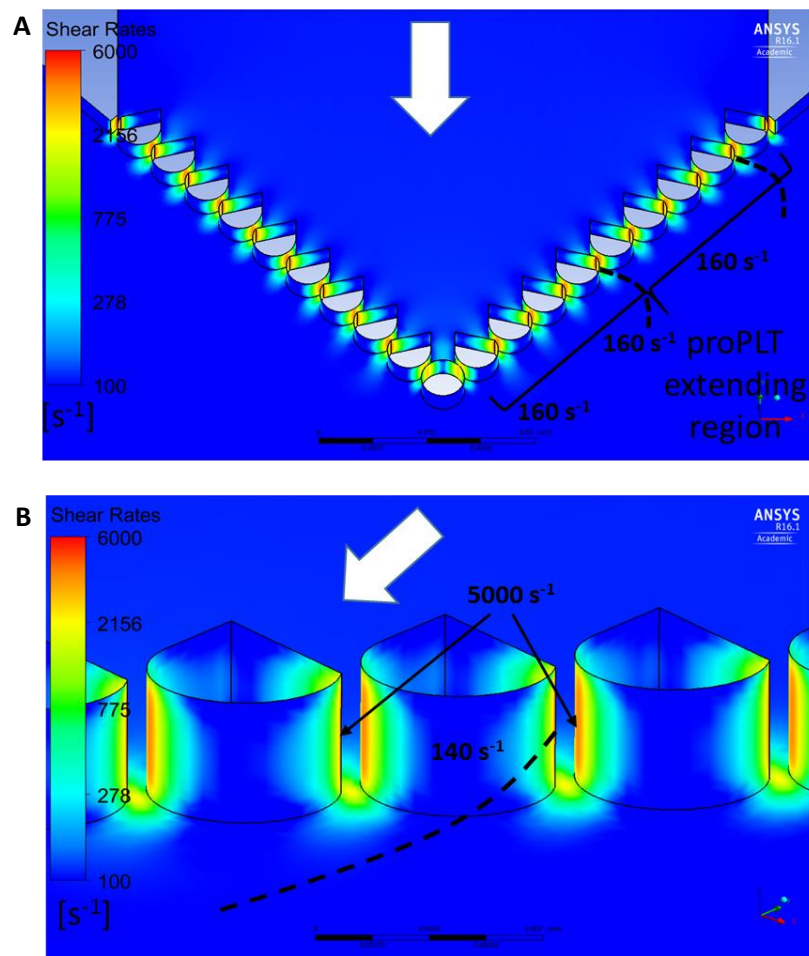


Figure 3.13 Shear rate analysis of USRB-7 μm with no outer channel flow. Shear rates through the entire region (A) and details for individual slits (B) for a flow rate of 1.5 $\mu\text{L}/\text{min}$ in the center channel with 0 $\mu\text{L}/\text{min}$ in the outer channels. White arrows indicate the flow direction. Estimated shear rates on proPLTs (dashed lines) are within 100 μm from the slits.

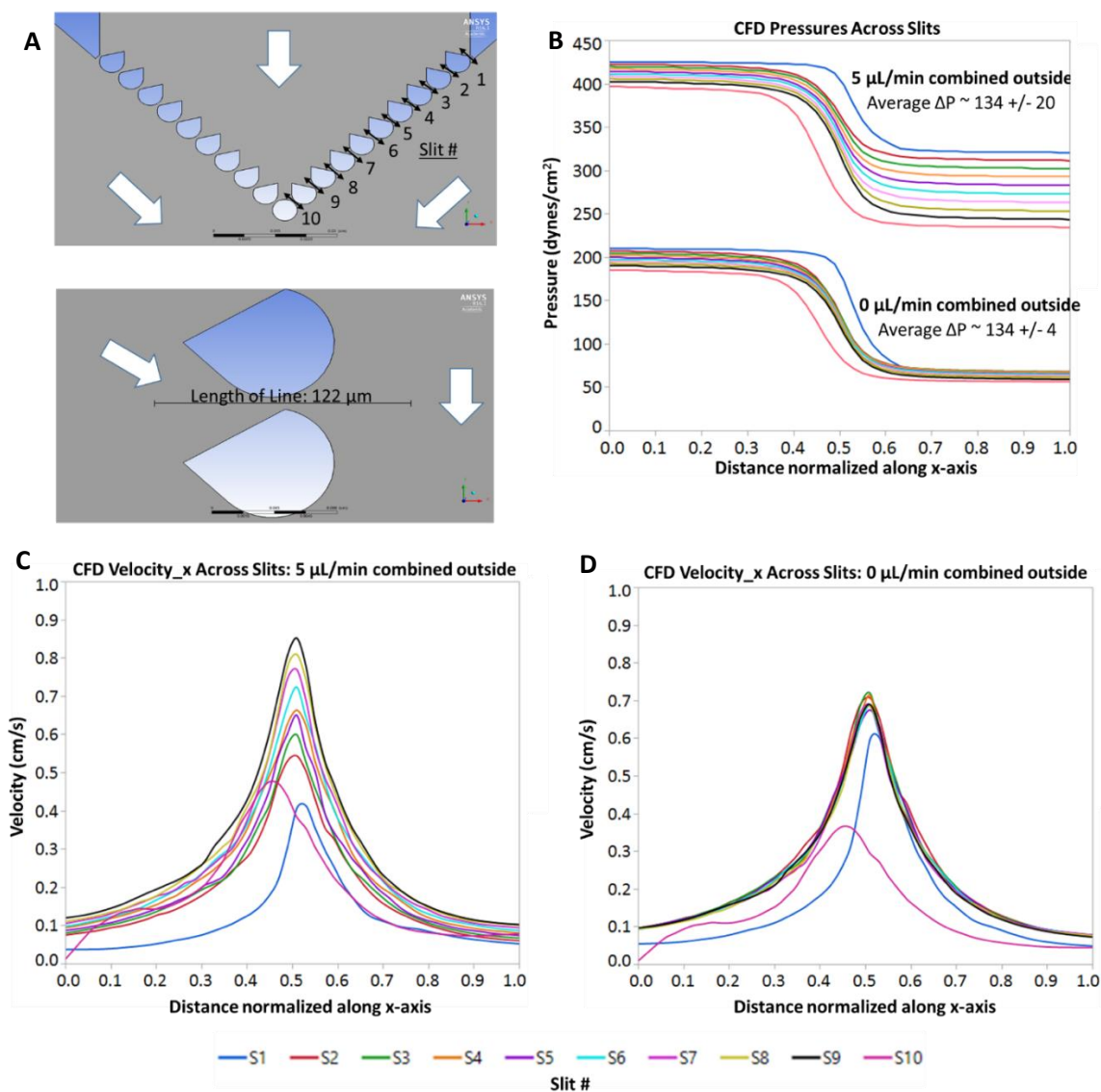


Figure 3.14 CFD analysis across slits along the x-axis and center height ($z = 20 \mu\text{m}$) of **USRB-7μm**. (A) Slit location for analysis. (B) Pressure along individual slits for two different outer channel combined flow rates ($5 \mu\text{L}/\text{min}$ and $0 \mu\text{L}/\text{min}$). (C) Individual slit velocities along the x-axis for a combined outer channel flow rate of $5 \mu\text{L}/\text{min}$. (D) Individual slit velocities along the x-axis for a combined outer channel flow rate of $0 \mu\text{L}/\text{min}$. For all outputs, the center channel flow rate was maintained at $1.5 \mu\text{L}/\text{min}$. White arrows

indicate the flow direction. Slit numbers shown in (A) are indicated by number and line colors, as indicated in the legend below the figure.

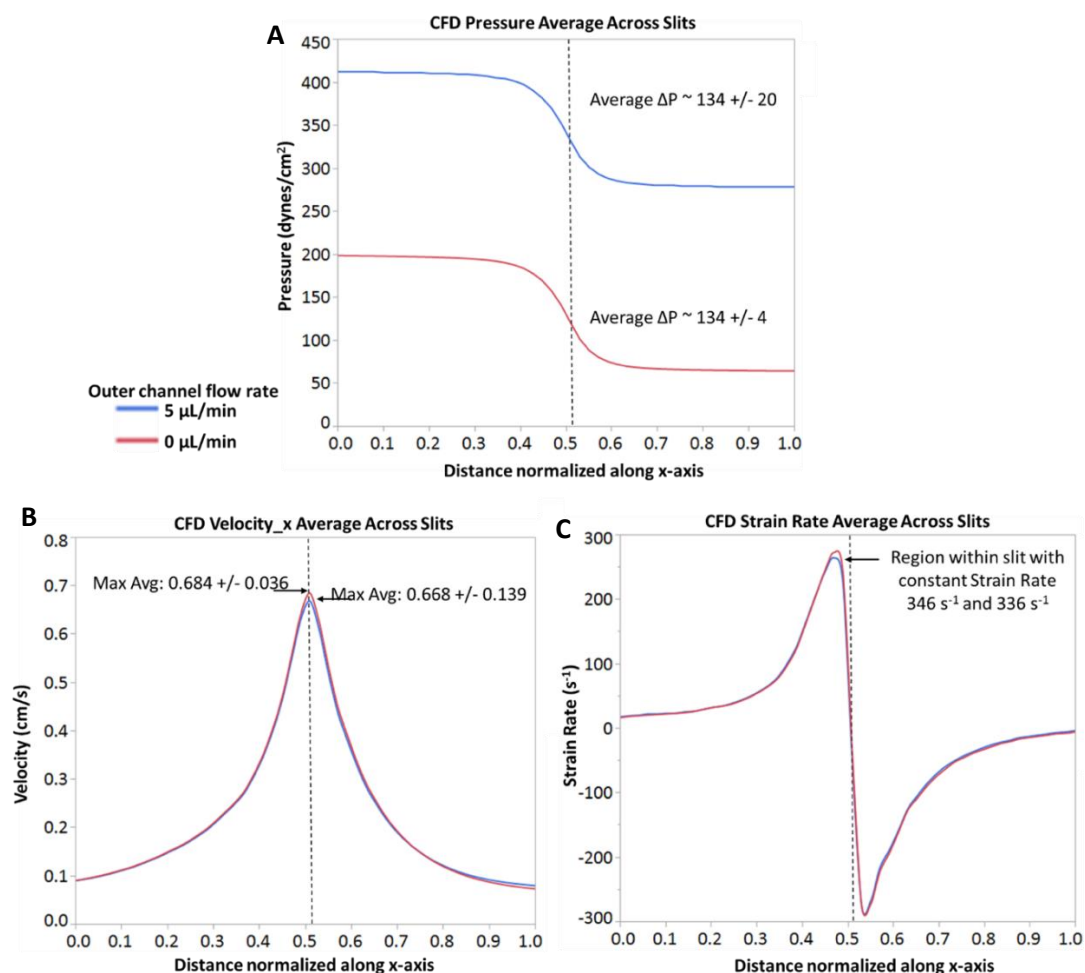


Figure 3.15 Average CFD outputs across the slits along the x-axis. (A) Average pressure, (B) velocity profile, (C) and strain rate across the slits for two combined outer channel flow rates. Blue = 5 μL/min, Red = 0 μL/min. The center channel flow rate was maintained at 1.5 μL/min. Dashed line on plots represent the 7-μm slit opening where velocity is the highest.

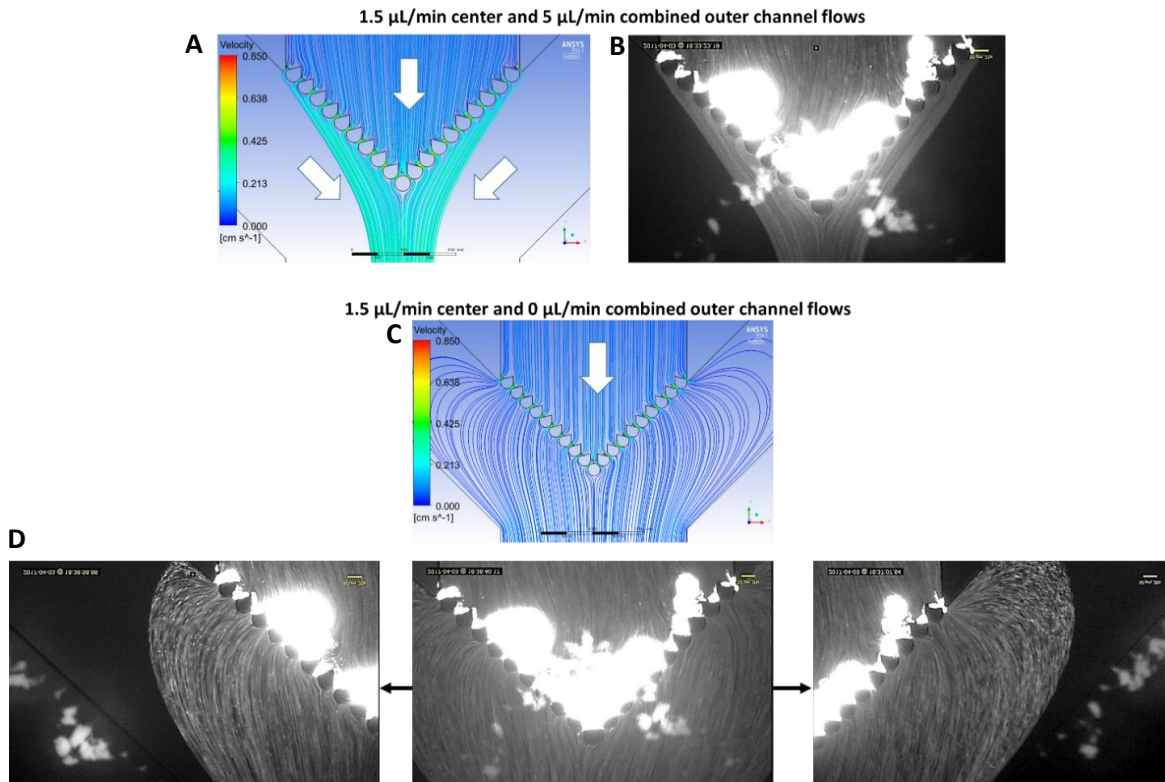


Figure 3.16 Streamline observations under different outside channel flow rates. (A) CFD streamlines and (B) experimental streamlines using 1- μm fluorescent beads and Calcein-stained cells for a flow rate of 1.5 $\mu\text{L}/\text{min}$ in the center channel with 5 $\mu\text{L}/\text{min}$ combined outer channel flow rate. (C) CFD streamlines and (D) experimental streamlines using 1- μm fluorescent beads and Calcein-stained cells for a flow rate of 1.5 $\mu\text{L}/\text{min}$ in the center channel with 0 $\mu\text{L}/\text{min}$ in the combined outer channel flow rate. White arrows indicate the flow direction. Scale bar = 50 μm .

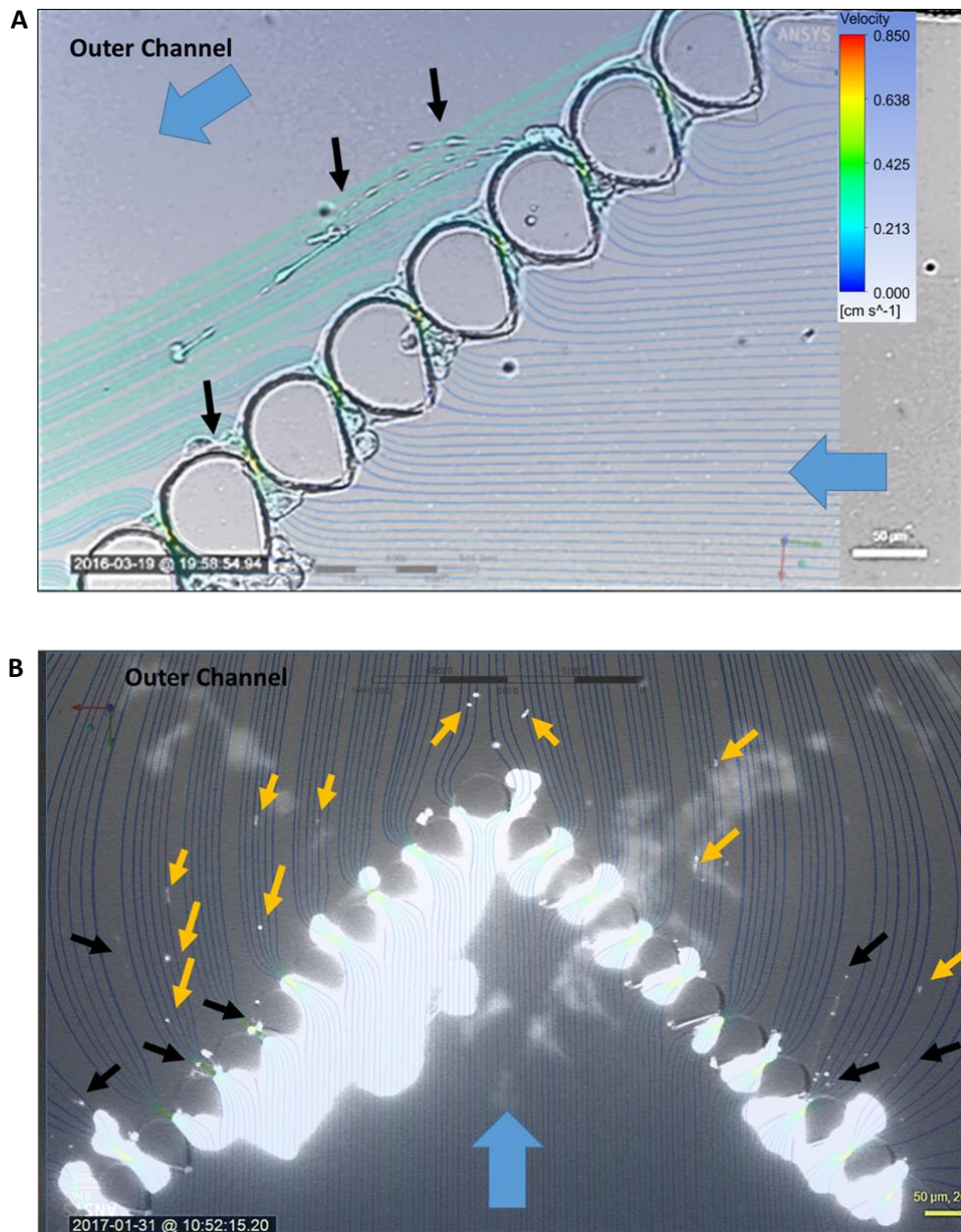


Figure 3.17 CFD streamlines overlaid on images from Mk experiments. Center channel flow rate of 1.5 $\mu\text{L}/\text{min}$ with (A) 5 $\mu\text{L}/\text{min}$ and (B) 0 $\mu\text{L}/\text{min}$ combined outer channel flow rate. Blue arrows indicate direction of flow. Black arrows indicate proPLTs. Yellow arrows indicate PLPs. Scale bar = 50 μm .

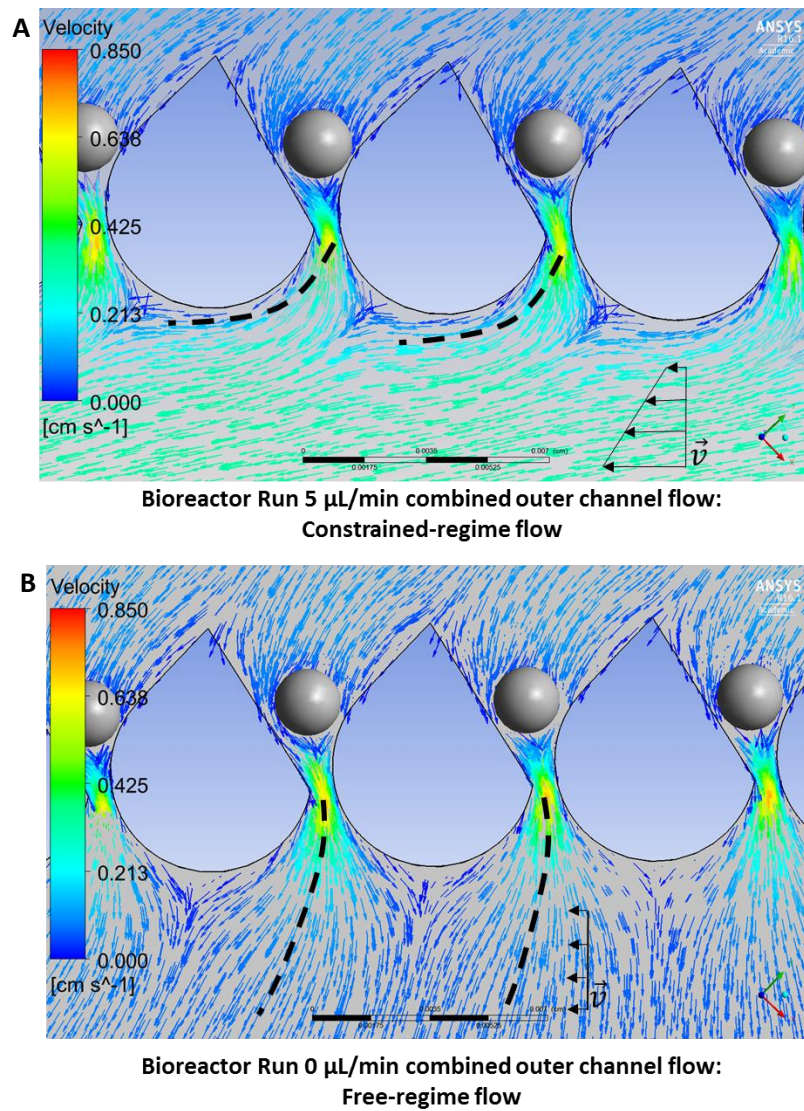


Figure 3.18 Difference of flow structures depicted with velocity vectors. (A) Velocity vectors within slits for a flow rate of 1.5 $\mu\text{L}/\text{min}$ in the center channel with a 5 $\mu\text{L}/\text{min}$ combined outer channel flow rate. (B) Velocity vectors within slits for a flow rate of 1.5 $\mu\text{L}/\text{min}$ in the center channel with a 0 $\mu\text{L}/\text{min}$ combined outer channel flow rate. 20- μm spheres shown within slits simulate the effects of cells in the slits, while dashed lines represent direction of proPLTs/PLPs.

Videos listed below can be found online in supplemental information for the published study in *Biotechnology Progress*. [76]

Video 1: proPLT Formation. Trapped Mk extending proPLTs through slit. Flow in the outer channels applies shear on the extensions further elongating them leading to fragmentation after several minutes. Time units: h:min:s. Scale bar = 50 μm . Flow rate of 1.5 $\mu\text{L}/\text{min}$ in the center channel with 5 $\mu\text{L}/\text{min}$ in the combined outer channels.

Video 2: Rapid PLPs releases. Trapped Mks in a slit, rapidly releasing many individual PLPs in seconds. Time units: h:min:s. Scale bar = 35 μm . Flow rate of 1.5 $\mu\text{L}/\text{min}$ in the center channel with 5 $\mu\text{L}/\text{min}$ in the combined outer channels.

Video 3: Major slit-blockage by Mks. Upon cell-capture at a slit, there is a noticeable increase in proPLT/PLP activity across the bioreactor. Scale bar = 50 μm . Flow rate of 1.5 $\mu\text{L}/\text{min}$ in the center channel with 5 $\mu\text{L}/\text{min}$ in the combined outer channels.

Video 4: Impact of turning off outside flow rate. Starting with an outside flow rate at 5 $\mu\text{L}/\text{min}$, Mks observed making proPLTs/PLPs. After turning off the outside flow rate, there is an increase in proPLT/PLP productivity across the bioreactor. Scale bar = 50 μm . Flow rate of 1.5 $\mu\text{L}/\text{min}$ in the center channel.

Video 5: Rapid proPLT formation and PLP releases. Mks are trapped and rapidly converted to proPLTs/PLPs at the slits. Scale bar = 50 μm . Flow rate of 1.5 $\mu\text{L}/\text{min}$ in the center channel with 0 $\mu\text{L}/\text{min}$ in the combined outer channels.

3.4 Discussion

Compared to slit bioreactor introduced by Thon et al., our USRB-7 μ m has a similar capture area of 20 slits vs. 15 slits, but a higher slit occupancy (90% vs 66%). More importantly, all the slits can be observed during an experimental run and we noted that on average 40-60% of occupied slits were actively making proPLTs/PLPs. In contrast, the length of the Thon et al. and Nakagawa et al. bioreactors makes it difficult to analyze proPLT/PLP formation from all the slits at the same time. In addition to supporting proPLT production, the USRB-7 μ m also promoted rapid release of many individual PLPs, which has not been reported for other published bioreactor systems. This observation is physiologically relevant since Mks have also been observed to make platelets *in vivo* (in mouse) via a rapid fragmentation process that releases platelets without the propPLT formation step.[12,30,32,33] Though we do not fully understand what factors influence proPLT vs. rapid-PLP release, we can observe that the rate of PLP production appears to be faster when PLPs are rapidly released (**Video 1 vs. Video 2**). We hypothesize that rapid PLP generation within the USRB-7 μ m is largely influenced by the unique slit geometry in which cells are pushed through a hyperbolic-like-converging region. As the area is reduced in this region, whole Mks bodies are squeezed and elongated through the 7- μ m gap where the shear rate and strain rate are the highest.

We show that the flow microenvironment can greatly affect the behavior of Mks in real-time. Within the system, we observed that Mk capture at an open slit increased the release of PLPs across the other Mk-blocked slits. Slit-blockage events could be influenced by the size of the Mks being trapped and are not easily controlled, thus, our observations highlight

the importance of understanding how the inherent dynamics of a bioreactor can impact the Mk response. A step-change in the center channel flow rate (while keeping the outside channel flow constant) transiently increased the rate of PLP releases, similarly to the slit-blockage events. The increase in immediate Mk productivity could be attributed to an increase in pressure drop across the slits, as presented by CFD analysis. While we can observe a temporary 3-fold increase in productivity after cell-blockages or flow rate changes in the USRB-7 μm , we recognize that the rates aren't sustained for the remainder of an experimental run largely due to the dynamic behavior of cell capture and slit openings. Nagakawa et al. did not study the effect of changing the flow conditions within their system.[82] Thon et al. found that the average proPLT extension rate did not change at different flow rates (same flow for both channels, 12.5-100 $\mu\text{L/hr}$),[50] but did not extend their CFD analysis to other flow regimes. It would be interesting to examine the Thon et al. system at higher flow rates or slit-blockage events to see if the number of active slits increased, even if the proPLT extension rate remained unchanged. Within the USRB-7 μm , we observed that step-changes to the center channel flow rate or a cell-blockage event led to ~30% and ~50% increases in active slits, respectively.

We anticipated that the presence of an outside channel flow would aid in shearing off proPLTs (increasing PLPs release rate), mimicking physiological blood flow *in vivo*. Thus, we were surprised that turning off the outside channel flow rate increased the average number of PLPs released by almost 6-fold. Using CFD simulations, we probed the predicted environment to try and understand the variables responsible for these unforeseen results.

Average velocity profiles, strain rates, and wall shear rates through the slits remained overall unchanged with or without flow in the outer channel. CFD predictions showed a slight increase in back-pressure by the outer flow on the center channel, which could inhibit Mks from releasing more PLPs. However, a significant change in the flow structure was observed, as confirmed by good agreement between the CFD streamlines and experimental streamlines. The CFD simulations showed that the slits appear to operate independently from each other with no outside flow (**Figure 3.18**), and within our experimental runs, we observed Mk behavior that supported the simulations in which proPLTs and PLPs are not contracted towards the center of the bioreactor (**Figure 3.17B vs. A**). Thus, we believe that the flow structure had the most significant impact on Mk behavior. Yet, the microenvironment that is being generated is certainly complex and the use of higher magnification, particle velocity imaging (PVI), and pressure transducers in the system could further refine our observations in future evaluations.

Analysis of the bioreactor effluent showed CD41⁺CD42b⁺ PLP populations that exhibited activation following thrombin addition. We acknowledge that some particles could have been pre-released before processing the Mks. Currently, we cannot discern which of the Calcein⁺ particles in the effluent were pre-released vs. generated in the USRB-7 μ m. However, our video analysis indicates that ~76% of Calcein-stained particles were generated at the slits in reactors with no outside flow. In recent work with the USRB-7 μ m, we are able to decrease the introduction of pre-released particles by ~50% by adding a low-spin step

prior to introducing Mks into the system. We are optimizing this protocol and plan to permanently implement this step in future studies.

ProPLTs are subjected to a shear environment typical of the bone marrow sinusoids in many of the current published bioreactor systems (Chapter 2, **Figure 2.1A**). Additionally, Mk bodies can be directly exposed to high shear environments that approach and exceed estimated values within the lung (Chapter 2, **Figure 2.1B**). Single flow environments that transport Mks into regions with high shear forces (operating similar to the lung capillary bed) as well as extensional forces are sufficient for PLP generation, as demonstrated in this study and in Blin et al.,[48] and challenge the need of using two flows to mimic the bone marrow niche. Though Nakagawa et al.[82] and Thon et al.[50] used two flows, these systems also contain high shear regions and could potentially benefit from utilizing a single flow for Mk elongation and fragmentation at the slits.

The diverse Mk responses to different real-time environmental changes within the USRB-7 μ m support its use as a characterization tool to study *ex vivo* PLP formation. Further work will focus on utilizing the USRB-7 μ m to study aspects and characteristics of the bone marrow niche that could be incorporated, such as ECM protein coatings, and to leverage CFD to identify more effective PLP-generating microenvironments. Additionally, preliminary results show the capability of the USRB-7 μ m to process Mks derived from umbilical cord-blood (CB) HSPCs with proPLT and PLP behavior similar to that presented in this study (see Chapter 4). Thon et al. observed that, even using 2- μ m slits, Mks were able

to deform, pass through the slits, and enter the lower channel.[50] We observe similar behavior of Mks passing through our 7- μm slits. Therefore, a secondary system, such as the spinning-membrane separator we described previously[52], must be used to separate PLPs from Mks, which could then be recycled back to the bioreactor. Overall, future USB-7 μm studies will increase understanding of proPLT and PLP formation in a uniform-flow environment and can reveal important variables and operating parameters through which *ex vivo* platelet production can be increased.

3.5 Acknowledgements

This research was supported by NSF grant CBET-1265029. Andres Martinez was supported in part by NIH Predoctoral Training Grant T32 GM008449. The authors acknowledge the use of the Micro/Nano Fabrication Facility (NUFAB), Flow Cytometry Core Facility, and Biological Imaging Facility (BIF) at Northwestern University. The computational fluid dynamic software Fluent was provided through an ANSYS Academic Partnership with Northwestern University. We acknowledge Mark Duncan for initiating microfluidic bioreactor work in the lab. We thank Kathleen Jenkins and Damien Doser for assistance with several experiments. We thank Jia Wu for helpful technical discussions. Additionally, we thank Dr. Wesley Burghardt (Northwestern University) and Dr. Marc Horner from ANSYS for valuable discussions on CFD.

CHAPTER 4: Engineering improved and scaled-up microfluidic platelet bioreactors

Work presented in this chapter (**Figure 4.7**) is part of the following paper under review:

- Wu JJ, Abbott DA, Martinez AF, Ranjan R, DeLuca TA, Doser DLP, Terzioglu MK, Mahmud D, Bagheri N, Mahmud N, Miller WM. Valproic acid improves ex vivo generation of human megakaryocytes and platelet-like-particles from pre-expanded cord blood-derived CD34⁺ cells.

4.1 Introduction

Recently, we have developed a uniform shear rate bioreactor (USRB-7 μ m) to study and characterize PLP and proPLT formation from mobilized peripheral blood (mPB) derived Mks (described in Chapter 2 and 3).[76] The novel device allowed us to examine the impact of shear and flow structures on Mk's productivity. The Miller Lab has also worked on developing a culture process for Mks derived from cord-blood (CB) HSPCs. These CB-Mks tend to be smaller in size compared to mPB-Mks due to their lower ploidy.[18] The lab was assessing whether adding valproic acid (VPA) to CB HSPCs during pre-expansion could yield higher Mk and PLP numbers. Two VPA conditions expanded for six (E6) or eight (E8) days were compared to E0 control without pre-expansion.[87] We were interested in using the microfluidic bioreactor USRB-7 μ m to study PLP generation from these three different conditions. Our initial studies used the USRB-7 μ m. However, to improve capture efficiency of the smaller CB-Mks we modified the system to create a new device with 5- μ m slits, USRB-5 μ m. Computational fluid dynamics (CFD) modeling was used to characterize the environment and to ensure that the slits retained uniform shear rate in the new USRB-5 μ m.

Additionally, we were interested in scaling-up the USRB systems to accommodate larger numbers of Mks. Using the findings from Chapters 2 and 3 as well as the USRB-5 μ m results presented in the first part of this chapter, we designed and engineered a new device, Lung-USRB. The concept for the device was inspired by *in vivo* observations in mice where Mks are rapidly processed into proPLTs and PLPs in the lung capillary bed.[27] CFD analysis was used to understand the hydrodynamics of the new system and proof-of-concept experiments demonstrate the potential to use the new device to generate PLPs.

4.2 Material and methods

Unless otherwise specified, all reagents were obtained from Sigma-Aldrich (St. Louis, MO), and cytokines from Peprotech (Rocky Hill, NJ). Antibodies for flow cytometry analysis from BD Biosciences. LSR II or LSR Fortessa (BD Biosciences, San Jose, CA) flow cytometers were used to collect data and analysis was done using FlowJo v.10 (FlowJo LLC, Ashland, OR).

4.2.1 CFD modeling – USRB-5 μ m

The slit bioreactor simulations were carried out using ANSYS version 16.1 (Canonsburg, PA) that includes the computational fluid dynamics solver FLUENT. The 3D models were created in Autodesk Inventor Professional software 2015 (San Rafael, CA). The files were converted to Parasolid binary text in Inventor and then imported into ANSYS Design Modeler. A mesh was created in which the geometry is discretized into small volumes

(elements) where the CFD software calculates an approximate solution to the discretized form of the governing equations. The mesh settings and CFD set up were the same as described in Chapter 2 and in our published study.[76] The final mesh-independent system and mesh settings are shown in **Figure 4.1A**. The bioreactor system contains a primary flow down the center channel that pushes Mks into the 5- μm slits and an outer channel flow that shears off proPLTs from Mks. The center channel flow rate was at 1.5 $\mu\text{L}/\text{min}$ and the outside combined flow rate was 0 $\mu\text{L}/\text{min}$. Since the geometry was cropped, the input velocity of the center channel is set to 0.0714 cm/s (V_1 in **Figure 4.1B**) and the combined outer channel is set to 0 cm/s (V_2 in **Figure 4.1B**).

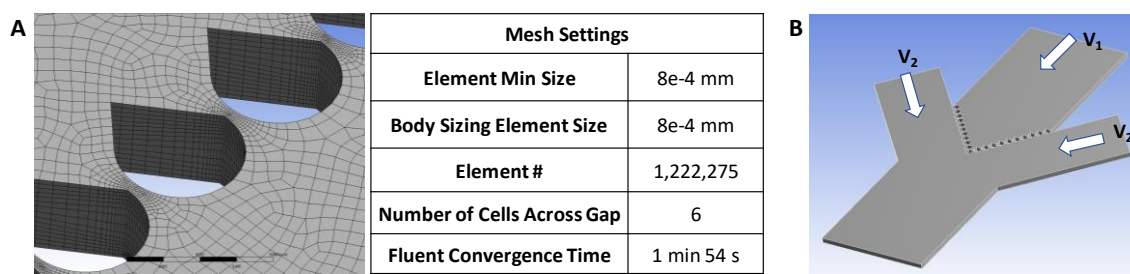


Figure 4.1 Mesh settings for uniform-shear rate bioreactor, USRB-5 μm . (A) Mesh settings used to generate the displayed mesh. The geometry has been slightly rotated to show the depth and elements across the slits. (B) Cropped region of the bioreactor used in CFD. White arrows indicate direction of flow.

4.2.2 CFD modeling – Lung-USRB

The bioreactor simulations were carried out using ANSYS version 16.1 and FLUENT. The 3D models were created in Autodesk Inventor Professional software 2015. The files were

converted to Parasolid binary text in Inventor and then imported into ANSYS Design Modeler. Because of the design, symmetry could be used to minimize simulation time and avoid computational power limitations while generating the mesh. Symmetry was defined along the Y-Z plane ($x = 0$), splitting the device in half down the center channel, and then along an X-Z plane ($y = 0, z = 20 \mu\text{m}$ height). The device has a height of $40 \mu\text{m}$. Through this approach, we only modeled a quarter of the device. The geometry was subdivided into two parts: Body and Slits. The $5.5\text{-}\mu\text{m}$ slits could be assigned a specific element size that could sufficiently resolve these small regions. The final mesh settings are shown in **Figure 4.2**. Four flow rates were simulated, $10 \mu\text{L}/\text{min}$ (inlet velocity of 0.00489 m/s), $40 \mu\text{L}/\text{min}$ (inlet velocity of 0.0195 m/s), $100 \mu\text{L}/\text{min}$ (inlet velocity of 0.0489 m/s) and $400 \mu\text{L}/\text{min}$ (inlet velocity of 0.195 m/s).

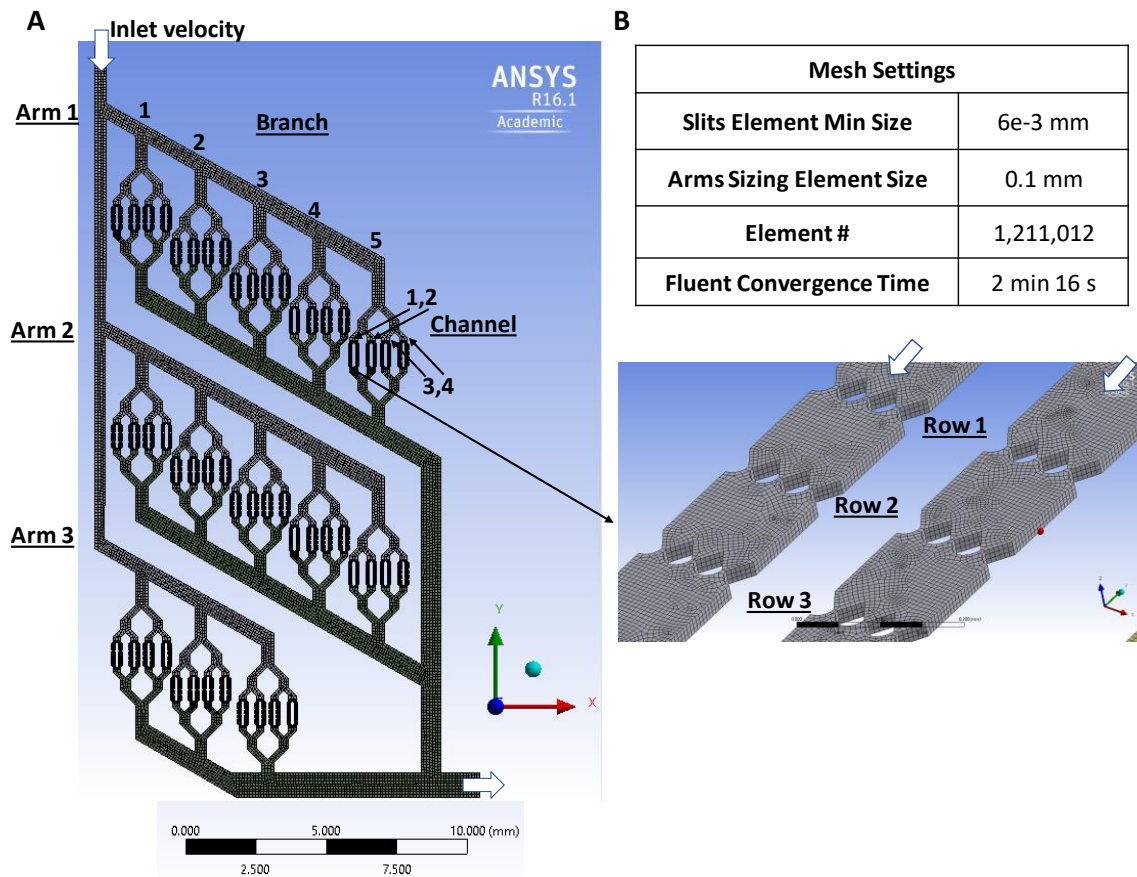


Figure 4.2 Mesh settings for Lung-USRB. (A) 3D geometry model represents a quarter of the bioreactor with the use of symmetry planes at Y-Z ($x = 0$) and X-Z plane ($y = 0, z = 20 \mu\text{m}$ height). The device has a height of $40 \mu\text{m}$. The Arms, Branches and Channels of the system are labeled/numbered as shown above. (B) Mesh settings used to generate the displayed mesh. White arrows indicate direction of flow.

For USRB- $5\mu\text{m}$ and Lung-USRB, boundary conditions were no-slip at the walls, constant inlet velocity, and default gauge pressure of 0 Pa at the outlet. FLUENT was used to solve the steady-state form of the Navier-Stokes Equation (see Chapter 2, **Eq. 2.1**) for an

incompressible Newtonian fluid subjected to the specified flow conditions. The convergence tolerance for all simulations, which is the normalized residual for each degree of freedom, was set to 10^{-3} . All simulations for the systems were run with the following computer and software settings:

Computer Specs: Dell Precision T1700, Intel® Core™ i7-4790 CPU @ 3.60GHz, 32GB RAM, 64-bit, Windows 10 Pro

FLUENT Settings:

Solver: 3D, double-precision, pressure-based, parallel (8 processors)

Time: steady-state

Pressure-Velocity Coupling Scheme: Simple

Discretization: Second-order upwinding

4.2.3 Cell culture – Cord Blood Mks

Purified CB CD34⁺ cells ($\geq 90\%$ CD34⁺) were seeded at 4×10^4 cells/mL in tissue culture-treated (TC) well plates in 6 well plates in 2.5 mL of Iscoves modified Dulbecco's medium (IMDM) (Biochrom) in serum-free medium (Sigma, St. Louis, MO) and supplemented with 100 ng/mL stem cell factor (SCF), 100 ng/mL FLT-3 ligand (FL), 100 ng/mL thrombopoietin (TPO) and 50 ng/mL interleukin 3 (IL-3). Cells were treated with 1 mM valproic acid (VPA) and added media and cytokine supplements as above except IL-3 at 16 hours and incubated for another 6 (E6 VPA+) or 8 (E8 VPA+) days at 37°C in a fully humidified atmosphere of 5% CO₂, then transferred to secondary culture. The cells were

then resuspended in 78% IMDM (Gibco, Carlsbad, CA), 20% BIT 9500 Serum Substitute (STEMCELL, Vancouver, BC, Canada), 1% Glutamax (Gibco), 1 $\mu\text{g}/\text{mL}$ low-density lipoproteins (Calbiochem, Whitehouse Station, NJ), 100 U/mL Pen/Strep, 100 ng/mL TPO, 100 ng/mL SCF, 10 ng/mL IL-6, 10 ng/mL IL-11 and 2.5 ng/mL IL-3 (R&D Systems, Inc., Minneapolis, MN) seeded in TC-treated T-flasks at 50,000 cells/mL. Cells were cultured in a fully humidified chamber at 37 °C, 5% CO₂, and 5% O₂ for 5 days (Panasonic incubator MCO-170M, Wood Dale, IL). On day 5, the cytokines were replaced with 100 ng/mL TPO, 100 ng/mL SCF, 10 ng/mL IL-9, 10 ng/mL IL-11 and 10 ng/mL IL-3. Cells were cultured at 20% O₂ thereafter. On day 7 cells were resuspended in fresh IMDM+20% BIT supplemented with 100 ng/mL TPO, 100 ng/mL SCF and 6.25 mM nicotinamide (Sigma). A control culture with no pre-expansion and VPA was also created (E0).

4.2.4 Cell culture – mPB Mks

Previously frozen mobilized peripheral blood (mPB) CD34⁺ cells from the Fred Hutchinson Cancer Research Center (Seattle, WA) with Northwestern University Institutional Review Board approval were grown in 78% IMDM, 20% BIT 9500 Serum Substitute, 1% Glutamax, 1 $\mu\text{g}/\text{mL}$ low-density lipoproteins, 100 U/mL Pen/Strep, 100 ng/mL TPO, 100 ng/mL SCF, 10 ng/mL IL-6, 10 ng/mL IL-11 and 2.5 ng/mL IL-3 (R&D Systems). Cells were maintained between 100,000 to 400,000 cells/mL at 37°C, 5% CO₂ and 5% O₂ for 5 days (Panasonic incubator MCO-170M). On day 5, the cytokines were replaced with 100 ng/mL TPO, 100 ng/mL SCF, 10 ng/mL IL-9, 10 ng/mL IL-11 and 10 ng/mL IL-3. Cells were maintained at a density of 250,000 to 500,000 cells/mL and kept at 37°C, 5% CO₂ and 20% O₂ until day

7. On day 7, cells were selected using anti-CD61-conjugated magnetic microbeads (Miltenyi Biotech Inc, San Diego, CA) and then cultured in medium with 100 ng/mL TPO, 100 ng/mL SCF and 6.25 mM nicotinamide thereafter. The cells were maintained at a density between 250,000 to 500,000 cells/mL and kept at 37°C, 5% CO₂, and 20% O₂.

4.2.5 Bioreactor fabrication

A 2D design of the bioreactor was created in AutoCAD 2014 (San Rafael, CA) and then printed onto a chrome mask (Front Range Photomask, Palmer Lake, CO). A silicon wafer (WRS Materials, San Jose, CA) was spin-coated with SU8-2035 photoresist (MicroChem Corp, Westborough, MA) at 4000 RPM for 30 s to achieve a photoresist height of 40 μm. The wafer was soft-baked at 65°C for 3 min and then hard-baked at 95°C for 6 min. Afterwards, the wafer was exposed to UV light for 17 s using a Karl Suss MA6 Mask Aligner (SUSS MicroTec, Garching, Germany). The exposed resist was then baked at 95°C for 6 min. Finally, the resist was developed using SU8 developer solution (MicroChem) for 2 min and dried with a nitrogen gun. The dry wafer was silanized overnight (5 μL of 1H,1H,2H,2H-perfluorooctyltrichlorosilane; Alfa Aesar, Ward Hill, MA) in a vacuum chamber. Next, a 1:10 curing agent to polydimethyl siloxane (PDMS) solution (Slygard 184 Kit; Electron Microscopy Sciences, Hatfield, PA) was poured over the wafer to cast a mold that was placed in an oven at 65°C overnight. The PDMS mold was then cut, holes for inlets and outlets created with a 2-mm punch, and the PDMS plasma-bonded (Model BD-20; Electro-Technic Products, INC, Chicago, IL) to an ethanol-cleaned premium plain glass slide (USRB-7μm

or USRB-5 μ m, 25 x 75 x 1 mm; VWR, Radnor, PA and Lung-USRB, 75 x 50 x 100; Fisher Scientific, Hampton, NH).

4.2.6 Bioreactor perfusion with Mks – USRB-7 μ m and USRB-5 μ m

The USRB-7 μ m or USRB-5 μ m was positioned on a Lumascope microscope v500 (Etaluma Inc., Carlsbad, CA) placed inside an incubator (Thermo Scientific, Waltham, MA) maintained at 37°C and 5% CO₂. Separate syringe pumps (NE-300, New Era Pump Systems Inc., Farmingdale, NY) were used for each flow channel. A 5-mL glass syringe (81520, Hamilton Company, Reno, NV) was used for the outer channels and a 2.5-mL glass syringe (81420, Hamilton) was used for the center channel. Media (78% IMDM, 20% BIT 9500 Serum Substitute, 1% Glutamax, 1 μ g/mL low-density lipoproteins, 100 U/mL Pen/Strep) without cytokines was perfused throughout the bioreactor for 15 min at 6.5 μ L/min prior to Mk introduction. CD61⁺ selected CB-Mks from E0, E6 or E8 VPA⁺ cultures at density of 50,000 cells/mL were stained for 15 min with 1 μ M Calcein AM at 37°C. After the media perfusion, 25,000 Mks (a sufficient number to observe the system dynamics and how often they might repeat and under what conditions, without clogging the slits) were microinjected into the tubing upstream from the reactor. No Mks were present within the syringes. A 1-hr video was recorded of each bioreactor run.

4.2.7 Bioreactor perfusion with Mks – Lung-USRB

The Lung-USRB was positioned on a Lumascope microscope v500 placed inside an incubator maintained at 37°C and 5% CO₂. With a syringe pump (NE-300), ethanol was

perfused through the system for 10 min followed by water and PBS. Media (78% IMDM, 20% BIT 9500 Serum Substitute, 1% Glutamax, 1 $\mu\text{g}/\text{mL}$ low-density lipoproteins, 100 U/mL Pen/Strep) without cytokines was perfused with a 10 mL polystyrene syringe (BD Biosciences) into the bioreactor for 20 min at 100 $\mu\text{L}/\text{min}$ prior to Mk introduction. CD61⁺ selected mPB-Mks or nonselected CB culture from E0 at 500,000 cells/mL were stained for 15 min with 1 μM Calcein AM at 37°C. After the media perfusion, ~250,000 Mks were microinjected into the tubing upstream from the reactor. No Mks were present within the syringe perfusing media. A video was recorded that captured 2 channels of a branch at any time.

Recirculation studies used a 3 mL polystyrene syringe (BD Biosciences) loaded with 2.5 mLs of CD61⁺ selected mPB-Mks or non-selected CB culture from E0 at cell densities of 500,00/mL. Cells were stained with Calcein AM prior to perfusion. After the syringe was empty, the effluent collected was loaded back into the syringe and placed back on the syringe pump to continue perfusion. The total number of passes was four.

4.2.8 Video analysis

Videos (6 frames-per-second) were recorded for each experimental run using the Lumascope v500, equipped with High Sensitivity Monochrome CMOS Sensor camera, using a 20x objective. For USRB-5 μm studies, each video was analyzed for every 5-min time interval for the duration of an experiment. One half of the bioreactor was analyzed at one time throughout 5-min time intervals for the entire video recorded. This process was repeated on

the other half of the reactor. The data from each half of the reactor was then combined for each 5-min time interval. During each interval, only proPLTs and PLPs that originated from trapped Mks the slits were counted. To increase accuracy, the videos were played at a slower speed during times of high PLP release activity. The 5-min interval was selected because it allowed us to effectively analyze and understand the dynamics of the process. Pre-staining Mks with Calcein AM allowed the Mks trapped in the reactor, as well as proPLTs/PLPs, to be clearly observed.

4.2.9 Bioreactor effluent preparation

Prostaglandin E1 (PGE1, Cayman Chemical, Ann Arbor, MI) was added at 140 nM final concentration to the effluent collected, which was then spun once at 2200 *g* for 20 min to pellet Mks/cells and PLPs. The pellet was then resuspended in HEPES/Tyrode's (HT) buffer (10 mM HEPES, 137 mM NaCl, 2.8 mM KCl, 1 mM MgCl₂, 12 mM NaHCO₃, 0.4 mM Na₂HPO₄, 0.35% BSA, 5.5 mM glucose, pH 7.4) and allowed to rest for 20 min at room temperature. 2 mM CaCl₂ was added to the suspension 5 min before use in assays described below.

4.2.10 Flow cytometry preparation of bioreactor effluent

Effluent from the bioreactor was analyzed for surface markers using the following antibodies against: CD41-APC (559777), CD42b-PE (555473) or CD42b-APC (551061) and CD62P-PE (555524). Antibodies were added and thrombin at 3 U/mL was added to activate PLPs. Samples were incubated for 15 min at room temperature. Prior to perfusion through the

bioreactor, Mks were stained with live stain Calcein AM so viable PLPs in the effluent also carried this live stain. Calcein⁺ PLP events were identified. Expression of markers on PLPs was compared to an unactivated (no thrombin), stained sample.

4.2.11 Confocal microscopy

Effluent collected from the bioreactor was analyzed via immunofluorescence. 8-well chamber glass slides (125658, Lab NunTek II, Thermo Scientific, Waltham, MA) were coated with fibrinogen (Innovative Research, Novi, MI) at 60 µg/mL in PBS or 1% BSA in PBS. The effluent suspension was added to each well and allowed to rest at 37°C for 20 min and then 3 U/mL of thrombin was added to one of the wells coated with fibrinogen, and incubated for 30 min at 37°C, 5% CO₂. The chamber slide was washed once with warm PBS and then fixed with 3.7% paraformaldehyde and permeabilized with 0.3% Triton X-100 before sequentially staining with 5 µg/mL mouse anti-beta-tubulin primary antibody (5656321, BD Biosciences), and 1 µg/mL of Alexa Fluor 488-conjugated goat anti-mouse secondary antibody (A11001, Thermo Scientific). After removing unbound secondary antibody, wells were incubated with TRITC-phalloidin, washed, and then stained with DAPI (Invitrogen, Carlsbad, CA) to identify Mk bodies from anucleate proPLTs and PLPs. Slides were imaged with a 63x oil objective on a Leica DMI6000 Spinning Disc Confocal Microscope (Leica, Wetzlar, Germany). It should be noted that on some confocal images, the tubulin isn't shown due to a misstep in preparation of the secondary antibody.

4.3 Results

4.3.1 Cord-blood derived Mks can be trapped in USRB-7 μ m

Our initial analysis with USRB-7 μ m and CB-Mks demonstrated that E6 VPA+ Mks were not retained efficiently at the slits due to what appears to be smaller cell-size. Interestingly, E8 VPA+ Mks were retained more efficiently at the 7- μ m slits than E6 VPA+ Mks. With a center channel flow rate of 1.5 μ L/min and an outer channel combined flow rate of 5 μ L/min, captured E8-Mks were able to generate proPLTs (**Figure 4.3A-yellow arrows**). Without the outer channel on, the activity of the CB-Mks increased as was described in our published study with mPB-Mks and in Chapter 3 (**Figure 4.3B-blue arrows**).^[76] Initial characteristic studies on the collected PLPs showed that they can spread in the presence of thrombin on fibrinogen-coated surfaces (**Figure 4.3C**). Though E8-Mks were captured at the slits, the cells squeezed through the slits more easily and in the case of E6-Mks, not enough retention occurred for proper analysis.

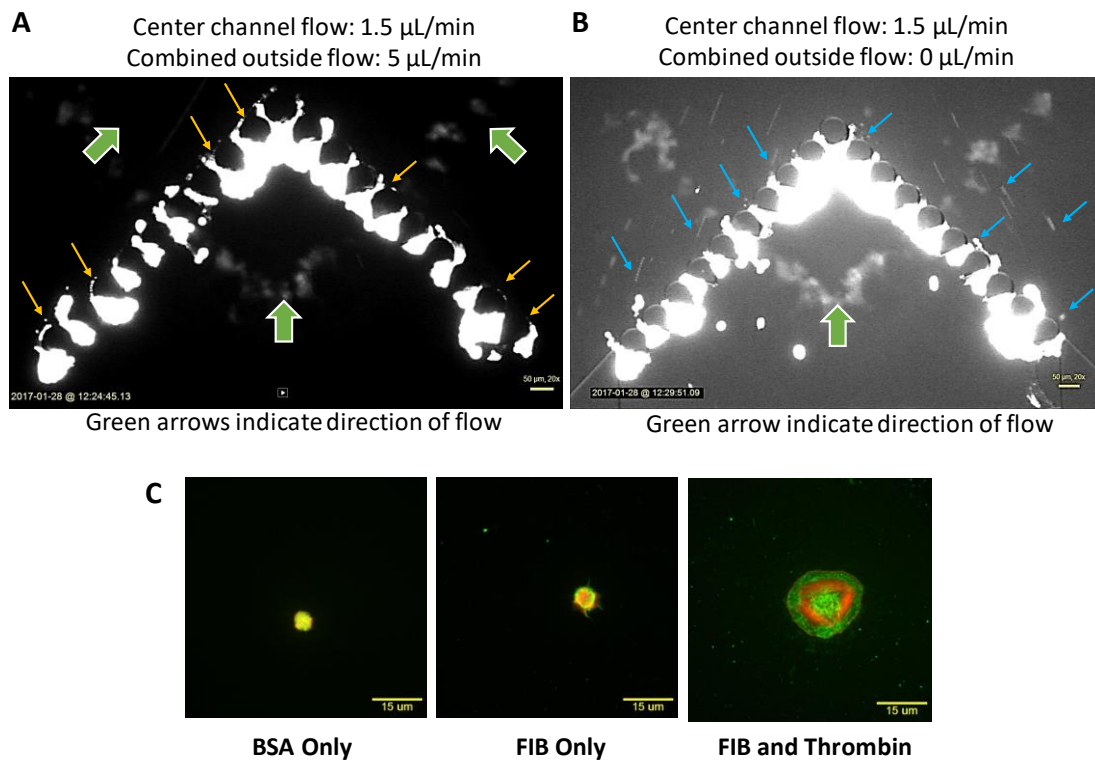


Figure 4.3 Cord blood-derived (CB) E8 VPA+ Mks in USRB-7 μm . (A) Calcein stained Mks inside USRB-7 μm making proPLTs (orange arrows). Center channel inlet flow rate = 1.5 $\mu\text{L}/\text{min}$ and outer channels combined inlet flow rate = 5 $\mu\text{L}/\text{min}$ each. (B) Calcein stained Mks inside USRB-7 μm making PLPs (blue arrows). Center channel inlet flow rate = 1.5 $\mu\text{L}/\text{min}$ and outer channels combined inlet flow rate = 0 $\mu\text{L}/\text{min}$ each. Scale bars = 50 μm . (C) Confocal analysis of PLPs collected from bioreactor experiment of center channel inlet flow rate = 1.5 $\mu\text{L}/\text{min}$ and outer channels combined inlet flow rate = 0 $\mu\text{L}/\text{min}$ each. PLPs resting on BSA and fibrinogen (FIB) and spreading on fibrinogen upon thrombin addition. Green = beta tubulin, red = actin, blue = DNA. Scale bars = 15 μm .

4.3.2 New USRB-5 μm retains a uniform shear rate environment

To improve the capture of CB-Mks at the slits, we decided to narrow the slits to 5 μm , USRB-5 μm , and kept the same slit geometry and design as the USRB-7 μm . Narrowing of the slit size also increased the number of available slits to 22 compared to 20. For simulations with no outside flow rate and a center channel flow rate of 1.5 $\mu\text{L}/\text{min}$, the range of shear stresses across the slits is shown in **Figure 4.4**. Only half of the slits are presented since there is symmetry across the reactor and the other slits would have similar shear stress ranges. CFD predictions show near-uniform shear stress at the slits (**Figure 4.4**). The new USRB-5 μm exposes Mks to a uniform environment with max shear rate at the slits of 8200 s^{-1} and shear on proPLTs at 50-90 s^{-1} (**Figure 4.5A, B**). The predicted velocity streamlines are shown in **Figure 4.5C** and the structure of the flow is similar to that reported for USRB-7 μm . [76]

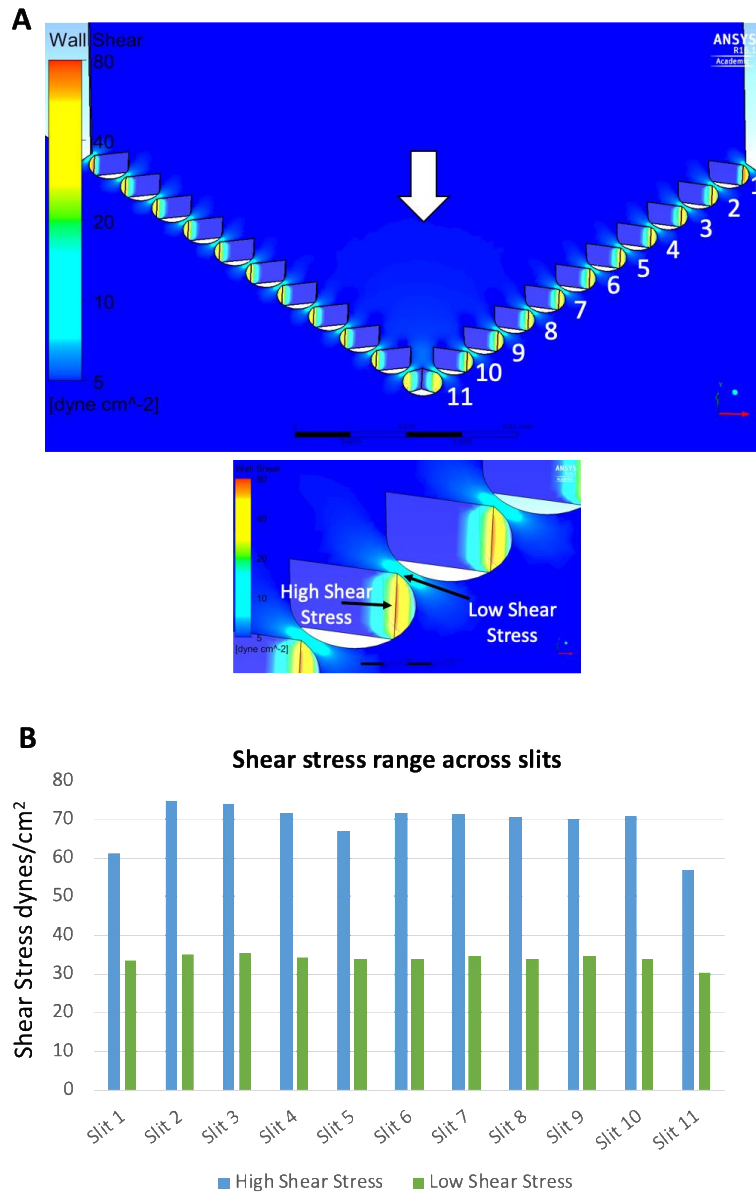


Figure 4.4 Individual slit shear stress range for uniform-shear rate bioreactor, USRB-5 μ m. (A) Shear stress profile for the reactor. Numbers represent slits. Inset shows the area of the slit that was designated high or low shear. Log-scale. White arrows indicate direction of flow. (B) Range of shear stress values for all the slits. Center channel inlet flow rate = 1.5 μ L/min and outer channels combined inlet flow rate = 0 μ L/min each.

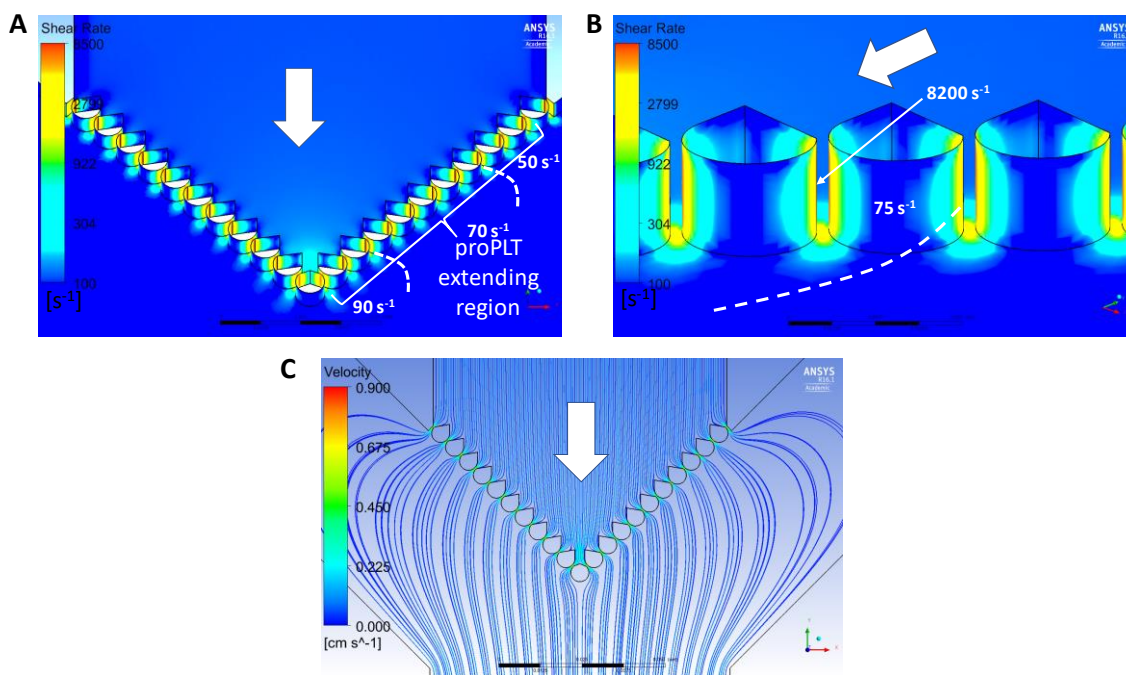


Figure 4.5 Shear rate analysis and streamlines of cell-free USRB-5 μ m. Shear rates in (A) the entire slit region and (B) a close-up view of individual slits. (C) CFD streamline plot. White arrows indicate the general flow direction. Estimated shear rates on proPLTs (dashed lines) are within 100 μ m from the slits. Bioreactor condition: 1.5 μ L/min flow rates in the center channel and 0 μ L/min in the combined outer channels.

The average CFD pressure drop across the 5- μm slits was 278 +/- 6 Pa which was nearly double the pressure drop in the USRB-7 μm (**Figure 4.6A**).^[76] The average velocity profile across the slits in the USRB-5 μm was 0.829 cm/s and in the USRB-7 μm it was 0.684 cm/s (**Figure 4.6B**). Strain rates (rate of deformation) represent extensional flow that is created due to a velocity gradient in the direction of flow. The CFD outputs of our bioreactor showed an increase in velocity along the slits. In CFD, the strain rate can be easily extracted from the velocity gradient tensor output as dV_x/dx . Plotting the average strain rate across the slits showed a maximum of 607 s^{-1} which was substantially higher than 346 s^{-1} for USRB-7 μm (**Figure 4.6C**). This increase in pressure drop, velocity and strain rate can be attributed to the smaller slit size.

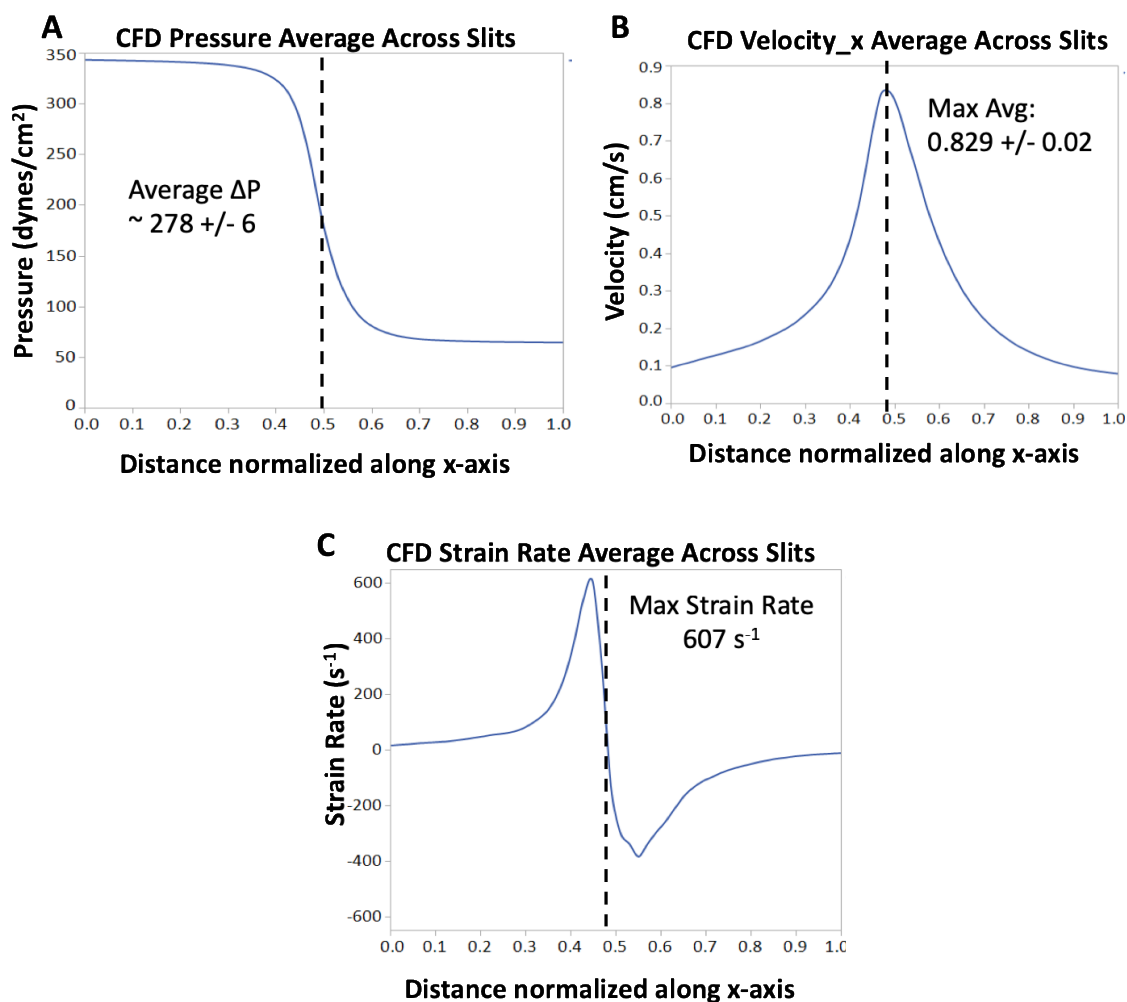


Figure 4.6 Average CFD outputs across the slits along the x-axis of USRB-5 μ m. (A) Average pressure, (B) velocity profile and (C) strain rate across the slits for center channel flow rate at 1.5 μ L/min and combined outer channel flow at 0 μ L/min. Dashed line on plots represent the 5- μ m slit opening where velocity is the highest.

4.3.4 CB-Mks are productive in the USRB-5 μ m

Selected CB-derived Mks from E0, E6 VPA+ or E8 VPA+ were introduced into USRB-5 μ m and the PLP kinetics analyzed over an hour of perfusion. Mks from all culture conditions were observed making proPLTs and rapidly releasing dozens of individual PLPs (**Figure 4.7A**). As described in Chapter 3, we can analyze the PLP release kinetics of the system through video analysis. Interestingly, the E0 Mks were more productive within the USRB-5 μ m, followed by E8 VPA+ and E6 VPA+ Mks for the same donor (**Figure 4.7B**), especially at the beginning of the perfusion run where the rate of PLP releases is higher in E0. For the individual reactors, the mean rate of PLP-release per 5-min time intervals was 791, 400, and 620, for E0, E6, and E8, respectively. Overall, the USRB-5 μ m improved the capture and retention of CB-Mks at the slits.

Figure 4.7 is part of the following paper under review:

- Wu JJ, Abbott DA, Martinez AF, Ranjan R, DeLuca TA, Doser DLP, Terzioglu MK, Mahmud D, Bagheri N, Mahmud N, Miller WM. Valporic acid improves ex vivo generation of human megakaryocytes and platelet-like-particles from pre-expanded cord blood-derived CD34⁺ cells.

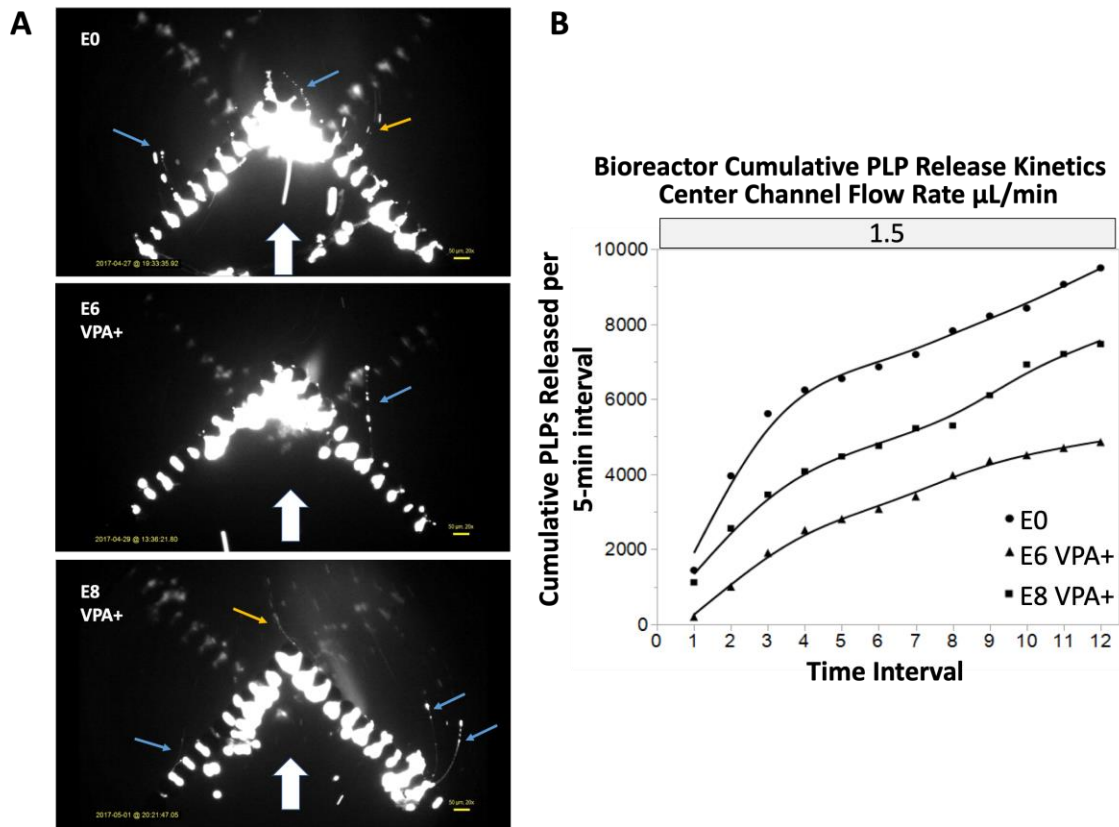


Figure 4.7 Evaluating Mk activity in USRB- $5\mu\text{m}$ from different CB culture conditions.

(A) Images of Calcein-stained Mks extending proPLTs and making PLPs from three different cord blood cultures, E0, E6 VPA+ and E8 VPA+; blue arrows = proPLTs and yellow arrows = PLPs. (B) Cumulative PLPs released per 5-min time interval for the different conditions. Bioreactor condition: $1.5 \mu\text{L}/\text{min}$ flow rates in the center channel and $0 \mu\text{L}/\text{min}$ in the combined outer channels. White arrows indicate direction of flow direction.

4.3.5 Designing a scaled-up lung-inspired USRB device

The USRB-7 μ m and USRB-5 μ m allowed a small number of cells to be introduced to study proPLT and PLP generation. We were interested in scaling up the devices to accommodate larger number of Mks so as to increase PLP yields. As such, we have developed a lung-inspired microfluidic bioreactor, Lung-USRB (**Figure 4.8**). This system was scaled based on the observations presented in Chapter 3 (and in our published study in *Biotechnology Progress* [76]) in which the use of a single flow to carry Mks into high-shear regions (slits), mimicking the lung, was more efficient than using two flows to mimic the low-shear regions in the bone marrow sinusoids. The Lung-USRB has 5.5- μ m slits and a ~90-fold increase in capture area compared to both smaller USRBs.

The main flow entering the lung-USRB splits into a series of left and right arms (**Figure 4.9A**). The branching angles were set at 30°. The height of the reactor was chosen to be 40 μ m, similar to blood sinusoid dimensions and the smaller USRBs. The arms have parallel branches that lead to smaller channels where 5.5- μ m slits are located. This geometry layout uses Murray's law that describes vessel diameters and branching, where the radius cubed of the parent branch (R_0) is equal to the sum of the radius cubed of the daughter branches (R_1 , R_2): $R_0^3 = R_1^3 + R_2^3$. This relationship assumes cylindrical geometries but can be applied to rectangular channels by using hydraulic diameter (D_H) calculations ($D_H = 2 * \text{height} * \text{width} / [\text{height} + \text{width}]$). Thus, using this relationship, the geometry of the system was defined (**Figure 4.9B**). Within the slit channels are 3 rows of 5.5- μ m slits (**Figure 4.9C**). The design of the bioreactor and the use of Murray's law was also inspired by microfluidic

systems that attempt to recapitulate key vasculature structures of the lung systems[88-90]. These earlier devices were not used for Mks/platelets. The final fabricated Lung-USRB is shown in **Figure 4.10**.

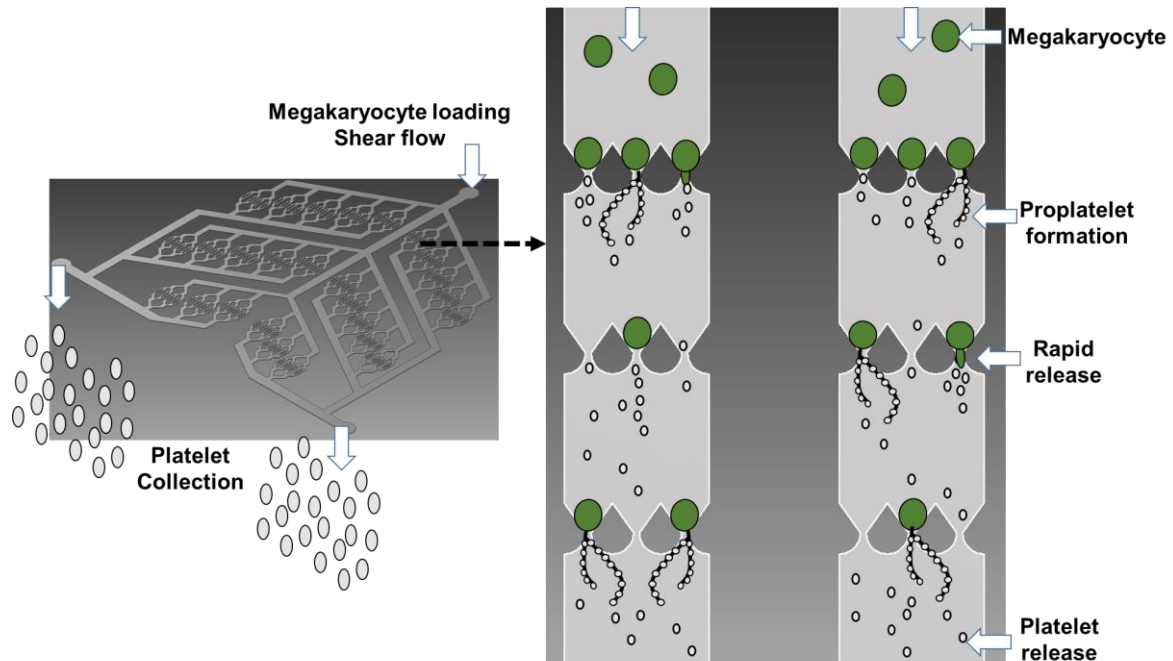


Figure 4.8 Schematic of Lung-USRB. Design and layout of Lung-USRB in which Mks are carried and distributed to channels with 5.5- μm slits.

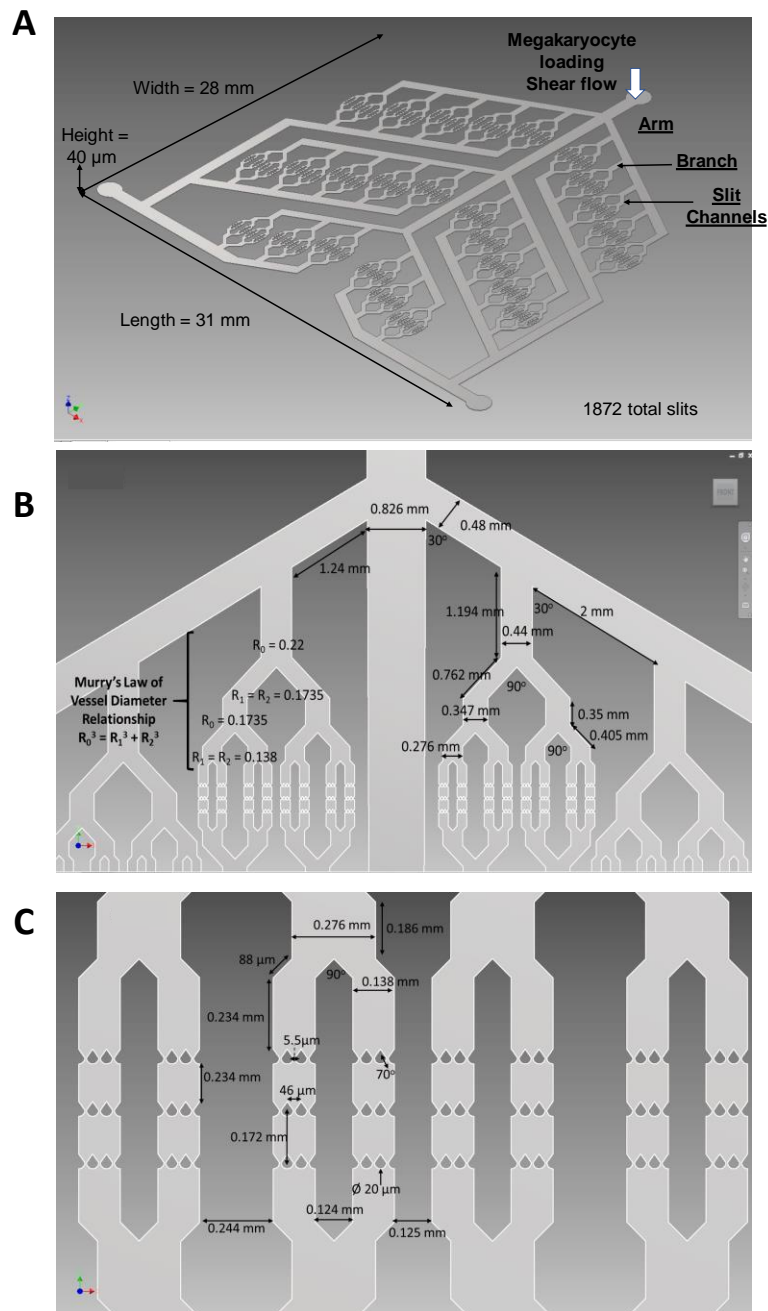


Figure 4.9 Design and dimensions of Lung-USRB. (A) Overview of dimensions of the Lung-USRB. (B) Design of arms and branches using Murray's law to set the dimensions.

(C) Dimensions of the channels where the 5.5- μm slits are located. The height was maintained at 40 μm throughout.

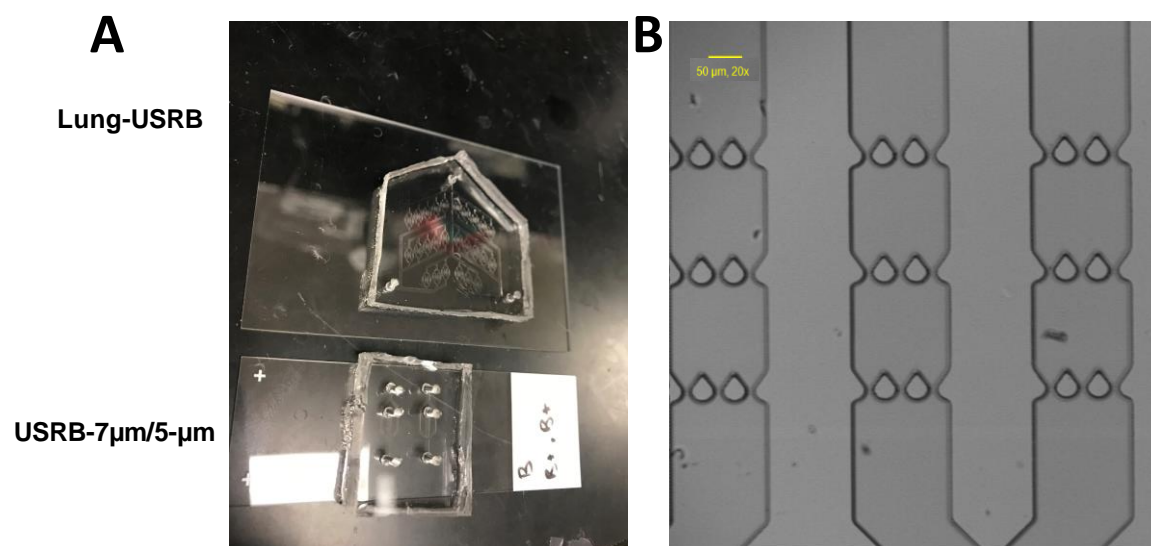


Figure 4.10 Fabricated Lung-USRB. (A) Lung-USRB device next to a fabricated smaller USRB. (B) Image of slit channels in Lung-USRB, 20x objective.

4.3.6 CFD analysis of Lung-USRB: velocity, shear rate and pressure drop

We used CFD to simulate 4 different flow rates: 10, 40, 100 and 400 $\mu\text{L}/\text{min}$ and extracted data to understand the velocity, shear rates and pressure drops across the Lung-USRB (**Figure 4.11-4.13**).

First, a heat map of velocity magnitudes at the center of the reactor ($z = 20 \mu\text{m}$) was generated and selected regions of the reactor (with velocity vectors) shown as insets in **Figure 4.11A** (flow rate = 40 $\mu\text{L}/\text{min}$). The heat map suggests that the velocity across the slits is high at the first branch of an arm, decreases across the branches (indicated by darker blue regions) and increases at the last branch of the arm (**Figure 4.11A**). To quantify the velocity magnitudes at the branches, the maximum velocity of the center slit in row #1 of channels #1 and 3 was extracted for all branches and arms (for labels/locations refer to **Figure 4.2** and top inset of **Figure 4.11A**). The max velocity magnitude varied across each arm and arm 2 had the lowest branch velocities (red bars in **Figure 4.11B**, flow rate = 40 $\mu\text{L}/\text{min}$). The first and last branches have the highest velocities compared to middle branches, especially in arms 1 and 2. For a flow rate of 40 $\mu\text{L}/\text{min}$, the predicted average velocity range of arm 1 is ~ 0.25 to 0.45 cm/s , arm 2 with ~ 0.15 to 0.3 cm/s and arm 3 at ~ 0.3 to 0.37 cm/s (**Figure 4.11B**). Simulations for additional flow rates were conducted and the average max velocity of each arm calculated further indicating that arms 1 and 3 have higher average velocities than arm 2 (**Figure 4.11C**). Finally, the average max velocity for each simulation was calculated and plotted for versus various inlet flow rates (**Figure 4.11D**). Through the velocity analysis conducted, we observe that although velocity ranges of each

arm overlap and have similar order of magnitude, there are significant differences between individual branches in each arm.

Next, the wall shear rates of the bioreactor were analyzed in the similar manner as described for the velocity and similar patterns and observations emerged. First, contours of wall shear rates were generated along with insets (**Figure 4.12A**, flow rate = 40 $\mu\text{L}/\text{min}$). Lower shear rates (darker blue regions) are predicted in the middle branches of each arm (**Figure 4.12A**). The maximum wall shear rate was quantified by extracting data from the center slit in row #1 of channels #1-4 for all branches and arms (for labels/locations refer to **Figure 4.2** and top inset of **Figure 4.12A**). Wall shear rates were the highest in the first and last branches compared to middle branches as was seen in the max velocity analysis (**Figure 4.12B**, flow rate = 40 $\mu\text{L}/\text{min}$). The average wall shear rate range for arms 1, 2 and 3 is predicted to be ~ 1200 to 2700 s^{-1} , ~ 800 to 1700 s^{-1} and ~ 1700 to 2200 s^{-1} , respectively (**Figure 4.12B**, flow rate = 40 $\mu\text{L}/\text{min}$). Additional flow rate simulations also predicted lower wall shear rates in arm 2 (**Figure 4.12C**) and the average wall shear rate of the entire bioreactor is linearly dependent on the flow rate (**Figure 4.12D**).

Finally, we analyzed the pressure drops across the bioreactor. The contours of pressure at the center of the bioreactor ($z = 20 \mu\text{m}$) were generated (**Figure 4.13A**, flow rate = 40 $\mu\text{L}/\text{min}$) and the pressure drop across each branch was estimated and an average for each arm calculated (**Figure 4.13B**). Arm 2 had the lowest pressure drop and this was also

consistent across various flow rates simulated (**Figure 4.13C**). The pressure drop of the bioreactor was linearly dependent on the inlet flow rate (**Figure 4.13D**).

The CFD analysis revealed that there are regions with highly different maximum and minimum velocities and shear rates and that within the cell-free simulations presented, the bioreactor does not have a completely uniform environment as was originally intended.

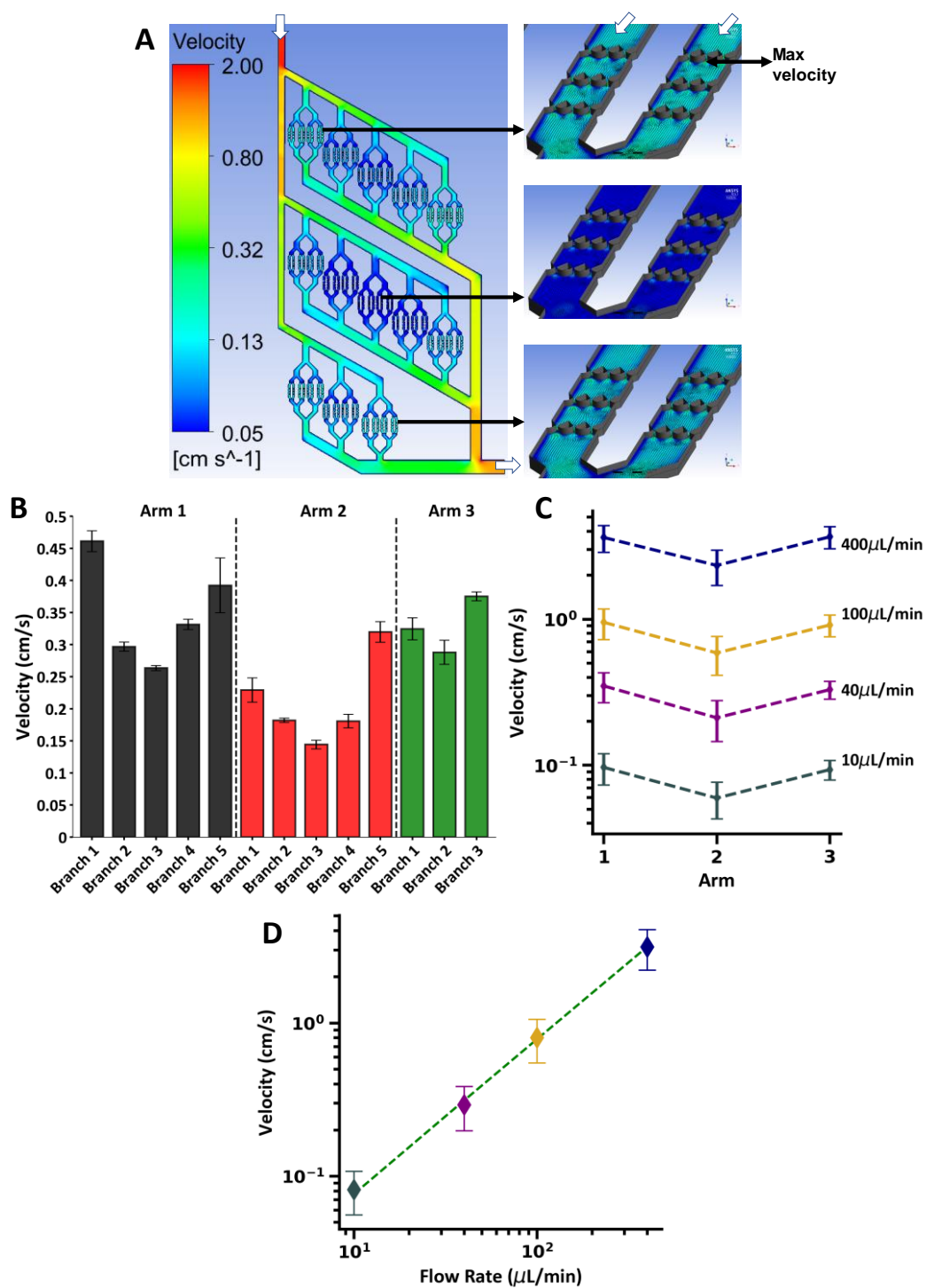


Figure 4.11 Velocity analysis in Lung-USRB at $z = 20 \mu\text{m}$. (A) Velocity heat map through middle of the bioreactor along with inset showing details and velocity vectors in slit channels

– flow rate = 40 $\mu\text{L}/\text{min}$. (B) Maximum velocity for each branch within each arm of the bioreactor – flow rate = 40 $\mu\text{L}/\text{min}$. The maximum velocity was obtained from the center slit in row #1 of channels #1 and 3. Top inset of (A) indicates the location. $n = 4$ for each branch in arms 1-3. (C) Maximum average velocity for arms 1, 2 and 3 across four flow rates. Points calculated from locations sampled in (B) totaling $n = 20$ for each point on arms 1 and 2 and $n = 12$ for arm 3. (D) The average velocity was calculated using the data points from (C) and plotted against flow rate and a line fitted. White arrows in (A) indicate direction of flow. Points and Bar plots = mean \pm standard deviation (SD). n = number of locations sampled from CFD.

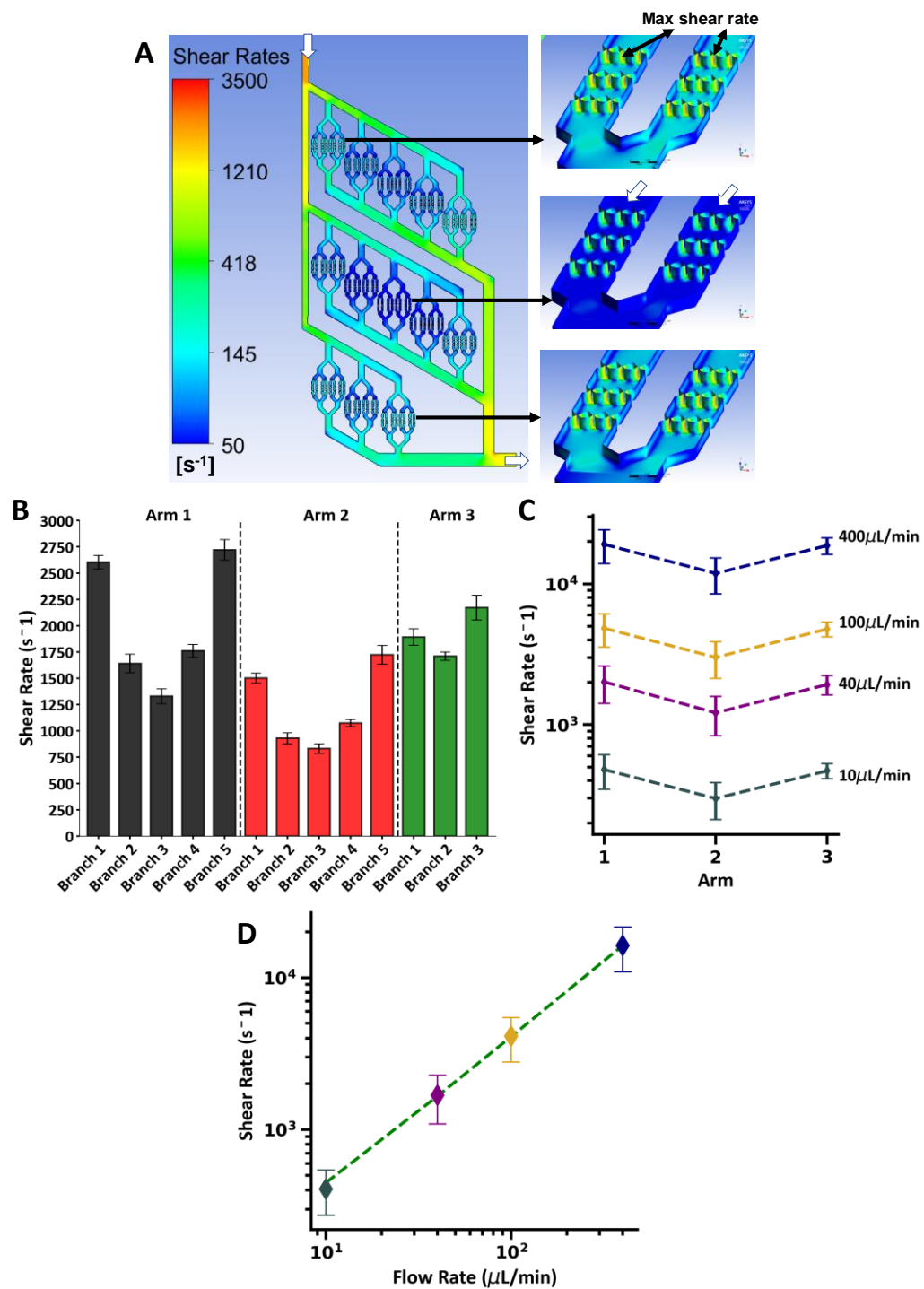


Figure 4.12 Wall shear rate analysis in Lung-USRB. (A) Shear rate contours on the wall of the bioreactor along with inset showing details in slit channels – flow rate = 40 $\mu L/min$.

(B) Maximum shear rate for each branch within each arm of the bioreactor – flow rate = 40 $\mu\text{L}/\text{min}$. The maximum shear rate was obtained from the center site in row #1 of channels #1-4. Top inset of (A) indicates the location. $n = 8$ for each branch in arms 1-3. (C) Shear rate for arms 1, 2 and 3 across four flow rates. Points calculated from locations sampled in (B) totaling $n = 40$ for each point on arms 1 and 2. $n = 24$ for arm 3. (D) The average wall shear rate was calculated using the data points from (C) and plotted against flow rate and a line fitted. White arrows in (A) indicate direction of flow. Points and Bar plots = mean \pm SD. n = number of locations sampled from CFD.

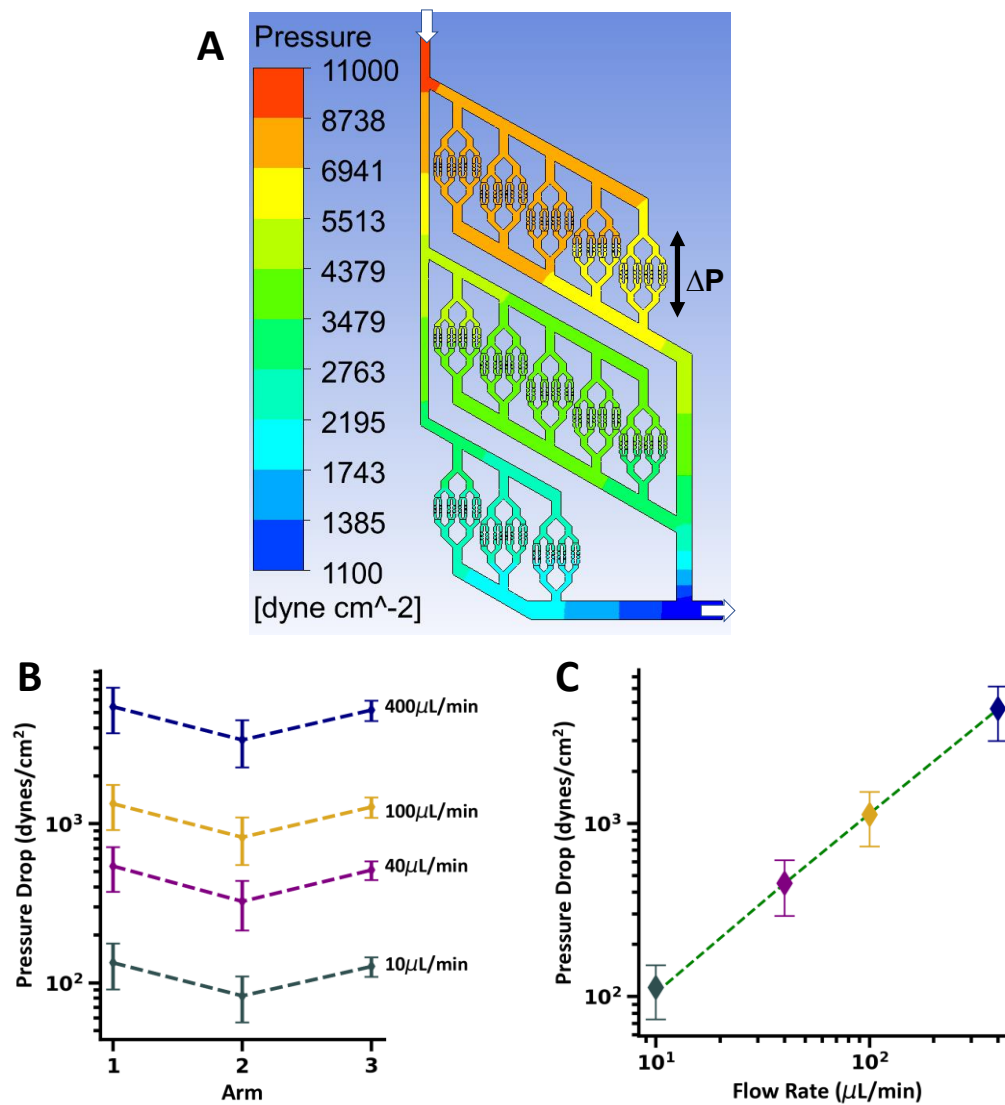


Figure 4.13 Pressure drop analysis in Lung-USRB at $z = 20 \mu\text{m}$. (A) Pressure contours in the middle of the bioreactor – flow rate = $40 \mu\text{L}/\text{min}$. The pressure drop was calculated from branch points above and below the slit channels as shown in (A). (B) Pressure drop for Arms 1, 2 and 3 across four flow rates. $n = 5$ for arms 1 and 2, $n = 3$ for arm 3. (C) The average pressure drop was calculated using the data points from (B) and plotted against flow

rate and a line fitted. White arrows in (A) indicate direction of flow. Points = mean +/- SD. n = number of locations sampled from CFD.

4.3.7 Evaluating single-pass experiments in Lung-USRB with mPB and CB-Mks

CD61⁺-selected mPB-Mks on Day 12 were injected upstream of the Lung-USRB to assess the proPLT and PLP potential of the system. The bioreactor was set to 10 μ L/min and the microscope positioned at arm 1 and branch 1. We observed that Mks were trapped along all the slits we were monitoring with larger number of cells located in the first row of slits (**Figure 4.14A**). Mks generated proPLTs and PLPs (yellow arrows) and released PLPs were able to move across the slits even if Mks were occupying them. Long proPLT extensions were also observed when the microscope was moved to another part of the bioreactor, arm 3 and branch 2 (**Figure 4.14B**). Since the field of view is small relative to the whole system, we couldn't assess many areas of the bioreactor over one run.

The effluent of the bioreactor was then collected after ~1 hr and assessed for PLP functionality. The fraction of Calcein⁺CD42b⁺ PLPs before the bioreactor run was ~57% and it surprisingly dropped to ~41% post reactor (**Figure 4.15A**) although there appeared to be a shift towards smaller Calcein⁺ particles. The bioreactor-PLPs displayed activation potential after adding thrombin and measuring CD62P expression and a pre-reactor sample had similar activity (**Figure 4.15B**). Finally, confocal images indicated that bioreactor-PLPs could spread over fibrinogen in the presence of thrombin (**Figure 4.15C**). Quick estimates indicated no substantial difference in CD42b⁺ PLPs produced before and after the bioreactor.

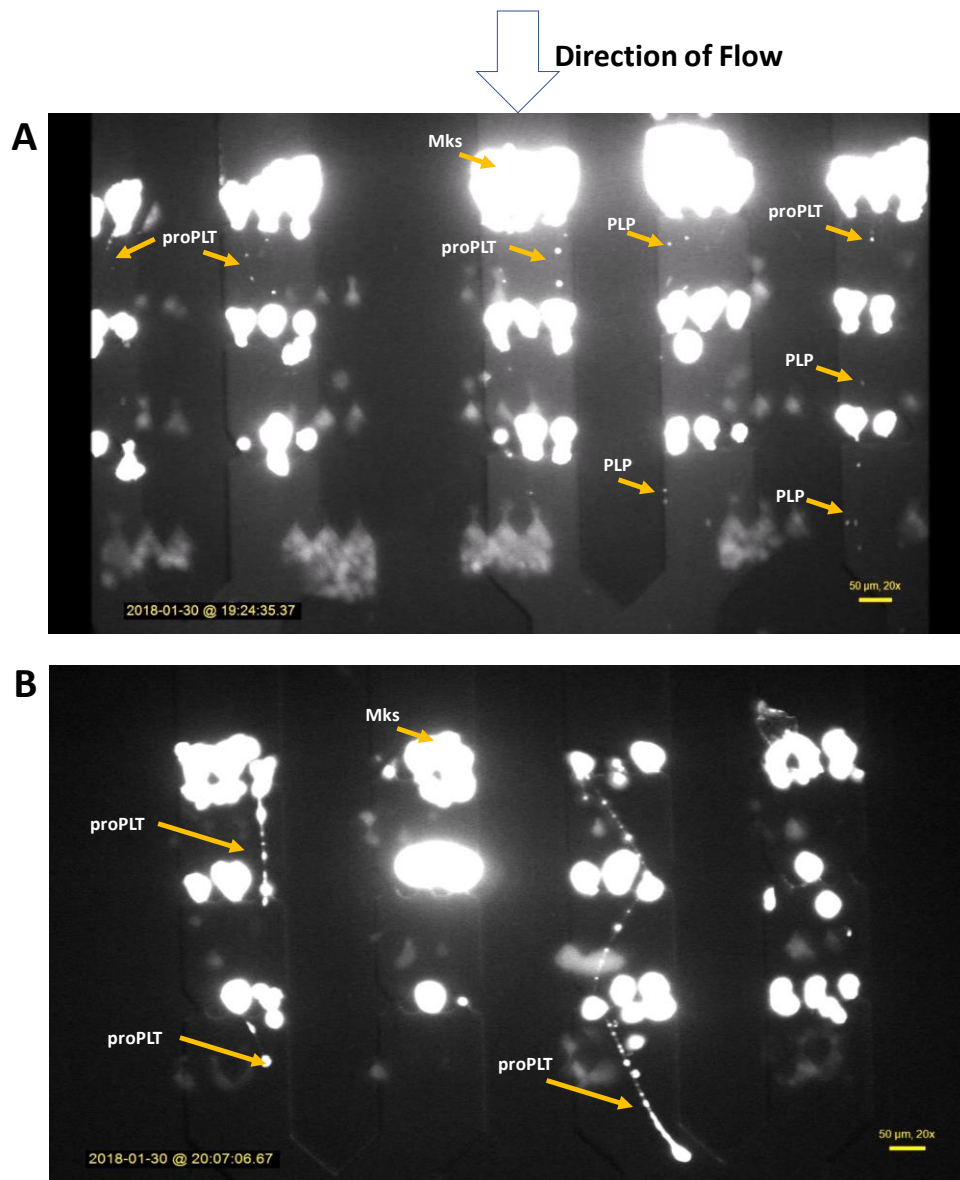


Figure 4.14 mPB-Mks generate proPLTs and PLPs in Lung-USRB. Trapped Mks at the slits generate proPLTs and PLPs (yellow arrows) with reactor positioned at (A) arm 1 and branch 1 and (B) arm 3 and branch 2. Flow rate = 10 $\mu\text{L}/\text{min}$. Mks stained with Calcein AM.

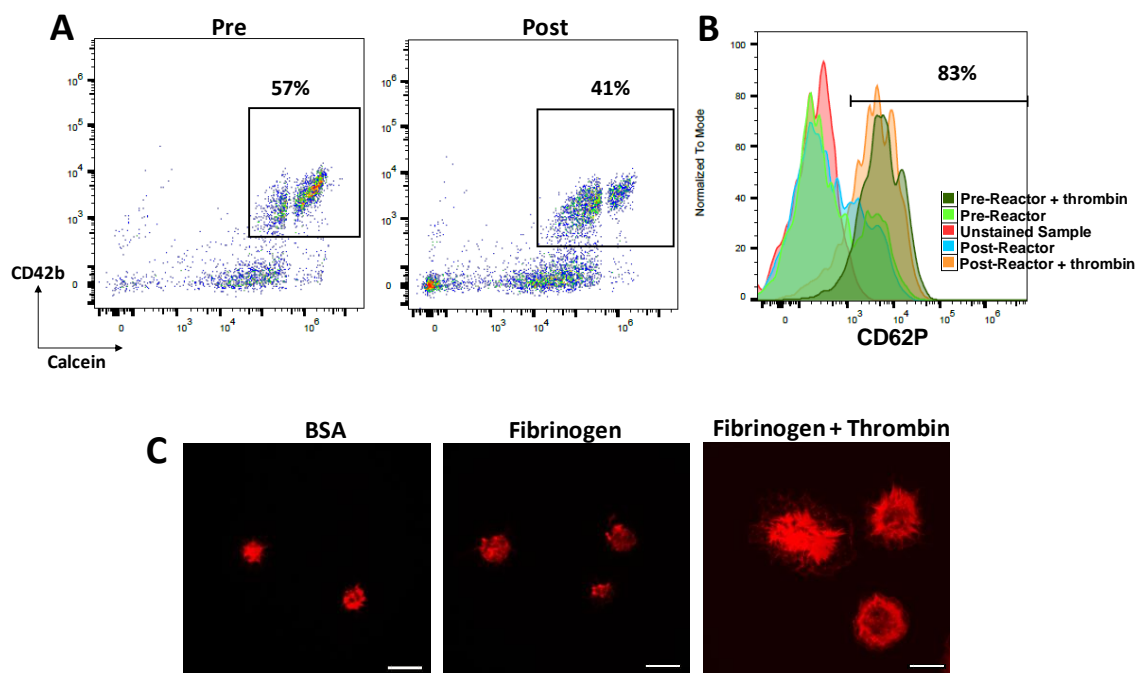


Figure 4.15 Effluent analysis of mPB-Mks from Lung-USRB at 10 μ L/min. (A) Flow cytometry plots for CD42b vs. Calcein indicating double positive PLPs before and after the reactor run. Two populations seen inside the box may indicate different sized PLPs. (B) CD62P expression on Calcein⁺CD42b⁺ PLPs before and after the reactor run in the presence or absence of thrombin. (C) Confocal images showing bioreactor-PLPs resting on BSA and fibrinogen and spreading over fibrinogen in presence of thrombin. Red = actin and blue = DNA. Scale bar = 10 μ m. Flow rate = 10 μ L/min.

In a future large-scale process, selection of Mks from the culture might be cost and labor prohibitive. Therefore, we processed non-selected cultures as well. We used non-selected CB cultures to test the potential for the bioreactor to process Mks in the presence of other cells. CB-cells (E0) were introduced into the bioreactor on Day 16 (10 μ L/min) and we observed characteristic PLP and proPLT activity in these experiments (**Figure 4.16A**). We compared flow cytometry plots before and after the bioreactor for Calcein⁺CD42b⁺ cells and PLPs. There was a slight reduction in the fraction of double positive cells (**Figure 4.16B**) and a drop in PLPs (**Figure 4.16C**). Similarly, to our previous experiment with selected mPB-Mks, there wasn't significant differences in PLP numbers before and after the bioreactor.

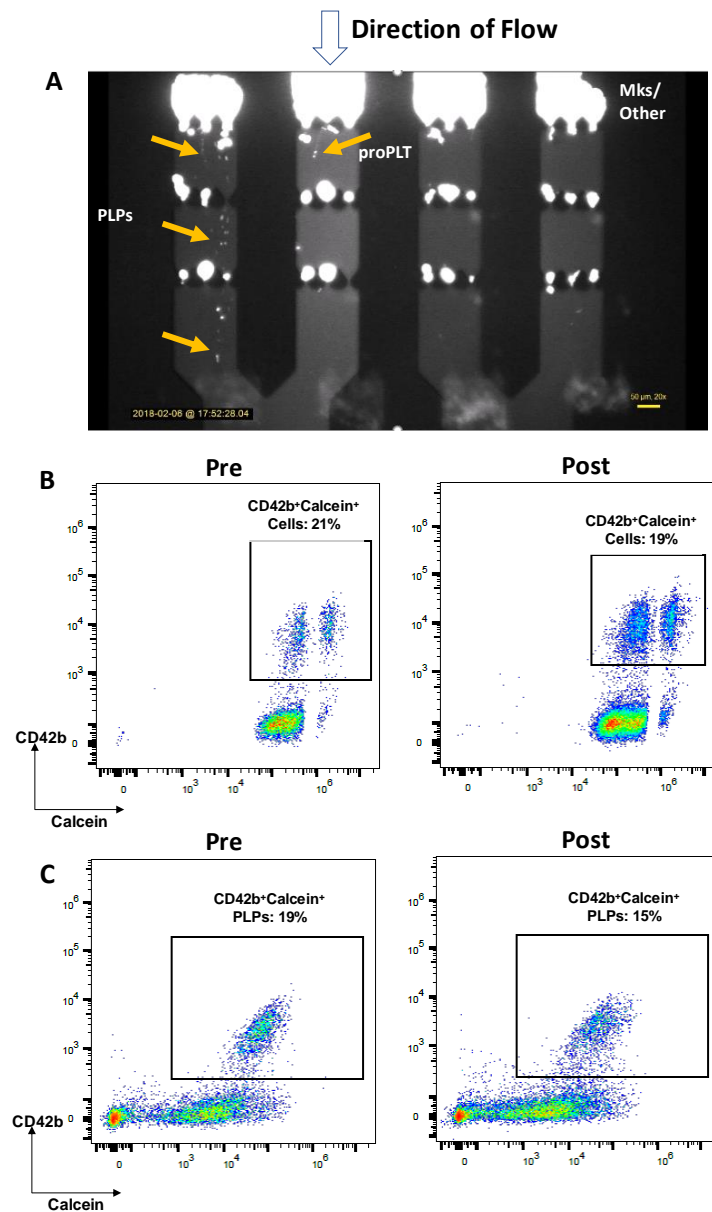


Figure 4.16 Effluent analysis of a non-selected CB culture from Lung-USRB at 10 $\mu\text{L}/\text{min}$. (A) Images of Calcein-stained cells from non-selected CB culture trapped at the slits of bioreactor. ProPLTs and PLPs can be seen (yellow arrows). Flow cytometry plots for CD42b vs. Calcein indicating (B) double positive cells and (C) double positive PLPs before and after the reactor run. Flow rate = 10 $\mu\text{L}/\text{min}$.

4.3.8 Recirculation of CB and mPB-Mks through the Lung-USRB

From the first set of experiments, we determined that the low flow rate, though enough to stimulate Mks to make PLPs and proPLTs, led to flow stagnation and overall low productivity. For the next experiments, we increased the flow rates and recirculated the processed volume four-times to try and increase PLP-yields. At 40 $\mu\text{L}/\text{min}$, a non-selected CB culture (E0) was placed in a syringe and 2.5 mLs perfused into the bioreactor. After one pass, the volume was reintroduced into the system. Flow cytometry plots before and after the 4th pass indicated that a dense population of particles was generated (**Figure 4.17A**). The fraction of cells that was Calcein⁺CD42b⁺ remained unchanged before and after the 4th pass (**Figure 4.17B**). The fraction of particles that were Calcein⁺CD42b⁺ was ~18% before and dropped to ~9% after the runs (**Figure 4.17C**). The activation potential of bioreactor-PLPs indicated a shift in CD62P expression after thrombin addition (**Figure 4.17D**).

Next, we introduced selected mPB-Mks at 100 $\mu\text{L}/\text{min}$ and processed the syringe volume four-times again. Image of the bioreactor run (**Figure 4.18A**) showed PLP generation and acceptable capture of Mks. The effluent characterization displayed similar results as the CB recirculation study. The fraction of CD41⁺CD42b⁺ PLPs dropped from 46% to 37% after the bioreactor runs (**Figure 4.18B**) while the bioreactor-PLPs still retained activation potential (**Figure 4.18C**). Confocal analysis of the effluent showed naked nuclei resting on BSA as well as PLPs that spread over fibrinogen in the presence of thrombin (**Figure 4.18D**). We then examined a higher flow rate of 200 $\mu\text{L}/\text{min}$ + recirculation. Images of the bioreactor run showed trapped Mks and PLP generation, but cells easily pushed through the slits at this

higher flow rate (streaks of Calcein in the images) and visually it was difficult at times to assess the productivity of the bioreactor at this speed (**Figure 4.19**). The fraction of CD41⁺CD42b⁺ PLPs had a greater drop after this experimental run from 51% to 24% (**Figure 4.20A**) yet retained activation potential (**Figure 4.20B, C**).

In summary, the experimental runs with mPB-Mks and non-selected CB cultures suggest minimal PLP improvements and larger fractions of CD42b-negative PLPs being produced through either the potential loss of CD42b⁺ PLPs as well as inefficient fragmenting of Mks, especially at high flow rates and recirculation.

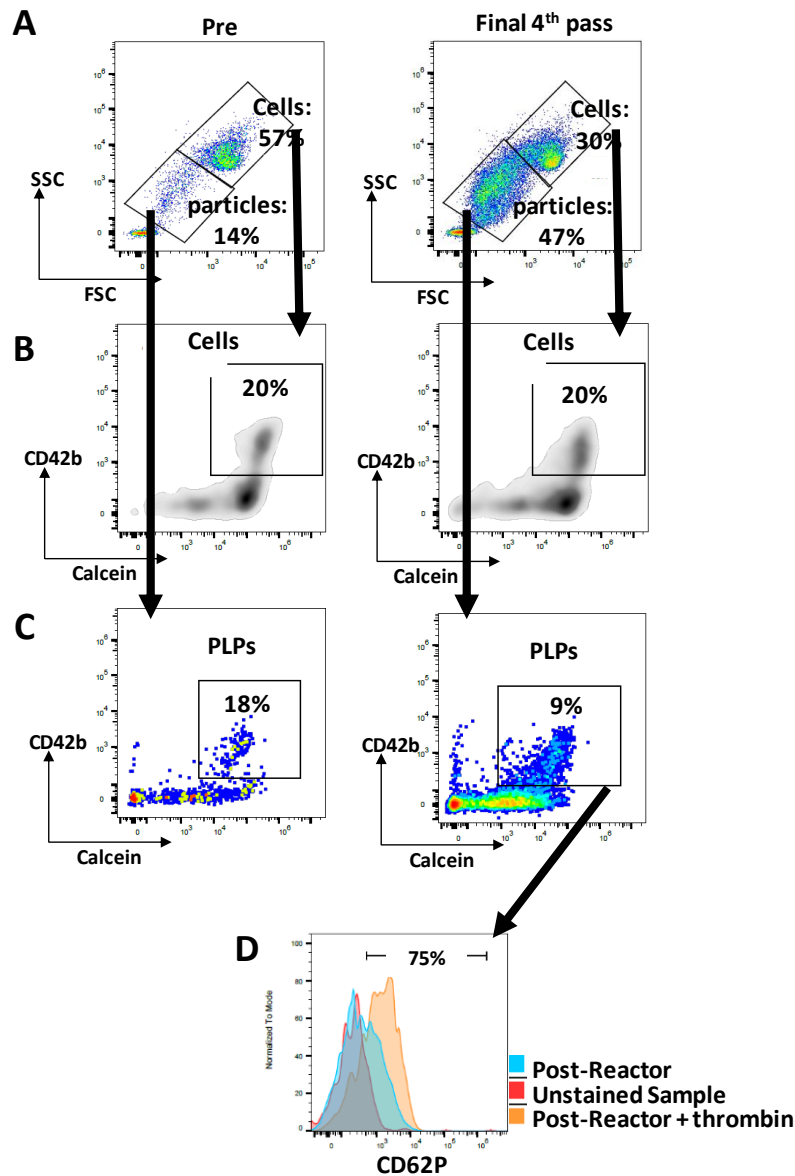


Figure 4.17 Recirculating a non-selected CB culture at 40 $\mu\text{L}/\text{min}$ in Lung-USRB. Flow cytometry plots for (A) Side Scatter (SSC) vs. Forward Scatter (FSC), (B) CD42b vs. Calcein for cells population and (C) CD42b vs. Calcein for particles before and after 4 passes through the reactor. (D) CD62P expression on Calcein⁺CD42b⁺ PLPs after the reactor run in the presence or absence of thrombin. Bioreactor flow rate = 40 $\mu\text{L}/\text{min}$.

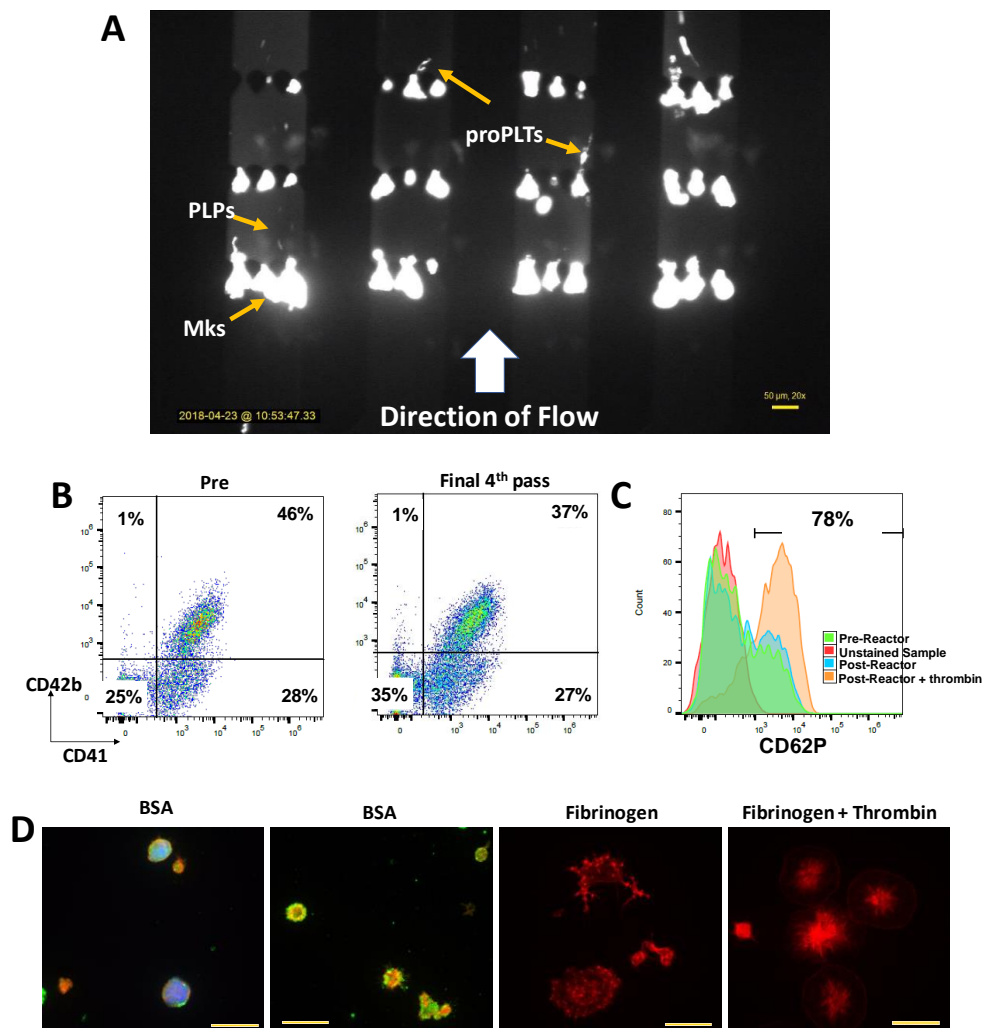


Figure 4.18 Effluent analysis of mPB-Mks after recirculation at 100 μ L/min in Lung-USRB. (A) Trapped Calcein-stained Mks at the slits generate proPLTs and PLPs (yellow arrows). (B) After gating on Calcein⁺ PLPs, flow cytometry plots for CD42b vs. CD41 indicating double positive PLPs before and after the reactor runs. (C) CD62P expression on Calcein⁺CD42b⁺ PLPs before and after the reactor runs in the presence or absence of thrombin. (D) Confocal images showing bioreactor-PLPs resting on BSA and fibrinogen and spreading over fibrinogen in presence of thrombin. For fibrinogen and fibrinogen +

thrombin, red = actin and blue = DNA. For BSA, red = actin, blue = DNA and green = beta-tubulin. Scale bar = 15 μm . Bioreactor flow rate = 100 $\mu\text{L}/\text{min}$.

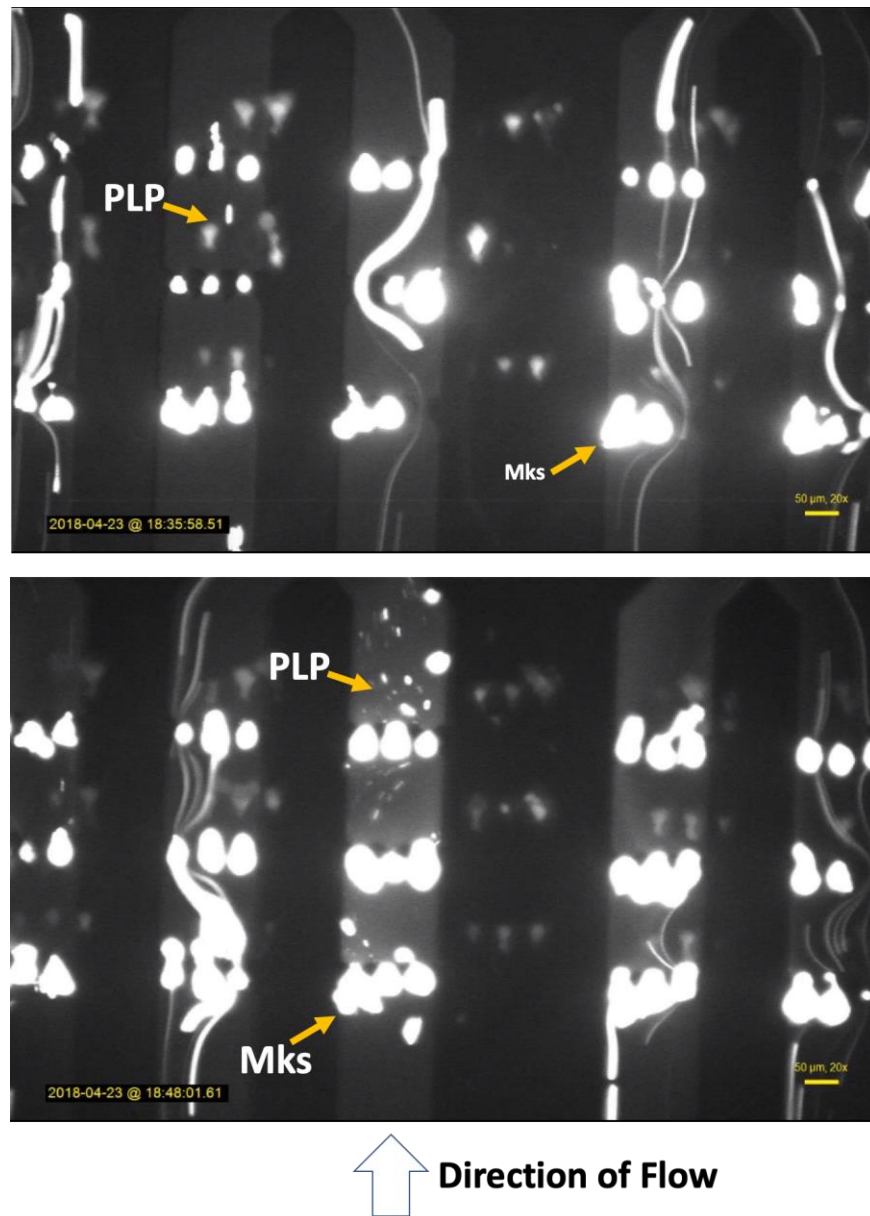


Figure 4.19 mPB-Mks recirculating through Lung-USRB at 200 $\mu\text{L}/\text{min}$. Trapped Mks at the slits generate PLPs (yellow arrows). Mks also move quickly through slits and do not get captured. Flow rate = 200 $\mu\text{L}/\text{min}$. Mks stained with Calcein AM.

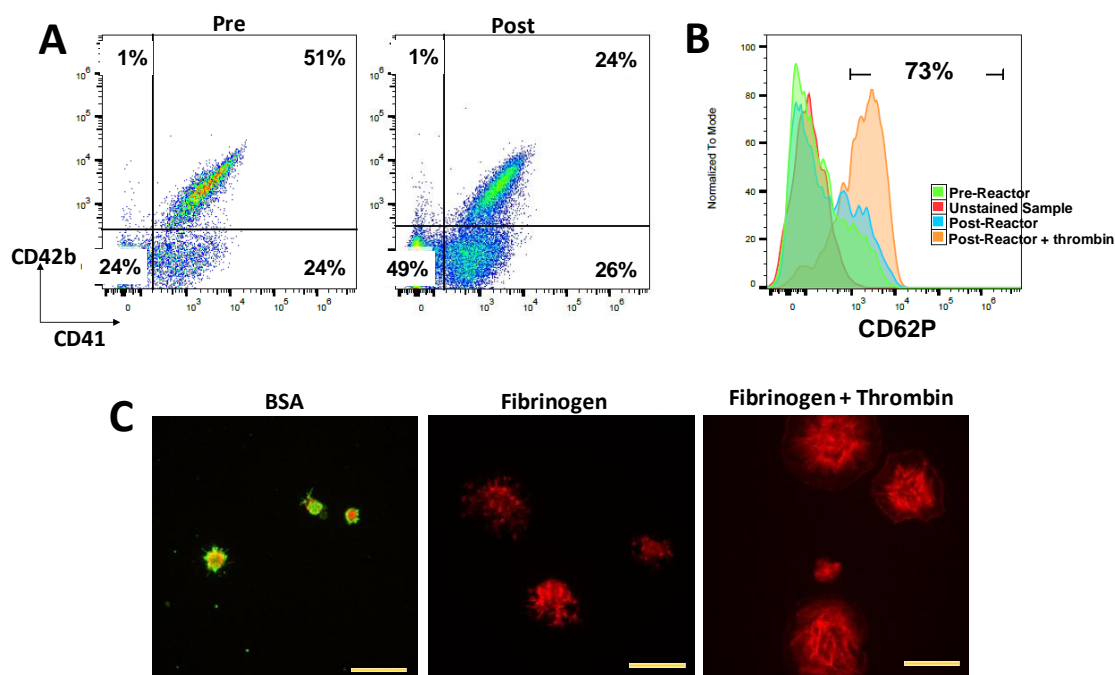


Figure 4.20 Effluent analysis of mPB-Mks after recirculation at 200 $\mu\text{L}/\text{min}$ in Lung-USRB. (A) After gating on Calcein⁺ PLPs, flow cytometry plots for CD42b vs. CD41 indicating double positive PLPs before and after the reactor runs. (B) CD62P expression on Calcein⁺CD42b⁺ PLPs before and after the reactor runs in the presence or absence of thrombin. (C) Confocal images showing bioreactor-PLPs resting on BSA and fibrinogen and spreading over fibrinogen in presence of thrombin. For fibrinogen and fibrinogen + thrombin, red = actin and blue = DNA. For BSA, red = actin, blue = DNA and green = beta-tubulin. Scale bar = 15 μm . Bioreactor flow rate = 200 $\mu\text{L}/\text{min}$.

4.4 Discussion

The use of microfluidic devices to study Mks has proven to be beneficial in understanding variables and environments that are conducive for proPLT and PLP generation.[48,50,77] We have previously introduced and discussed our uniform shear rate bioreactor, USRB-7 μ m, and demonstrated that a single flow carrying Mks into high shear rate regions led to high productivity from mPB-Mks.[76] In this chapter, we adapted the bioreactor to incorporate 5- μ m slits (USRB-5 μ m) to improve the capture of CB-Mks due to their smaller size and ploidy compared to mPBs-Mks. The new version of the bioreactor retained uniform shear rate environments at all the slits, determined through CFD modeling. At the same flow rate of 1.5 μ L/min in the center channel, the USRB-5 μ m generated max wall shear rates at the slits of 8200 s^{-1} which was higher than 5000 s^{-1} in the USRB-7 μ m[76], though similar orders of magnitude. The goal of the USRBs is to function as characterization tools to understand the potential of PLP generation. In this chapter, we evaluated three different CB cultures in the USRB-5 μ m and observed that the PLP-potential differed among the cultures. By determining that the culture protocol can impact PLP generation, the USRB-5 μ m could identify optimal cultures and provide additional information to further refine the Mk-generation process upstream.

In vivo studies in mice demonstrated that Mks entered the blood and were rapidly processed in the lung with nearly 50% of platelets being generated in the lung.[27] Shear rates in the lung capillaries have been estimated to be \sim 2800 s^{-1} [84]. Given our observations that a single flow carrying Mks into these high slit regions was enough to initiate and promote

proPLT formation and due to the *in vivo* mice observations, we attempted to scale up the device. The new device, Lung-USRB, retained the slit features and geometries from the smaller devices and used 5.5- μm slits.

The Lung-USRB structure was inspired by a published lung-microfluidic device by Hoganson et al.[88] The authors were focused on studying oxygen and gas transfer across a gas permeable membrane and through the microfluidic network. Also using Murray's law to set channel dimensions, the final width and height of their capillary region was 100 μm . The equivalent capillary region of the Lung-USRB is where the 5.5- μm slits are located and the width was 138 μm and height 40 μm . The Hoganson device was built using micro milling which allowed greater control of feature sizes and allowed aspect ratios to remain at 1:1. Our photolithography fabrication makes it difficult to retain the aspect ratio at 1:1 due to the need of having multiple exposures at various heights which can introduce fabrication defects.

CFD analysis of the Lung-USRB revealed non-uniform velocity and shear rate environments across multiple simulated flow rates. Branches and channels located in the middle of the device had on average $\sim 2x$ lower shear rates compared to outside locations. The ability to generate largely uniform environments within a branching-rectangular network was demonstrated Hoganson et al.[88] Therefore, improvements of the channel design of this first-generation Lung-USRB is highly desired and a more uniform shear environment should be achievable. Studies have used modified numerical methods to solve Murray's law to

generate improved microfluidic models for rectangular-PDMS systems that predict and control the flow through branching networks more efficiently [91,92].

Our Mk experiments within the Lung-USRB at various flow rates highlighted several promising observations and challenges that need to be addressed. We were able to process CD61⁺ selected mPB-Mks and non-selected CB-Mks. At all flow rates tested, we could observe Mks generating proPLTs and PLPs, though at higher flow rates visual assessment was more difficult. Collected PLPs could activate in the presence of thrombin and expose CD62P as well spread on fibrinogen-coated surfaces. Furthermore, recirculation experiments did not reveal any negative effects to the activation potential of the PLPs collected.

On the other hand, we observed significant moments of flow stagnation at low flow rates which prevented a complete assessment of the Lung-USRB. To address this challenge, we could incorporate flow reversal with a peristaltic pump to dislodge trapped cells at the slits and allow flow to resume. Importantly, our estimates of PLP-yields did not lead to significant (if any) increases in CD42b⁺ PLP production for any of the conditions. Flow cytometry data indicated that our fraction of CD42b⁺ PLPs was lower compared to the pre-reactor samples and at high flow rates and recirculation we were generating smaller CD42b-negative particles. Whether these particles were CD42b⁺ and then shed the marker is unclear. Studies have shown that the fraction of nearly 100% CD42b⁺ blood platelets dropped to 80-70% after exposure for 0.5 seconds to non-physiological high shear rates (~40,000 to 80,000 s⁻¹

¹).[93] Though we did not achieve similar shear rates in the Lung-USRB, continuous exposure to our shear rates over multiple passes could lead to some CD42b shedding. Future studies could also be done with the GM6001 metalloproteinase inhibitor that has been shown to prevent CD42b shedding *in vitro* and *in vivo*. [94-96] Studies with expired blood platelets inside the Lung-USRB could also inform us of the potential loss of CD42b at various flow rates. Additionally, PLPs could be adhering to the PDMS or glass surface.

To date, microfluidic systems for PLP generation have largely been focused on the slit-capture aspect or the use of protein-coated pillars for Mk adherence. [48,50,76,82] The Lung-USRB is the first microfluidic platelet bioreactor that has incorporated large physiological networks that mimic blood vasculature alongside with slit-capture to assess PLP potential. Though this first-generation device is not yet suitable to increases in PLP-yields, improving the design to generate a more controlled and uniform environment should provide a better assessment of the Lung-USRB potential.

4.5 Acknowledgements

This research was supported by NIH 1R01HL130760-01. AM was also partially supported by NIH Predoctoral Training Grant T32 GM008449. This work utilized Northwestern University Micro/Nano Fabrication Facility (NUFAB), the Flow Cytometry Core Facility and the Biological Imaging Facility at Northwestern University. We thank Damien Doser and Afra Siddiqui with setting up experiments and Jia Wu for contributing the cord-blood cells for the bioreactor experiments.

CHAPTER 5: Enabling large-scale ex vivo production of megakaryocytes from CD34⁺ cells using gas-permeable surfaces

This chapter from a published study[97]:

- Martinez AF, Miller WM. Enabling Large-Scale ex vivo Production of Megakaryocytes from CD34⁺ Cells Using Gas-Permeable Surfaces. *STEM CELLS Translational Medicine*. 2019;10.1002/sctm.18-0160

5.1 Introduction

A major challenge of generating large numbers of culture-derived platelets is producing large numbers of mature Mks from each input CD34⁺ cell.[10,34,98] Mks can be derived from either umbilical cord blood (UCB), bone marrow (BM), or mobilized peripheral blood (mPB) CD34⁺ HSPCs.[10] Also, induced pluripotent stem cells (iPSCs) have been used to generate Mks and Mk cell lines.[43,99-101] Media conditions and cytokine combinations, as well as manipulating the pH and pO₂ during culture, are continuously being optimized for Mk production.[35,36,42] Although HSPC expansion has been studied in various technologies such as 2D static cultures, stirred systems and rocking bags [44,45], there has been minimal evaluation of new technologies for Mk production. Developing new culture processes for generating Mks should also improve culture productivities. Yang et al. demonstrated that a rotary cell culture system, which keeps cells in a continuous free-falling 3D environment, enhanced the number of mature Mks from CB CD34⁺ cells.[46]

Recently, the G-Rex membrane system has been used to expand large numbers of T-cells, NK cells, HSPCs, and other cell lines within a scalable closed system.[102-107] The gas-

permeable membrane provides efficient oxygen transfer from the incubator atmosphere to the cells. CO₂/O₂ diffusion is no longer dictated by the media height, which usually restricts media usage in standard tissue culture flasks and wells. The G-Rex allows the use of various cell densities and larger volumes of media without the need for numerous media exchanges. Although the G-Rex system has shown extensive benefits for other cell types, it has not been evaluated for the expansion and differentiation of CD34⁺ cells into Mks.

We investigated the G-Rex system for Mk production from mPB CD34⁺ cells using our three-phase protocol (**Figure 5.1**).[42] Recent studies have shown that fed-batch media dilution schemes increase HSPC expansion [108] so we also studied media dilutions. A key parameter for G-Rex is the seeding cell-surface density. Previous studies using the megakaryoblastic K562 cell line showed that cell-surface densities between 125 to 1000 x 10³ cells/cm² yielded similar expansions, whereas a density of 62.5 x 10³ cells/cm² produced little to no expansion.[109] We screened various cell-surface densities and found that a seeding density of 40 x 10³ cells/cm² plus culturing the cells in G-Rex for the first 5 days, along with media dilutions, more than doubled Mk production per input CD34⁺ cell compared to using a standard tissue culture surface (STCS) and full media exchanges. G-Rex conditions also increased the number of CD34⁺CD41⁺ cells produced by Day 7 of culture. Although the mean Mk ploidy was lower in G-Rex cultures, these conditions produced equal or greater numbers of high-ploidy Mks compared to STCS cultures. G-Rex Mks displayed characteristic proPLT extensions and PLPs collected from G-Rex Mks

showed *in vitro* functionality. These results demonstrate the potential of using gas-permeable surfaces and improved cell-culture techniques to increase *ex vivo* generation of Mks.

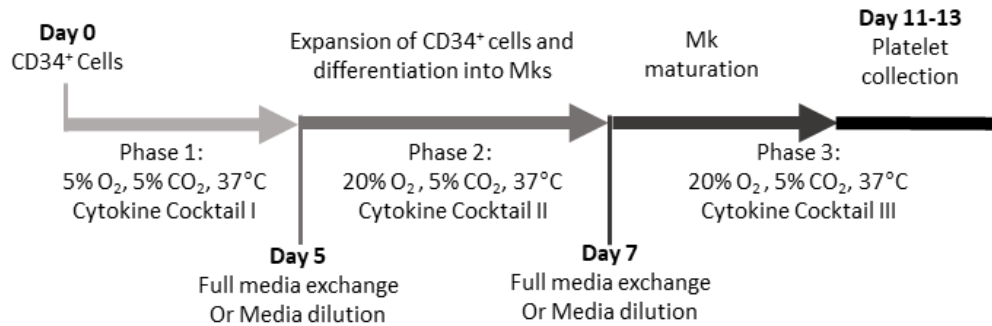


Figure 5.1 Megakaryocyte (Mk) production protocol. Three-phase culture to expand and differentiate CD34⁺ mobilized peripheral blood (mPB) hematopoietic stem and progenitor cells (HSPCs) into Mks, utilizing different cytokine cocktails and/or oxygen levels in each stage.

5.2 Materials and methods

Unless otherwise specified, all reagents were obtained from Sigma-Aldrich (St. Louis, MO), cytokines from Peprotech (Rocky Hill, NJ), and antibodies for flow cytometry analysis from BD Biosciences. LSR II or LSR Fortessa (BD Biosciences, San Jose, CA) flow cytometers were used to collect data and analysis was done using FlowJo v.10 (FlowJo LLC, Ashland, OR).

5.2.1 Cell culture

Previously frozen mPB CD34⁺ cells obtained from the Fred Hutchinson Cancer Research Center (Seattle, WA) with Northwestern University Institutional Review Board approval were grown in 78% IMDM (Gibco, Carlsbad, CA), 20% BIT 9500 Serum Substitute (STEMCELL, Vancouver, BC, Canada), 1% Glutamax (Gibco), 1 µg/mL low-density lipoproteins (Calbiochem, Whitehouse Station, NJ), 100 U/mL Pen/Strep, 100 ng/mL TPO, 100 ng/mL SCF, 10 ng/mL IL-6, 10 ng/mL IL-11, and 2.5 ng/mL IL-3 (R&D Systems, Inc., Minneapolis, MN). Conditions were kept at 37°C, 5% CO₂, and 5% O₂ for 5 days (Panasonic incubator MCO-170M, Wood Dale, IL). After Day 5 and through rest of culture, cultures were grown in 37°C, 5% CO₂, and 20% O₂.

Culture conditions have been labeled in the format XyyZ, where X represents major culture type (C, G), yy is the seeding density in thousands per cm², and Z represents a modification (if relevant; R, D). R describes a G-rbx condition that has restricted oxygen transfer and D describes diluted conditions. For example, STCS controls and G-Rbx conditions seeded at 11×10^3 cells/cm² are C11 and G11, respectively. Diluted conditions would then be C11D or G11D.

For STCS controls (C11), on Day 0 cells were seeded at 40,000 cells/mL in 6-well (9.5 cm²) plates with 0.28 mL of media/cm². On Day 5, cells were resuspended in fresh media at a density of 250,000 to 450,000 cells/mL with 100 ng/mL TPO, 100 ng/mL SCF, 10 ng/mL IL-9, 10 ng/mL IL-11, and 10 ng/mL IL-3. On Day 7, cells were resuspended in fresh media

to a density of 450,00 to 600,000 cells/mL with 100 ng/mL TPO, 100 ng/mL SCF and 6.25 mM nicotinamide.

G-Rex experiments had seeding cell-surface density of 40×10^3 cells/cm² (G40D), unless otherwise stated, in G-Rex 6-well (10 cm²) or 24-well (2 cm²) plates (Wilson Wolf Corp., Saint Paul, MN). Volumetric cell density was 40,000 cells/mL with 1 mL of media/cm². On Day 5, the cells were removed from G-Rex and diluted with fresh media between a 1 and 1.5-fold dilution ratio based on initial volume. Cytokines (same as STCS Day 5) were added for the full volume. On Day 7, a dilution ratio with fresh media was used (between 0.3 and 1-fold) based on the Day 5 volume. Cytokines (same as STCS Day 7) were added for the full volume.

A dilution control (C11D) condition was also created, seeded similarly to STCS control C11, but at Days 5 and 7 treated similarly to G-Rex cells as described above.

To minimize differences in media volumes added and media heights, on Days 5 and 7, G40D and C11D dilutions targeted C11 density ranges specified above. Media heights for all conditions outside of G-Rex were kept between 0.25 to 0.30 cm. We observe donor-to-donor variability, but the same media heights were used for conditions from a single donor. Post Day 7, all conditions were maintained at a density between 700,000 to 1 million cells/mL.

Culture conditions have been labeled in the format XyyZ, where X represents major culture type (C, G), yy is the seeding density in thousands per cm^2 , and Z represents a modification (if relevant; R, D). R describes a G-rbx condition that has restricted oxygen transfer and D describes diluted conditions. For example, STCS controls and G-Rbx conditions seeded at 11×10^3 cells/ cm^2 are C11 and G11, respectively. Diluted conditions would then be C11D or G11D.

5.2.2 Initial screening of high cell-surface-density experiments

On Day 0, cells were seeded in a G-Rbx 24-well plate (2 cm^2) (Wilson Wolf Corp., Saint Paul, MN) at cell surface densities of 100, 140, and 200×10^3 cells/ cm^2 . The starting media volume for all G-Rbx conditions was 8 mL. Four different media handling conditions were set-up as shown in **Figure 5.2** and **Table 5.1**.

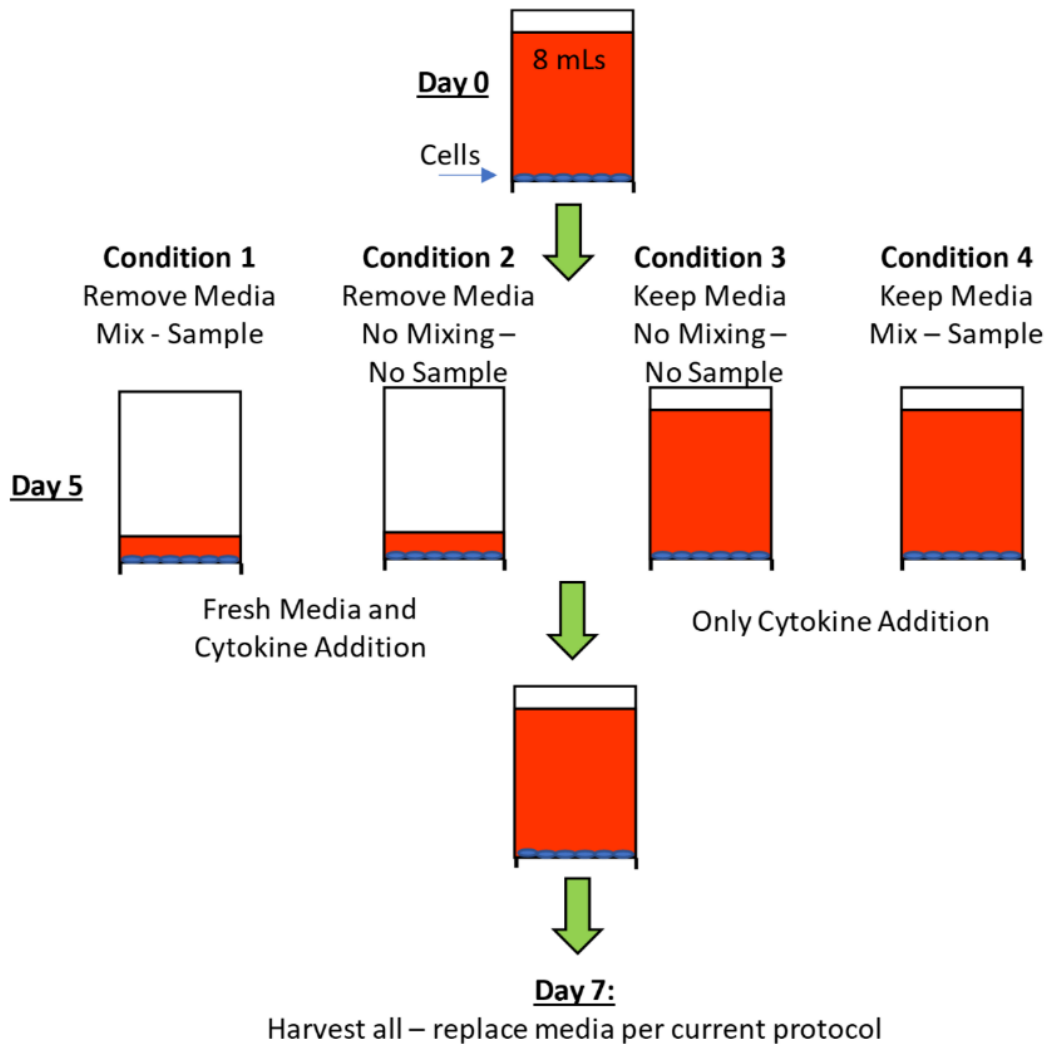


Figure 5.2 Preliminary screening of high surface densities in G-Rex. Three different surface densities, $100, 140, 200 \times 10^3$ cells/cm² were tested in G-Rex 24-well plates with 2 cm² surface area per well using a single donor. Four different media handling conditions were tested for each density for a total of 12 conditions. Cells were transferred out of G-Rex on Day 7 into standard tissue culture surfaces. See **Table 5.1** for additional details.

Table 5.1 Experimental set-up for high cell-surface-density conditions in G-Rex

ID	Media handling condition	Surface density x 10³ cells/cm²	Volumetric density cells/mL	Day 5	Day 7
G100	1	100	25,000	Remove 3/4 media, mix, sample, replace 3/4 media, add new cytokines.	Transfer cells out of G-Rex, rinse well with 2 mL of media, mix, sample, and spin down cells. Replace media, add new cytokines.
G140	1	140	35,000		
G200	1	200	50,000		
G100	2	100	25,000	Remove 3/4 media, replace 3/4 media, add new cytokines. No mixing or sampling.	
G140	2	140	35,000		
G200	2	200	50,000		
G100	3	100	25,000	Spike new cytokines (same amount as in Conditions 1 and 2). No new media. No mixing or sampling	
G140	3	140	35,000		
G200	3	200	50,000		
G100	4	100	25,000	Mix contents and sample. Spike new cytokines (same amount as in Conditions 1 and 2). No new media.	
G140	4	140	35,000		
G200	4	200	50,000		

5.2.3 Initial screening of low cell-surface-density experiments and media dilutions

On Day 0, cells were seeded in a G-Rex 6-well plate (10 cm²) at cell surface densities of 11 or 40 x 10³ cells/cm² (G11D and G40D respectively). We tested leaving cells in G-Rex through Day 5 or Day 7 and using fed-batch media dilutions as well. A dilution control (C11D) was also created and seeded in standard tissue culture surface (STCS). All G-Rex conditions were seeded at 40,000 cells/mL volumetric density to match C11 and C11D controls. To minimize differences in media volumes added and media heights, on Day 5 and Day 7, dilutions targeted C11 density ranges of 250,000 to 450,000 cells/mL for Day 5 and 450,00 to 600,000 cells/mL for Day 7. For all conditions, cytokines added for Day 5 and Day 7 was for the total final volume. Conditions are shown in **Figure 5.3** and **Table 5.2**.

Day 0 cytokines: 100 ng/mL TPO, 100 ng/mL SCF, 10 ng/mL IL-6, 10 ng/mL IL-11, and 2.5 ng/mL IL-3 (R&D Systems, Inc., Minneapolis, MN). **Day 5 cytokines:** 100 ng/mL TPO, 100 ng/mL SCF, 10 ng/mL IL-9, 10 ng/mL IL-11, and 10 ng/mL IL-3. **Day 7 cytokines:** 100 ng/mL TPO, 100 ng/mL SCF and 6.25 mM nicotinamide

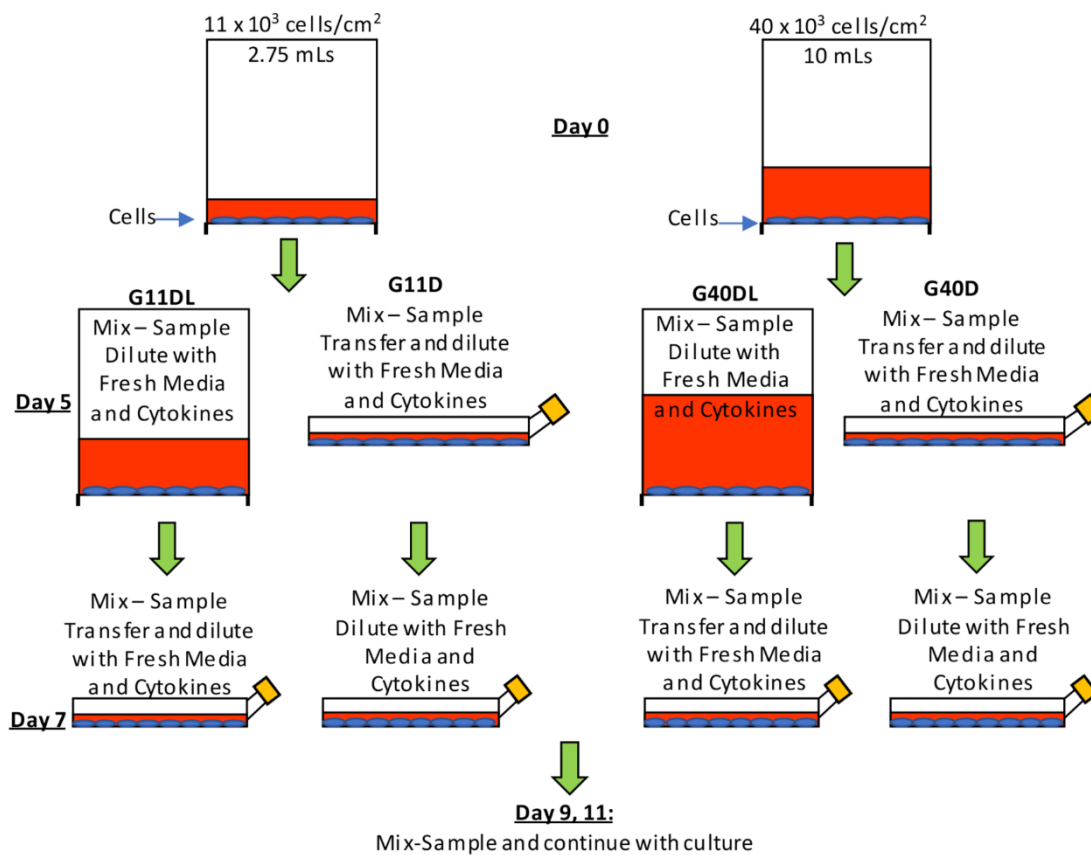


Figure 5.3 Screening lower surface densities in G-Rex. Two different surface densities, 11 (G11D) and 40 x 10³ cells/cm² (G40D) were tested in G-Rex 6-well plates with 10 cm² surface area per well using a single donor. Cells were removed from the G-Rex on Day 5 (G11D, G40D) or Day 7 (G11DL, G40DL) and transferred to standard tissue culture surfaces. See **Table 5.2** for additional details.

Table 5.2 Experimental set-up for low cell-surface-density and media dilution conditions

ID	Surface density x 10³ cells/cm²	Volumetric density cells/mL	Day 5	Day 7
C11	11	40,000	Sample, and replace media per current protocol.	Sample, and replace media per current protocol.
C11D	11	40,000	Sample, dilute cells to match new C11 density (between 1 and 1.5 dilution ratio based on initial volume).	Sample, dilute cells to match new C11 density (between 0.3 and 1 dilution ratio based on initial volume).
G11D	11	40,000	Transfer cells out of G-Rex, sample, dilute cells to match new C11 density (between 1 and 1.5 dilution ratio based on initial volume).	
G40D	40	40,000		
G11DL	40	40,000	Sample, dilute cells to match new C11 density (between 1 and 1.5 dilution ratio based on initial volume).	Transfer cells out of G-Rex, sample, dilute cells to match new C11 density (between 0.3 and 1 dilution ratio based on initial volume).
G40DL	11	40,000		

5.2.4 Restricted oxygen and soft-surface studies in G-Rex

To examine the contribution of the G-Rex soft surface and improved oxygen transfer, G-Rex10 devices (Wilson Wolf Corp., Saint Paul, MN) were modified by the manufacturer by bonding a polystyrene film below the membrane to prevent oxygen transfer. Oxygen transfer would then occur through the media. G-Rex10 devices have the same surface area as the G-Rex 6-well devices (10 cm^2) that were used for comparisons. Seeding surface density was $11 \times 10^3 \text{ cells/cm}^2$ for restricted (G11R) and standard (G11) devices and similar to controls seeded in standard tissue culture 6-well plates (C11). Dilutions of these conditions were also tested (G11RD, G11D, C11D). All conditions were seeded at volumetric density of 40,000 cells/mL and had the same starting media of 2.75 mL.

5.2.5 Platelet-like-particle (PLP) preparation and collection

Cells seeded in a culture dish at a cell density of $1 \times 10^6 \text{ cells/mL}$ were placed on an orbital shaker (SK-O180-E, SCILOGEX, Rocky Hill, CT) set to 50 rpm on Day 11. On Day 13, the shaken cells and PLPs were harvested from the dish and spun down at 150 g for 5 min to pellet large cells. The supernatant was transferred to a fresh tube, prostaglandin E1 (PGE1, Cayman Chemical, Ann Arbor, MI) was added at 140 nM final concentration, and the solution was spun down at 2200 g for 20 min at room temperature to pellet PLPs. After the supernatant was discarded, the pellet was resuspended in HEPES/Tyrode's (HT) buffer (10 mM HEPES, 137 mM NaCl, 2.8 mM KCl, 1 mM MgCl_2 , 12 mM NaHCO_3 , 0.4 mM Na_2HPO_4 , 0.35% BSA, 5.5 mM glucose, pH 7.4) and allowed to rest for 20 min at room

temperature. CaCl_2 at a final concentration of 2 mM was added to the suspension 5 min before use in assays.

5.2.6 Flow cytometry

Cells were washed twice at 4° C with cold PBS containing 2 mM EDTA and 0.5% BSA (PEB). Antibodies anti-CD41-FITC (555466), anti-CD42b-APC (551061) and anti-CD34-PE (555822) were added to the samples and incubated for 30 min at 4° C. Cells were washed twice with PEB and incubated with DAPI (Invitrogen, Carlsbad CA) for 15 min at room temperature before analysis.

5.2.7 Mk ploidy analysis

Cells were washed twice at 4° C with cold PEB and then incubated with anti-CD41 antibody for 30 min at 4° C. Cells were washed twice with PEB and then fixed with 0.5 % paraformaldehyde in PBS and incubated for 15 min at room temperature. Cells were then permeabilized with 70% methanol for 1 h at 4° C, treated with RNase for 30 min at 37° C and finally incubated with 50 $\mu\text{g}/\text{mL}$ of propidium iodide to stain DNA before analysis.

5.2.8 PLP flow cytometry

PLP suspension was analyzed with antibodies against CD41, CD42b, CD62P-BV421 (564038), and PAC-1-FITC (340507) or PAC-1-Alexa647 (362805, BioLegend, San Diego, CA). Thrombin at 3 U/mL was added to activate PLPs and samples were incubated for 15

min at room temperature. Expression of markers on PLPs was compared to unactivated (no thrombin), stained samples.

5.2.9 proPLT and PLP immunofluorescence microscopy

Cells were seeded on 8-well chamber glass slides (125658, Lab NunTek II, Thermo Scientific, Waltham, MA) on Day 11 at a density of 80,000 cells/mL. On Day 13, cells were fixed with 3.7% paraformaldehyde and then permeabilized with 0.3% Triton X-100 before sequentially staining with 5 $\mu\text{g/mL}$ mouse anti-beta-tubulin primary antibody (5656321, BD Biosciences) and 1 $\mu\text{g/mL}$ of Alexa Fluor 488-conjugated goat anti-mouse secondary antibody (A11001, Thermo Scientific). Cells were then incubated with TRITC-phalloidin, washed, and then stained with DAPI to identify nuclei. For PLPs, 8-well chamber slides were coated with fibrinogen (Innovative Research, Novi, MI) at 60 $\mu\text{g/mL}$ in PBS or 1% BSA in PBS. On Day 13, the collected PLP suspension was added to each well and allowed to rest at room temperature for 15 min and then 3 U/mL of thrombin was added to one of the wells coated with fibrinogen and incubated for 20 min at room temperature. The wells were washed with warm PBS and then fixed as described above for proPLTs. PLP and proPLT slides were imaged using a 63x oil objective on a Leica DMI6000 Spinning Disc Confocal Microscope (Leica, Wetzlar, Germany).

5.2.10 Aggregation flow chamber assay

We created an open channel system that was derived and fabricated similarly to our previously published microfluidic slit-bioreactor wherein the slits were removed to create a

simple open channel device.[76] Fibrinogen at 60 $\mu\text{g}/\text{mL}$ in PBS was introduced into the chamber and incubated for 1 h at 37°C. The chamber was positioned on a Lumascope microscope v500 (Etaluma Inc., Carlsbad, CA) placed inside an incubator (Thermo Scientific, Waltham, MA) at 37°C and 5% CO_2 . After the fibrinogen incubation, a syringe pump (NE-300, New Era Pump Systems Inc., Farmingdale, NY) with a 5-mL glass syringe (81520, Hamilton Company, Reno, NV) was used to rinse any unbound fibrinogen with PBS for 30 min. Then, HT buffer with final concentration of 2 mM CaCl_2 and 25 μM ADP was added to a new syringe and flowed through the protein-coated chamber for 15 min before introducing PLP suspension. The density of particles between 2-6 μm was counted using a Coulter Multisizer (Beckman Coulter, Indianapolis, IN) and the PLP suspension density was adjusted to 45×10^6 particles/mL. The PLP suspension was stained with 1 μM Calcein AM at 37°C for 10 min and then 25 μM ADP added to the PLP suspension for another 5 min. 200 μL of stained-PLP suspension was microinjected into the system. The flow-rate of the pump was set to 1.5 $\mu\text{L}/\text{min}$ which is equivalent to a wall shear rate of $\sim 100 \text{ s}^{-1}$. A video was recorded using the Lumascope with a 20x objective.

5.2.11 Bioreactor fabrication

A 2D design of the USRB-7 μm was created in AutoCAD 2014 (San Rafael, CA) and then printed onto a chrome mask (Front Range Photomask, Palmer Lake, CO). A silicon wafer (WRS Materials, San Jose, CA) was spin-coated with SU8-2035 photoresist (MicroChem Corp, Westborough, MA) at 4000 RPM for 30 s to achieve a photoresist height of 40 μm . The wafer was soft-baked at 65°C for 3 min and then hard-baked at 95°C for 6 min.

Afterwards, the wafer was exposed to UV light for 17 s using a Karl Suss MA6 Mask Aligner (SUSS MicroTec, Garching, Germany). The exposed resist was then baked at 95°C for 6 min. Finally, the resist was developed using SU8 developer solution (MicroChem) for 2 min and dried with a nitrogen gun. The dry wafer was silanized overnight (5 μ L of 1H,1H,2H,2H-perfluorooctyltrichlorosilane; Alfa Aesar, Ward Hill, MA) in a vacuum chamber. Next, a 1:10 curing agent to polydimethyl siloxane (PDMS) solution (Slygard 184 Kit; Electron Microscopy Sciences, Hatfield, PA) was poured over the wafer to cast a mold that was placed in an oven at 65°C overnight. The PDMS mold was then cut, holes for inlets and outlets created with a 2-mm punch, and the PDMS plasma-bonded (Model BD-20; Electro-Technic Products, INC, Chicago, IL) to an ethanol-cleaned premium plain glass slide (USRB-7 μ m or USRB-5 μ m, 25 x 75 x 1 mm; VWR, Radnor, PA and Lung-USRB, 75 x 50 x 100; Fisher Scientific, Hampton, NH).

5.2.12 Bioreactor perfusion with Mks in USRB-7 μ m

The USRB-7 μ m was positioned on a Lumascope microscope v500 (Etaluma Inc., Carlsbad, CA) placed inside an incubator (Thermo Scientific, Waltham, MA) maintained at 37°C and 5% CO₂. Separate syringe pumps (NE-300, New Era Pump Systems Inc., Farmingdale, NY) were used for each flow channel. A 5-mL glass syringe (81520, Hamilton Company, Reno, NV) was used for the outer channels and a 2.5-mL glass syringe (81420, Hamilton) was used for the center channel. Media (78% IMDM, 20% BIT 9500 Serum Substitute, 1% Glutamax, 1 μ g/mL low-density lipoproteins, 100 U/mL Pen/Strep) without cytokines was perfused throughout the bioreactor for 15 min at 6.5 μ L/min prior to Mk introduction.

Nonselected Grex-Mks at density of 50,000 cells/mL were stained for 15 min with 1 μ M Calcein AM at 37°C. After the media perfusion, 25,000 cells were microinjected into the tubing upstream from the reactor. No cells were present within the syringes. A video was recorded of each bioreactor run.

5.2.13 Statistical analysis

Paired t-tests were conducted for all pairs of conditions, and the significance level was set at $p < 0.05$. Bar graphs and plots are shown with standard errors of mean (SEM) and standard deviation (SD, used in **Figures 5.12, 5.16 and 5.17**).

5.3 Results

5.3.1 Initial cell-surface screening studies in G-Rex

First, we screened initial cell surface densities of 100, 140, and 200 $\times 10^3$ CD34⁺ cells/cm² based on results published for K562 cells.[109] We also evaluated a media exchange on Day 5 vs. spiking in the new cytokine cocktail (**Figure 5.2 and Table 5.1**). Conditions were kept in G-Rex until Day 7. Surprisingly, all of the G-Rex conditions yielded lower total nucleated cell (TNC) and CD42b⁺ cell production compared to the control, while spiking cytokines instead of media exchanges did not significantly affect the results (**Table 5.3**). Since the lower surface density of 100 $\times 10^3$ cells/cm² tended to outperform the higher surface densities, we next screened lower surface densities while keeping cultures in G-Rex until Day 5 or Day 7 and performed media dilutions (G11D, G40D in **Figure 5.3**). G40D started at 40 $\times 10^3$ cells/cm² and G11D matched the control surface density (C11) of 11 $\times 10^3$

cells/cm². A control media dilution (C11D) was also tested. C11D increased CD42b⁺ cell production compared to C11. G11D showed 30% improvement over C11 but produced less than C11D. G40D provided the most effective CD42b⁺ cell production from all conditions (**Table 5.4**). Harvesting cells from the G-Rex on Day 5 instead of Day 7 led to increased CD42b⁺ cell production for both G11D and G40D.

Table 5.3 Results for screening of high surface densities in G-Rex

ID	Media handling condition	Surface density x 10 ³ cells/cm ²	Volumetric density cells/mL	%CD41 ⁺ CD42b ⁺ cells	TNC Fold	CD42b ⁺ cells produced
G100	1	100	25,000	30.1	29	7
G140		140	35,000	22	25	6
G200		200	50,000	22.3	21	4
G100	2	100	25,000	29	23	7
G140		140	35,000	27.5	21	5
G200		200	50,000	23	22	4
G100	3	100	25,000	32.6	25	8
G140		140	35,000	22	22	4
G200		200	50,000	19.3	19	3
G100	4	100	25,000	29.3	26	7
G140		140	35,000	27.4	24	5
G200		200	50,000	20.6	23	5
C10	Control	10	50,000	37.6	46	15

For G-Rex conditions shown in **Figure 5.2 and Table 5.1**, plus a control (C10), the maximum %CD41⁺CD42b⁺ cells, viable total nucleated cell expansion (TNC Fold), and CD42b⁺ cells produced per input CD34⁺ cell, are shown. Results are for a single donor.

Table 5.4 Results from screening lower surface densities in G-Rex and media dilutions

ID	Surface density x 10³ cells/cm²	Volumetric density cells/mL	%CD41⁺ CD42b⁺ cells	TNC Fold	CD42b⁺ cells produced
C11	11	40,000	47.8	39	18
C11D	11	40,000	48.5	58	28
G11DL	11	40,000	44.8	40	18
G11D	11	40,000	43.5	54	24
G40DL	40	40,000	52.2	78	41
G40D	40	40,000	52	87	45

For G-Rex conditions shown in supplemental information **Figure 5.3 and Table 5.2**, plus a control (C11), and a dilution control (C11D), the maximum %CD41⁺CD42b⁺ cells, viable total nucleated cell expansion (TNC Fold), and CD42b⁺ cells produced per input CD34⁺ cell, are shown. Results are for a single donor.

5.3.2 Cell-surface density of 40×10^3 cells/cm² in G-rex improves total nucleated cell (TNC) and Mk production

Through early screening experiments with single donors, we identified that seeding the cells at a surface density of 40×10^3 cells/cm² through the first 5 days of culture and employing media dilutions on Days 5 and 7 provided effective CD42b⁺ Mk production – condition G40D. We further investigated G40D and compared it to a dilution control C11D and the standard process C11 across multiple donors. The viability of G40D and C11D remained significantly higher compared to C11, which correlated with an increased viable TNC for these conditions by Day 11 (**Figure 5.4A, B**). The CD41⁺ cell fraction over time was similar across the conditions until Day 13 and CD41⁺ cell production per input CD34⁺ cell was greatest in G40D by Day 11 (**Figure 5.5**). The %CD41⁺CD42b⁺ cells increased similarly across the conditions with G40D cultures generating on average larger numbers of CD42b⁺ cells produced per input CD34⁺ cell by Day 11 (**Figure 5.4C, D**). Interestingly, there was a larger drop in purity and Mk numbers on Day 13 in both C11D and G40D compared to C11.

Peak TNC expansion per input CD34⁺ cell was significantly higher in G40D compared to all conditions, and C11D was also higher compared to C11 (C11 vs. G40D, $p = 1e-4$; C11 vs. C11D, $p = 2e-3$; C11D vs. G40D, $p = 8e-3$; **Figure 5.4E**). Peak CD42b⁺ cell production per input CD34⁺ cell was highest in G40D at 39 ± 19 compared to 28 ± 9 for C11D and 18 ± 8 for C11 (C11 vs. G40D, $p = 3e-4$; C11 vs. C11D, $p = 1e-4$; C11D vs. G40D, $p = 0.01$; **Figure 5.4F**). The number of CD42b⁺ cells produced per mL of media used was 2-fold and 3-fold higher than C11 for C11D and G40D, respectively (C11 vs. C11D, $p = 1-e5$; C11 vs.

C40D, $p = 2e-4$; C11D vs. G40D, $p = 0.04$; **Figure 5.4G**). It should be noted that there were no differences in cytokine usage between the conditions in these experiments and that G40D and C11D had similar media dilutions on Days 5 and 7. Importantly, we observed positive effects for a high-performing donor that generated 29 CD42b⁺ cells per input CD34⁺ cell for C11 and 75 CD42b⁺ cells for G40D and for a low-performing donor that yielded only 4 CD42b⁺ cells for C11 but 9 CD42b⁺ cells per input CD34⁺ cell for G40D. Based on these results, the combination of G-Rex and media dilutions significantly improved culture productivities.

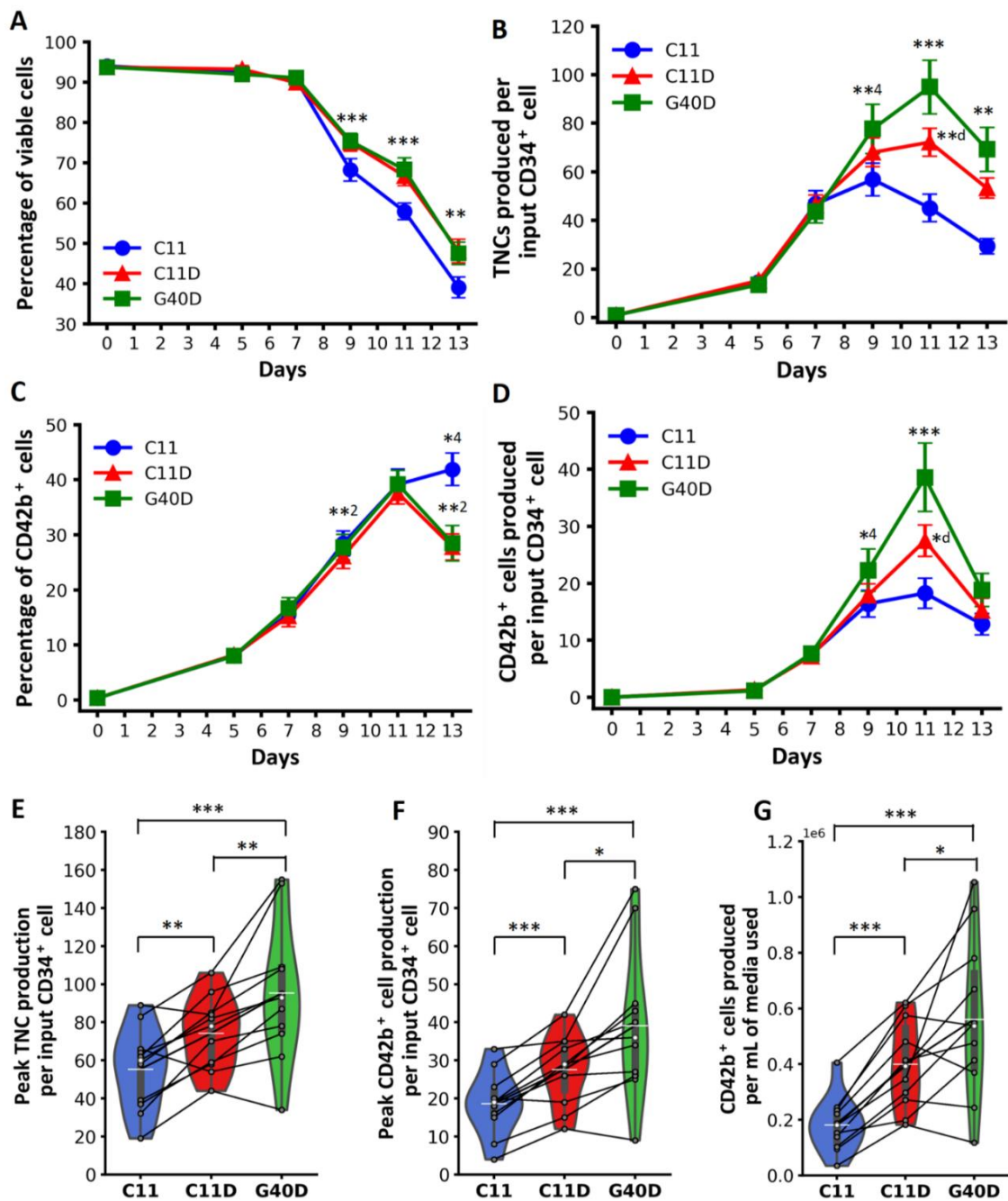


Figure 5.4 G-Rex at seeding density of 40×10^3 cells/cm² and dilutions improve overall culture productivity. (A-D) Time course profiles for G-Rex at seeding density of 40×10^3 cells/cm² with dilutions (green, G40D) compared to control (blue, C11), and dilution control

(red, C11D). (A) Viability profiles. (B) Viable total nucleated cell (TNC) fold expansion per input CD34⁺ cell. (C, D) The percentage of cells that are CD41⁺ CD42b⁺ and production of CD41⁺CD42b⁺ cells per input CD34⁺ cell over time. Points = mean +/-SEM. n = 11 for all points except Day 13 where n = 9. For points with both C11D and G40D significantly different from C11: *** $p < 0.001$, ** $p < 0.01$, * $p < 0.05$. For G40D vs. C11 only **4 = $p < 0.01$, *4 = $p < 0.05$. For G40D vs. C11D only **d = $p < 0.01$, *d = $p < 0.05$. For C11D vs. C11 only **2 = $p < 0.01$. Violin plots for (F) peak TNC production, (G) peak CD42b⁺ cells produced per input CD34⁺ cell and (H) CD42b⁺ cells produced per mL of media used. Individual donors (n =11) represented as grey dots and connected by lines. White dot = median, black bars = 25/75 quantiles, white line = mean.

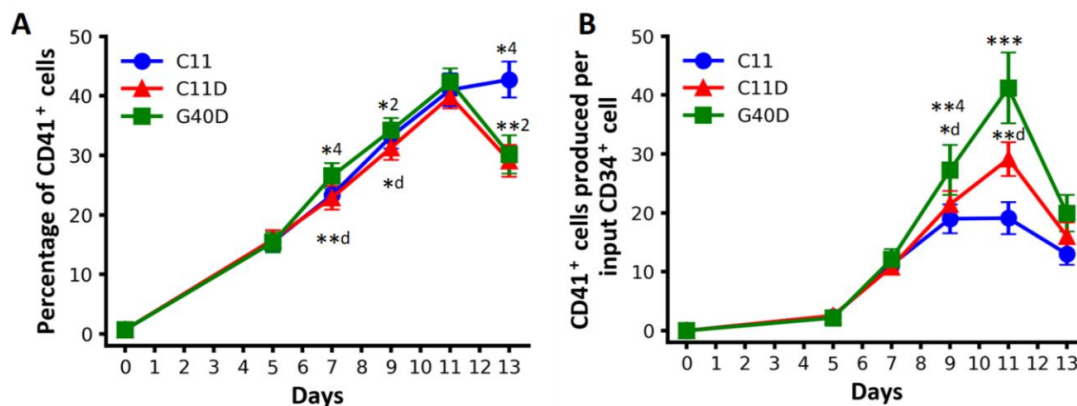


Figure 5.5 CD41⁺ cell production of G-Rex at seeding density of 40×10^3 cells/cm² and dilutions. Time course profiles for G-Rex at seeding density of 40×10^3 cells/cm² with dilutions (green, G40D) compared to control (blue, C11), and dilution control (red, C11D). (A) The percentage of cells that are CD41⁺ CD42b⁺ and (B) production of CD41⁺CD42b⁺ cells per input CD34⁺ cell over time for the cultures shown in **Figure 5.4**. Points = mean +/-

SEM. $n = 11$ for all points except Day 13 where $n = 9$. For points with both C11D and G40D significantly different from C11: *** $p < 0.001$, ** $p < 0.01$, * $p < 0.05$. For G40D vs. C11 only **4 = $p < 0.01$, *4 = $p < 0.05$. For G40D vs. C11D only **d = $p < 0.01$, *d = $p < 0.05$. For C11D vs. C11 only **2 = $p < 0.01$, *2 = $p < 0.05$.

5.3.3 G-Rex cells retain CD34 longer

CD34 expression was lost over the culture across all conditions, but surprisingly remained significantly higher in G40D (C11 vs. G40D, $p = 2 \times 10^{-5}$; C11D vs. C40D, $p = 2 \times 10^{-4}$; **Figure 5.6A**) which produced 1.5-fold more CD34⁺ cells by Day 7 (**Figure 5.6B**). In all conditions, we observed populations of cells that were CD34⁺CD41⁺ and CD34⁺CD41⁺CD42b⁺, and G40D had consistently higher percentages of these cells (**Figure 5.6C-E**). On Day 7, the fraction of CD34⁺CD41⁺ cells was significantly higher in G40D with nearly double the numbers of CD34⁺CD41⁺ cells produced compared to C11 and C11D (**Figure 5.6D**). The fraction and numbers of CD34⁺CD41⁺CD42b⁺ cells produced was also significantly higher in G40D by Day 7 (**Figure 5.6E**). G40D had the lowest %CD34⁻CD41⁺ cells on Day 7 and a lower number of CD34⁻CD41⁺ cells produced (**Figure 5.7**). Since the TNC fold expansion on Day 7 was similar across conditions (**Figure 5.4B**), these results suggest that the G-Rex affected the retention of CD34. This was likely not due to the media dilution since C11 and C11D had similar results.

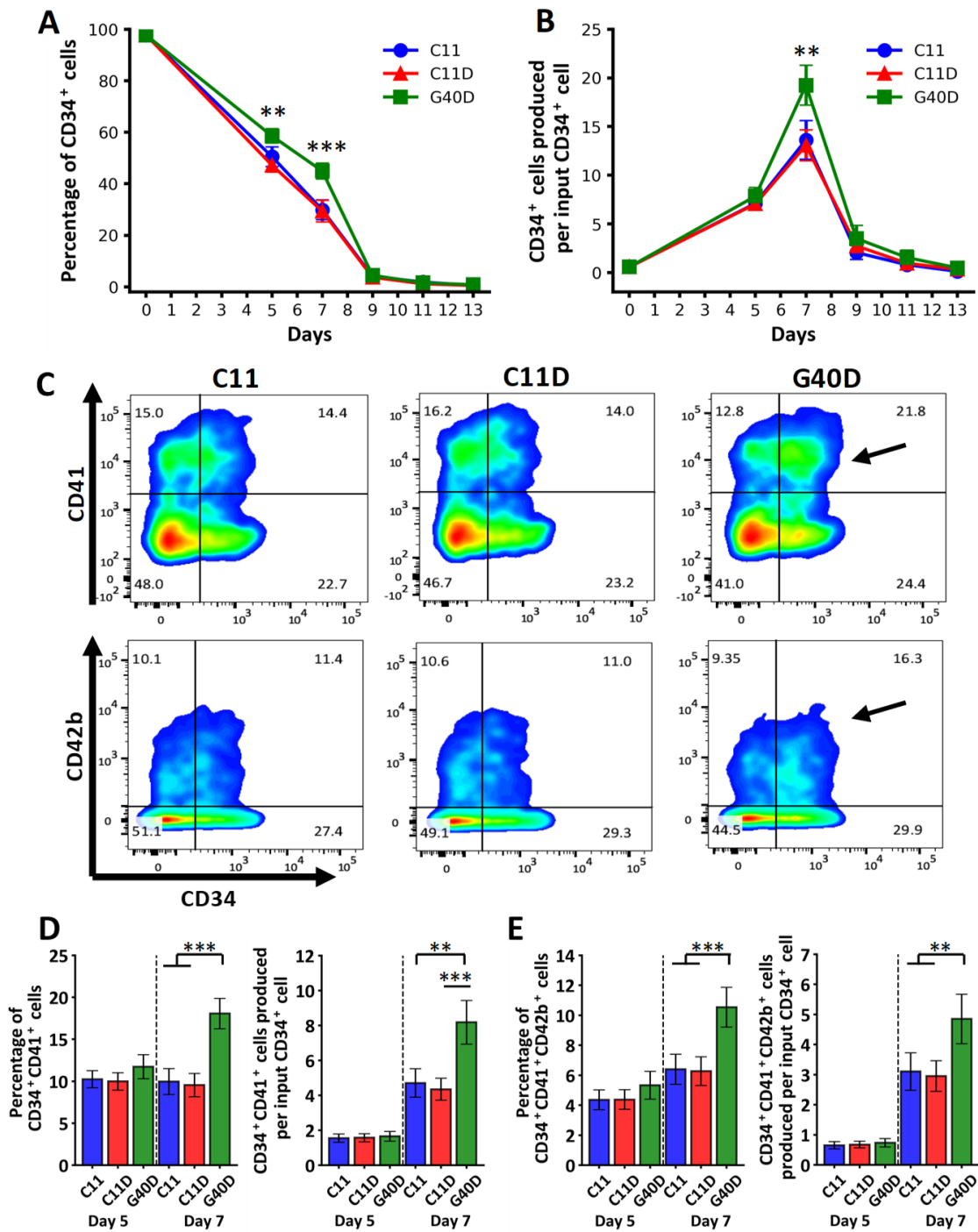


Figure 5.6 G-Rex cells retain CD34 longer and exhibit increased CD34⁺CD41⁺ cell production. (A) Percentage of the culture that is CD34⁺ and (B) fold expansion of CD34⁺

cells per input CD34⁺ cell. (C) Representative flow cytometry plots on Day 7 for CD41 and CD42b vs. CD34 for control C11, dilution control C11D and G40D. Black arrows denote higher percentages of CD34⁺CD41⁺ and CD34⁺CD41⁺CD42b⁺ cells in G40D. For Days 5 and 7, percentage and fold production of (D) CD34⁺CD41⁺ cells and (E) CD34⁺CD41⁺CD42b⁺ cells. (A, B), points = mean +/- SEM, n = 11 for Days 0-7, n = 9 for all other points. (D, E), bars = mean +/- SEM, n = 11. For all, ****p* < 0.001, ***p* < 0.01, **p* < 0.05.

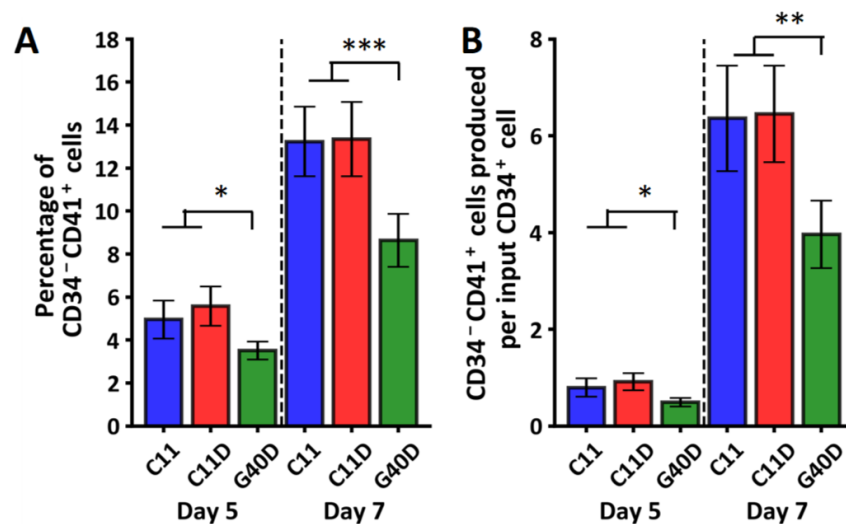


Figure 5.7 G-Rex cells have lower numbers of CD34⁺CD41⁺ cells. (A) Percentage of the culture that is CD34⁺CD41⁺ and (B) fold expansion of CD34⁺CD41⁺ cells per input CD34⁺ cell for the cultures shown in **Figure 5.6**. Bars = mean +/- SEM, n = 11. ****p* < 0.001, ***p* < 0.01, **p* < 0.05.

5.3.4 G-Rex conditions have lower %high-ploidy and higher numbers of 2N and 4N Mks

Mk ploidy was measured on Day 11 (**Figure 5.8A, B**). G40D cultures exhibited generally lower ploidy than C11 cultures with a greater percentage of 2N Mks ($40 \pm 6\%$ C11 vs. $47 \pm 5\%$ G40D, $p = 1e-3$, **Figure 5.8B**). G40D also had significantly lower fractions of 6N+8N, 16N and 32N Mks (**Figure 5.8B**). C11 had a higher mean ploidy (inset **Figure 5.8B**) and increased %high-ploidy compared to G40D ($32 \pm 7\%$ C11 vs. $23 \pm 5\%$ G40D, $p = 2e-4$, **Figure 5.8C**). C11D demonstrated mean ploidy and %high-ploidy similar to G40D. An additional late sample on Day 13 for one donor showed a decrease in %high-ploidy fractions across all conditions, but no changes to the relative ploidy distributions (**Figure 5.9**).

G40D generated 2.5-fold more 2N and 4N Mks, ~2-fold more 6N+8N Mks and similar numbers of 16N Mks compared to C11 (**Figure 5.10**). C11D also increased 2N and 4N Mk numbers by ~1.7-fold but had minimal effect on 6N+8N Mks (**Figure 5.10**). Though G40D conditions had lower %high-ploidy, this was more than offset by the greater Mk expansion. By Day 11, G40D generated 9 ± 3 high ploidy Mks per input CD34⁺ cell compared to 6 ± 2 for C11 and C11D ($p = 9e-5$, **Figure 5.8D**). To estimate the overall platelet-like-particle (PLP) production potential, we calculated the total Mk DNA produced per input CD34⁺ cell on Day 11, which is equal to the sum of Mks produced per input CD34⁺ cell for each ploidy fraction times their respective DNA content (i.e., 2N Mks = 1, 4N Mks = 2). G40D increased the total Mk DNA content by 1.8-fold (**Figure 5.8E** and **Table 5.5**). Therefore, media

dilutions (C11D) and G-Rex + media dilutions both decreased %high-ploidy, but G40D significantly expanded the Mk DNA pool compared to C11 and C11D.

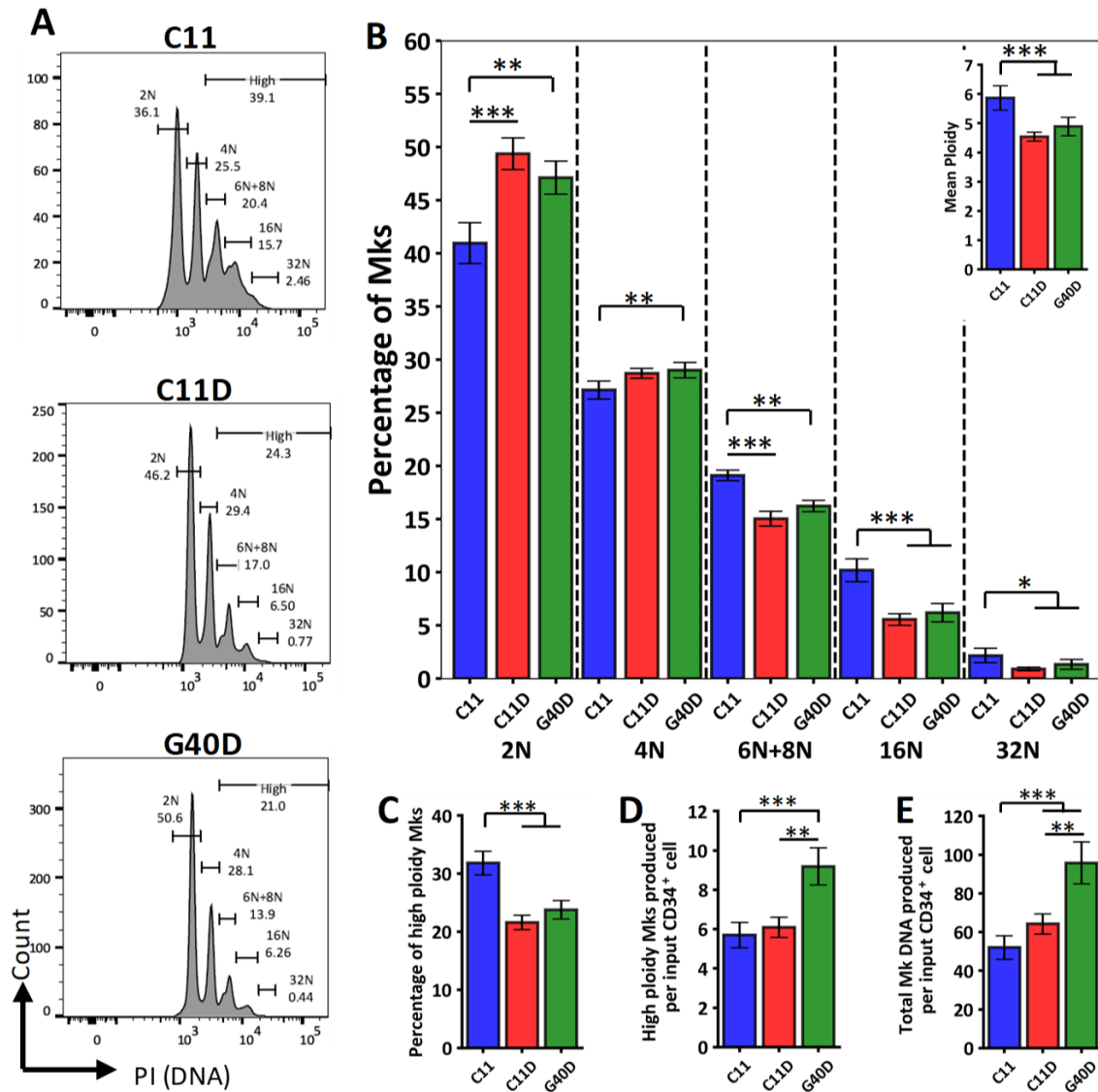


Figure 5.8 G-Rex with media dilutions have lower %high-ploidy but greater total Mk DNA. (A) Representative Day 11 ploidy plots for control C11, dilution control C11D, and

G40D conditions. (B) The percentages of 2N, 4N, 6N+8N, 16N, and 32N cells with inset showing mean ploidy. (C) %high-ploidy ($> 4N$) of each condition. (D) Number of high ploidy ($> 4N$) megakaryocytes (Mks) produced per input $CD34^+$ cell. (E) Total Mk DNA produced is equal to the sum of Mks produced per input $CD34^+$ cell for each ploidy fraction times their respective DNA content (i.e., 2N Mks = 1, 4N Mks = 2; See Supplemental Information Table S5 for example). Bars = mean \pm SEM, $n = 11$. $***p < 0.001$, $**p < 0.01$, $*p < 0.05$.

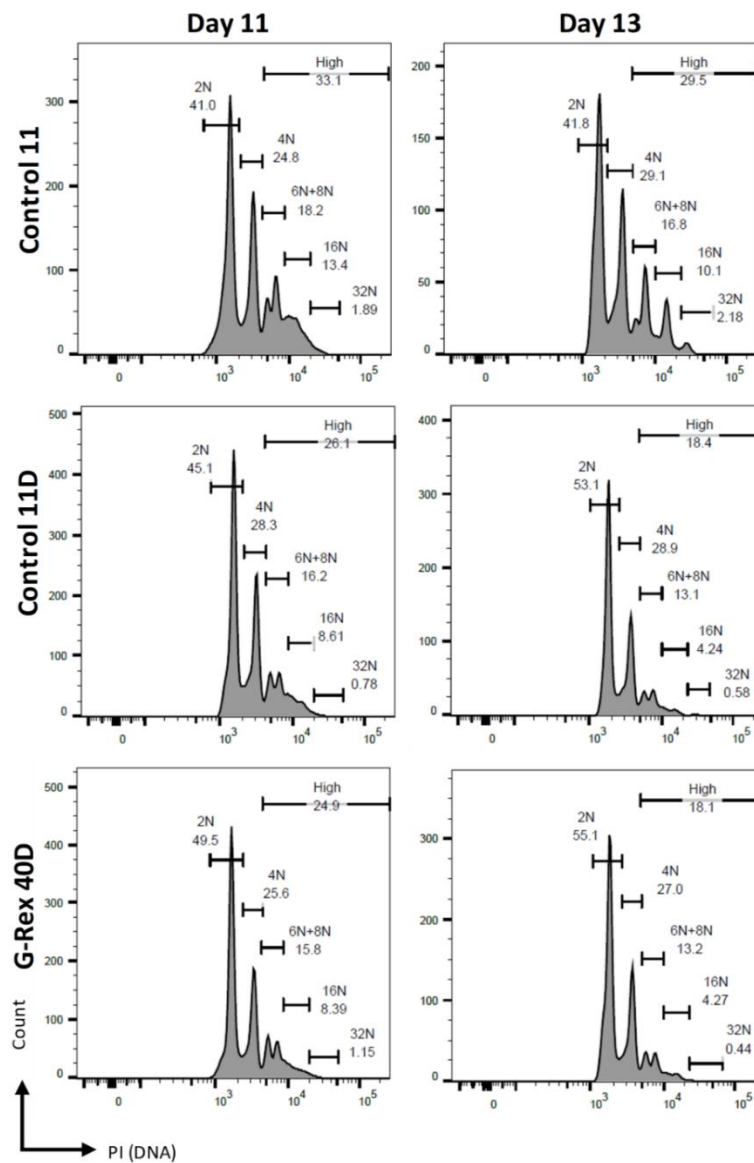


Figure 5.9 Ploidy distributions of G-Rex at seeding density of 40×10^3 cells/cm² and dilutions between Days 11 and 13. Ploidy plots for Day 11 and Day 13 for control C11, dilution control C11D and G40D for a single donor. The Day 11 and Day 13 plots for each condition show similar patterns, but lower %high-ploidy cells at Day 13.

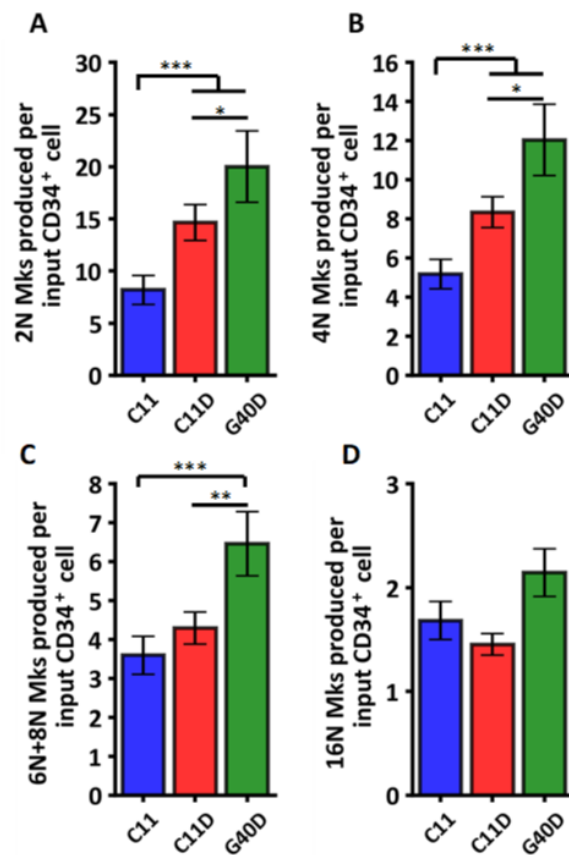


Figure 5.10 G-Rex at seeding density of 40×10^3 cells/cm² yield greater numbers of 2N, 4N and high-ploidy Mks. For control C11, dilution control C11D, and G40D, the number of CD41⁺ Mks produced per input CD34⁺ cell that are (A) 2N, (B) 4N, (C) 6N+8N, and (D) 16N for the cultures shown in **Figure 5.8**. Bars = mean \pm SEM, n = 11. *** $p < 0.001$, ** $p < 0.01$, * $p < 0.05$.

Table 5.5 Example calculations for total Mk DNA produced per input CD34⁺ cell for five separate mPB donors

		Ploidy Level * DNA Content					
Donor 1	CD41 ⁺ Fold	2N	4N	6N+8N	16N	32N	DNA _{Prod}
C11	31.2	14.6	15.7	25.2	16.7	0.0	72
C11D	45.5	23.9	25.8	26.6	13.0	0.0	89
G40D	78.7	44.7	43.8	42.2	11.5	0.0	142
Donor 2	CD41 ⁺ Fold	2N	4N	6N+8N	16N	32N	DNA _{Prod}
C11	19.5	7.9	12.1	13.8	11.4	6.2	51
C11D	20.5	9.5	12.6	11.7	10.1	4.3	48
G40D	27.4	12.9	16.4	16.5	12.5	6.0	64
Donor 3	CD41 ⁺ Fold	2N	4N	6N+8N	16N	32N	DNA _{Prod}
C11	16.5	6.0	8.4	13.5	19.8	6.5	54
C11D	29.6	13.7	17.4	20.1	15.4	3.6	70
G40D	47.2	23.9	26.5	26.8	23.2	3.7	104
Donor 4	CD41 ⁺ Fold	2N	4N	6N+8N	16N	32N	DNA _{Prod}
C11	15.8	6.5	7.8	11.5	13.9	4.8	44
C11D	31	14.0	17.5	20.1	14.9	3.9	70
G40D	36.3	18.0	18.6	22.9	18.4	6.7	85
Donor 5	CD41 ⁺ Fold	2N	4N	6N+8N	16N	32N	DNA _{Prod}
C11	4.5	1.8	1.3	0.9	0.4	0.5	12
C11D	12.5	5.9	3.4	2.2	0.7	0.8	28
G40D	9.6	4.4	2.7	1.9	0.6	0.4	22

$$DNA_{Prod} = \sum CD41^{+}Fold * \%Ploidy\ Level * DNA_content$$

CD41⁺Fold → CD41⁺ Mks produced per input CD34⁺ cell on Day 11

Ploidy Level → Percentage of CD41⁺ population that is 2N, 4N, ..., 32N

DNA_content → 2N = 1, 4N = 2, 6N+8N = 4, 16N = 8, 32N = 16

5.3.5 G-Rex-grown Mks are capable of making proPLTs and PLPs

Next, we studied proPLT formation. Cells were seeded in wells on Day 11 and proPLTs were imaged on Day 13. Brightfield images of cells making proPLTs are denoted with yellow-arrow heads for C11, C11D and G40D (**Figure 5.11-A1, B1, C1**). Additionally, confocal microscopy was used to assess proPLT morphology. Across all three conditions, polyploid cells were observed (**Figure 5.11-A2, B2, C2**). Mks undergoing initial stages of proPLT formation exhibited extensive cytoskeletal re-arrangement and thick cytoplasmic projections (**Figure 5.11-A3, B3, C3**) eventually leading to beads-on-a-string extensions (**Figure 5.11-A4, B4, C4**). We have previously shown that Mks from our standard culture process can generate PLPs after shaking the suspension on an orbital shaker.[42] To evaluate the quality of PLPs from G40D cultures, cells were shaken starting on Day 11 and sampled on Day 13. CD42b⁺ PLPs demonstrated the potential for activation in the presence of thrombin via the binding of PAC-1 (**Figure 5.11D**) and via translocation of CD62P to the membrane (**Figure 5.11E**). Additionally, confocal analysis of the collected PLPs showed characteristic changes in morphology when thrombin was added, as they spread on fibrinogen and increased in surface area (**Figure 5.11E**). Finally, PLPs were able to form clots within a flow aggregation study in the presence of ADP over a fibrinogen-coated surface (**Figure 5.11G**). We estimated that the number of CD42b⁺ PLPs per input Mk was lower in G40D and C11D but the yields per input CD34⁺ cell was similar to C11 (**Figure 5.12**). Additionally, using our published uniform shear rate bioreactor, USRB-7 μ m, G40D-Mks were able to generate proPLTs and PLPs in the presence of shear forces (**Figure 5.13**).

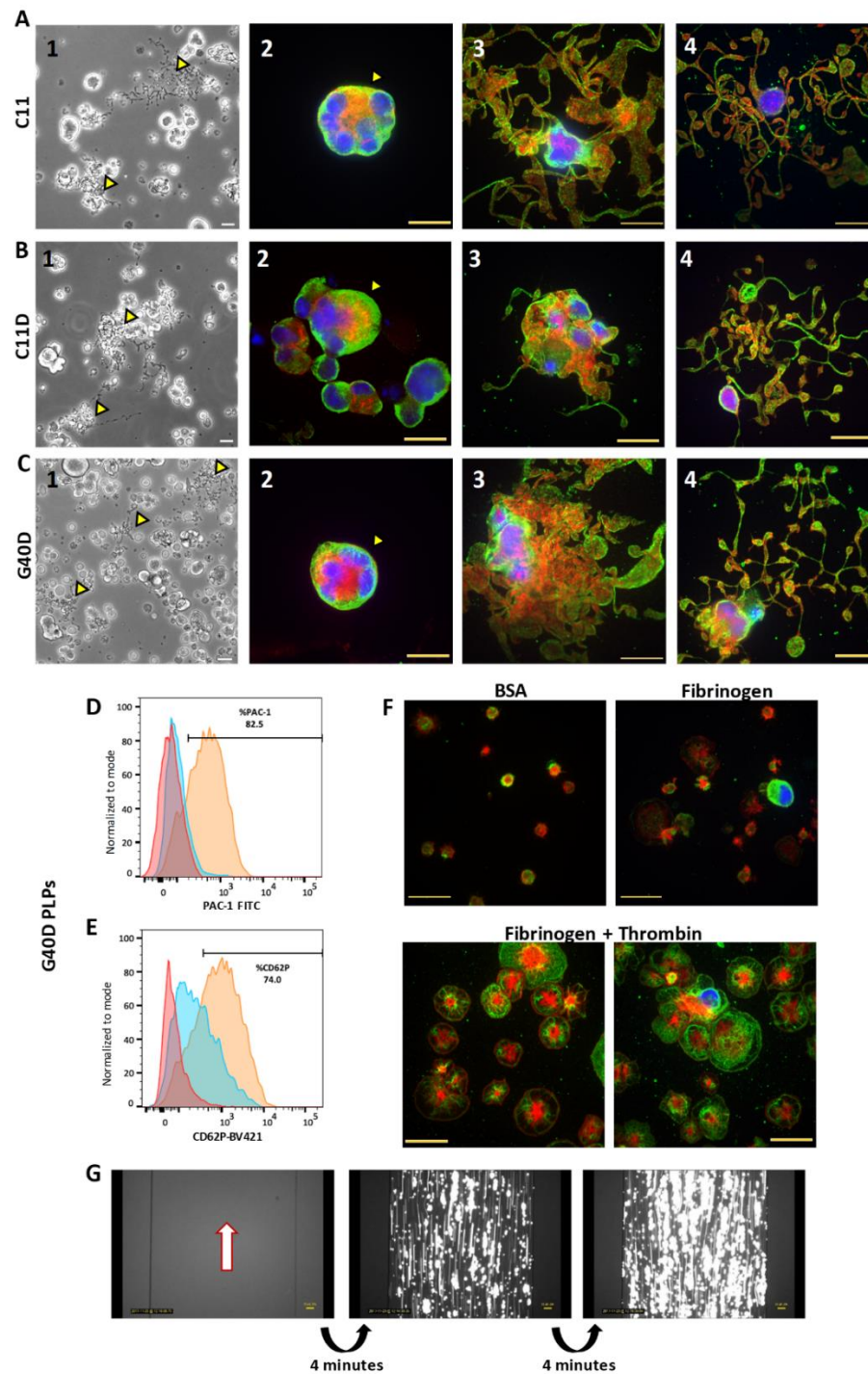


Figure 5.11 G-Rex Mk form proPLTs and generate PLPs. proPLT formation on Day 13 for culture conditions C11 (A), dilution control C11D (B), and G40D (C): (1) brightfield

images with yellow arrow-heads pointing to proPLT-making megakaryocytes (Mks), (2) large high-ploidy Mk (yellow arrow-head), (3) early stages of proPLT formation, (4) late-stage proPLT formation. Scale bars = 15 μm . (D) PAC-1 binding of G40D-PLPs in the absence (blue) and presence (orange) of thrombin. (E) CD62P expression of G40D-PLPs in the absence (blue) and presence (orange) of thrombin. For (D) and (E), analysis shown for gated CD42b^+ PLPs, and the unstained sample shown as red. (F) Confocal microscopy analysis of resting G40D-PLPs on BSA and on fibrinogen in the absence (upper) or presence (2 lower) of thrombin. Scale bar = 15 μm . (G) Collected G40D-PLPs were introduced into a fibrinogen-coated flow chamber to demonstrate aggregation potential in the presence of 25 μM ADP and 2 mM CaCl_2 . Images shown are 4 minutes apart. PLPs have been stained with Calcein AM. White arrow is direction of flow. Scale bar = 50 μm . For confocal images, red = actin, green = beta-tubulin, blue = DNA.

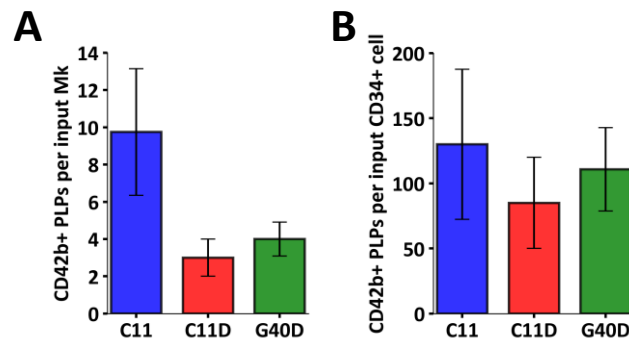


Figure 5.12 G-Rex PLP generation estimates from orbital shaker on Day 13. (A) CD42b^+ PLPs produced per seeded Mk on Day 11 and sampled on Day 13. (B) CD42b^+ PLPs per input CD34^+ cell sampled on Day 13. Bars = mean \pm SD. $n = 4$ for C11 and G40D and $n = 2$ for C11D.

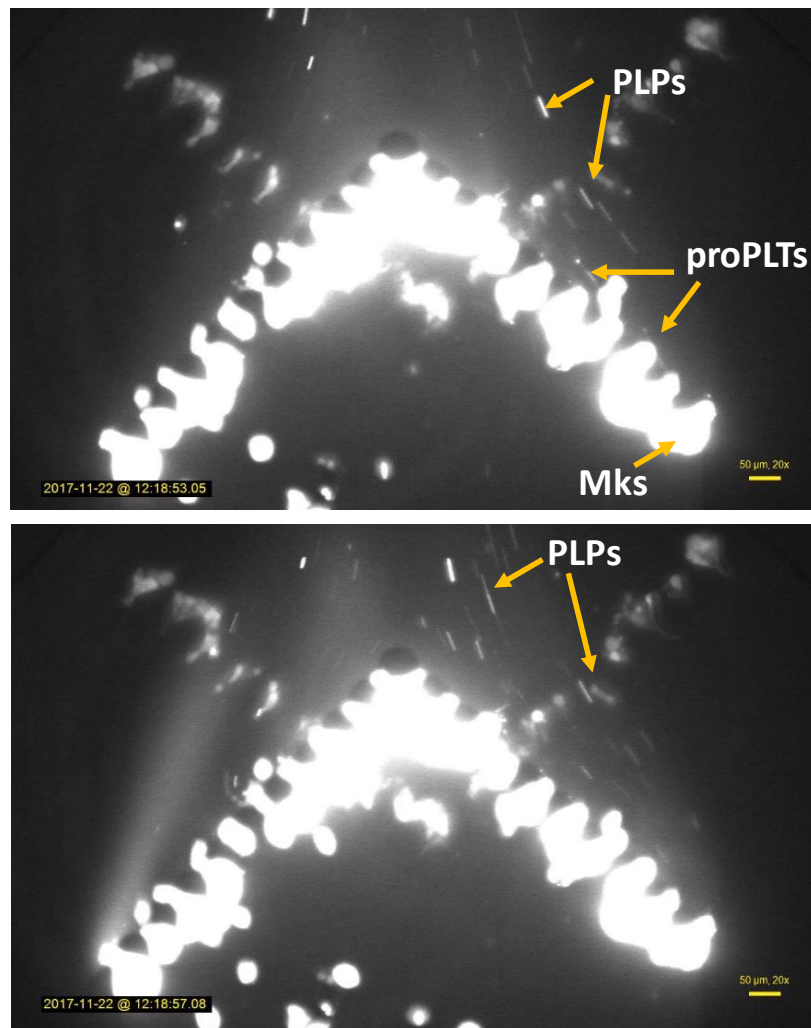


Figure 5.13 Analysis of proPLT and PLP generation from G40D-Mks in bioreactor. Calcein stained Mks on Day 13 from G40D conditions demonstrating proPLT and PLP potential under shear conditions inside uniform shear rate bioreactor, USBR-7 μ m. Yellow arrows = Mks/proPLTs/PLPs. Center channel flow rate = 1.5 μ L/min and combined outside flow = 0 μ L/min.

5.3.6 Increased Mk production is driven by media retention and an increase in Mk progenitors at higher G-Rex densities

We sought to understand what was driving the increase in Mk production from G40D conditions. First, the soft-surface was analyzed by using modified G-Rex devices that restricted oxygen transfer across the membrane (G11R) and thus operated as standard culture wells in terms of oxygen transfer. Second, the impact of improved oxygen transfer and higher oxygen tension was evaluated by comparing G11R to non-restricted G11 cultures (standard G-Rex device). The G11R and G11 conditions were seeded at same cell-surface densities as C11. Third, standard G-Rex devices were tested across four increasing seeding densities G11, G25, G40, and G80. Finally, media dilutions were evaluated across all conditions, i.e., G40 vs. G40D (**Figure 5.14**).

	Surface density x 10 ³ cells/cm ²	Volumetric density (cells/mL)	Oxygen	Soft-Surface	Dilution
C11	11	40,000	-	-	-
			-	-	+
G11R	11	40,000	-	+	-
			-	+	+
G11	11	40,000	+	+	-
			+	+	+
G25	25	40,000	+	+	-
			+	+	+
G40	40	40,000	+	+	-
			+	+	+
G80	80	40,000	+	+	-
			+	+	+

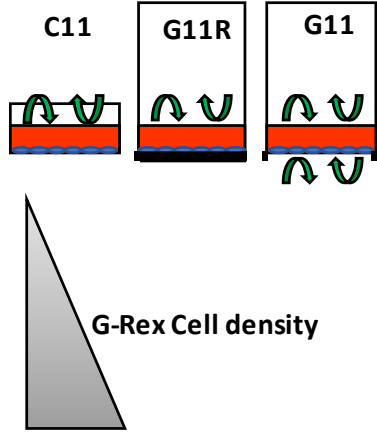


Figure 5.14 Experimental layout for variables that may affect Mk expansion in G-Rex and diluted conditions.

TNC and Mk expansion between C11 and G11R were similar demonstrating that the soft surface at this density has minimal impact (**Figure 5.15-A1, 2**). However, G11 cultures had on average lower production than G11R and C11 cultures and seemed to have delayed TNC expansion, Mk commitment and Mk production (**Figure 5.15-A1, 2** and **Figure 5.16**). This could potentially be attributed to higher oxygen tension near the cells in G11. There were no differences in %CD34⁺CD41⁺ cells by Day 7 (**Figure 5.15-A3**) and there was a greater increase in %high-ploidy Mks by Day 11 for G11R and G11 compared to C11 (**Figure 5.15-A4**). For all conditions, media dilutions improved TNC and Mk expansion, while reducing %high-ploidy.

Increasing the G-Rex seeding density appeared to overcome the expansion limitation seen for G11 with further positive effects with media dilutions (**Figure 5.15-B1, 2** and **Figure 5.16**). At surface densities above 25×10^3 cells/cm², the %CD34⁺CD41⁺ cells were significantly higher by Day 7 regardless of media dilutions (**Figure 5.15-B3**). Our high-surface-density screening experiments ($\geq 100 \times 10^3$ cells/cm²) also had higher %CD34⁺CD41⁺ cells that further increased from Day 7 to Day 9 compared to controls (**Figure 5.17**). G40D cells kept in G-Rex until Day 7 (G40DL) had higher %CD34⁺CD41⁺ cells (**Figure 5.18**). %High-ploidy decreased with increasing surface density among diluted conditions (**Figure 5.15-B4**). For all conditions shown in Figure 5.15, culture viability was higher with media dilutions (**Figure 5.19**).

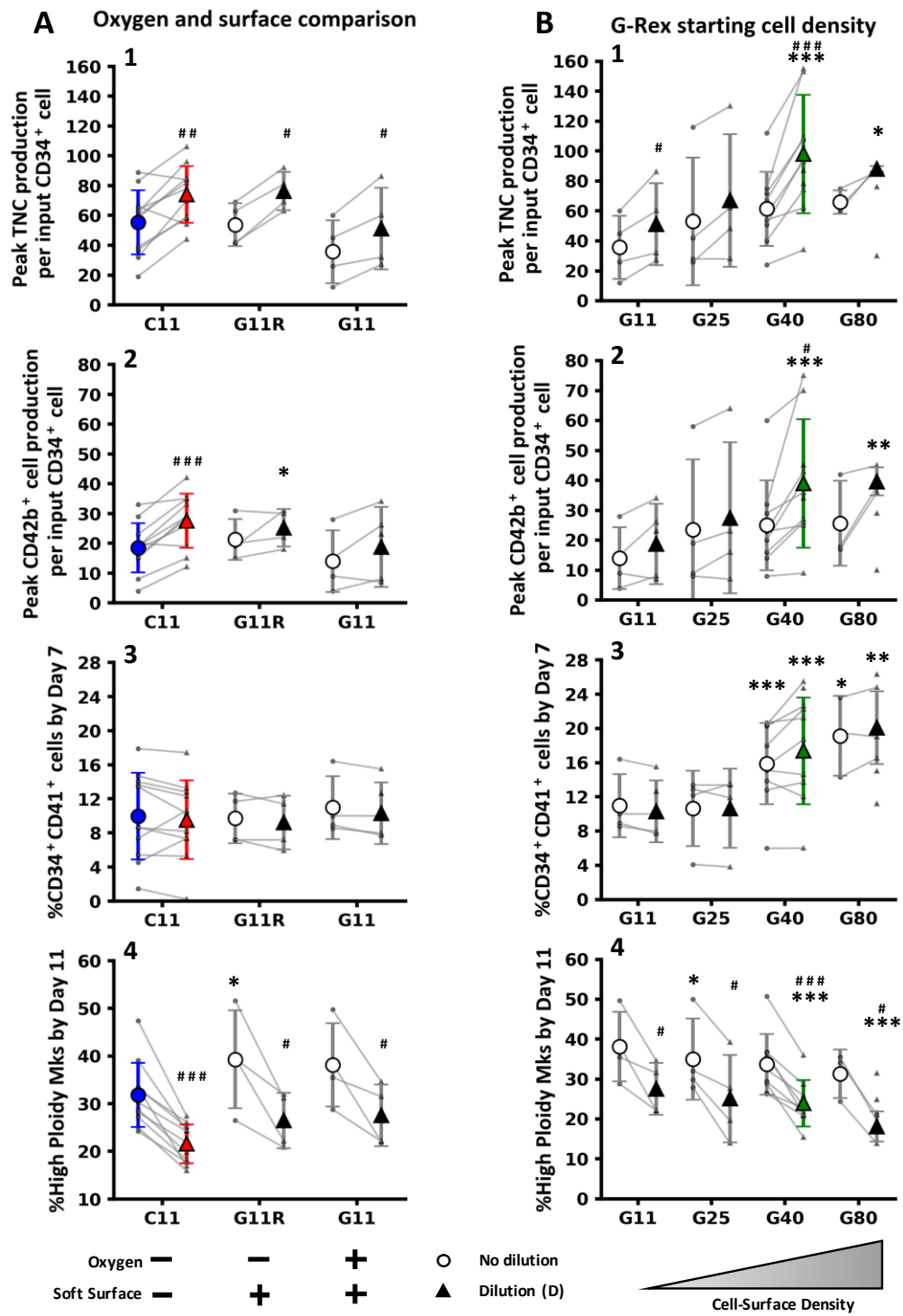


Figure 5.15 Factors contributing to expansion in G-Rex cultures. (A) Oxygen and surface comparison across C11, a restricted oxygen G-Rex device (G11R), and a standard

G-Rex device (G11) all seeded at the same cell-surface density of 11×10^3 cells/cm². (B) Increasing G-Rex cell-surface density: 11 (G11), 25 (G25), 40 (G40) and 80 (G80) $\times 10^3$ cells/cm². All conditions in (A) and (B) were also tested with dilution (triangle) or no dilution (open circle). Mean (+/- SD) calculated for conditions using paired points with grey lines connecting individual donors across diluted/non-diluted conditions. Dilution denoted with “D” added to condition name. Total cultures C11/C11D, n = 11; G11R/G11RD, n = 4; G11, n = 4; G11D, n = 5; G25/G25D, n = 4; G40, n = 9; G40D, n = 11; G80, n = 3 and G80D, n = 6. TNC = total nucleated cell. Statistics were evaluated by comparing (1) to respective C11 controls paired across the same donors, (2) diluted/non-diluted conditions paired across the same donors (grey lines), (3) dilution control C11D to G-Rex conditions paired across same the donors when $n \geq 3$, and (4) G-Rex conditions paired across the same donors when $n \geq 3$. For reference, colors for C11 (blue), C11D (red) and G40D (green) are the same as presented starting from **Figure 5.4**.

Compared to main control C11: * $p < 0.05$, ** $p < 0.01$, *** $p < 0.001$

Comparing No Dilution vs. Dilution (grey lines): # $p < 0.05$, ## $p < 0.01$, ### $p < 0.001$

(B1, C1) Peak TNC

C11D vs. G11R**, G11*, G11D*, G40* ; **G40D** vs. G11R**, G11RD*, G11**, G11D**;
G11RD vs. G11**, G11D*; **G11R** vs. G11*

(B2, C2) Peak CD42b cells

C11D vs. G80D*; **G40D** vs. G11R*, G11RD*, G11*, G11D*; **G11RD** vs. G11*

(B3, C3) %CD34⁺CD41⁺ cells

C11D vs. G40***, G80*, G80D**; **G40D** vs. G11R**, G11RD*, G11*, G11D**, G25*, G25D*

(C4, C4) %High Ploidy Mks

C11D vs. G11R*, G11RD*, G11*, G25*, G40***, G80*; **G40D** vs. G11R*, G11*, G25*;
G11RD vs. G11*, **G11R** vs. G11D*

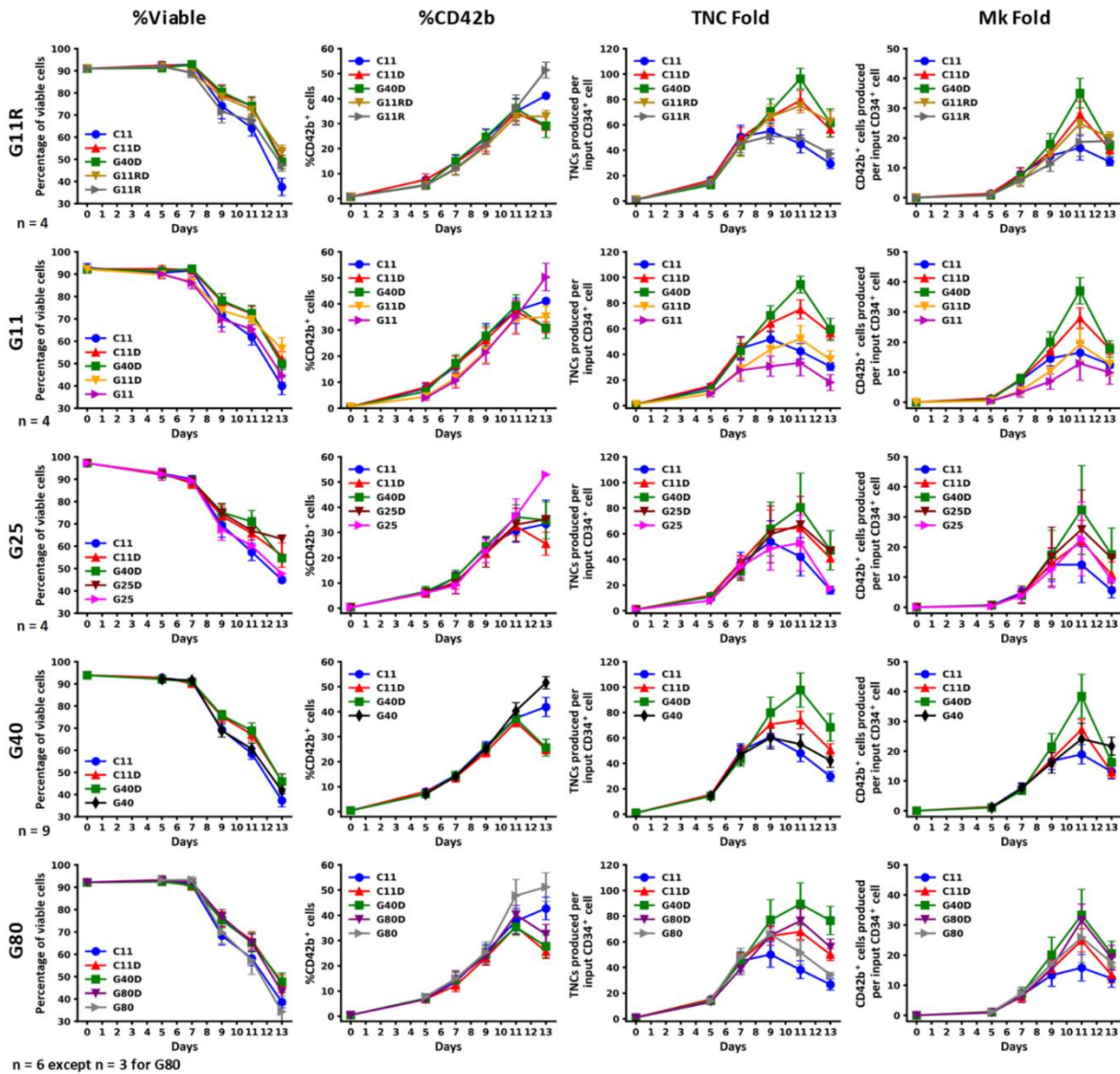


Figure 5.16 Time profiles for conditions shown in Figure 5.15. Different seeding densities, whether the oxygen transfer had been restricted in a G-Rex device, and the soft-surface component were evaluated. Each row indicates a condition and each column the variable of interest. Dilution denoted with “D” added to condition name. Control C11, restricted oxygen G-Rex device (G11R), and a standard G-Rex device (G11) all seeded at same cell-surface density of 11×10^3 cells/cm². G-Rex surface cell densities of 11 (G11), 25

(G25), 40 (G40) and 80 (G80) $\times 10^3$ cells/cm² were tested. Points = mean \pm SEM. TNC = total nucleated cells. Mk = megakaryocyte.

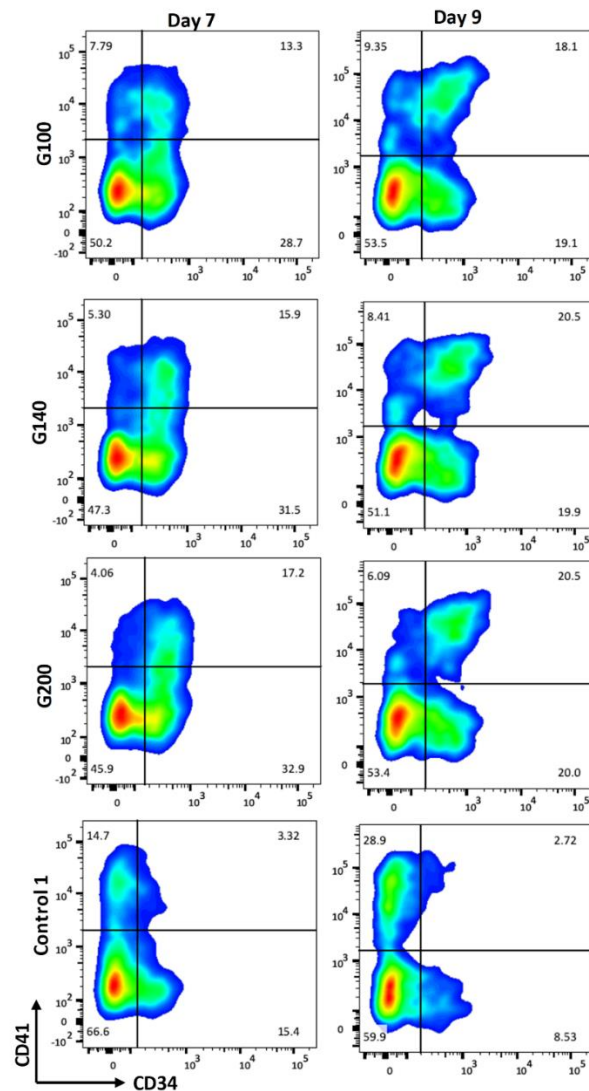


Figure 5.17. High G-Rex surface densities have greater CD34 retention. Plots for three high surface densities tested on Days 7 and 9 showing higher %CD34⁺CD41⁺ cells in G-Rex cultures compared to a control (one donor). Densities: 100 (G100), 140 (G140) and 200 (G200) $\times 10^3$ cells/cm².

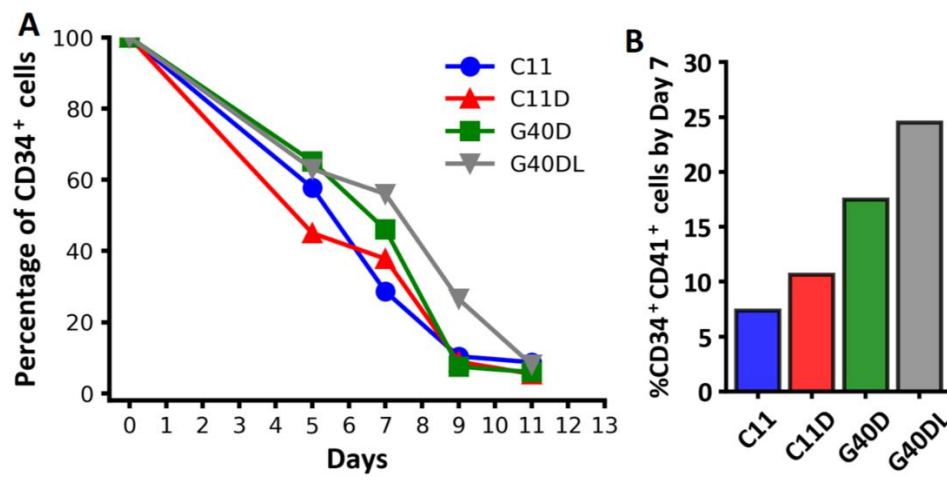


Figure 5.18 Cells kept in G-rex until Day 7 (G40DL) vs. Day 5 (G40D) retain CD34 longer. (A) G40DL has greater and more sustained CD34 retention than G40D, control C11 and dilution control C11D. (B) %CD34⁺CD41⁺ cells on Day 7. Results shown for a single donor.

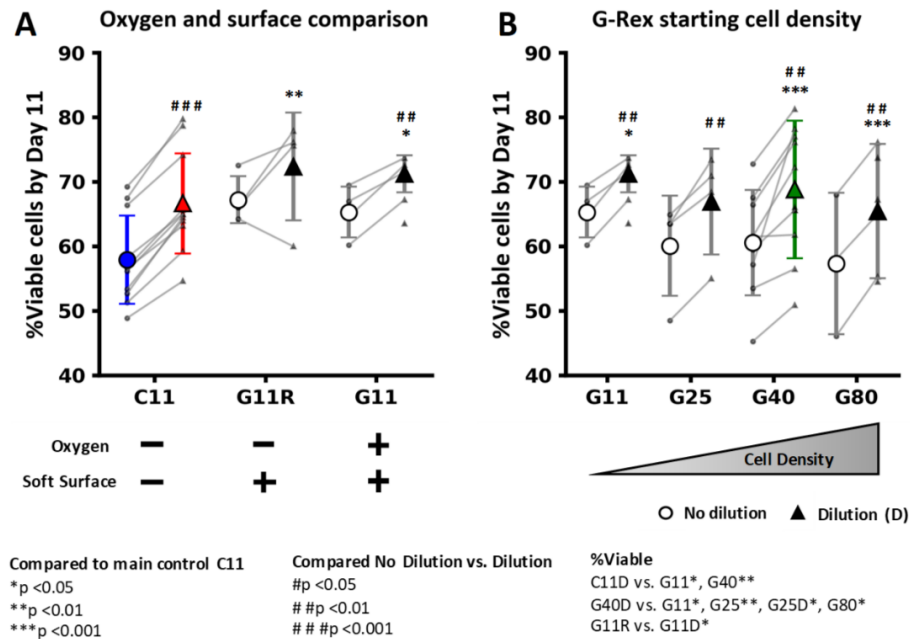


Figure 5.19 Factors contributing to greater % Viability in G-Rex and diluted cultures.

(A) Oxygen and surface comparison across C11, a restricted oxygen G-Rex device (G11R), and a standard G-Rex device (G11) all seeded at the same cell-surface density of 11×10^3 cells/cm². (B) Increasing G-Rex cell-surface density 11 (G11), 25 (G25), 40 (G40) and 80 (G80) $\times 10^3$ cells/cm². All conditions in (A) and (B) were also tested with dilution (triangle) or no dilution (open circle). Mean (+/- SD) calculated for conditions that have paired points with grey lines connecting individual donors across diluted/non-diluted conditions. Dilution denoted with “D” added to condition name. Total cultures C11/C11D, n = 11; G11R/G11RD, n = 4; G11, n = 4; G11D, n = 5; G25/G25D, n = 4; G40, n = 9; G40D, n = 11; G80, n = 3 and G80D, n = 6. Statistics were evaluated by comparing (1) to respective C11 controls paired across the same donors, (2) diluted/non-diluted conditions paired across the same donors (grey lines), (3) dilution control C11D to G-Rex conditions paired across same the donors

when $n \geq 3$, and (4) G-Rex conditions paired across the same donors when $n \geq 3$. Cultures are the same as those shown in **Figure 5.15**. For reference, colors for C11 (blue), C11D (red) and G40D (green) are the same as presented starting from **Figure 5.4**.

Given that media dilutions improved expansion regardless of surface, system or seeding density, we further explored the media component in G40D (**Figure 5.20A**). We exchanged the media once on either Day 7 (G40D-x7) or Day 9 (G40D-x9) and also tested a diluted condition without any IL-3 added on Day 5 (G40D-3i) since studies have shown that IL-3 could preferentially expand CD34⁺CD41⁺ Mk progenitors.[110,111] Compared to C11, peak TNC production for G40D-x7 was comparable and for G40D-x9 it was ~1.4-fold higher (**Figure 5.20B**). Additionally, G40D-x9 peak Mk production was ~1.6-fold higher than C11 (**Figure 5.20C**). G40D-3i had a slower expansion (**Figure 5.21A-D**) but peak Mk numbers were ultimately ~1.5-fold higher than C11 and ~25% lower than G40D (**Figure 5.20C**). Compared to G40D, viability was lower and %high-ploidy was higher due to lower numbers of 2N and 4N Mks for G40D-x7, G40D-x9 and G40D-3i (**Figure 5.20D, Figure 5.21E, F**). The total Mk DNA produced per input CD34⁺ cell for G40D-x7, G40D-x9, and G40D-3i was ~30% lower than G40D but ~1.4-fold higher than C11 (**Figure 5.20F**). Also, %CD34⁺CD41⁺ cell fractions remained high in G40D-3i compared to C11 and C11D (**Figure 5.20G**). Overall, the results of **Figures 5.15 through 5.21** demonstrate that increasing G-Rex cell-surface density improved expansion while at the same time increasing %CD34⁺CD41⁺ cell fractions, whereas media/IL-3 retention significantly improved culture productivity.

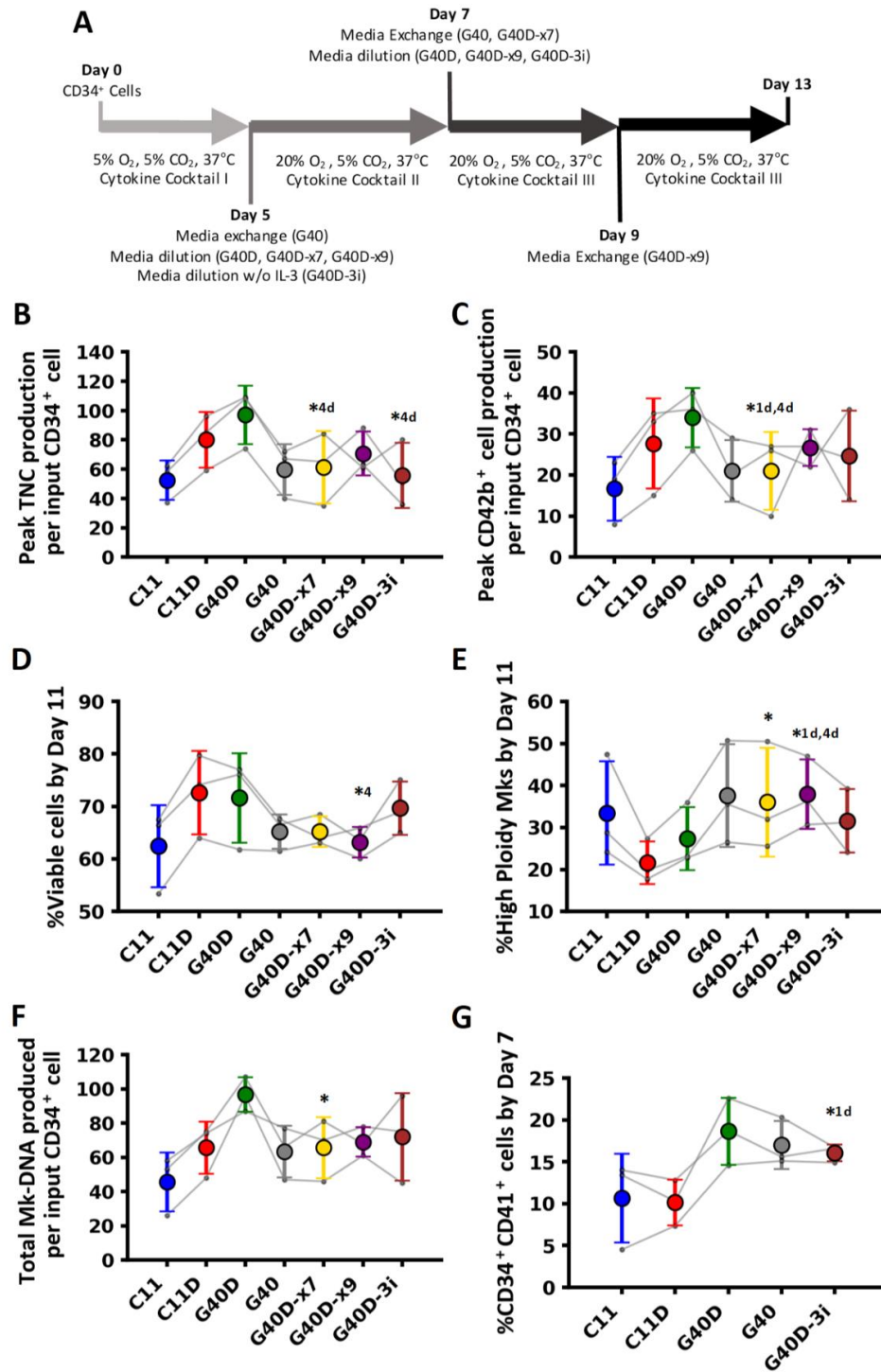


Figure 5.20 Late media exchange and IL-3 removal reduce Mk expansion. (A)

Experimental layout testing media exchanges for G-Rex cell-surface density of 40×10^3

cells/cm²: no dilutions (G40), dilution Days 5/7 (G40D), dilution Day 5 + media exchange Day 7 (G40D-x7), dilution Days 5/7 + media exchange Day 9 (G40D-x9), and dilution Days 5/7 with no IL-3 added on Day 5 (G40D-3i). Control C11 and dilution control C11D were tested as well. (B) Peak total nucleated cell (TNC) production and (C) peak CD42b⁺ cells produced per input CD34⁺ cell. (D) %Viable cells by Day 11. (E) %High-ploidy megakaryocytes (Mks) by Day 11. (F) Total Mk DNA produced. (G) %CD34⁺CD41⁺ cells by Day 7. Grey lines connect individual donors. Mean +/- SD, n = 3. * = $p < 0.05$ compared to C11, *1d = $p < 0.05$ compared to C11D, *4 = $p < 0.05$ compared to G40, *4d = $p < 0.05$ compared to G40D.

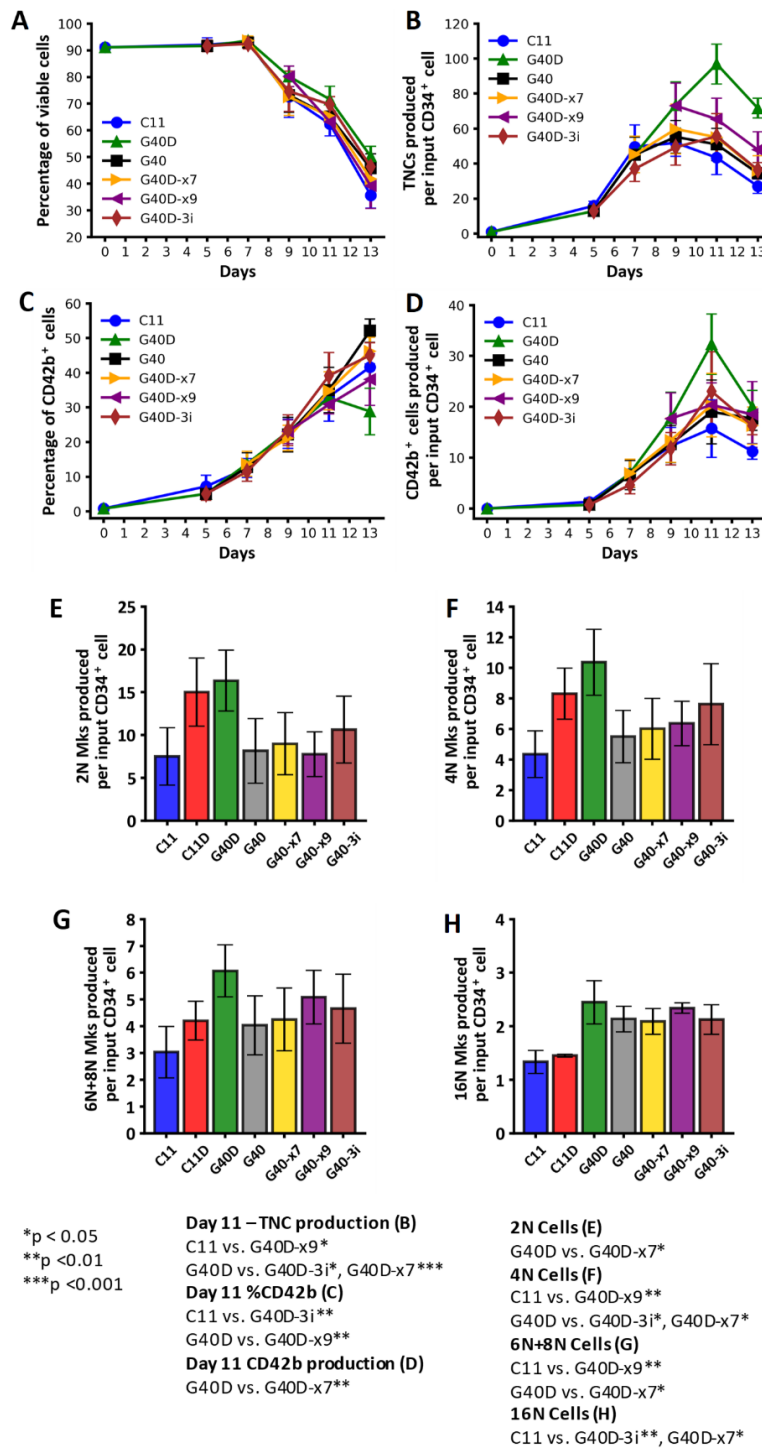


Figure 5.21 Removing G-Rex media or IL-3 late in culture diminishes culture productivity. Testing media exchanges for G-Rex seeding density of 40×10^3 cells/cm²: no

dilutions (G40), dilution Days 5/7 (G40D), dilution Day 5 + media exchange Day 7 (G40D-x7), dilution Days 5/7 + media exchange Day 9 (G40D-x9), and dilution Days 5/7 with no IL-3 added on Day 5 (G40D-3i). Control C11 and dilution control C11D were tested as well. (A) % Viability. (B) Total nucleated cell (TNC) production per input CD34⁺ cell. (C) %CD42b⁺ cells. (D) CD42b⁺ cells produced per input CD34⁺ cell. The number of CD41⁺ Mks produced per input CD34⁺ cell that are (E) 2N, (F) 4N, (G) 6N+8N, and (H) 16N. Points/Bars = mean +/- SEM, n = 3. These cultures are the same as those shown in **Figure 5.20**.

For all the cultures in **Figure 5.20**, we assessed proPLT morphology on Day 13 (**Figure 5.22**) and saw similar characteristic proPLT structures and branching. Our PLP estimates after shaking C11, G40D and G40D-x9 from Days 11 through 13 for 2 donors indicated similar levels of PLPs generated (**Figure 5.23**). Additionally, flow cytometry analysis of these shaken cultures indicated that larger differences in activation exist between donors than within the conditions (**Figure 5.24**)

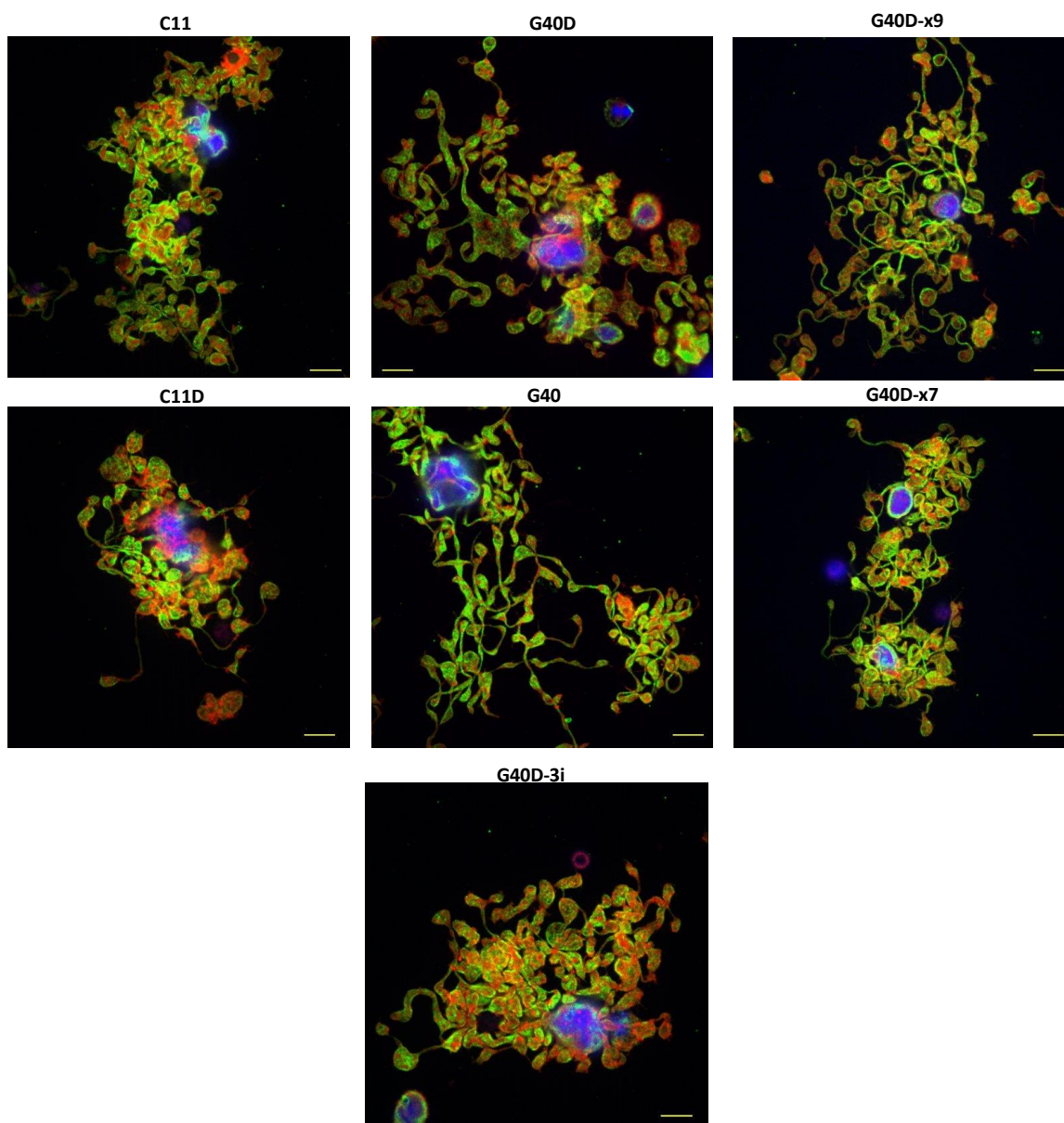


Figure 5.22 proPLTs from various G-Rex 40 conditions. Confocal microscopy analysis of proPLTs on Day 13 for G-Rex seeding density of 40×10^3 cells/cm²: no dilutions (G40), dilution Days 5/7 (G40D), dilution Day 5 + media exchange Day 7 (G40D-x7), dilution Days 5/7 + media exchange Day 9 (G40D-x9), and dilution Days 5/7 with no IL-3 added on Day

5 (G40D-3i). Control C11 and dilution control C11D also shown. Images from the same donor. Scale bar = 15 μ m. Red= actin, green = beta-tubulin, blue = DNA.

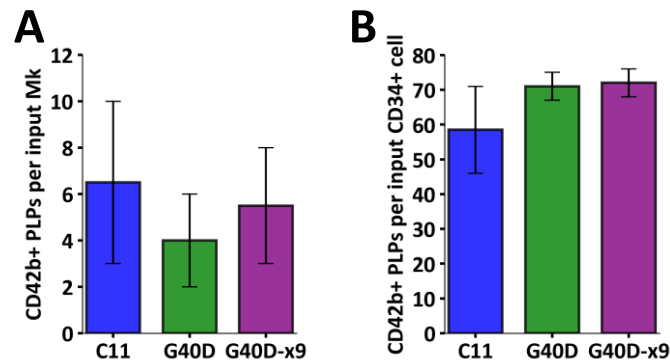


Figure 5.23 G40D and G40D-x9 PLP generation estimates from orbital shaker on Day 13. (A) CD42b⁺ PLPs produced per seeded Mk on Day 11 and sampled on Day 13. (B) CD42b⁺ PLPs per input CD34⁺ cell sampled on Day 13. G-Rex seeding density of 40×10^3 cells/cm² dilution Days 5/7 (G40D), and dilution Days 5/7 + media exchange Day 9 (G40D-x9). Control = C11. Bars = mean +/- standard deviation. n = 2. No significant difference of PLP yields observed.

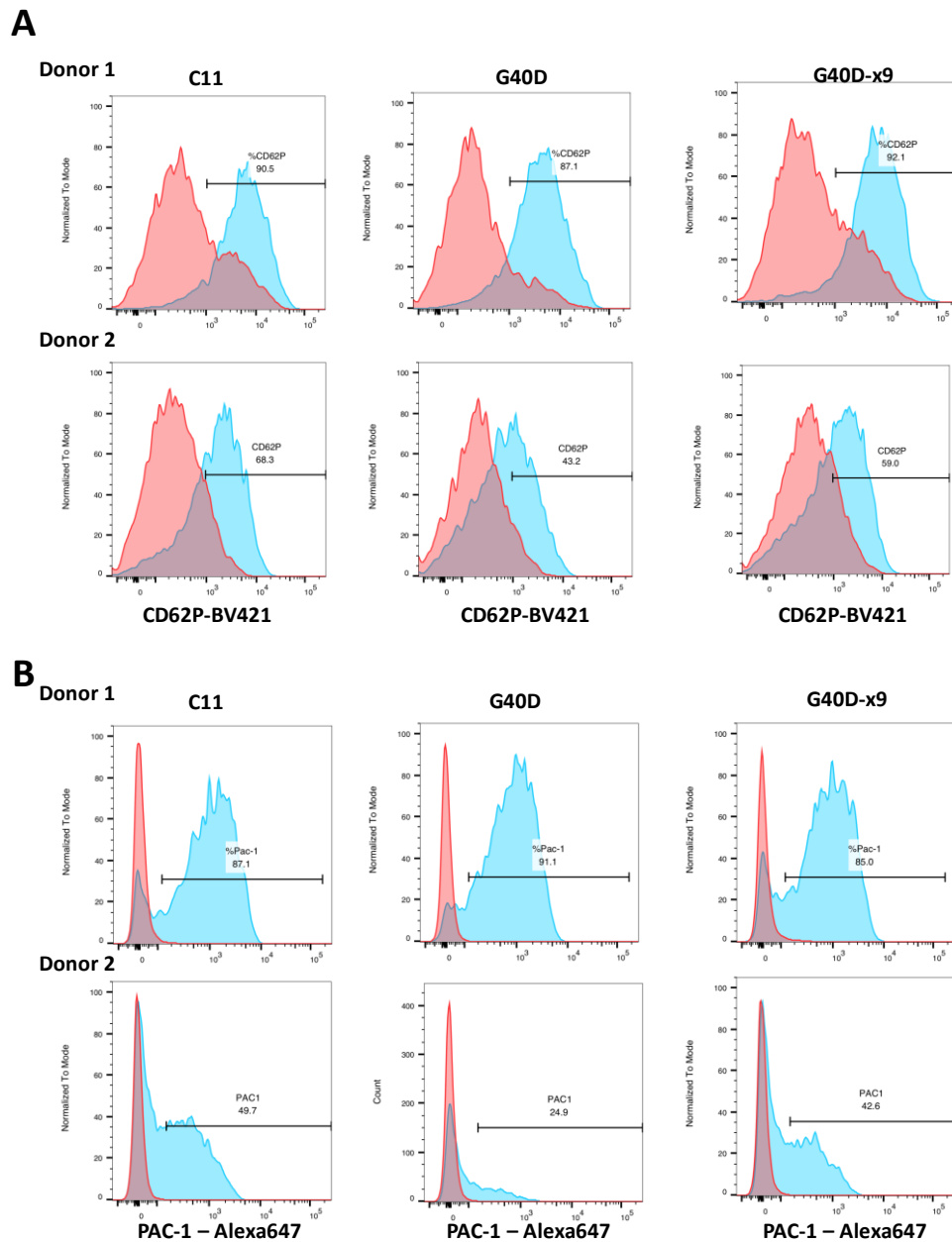


Figure 5.24 G40D and G40D-x9 PLP activation analysis. (A) CD62P expression of CD42b⁺PLPs in the absence (red) and presence (blue) of thrombin. (B) PAC-1 binding of CD42b⁺PLPs in the absence (red) and presence (blue) of thrombin. Results shown for two

different donors. G-Rex seeding density of 40×10^3 cells/cm² dilution Days 5/7 (G40D), and dilution Days 5/7 + media exchange Day 9 (G40D-x9). Control = C11.

5.4 Discussion

Various studies have demonstrated benefits of the G-Rex system for expanding different cell types due to their scalability, improved oxygen transfer, and higher culture viability.[106,112] Additionally, the use of fed-batch media dilutions have proven positive for the expansion of CD34⁺ cells from CB compared to full media exchanges.[108] In this study, we used the G-Rex system coupled with a fed-batch dilution strategy to generate Mks from mPB CD34⁺ HSPCs and identified an efficient starting cell-surface density of 40×10^3 cells/cm² (G40D). This cell density is much lower than the density range of $125\text{-}500 \times 10^3$ cells/cm² used in G-Rex cultures of K562 cells, T-cells, and other cell types.[104,109] G40D cultures generated 39 ± 19 CD41⁺CD42b⁺ Mks per input CD34⁺ cell, which was higher than our current process with (C11D) or without (C11) a fed-batch strategy at 28 ± 9 and 18 ± 8 , respectively. G40D cultures were also higher than recently reported mPB-Mk yield of 27.[113] C11D and G40D had increased culture viability, improved the number of Mks produced per mL of media used, and had lower %high-ploidy cultures with similar production of $\geq 16N$ Mks compared to C11. However, G40D cultures had higher fractions of CD34⁺CD41⁺ cells (Mk progenitors) by mid culture and yielded significantly greater numbers of 2N, 4N, and 6N+8N Mks, while increasing the total Mk DNA pool. We observed substantial donor-to-donor variability but G40D trends held true for both high and low-performing donors.

The soft silicone rubber membrane surface in the G-Rex is very different from the polystyrene culture surface used in C11/C11D. Recent studies have shown that soft surfaces could have a positive effect on HSPC expansion.[114,115] With the same seeding cell-surface density of C11 and restricting gas-transfer across the membrane (G11R), the G-Rex soft-surface did not improve TNC or Mk expansion. Surprisingly, a G-Rex device with restricted oxygen transfer had higher expansion than a standard G-Rex device (G11R vs. G11). Due to the permeable membrane, oxygen tension would be higher near the cells in G-Rex devices than in standard wells or restricted G-Rex devices. The differences in oxygen tension could explain these results since our previous studies have shown that higher oxygen tension early in culture decreases total Mk expansion.[35] Increasing the G-Rex cell-surface density up to 80×10^3 cells/cm² improved expansion, consistent with past G-Rex studies showing the importance of increased cell-cell contact for growth.[109]

G-Rex systems have been used to expand HSPCs from various sources using a surface density of 500×10^3 cells/cm² that resulted in a 13.6-fold expansion of CD34⁺ cells after 12 days.[102] In the present study after 7 days, G40D conditions yielded a 19-fold expansion of CD34⁺ cells and contained higher fractions of CD34⁺CD41⁺ cells compared to controls. Neither the soft surface nor improved gas transfer in the G-Rex increased Mk progenitors at low cell density. Higher G-Rex cell-surface densities led to more extensive and longer CD34 retention and increased numbers of Mk progenitors regardless of dilutions. In a previous study, culturing CD34⁺ cells at high volumetric densities increased Mk progenitor populations.[116] The authors seeded cells at 400,00 cells/mL (in 20% oxygen) and

performed daily dilutions. In the present study, because a low oxygen period is employed during the first 5 days of culture without disruption, cells were not seeded at higher volumetric densities in standard tissue culture wells due to concern of overgrowth and nutrient depletion along with rapid accumulation of secreted soluble factors. The use of G-Rex systems allowed us to increase seeding cell numbers while maintaining the starting volumetric density at 40,000 cells/mL. Importantly, volumetric and cell-surface densities post Day 5 were kept similar across the conditions. Therefore, the increase in CD34⁺CD41⁺ cells is largely driven by increased cell-surface densities and cell-cell contact during the low oxygen phase in the first 5 days of culture.

Media dilutions improved productivities across all conditions. G-Rex cell-surface densities above 25×10^3 cells/cm² produced over 2-fold more Mks than controls. Exchanging the media on Days 5, 7 or 9 diminished the expansion potential of G40D cultures, while reducing culture viability. It's been reported that IL-3 has a positive effect on expansion of Mk progenitors [110,111] and our results demonstrate that retention of the conditioned media/IL-3 maintains the expansion of CD41⁺CD42b⁺ Mks. Though C11/C11D produced Mk progenitors, the numbers were ~2-fold lower by mid-culture compared to G-Rex at high densities. Thus, by increasing the cell-surface density in G-Rex to produce more Mk progenitors and by retaining the conditioned media/IL-3, greater Mk numbers were produced (**Figure 5.25**).

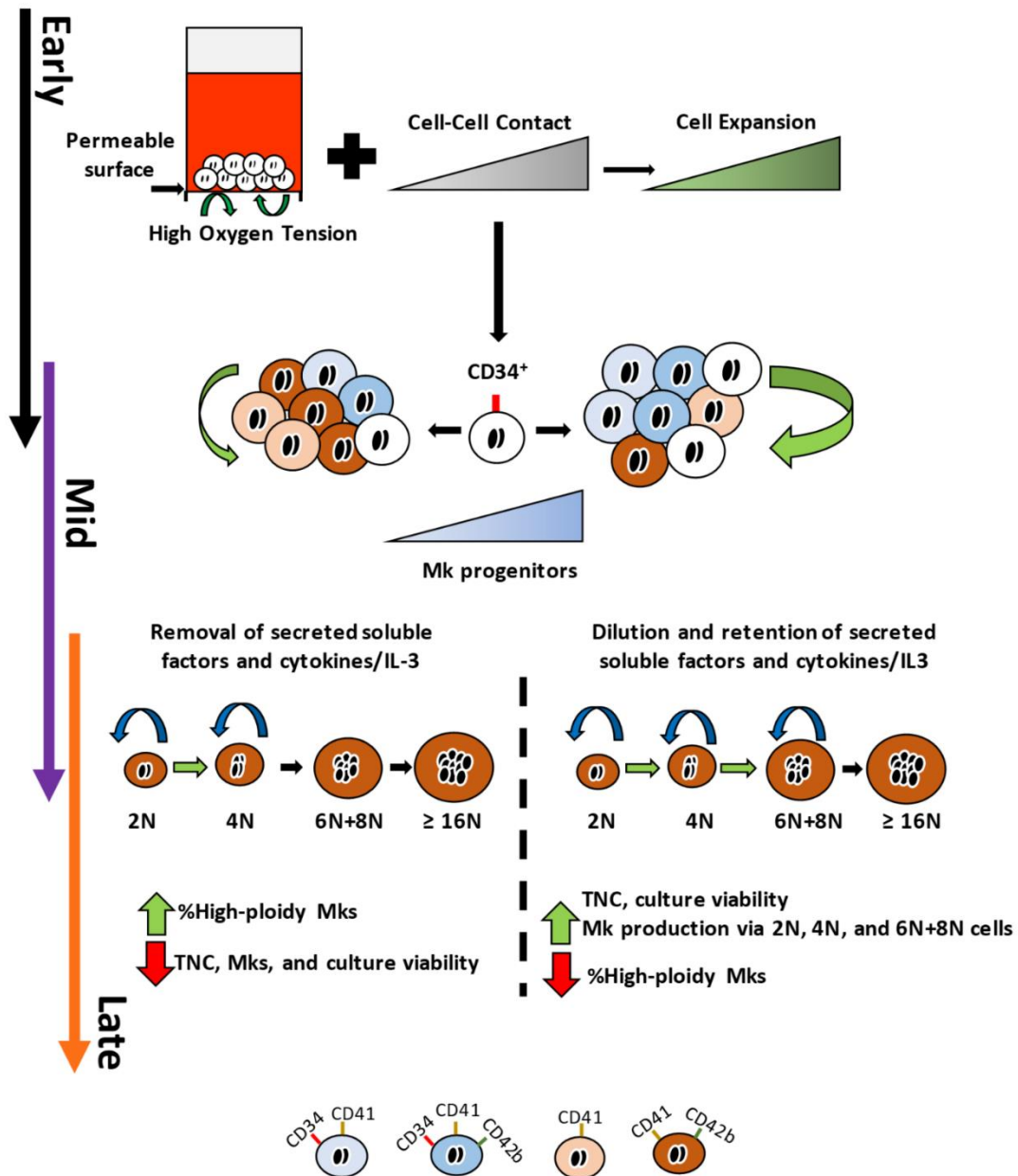


Figure 5.25 Proposed model of how G-Rex and media dilutions enhance Mk production from mPB CD34⁺ cells. High cell-surface seeding density early in G-Rex improves expansion and increases the fraction of cells that are Mk progenitors by mid culture. The larger numbers of Mk progenitors benefit from retention of conditioned media and IL-3 to

further expand and increase final numbers of CD41⁺CD42b⁺ megakaryocytes (Mk) produced. Retention of the media for low G-Rex cell-surface densities or non-G-Rex devices also had a benefit on Mk expansion.

Omitting IL-3 from Day 5 dilutions (G40D-3i vs. G40D, **Figure 5.20**) reduced Mk production, but it was still 50% higher than C11. These observations provide evidence that the conditioned media itself retains potential for Mk production, absent fresh IL-3. It has been reported that various endogenous soluble factors are secreted by HSPCs with both a negative and positive impact on HSPC expansion.[108,117] Positive synergistic effects between cytokines have shown to be beneficial for Mk production, specifically between TPO, SCF and IL-3.[42,111] Insulin-like growth factor-1 (IGF-1) and insulin-like growth factor binding protein-3 (IGFBP-3) secreted from Mks has been reported to support HSPC expansion.[118] Also, studies have shown that exogenous cytokines can stimulate Mks to secrete IL-3 and IL-6.[119] All these findings indicate various ways in which dilutions vs. media exchange are beneficial through diluting negative factors, while retaining positive factors that benefit Mk production.

G-Rex Mks displayed proPLTs and the PLPs collected displayed *in vitro* activation potential and aggregation potential in flow chambers, similar to that reported for other culture-derived PLPs.[48,49] Estimates for several donors revealed similar levels of CD41⁺CD42b⁺ PLPs per input CD34⁺ cell on Day 13. This indicates that, although the Mk pool was expanded in G40D, we may not have changed the PLP-producing Mk population. However, we have not

yet optimized PLP collection in these cultures. Microfluidic systems appear to be effective at promoting PLP release by mimicking *in vivo* environments. [48,50,76] G-Rex Mks introduced into our uniform-shear rate microbioreactor displayed similar proPLT and PLP behavior as previously described for Mks cultured in STCS [76] and we are working to scale-up the bioreactor. Recent work has also identified turbulence as a key variable for PLP generation.[51] Yet, further advancements in engineering systems that can efficiently generate PLPs *ex vivo* are crucial.[77]

Platelet transfusions typically contain 3×10^{11} platelets per unit.[120] In contrast, Mk expansion and PLP yields *ex vivo* remain low with required starting cell numbers approaching 10^8 - 10^9 input CD34⁺ cells per unit with current methods.[10,34,121] The median number of CD34⁺ cells recovered from healthy donors after G-CSF treatment was reported to be ~500 million cells [122] and with our Mk yields we could generate $\sim 2 \times 10^{10}$ Mks per donor. With a conservative yield of 15 PLPs/Mk, one donor could give rise to one platelet unit for transfusion. However, since millions of platelet units are transfused each year, to create a clinically relevant process, one donor should give rise to multiple transfusion units. Increasing our Mk yields by an order of magnitude would be a substantial improvement and lead to 10 platelet units but would still require 10^4 - 10^5 donors a year.

An alternative strategy is to infuse culture-derived Mks into the body for *in vivo* PLP production as has been done in mice.[26,123-125] Though the estimated yield of PLPs per infused ex-vivo-derived human Mk was low (10-100) [125], G-Rex systems could be used

to produce larger numbers of Mks for infusion. Additionally, transfusions of Mk progenitors have been safely reported in humans with transfusion cell numbers in the range of 10^5 - 10^6 Mk progenitors per kg of body weight.[126-129] Mk progenitors have been reported to be responsible for platelet recovery after transplantation [39,130]. In this study, we estimate a yield of 8 ± 4 Mk progenitors produced per input CD34⁺ cell and thus could generate 4×10^9 Mk progenitors by Day 7 per donor. With a body weight of 70 kg, a single donor could provide 50-500 transfusions. Further mouse studies on the *in vivo* PLP potential of G-Rex-derived Mks as well as the clonogenic potential from G-Rex-derived Mk progenitors are required. Additional safety studies should address the concern of larger cell-size of Mks that could obstruct small vessels along with the concern of tumorigenesis.[11] Studies have shown, however, that irradiated iPSC-derived Mks retained potential to produce PLPs *in vivo* after being infused into mice.[131]

Additional advances are clearly required to produce clinically relevant Mk numbers from the process described in this study. Future G-Rex studies would include re-examining higher seeding cell-surface densities with the fed-batch dilution method from this study, adjusting cytokine concentrations and evaluating CB HSPCs. A lower oxygen setting for the first 5 days should be explored when using G-Rex. Also, the cell-cell contact mechanism for prolonged CD34 expression could be explored. Nonetheless, our results highlight distinct methods of increasing Mk numbers through a fed-batch dilution scheme and utilizing technologies that permit higher input cell numbers.

5.5 Acknowledgements

This research was supported by NIH 1R01HL130760-01. AM was also partially supported by NIH Predoctoral Training Grant T32 GM008449. This work utilized Northwestern University Micro/Nano Fabrication Facility (NUFAB), partially supported by Soft and Hybrid Nanotechnology Experimental (SHyNE) Resource (NSF ECCS-1542205), the Materials Research Science and Engineering Center (DMR-1720139), the State of Illinois, and Northwestern University. This work used the Flow Cytometry Core Facility supported by Cancer Center Support Grant (NCI CA060553) and the Biological Imaging Facility at Northwestern University. We thank Damien Doser, Darryl Abbot, Vasil Kukushliev, and Jia Wu for helping with some of the data collection. We also thank Jia Wu for discussions on statistics and data analysis. G-Rex plates were generously supplied by Wilson Wolf.

Conflicts of interest

G-Rex 6- and 24-well plates were generously provided by Wilson Wolf Corporation. Wilson Wolf did not influence the experimental design and did not provide input on the manuscript.

CHAPTER 6: Evaluating culture methods of increasing PLP production via pharmacological inhibition of Rho GTPases

6.1 Introduction

In elucidating the mechanism of proplatelet (proPLT) formation to enhance platelet production, several studies have investigated elements impacting cytoskeletal rearrangements of megakaryocytes (Mks) during maturation, proPLT formation and platelet release. Specifically, several signaling pathways, particularly those affecting actin and microtubule organization, have been implicated including Rho-family GTPases: RhoA, Cdc42, and Rac1.[75] Rho GTPases are small molecular switches that are in an active state when bound to GTP.[132] Guanine exchange factors (GEFs) catalyze the exchange of GDP to GTP. When GTPases are bound to GTP, they are active and can interact with their downstream effectors. Then, GTPase-activating proteins (GAPs) can accelerate the hydrolysis of the bound GTP to GDP, halting the GTPase activity.

While studies on RhoA, Cdc42 and Rac1 have primarily focused on mouse Mks and knockout models, limited work has been done to understand inhibition of these GTPases in human Mks. The studies in this chapter focused on using reversible pharmacological inhibitors for RhoA (Rhosin), Cdc42 (ML141) and Rac1 (NSC23766) to improve Mk ploidy and/or proPLT formation that could lead to higher PLP yields. Rhosin specifically targets the GEF binding domain on RhoA and thus GDP cannot be exchanged for GTP.[133] NSC23766 selectively inhibits binding between Rac1 and its GEFs and does not interfere with Cdc42 and its GEFs.[70] Finally, ML141 is a potent and selective inhibitor that prevents

GTP binding to Cdc42.[134] ML141 and NSC23766 have been studied in mouse Mks,[29,135] but along with Rhosin, they have not been studied in human Mks. CD61⁺ mPB-Mks selected from our culture on Day 7 usually start making proPLTs on Day 10 and ploidy levels peak between Days 10 and 11. Therefore, we seeded CD61⁺ Mks on Day 9 with the selected inhibitors and monitored changes to Mk culture up to Day 13. The literature suggests that inhibition of Rac1 or Cdc42 could lead to higher ploidy Mks, but with potential diminished proPLTs.[74] Reduced RhoA activity could lead to increase proPLT formation and higher ploidy in Mks.[58,61,62] Our experiments demonstrated minimal impact to proPLT formation by inhibiting Cdc42 or RhoA but diminished proPLT formation after Rac1 inhibition. No significant changes to ploidy were measured. Finally, PLP estimates from selected inhibitor conditions did not lead to improved PLP yields.

6.2 Material and methods

Unless otherwise specified, all reagents were obtained from Sigma-Aldrich (St. Louis, MO), cytokines from Peprotech (Rocky Hill, NJ), and antibodies for flow cytometry analysis from BD Biosciences. LSR II (BD Biosciences, San Jose, CA) flow cytometer was used to collect data and analysis was done using FlowJo v.10 (FlowJo LLC, Ashland, OR).

6.2.1 Cell culture

Previously frozen mobilized peripheral blood (mPB) CD34⁺ cells from the Fred Hutchinson Cancer Research Center (Seattle, WA) with Northwestern University Institutional Review Board approval were grown in 78% IMDM (Gibco, Carlsbad, CA), 20% BIT 9500 Serum

Substitute (STEMCELL, Vancouver, BC, Canada), 1% Glutamax (Gibco), 1 $\mu\text{g}/\text{mL}$ low-density lipoproteins (Calbiochem, Whitehouse Station, NJ), 100 U/mL Pen/Strep, 100 ng/mL TPO, 100 ng/mL SCF, 10 ng/mL IL-6, 10 ng/mL IL-11 and 2.5 ng/mL IL-3 (R&D Systems, Inc., Minneapolis, MN). Cells were maintained between 100,000 to 400,000 cells/mL at 37°C, 5% CO₂ and 5% O₂ for 5 days. On day 5, the cytokines were replaced with 100 ng/mL TPO, 100 ng/mL SCF, 10 ng/mL IL-9, 10 ng/mL IL-11 and 10 ng/mL IL-3. Cells were maintained at a density of 250,000 to 500,000 cells/mL and kept at 37°C, 5% CO₂, and 20% O₂ until day 7. On day 7, cells were selected using anti-CD61-conjugated magnetic microbeads (Miltenyi Biotech Inc, San Diego, CA) and then cultured in medium with 100 ng/mL TPO, 100 ng/mL SCF and 6.25 mM nicotinamide thereafter. The cells were maintained at a density between 250,000 to 500,000 cells/mL and kept at 37°C, 5% CO₂ and 20% O₂. Conditions were treated on Day 9 with the following inhibitors: Rhosin (555460, Millipore Sigma, Burlington, MA) for RhoA, ML141 (SML0407, Sigma) for Cdc42, NSC23766 (SML0952, Sigma) for Rac1 and CK-636 (C7374, Sigma) for Arp2/3. For reversibility of inhibition studies, after 24 or 48 hrs of exposure to the inhibitor, media was replaced with fresh media without inhibitor. Rhosin conditions are labeled as iRhoA, ML141 conditions labeled as iCdc42 and NSC23766 conditions as iRac1. For dual inhibition studies of Rac1 and Cdc42, labeling is iRac1+iCdc42 and NSC23766 was used at 50 μM and ML141 at 10 μM .

6.2.2 Flow cytometric analysis of Mk viability

Selected Mks were washed twice at 4° C with cold PBS containing 2 mM EDTA and 0.5% BSA (PEB). Antibodies anti-CD41-FITC (555466) and anti-CD42b-APC (551061) were added to the samples and incubated for 30 min at 4° C. Cells were washed twice with PEB and incubated with DAPI (Invitrogen, Carlsbad CA) for 15 min at room temperature before analysis.

6.2.3 Flow cytometric analysis of MK apoptosis

Selected Mks were washed with PBS, then with 1X Annexin V binding buffer, incubated with PE-conjugated Annexin V (BD559763) and DAPI for 15 min at room temperature prior to analysis.

6.2.4 Mk ploidy analysis

Cells were washed twice at 4° C with cold PEB and then incubated with anti-CD41 antibody for 30 min at 4° C. Cells were washed twice with PEB and then fixed with 0.5 % paraformaldehyde in PBS and incubated for 15 min at room temperature. Cells were then permeabilized with 70% methanol for 1 h at 4° C, treated with RNase for 30 min at 37° C and finally incubated with 50 µg/mL of propidium iodide to stain DNA 15 min before analysis.

6.2.5 Quantification of proPLT forming Mks

Selected Mks were seeded on Day 9 at a density of 70,000 cells/mL. From Day 10-13, the percentage Mks making proPLTs was determined by dividing the number of cells observed making proPLTs by the total number of cell bodies in each image. Approximately 100 cells were analyzed at each time point for each condition.

6.2.6 Bioreactor fabrication

A 2D design of the bioreactor (USRB-7 μ m) was created in AutoCAD 2014 (San Rafael, CA) and then printed onto a chrome mask (Front Range Photomask, Palmer Lake, CO). A silicon wafer (WRS Materials, San Jose, CA) was spin-coated with SU8-2035 photoresist (MicroChem Corp, Westborough, MA) at 4000 RPM for 30 s to achieve a photoresist height of 40 μ m. The wafer was soft-baked at 65°C for 3 min and then hard-baked at 95°C for 6 min. Afterwards, the wafer was exposed to UV light for 17 s using a Karl Suss MA6 Mask Aligner (SUSS MicroTec, Garching, Germany). The exposed resist was then baked at 95°C for 6 min. Finally, the resist was developed using SU8 developer solution (MicroChem) for 2 min and dried with a nitrogen gun. The dry wafer was silanized overnight (5 μ L of 1H,1H,2H,2H-perfluorooctyltrichlorosilane; Alfa Aesar, Ward Hill, MA) in a vacuum chamber. Next, a 1:10 curing agent to polydimethyl siloxane (PDMS) solution (Slygard 184 Kit; Electron Microscopy Sciences, Hatfield, PA) was poured over the wafer to cast a mold that was placed in an oven at 65°C overnight. The PDMS mold was then cut, holes for inlets and outlets created with a 2-mm punch, and the PDMS plasma-bonded (Model BD-20;

Electro-Tech Products, INC, Chicago, IL) to an ethanol-cleaned premium plain glass slide (25 x 75 x 1 mm; VWR, Radnor, PA).

6.2.7 Bioreactor perfusion with Mks

The USRB-7 μ m was positioned on a Lumascope microscope v500 (Etaluma Inc., Carlsbad, CA) placed inside an incubator (Thermo Scientific, Waltham, MA) maintained at 37°C and 5% CO₂. Separate syringe pumps (NE-300, New Era Pump Systems Inc., Farmingdale, NY) were used for each flow channel. A 5-mL glass syringe (81520, Hamilton Company, Reno, NV) was used for the outer channels and a 2.5-mL glass syringe (81420, Hamilton) was used for the center channel. Media (78% IMDM (Gibco, Carlsbad, CA), 20% BIT 9500 Serum Substitute (STEMCELL, Vancouver, BC, Canada), 1% Glutamax (Gibco), 1 μ g/mL low-density lipoproteins (Calbiochem, Whitehouse Station, NJ), 100 U/mL Pen/Strep) without cytokines was perfused throughout the bioreactor for 30 min at 6.5 μ L/min prior to Mk introduction. On day 11 or 12 Mks at density of 50,000/mL were stained for 15 min with 1 μ M Calcein AM at 37°C. After the 30-min media perfusion, 25,000 Mks were microinjected into the tubing upstream from the reactor. No Mks were present within the syringes. A video was recorded of each bioreactor for 1-2 hr.

6.2.8 Bioreactor effluent preparation

Effluent collected was spun once at 2200 g for 20 min to pellet Mks and PLPs. The pellet was then resuspended in HEPES/Tyrode's (HT) buffer (10 mM HEPES, 137 mM NaCl, 2.8 mM KCl, 1 mM MgCl₂, 12 mM NaHCO₃, 0.4 mM Na₂HPO₄, 0.35% BSA, 5.5 mM

glucose, pH 7.4) and allowed to rest for 20 min at room temperature. 2 mM CaCl₂ was added to the suspension 5 min before use in assays.

6.2.9 Platelet-like-particle (PLP) preparation and collection from orbital shaker

Cells in a culture dish at a cell density between 300,000 to 500,000 cells/mL were placed on an orbital shaker (SK-O180-E, SCIOLOGEX, Rocky Hill, CT) set to 50 rpm on Day 9 once inhibitors were added. On Day 12, the shaken cells and PLPs were harvested from the dish and spun down at 150 g for 5 min to pellet large cells. The supernatant was transferred to a fresh tube, prostaglandin E1 (PGE1, Cayman Chemical, Ann Arbor, MI) was added at 140 nM final concentration, and the solution was spun down at 2200 g for 20 min at room temperature to pellet PLPs. After the supernatant was discarded, the pellet was resuspended in HEPES/Tyrode's (HT) buffer (10 mM HEPES, 137 mM NaCl, 2.8 mM KCl, 1 mM MgCl₂, 12 mM NaHCO₃, 0.4 mM Na₂HPO₄, 0.35% BSA, 5.5 mM glucose, pH 7.4) and allowed to rest for 20 min at room temperature. CaCl₂ at a final concentration of 2 mM was added to the suspension 5 min before use in assays.

6.2.10 Flow Cytometry Preparation of PLPs from orbital shaker and bioreactor

Effluent from the bioreactor was analyzed for surface markers using the following antibodies against CD41-APC (559777) and CD42b-PE (555473). Samples were incubated for 15 min at room temperature (RT). Prior to perfusion through the bioreactor, Mks were stained with live stain Calcein AM so viable PLPs in the effluent also carried this live stain. Calcein⁺ PLP events were identified for bioreactor experiments. For PLPS collected on the orbital shaker,

CD41-FITC and CD42b-APC antibodies were used and the ratio of CD41⁺CD42b⁺ PLPs to viable Mks was used to estimate PLP-yields.

6.2.11 proPLT and PLP immunofluorescence microscopy

Cells were seeded on 8-well chamber glass slides (125658, Lab NunTek II, Thermo Scientific, Waltham, MA) on Day 9 at a density of 70,000 cells/mL. On Day 12, cells were fixed with 3.7% paraformaldehyde and then permeabilized with 0.3% Triton X-100 before sequentially staining with 5 µg/mL mouse anti-beta-tubulin primary antibody (5656321, BD Biosciences) and 1 µg/mL of Alexa Fluor 488-conjugated goat anti-mouse secondary antibody (A11001, Thermo Scientific). Cells were then incubated with TRITC-phalloidin, washed, and then stained with DAPI to identify nuclei. For PLPs, 8-well chamber slides were coated with fibrinogen (Innovative Research, Novi, MI) at 60 µg/mL in PBS or 1% BSA in PBS. Collected PLPs from bioreactor effluent suspension were added wells and allowed to rest at room temperature for 15 min and then 3 U/mL of thrombin was added to one of the wells coated with fibrinogen and incubated for 20 min at room temperature. The wells were washed with warm PBS and were prepped on the same day of the experiment and fixed as described above. PLP and proPLT slides were imaged using a 63x oil objective on a Leica DMI6000 Spinning Disc Confocal Microscope (Leica, Wetzlar, Germany).

6.2.12 Statistical Analysis

Paired t-tests were conducted for all pairs of conditions, and the significance level was set at $p < 0.05$. Bar graphs and plots are shown with standard errors of mean (SEM).

6.3. Results

6.3.1 Screening inhibitor concentrations and assessing viability and apoptosis

First, a screening experiment testing various inhibitor concentrations was carried out to initially understand the impact of individual GTPase inhibition on Mk viability by Day 11 (**Figure 6.1A**). RhoA inhibition with Rhosin (iRhoA) at high concentrations ($> 1 \mu\text{M}$) reduced cell viability versus the control. The viability of Rac1 inhibited Mks by NSC23766 (iRac1) was comparable to the control, though at $50 \mu\text{M}$ it was slightly lower. Cdc42 inhibition with ML141 (iCdc42) retained similar viability as the control up to $10 \mu\text{M}$. ML141 has been used in previous mouse Mks studies at $20 \mu\text{M}$.^[135] NSC23766 has been studied between $25\text{-}50 \mu\text{M}$ on mouse Mks.^[29] No studies on Mks have used Rhosin but it has been used on fresh human platelets at a range of $1\text{-}30 \mu\text{M}$.^[136] Based on the literature and from this screening study, the following conditions were chosen for subsequent analysis: iRhoA- $1 \mu\text{M}$, iCdc42- $10 \mu\text{M}$ and iRac1- $50 \mu\text{M}$. The viability profiles between Days 10-13 were overall comparable to controls (**Figure 6.1B**). Similar apoptosis profiles were also measured for the conditions with an increased apoptotic Mk fraction on Day 13 for iRhoA- $1 \mu\text{M}$ and iRac1- $50 \mu\text{M}$ (**Figure 6.1C**).

Cdc42 inhibition yielded interesting viability results. Mks in this condition shifted higher in DAPI fluorescence compared to the control (**Figure 6.2A**), possibly indicating DAPI uptake, yet Mks also double stained for live-stain of Calcein (**Figure 6.2B**). DAPI is usually excluded from live cells but compromised membranes can allow DAPI to enter the cell.

However, dead cells with compromised cell membranes do not retain Calcein. Therefore, Cdc42 inhibition appears to impact the cell membrane in a manner which allows DAPI uptake yet prevents Calcein loss. Additionally, visual assessment showed Calcein⁺ Mks in both control and iCdc42 conditions (**Figure 6.2C**).

Since inhibition of RhoA, Cdc42 or Rac1 at the selected concentrations was not detrimental to the culture viability across the days tested, we proceeded to analyze the cultures for Mk properties such as proPLT formation and ploidy.

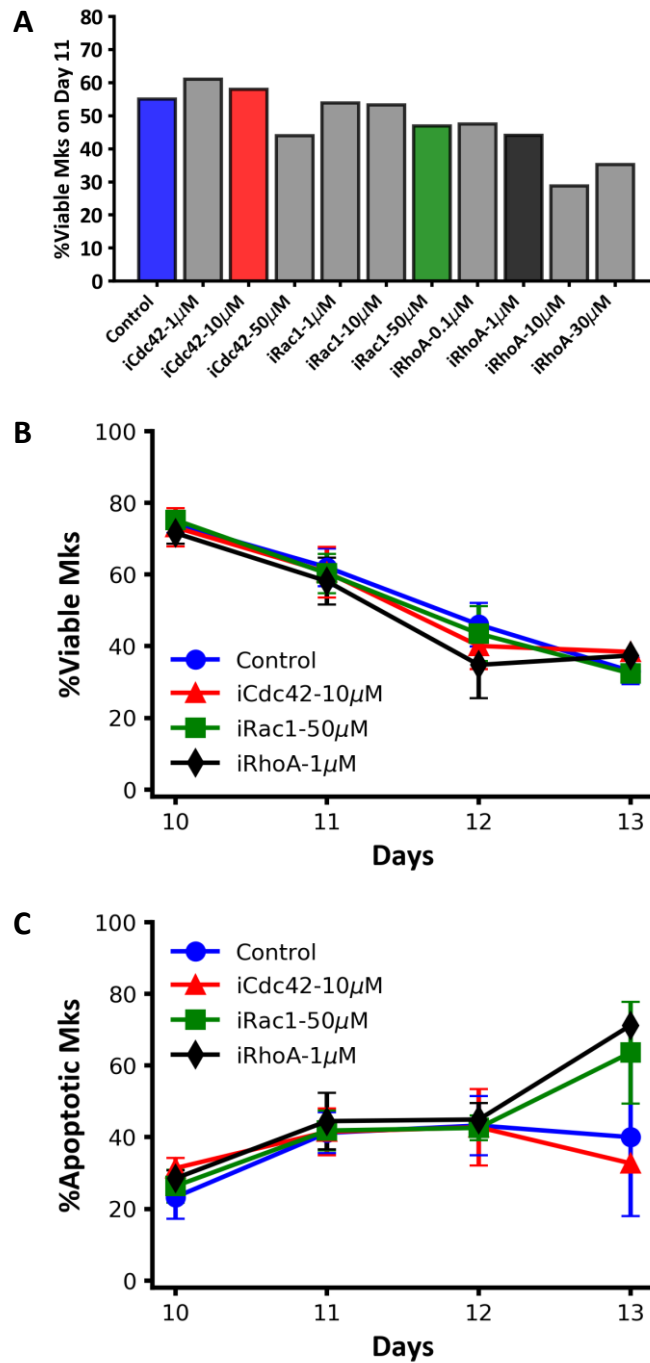


Figure 6.1 Screening GTPase inhibitor concentrations seeded on Day 9. (A) Viability of Mks on Day 11 across different inhibitor concentrations for a single donor. Time course

profiles of (B) viability and (C) apoptosis. For (B) Day 10: Control n =5, iCdc42 n = 3, iRac1 n = 4, iRhoA n = 3; Day 11: Control n =7, iCdc42 n = 5, iRac1 n = 6, iRhoA n = 6, Day 12: Control n =5, iCdc42 n = 3, iRac1 n = 4, iRhoA n = 4; Day 13: Control n =2, iCdc42 n = 1, iRac1 n = 2, iRhoA n = 1. For (C) Day 10: Control n =3, iCdc42 n = 2, iRac1 n = 3, iRhoA n = 2; Day 11: Control n =5, iCdc42 n = 4, iRac1 n = 5, iRhoA n = 4; Day 12: Control n =4, iCdc42 n = 3, iRac1 n = 3, iRhoA n = 3; Day 13: Control n =2, iCdc42 n = 1, iRac1 n = 2, iRhoA n = 1. Points = +/- SEM.

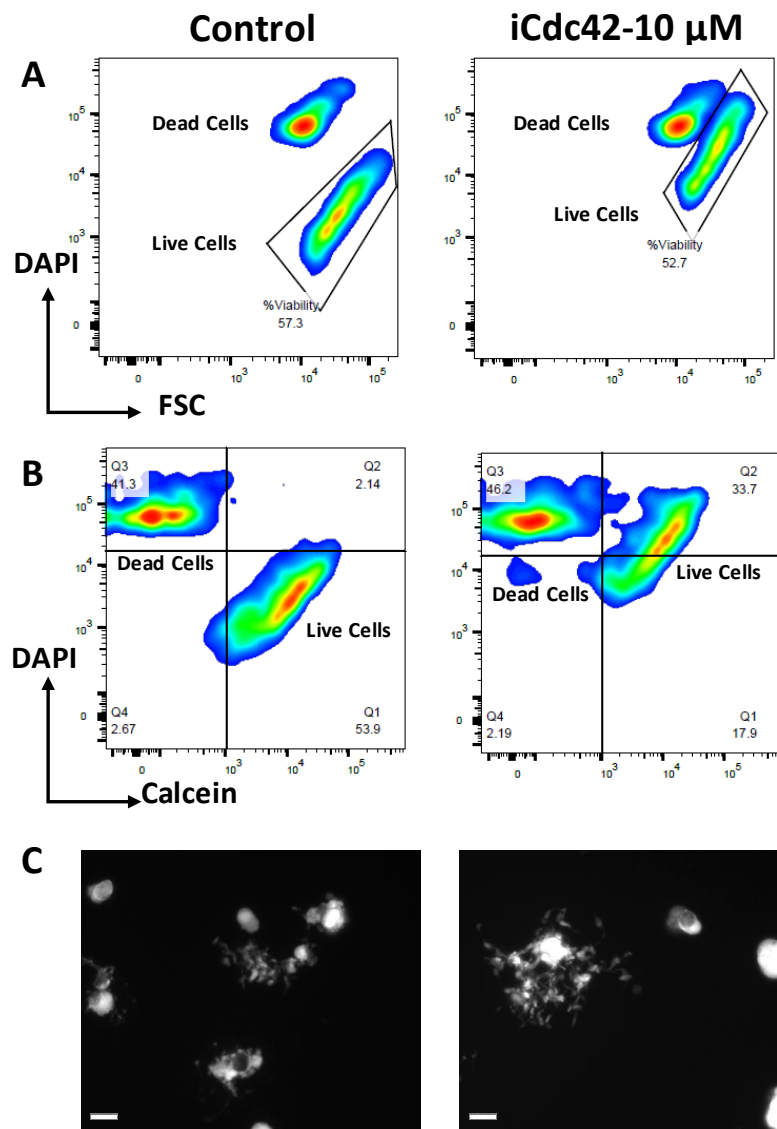


Figure 6.2 Inhibition of Cdc42 with ML141 impacts DAPI uptake. (A) DAPI versus forward scatter and (B) DAPI versus Calcein plots for control and iCdc42-10 μ M showing a shift up in DAPI fluorescence for iCdc42-10 μ M. (C) Image of Calcein AM stained Mks for both control (left) and iCdc42-10 μ M (right). Scale bar = 15 μ m.

6.3.2 proPLT formation is dependent on Rac1 but not Cdc42 or RhoA

Time profile of the percentage of Mks displaying proPLTs showed that iRac1-50 μ M was the lowest among all the conditions (**Figure 6.3A**). No appreciable difference in proPLT formation was observed for iCdc42-10 μ M or iRhoA-1 μ M. For all the conditions there was an increase in proPLTs into Days 12 and 13. Images of conditions on Day 12 are shown in **Figure 6.3B** with control, iCdc42-10 μ M and iRhoA-1 μ M displaying proPLTs, but little to no proPLT formation in iRac1-50 μ M. Confocal analysis of Mks from the conditions indicated characteristic proPLT formation in control, iCdc42-10 μ M and iRhoA-1 μ M (**Figure 6.3C**).

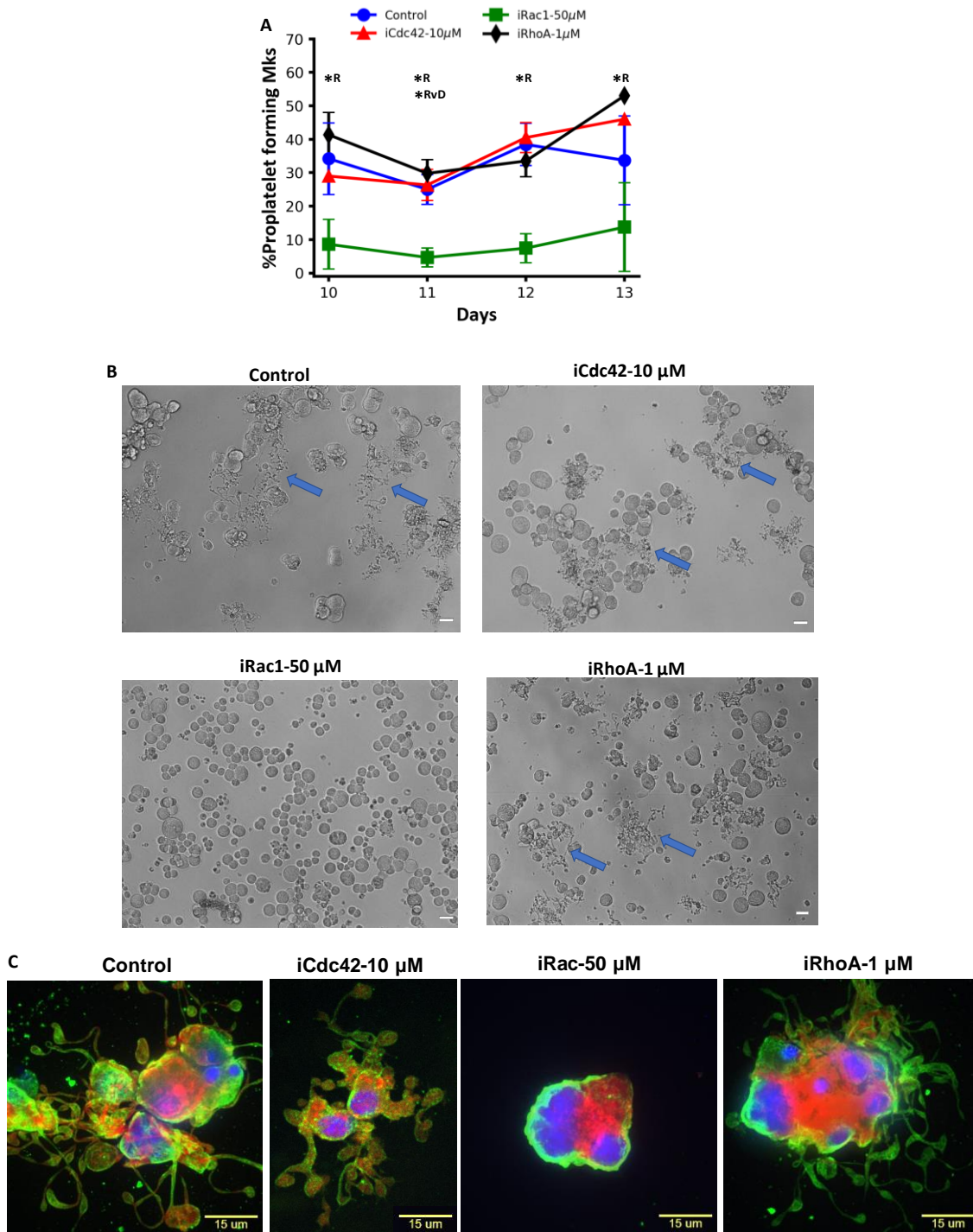


Figure 6.3 Analysis of proplatelet formation of inhibitor conditions. (A) Time course profile of percentage of Mks forming proPLTs. (B) Brightfield images of conditions on Day

12 with blue arrows pointing to proPLTs. (C) Confocal images of Mks from each condition, red = actin, green = beta-tubulin, blue = DNA. Scale bars = 15 μm . For Controls versus iRac1-50 μM : *R, $p < 0.05$. For iRac1-50 μM versus iCdc42-10 μM : *RvD, $p < 0.05$. Day 10: Control n =4, iCdc42 n = 1, iRac1 n = 2, iRhoA n = 3; Day 11: Control n =8, iCdc42 n = 3, iRac1 n = 5, iRhoA n = 5; Day 12: Control n =5, iCdc42 n = 2, iRac1 n = 3, iRhoA n = 4; Day 13: Control n =2, iCdc42 n = 1, iRac1 n = 2, iRhoA n = 1. Points = +/- SEM.

6.3.3 Evaluating reversibility of Rac1 inhibition on proPLT formation

Next, we were interested in reversing the negative inhibition of proPLT formation from the iRac1-50 μ M condition. Mks were seeded on Day 9 of culture and after 24 hrs (iRac1-50 μ M-W10) or 48 hrs (iRac1-50 μ M-W11), the media was replaced with fresh media without the Rac1 inhibitor, NSC23766. By Day 11, Mks previously exposed to NSC23766 were making proPLTs and by Day 12, iRac1-50 μ M-W10 and control had similar percentages of Mks making proPLTs (**Figure 6.4**). iRac1-50 μ M-W11 started to show increased proPLT formation as well by Day 13 though it remained lower than control and iRac1-50 μ M-W10. Based on this single experiment, the inhibition on proPLT formation could be reversed with media replacement after short exposure time.

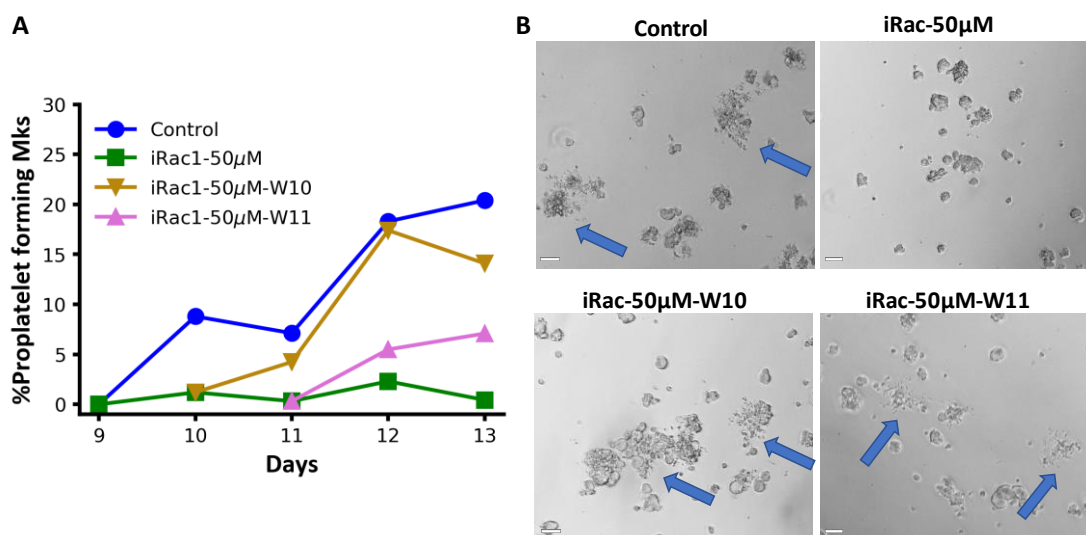


Figure 6.4 Analysis of proplatelet formation of washed Rac1 inhibitor conditions. (A) Time course profile of percentage of Mks forming proPLTs. (B) Brightfield images of conditions on Day 12 with blue arrows pointing to proPLTs. Scale bars = 30 μ m.

6.3.4 Inhibition of Rac1, Cdc42 or RhoA does not significantly impact ploidy levels in Mks

After seeding the conditions on Day 9, ploidy was measured from Days 10-13. The %high-ploidy (>4N) Mk fraction was not significantly different for all conditions (**Figure 6.5A**). iRac1-50 μ M displayed overall constant %high-ploidy across the days whereas iCdc42-10 μ M and iRhoA-1 μ M peaked on Day 11 and then dropped into Days 12 and 13 (**Figure 6.5A**). The control condition also displayed a drop in %high-ploidy into Day 13. The mean ploidy of Mks in iRhoA-1 μ M and iCdc42-10 μ M was significantly higher than the control on Day 11 and 12, respectively (**Figure 6.5B**). The distribution of ploidy levels on Day 11 remained largely unchanged across the conditions (**Figure 6.5C**).

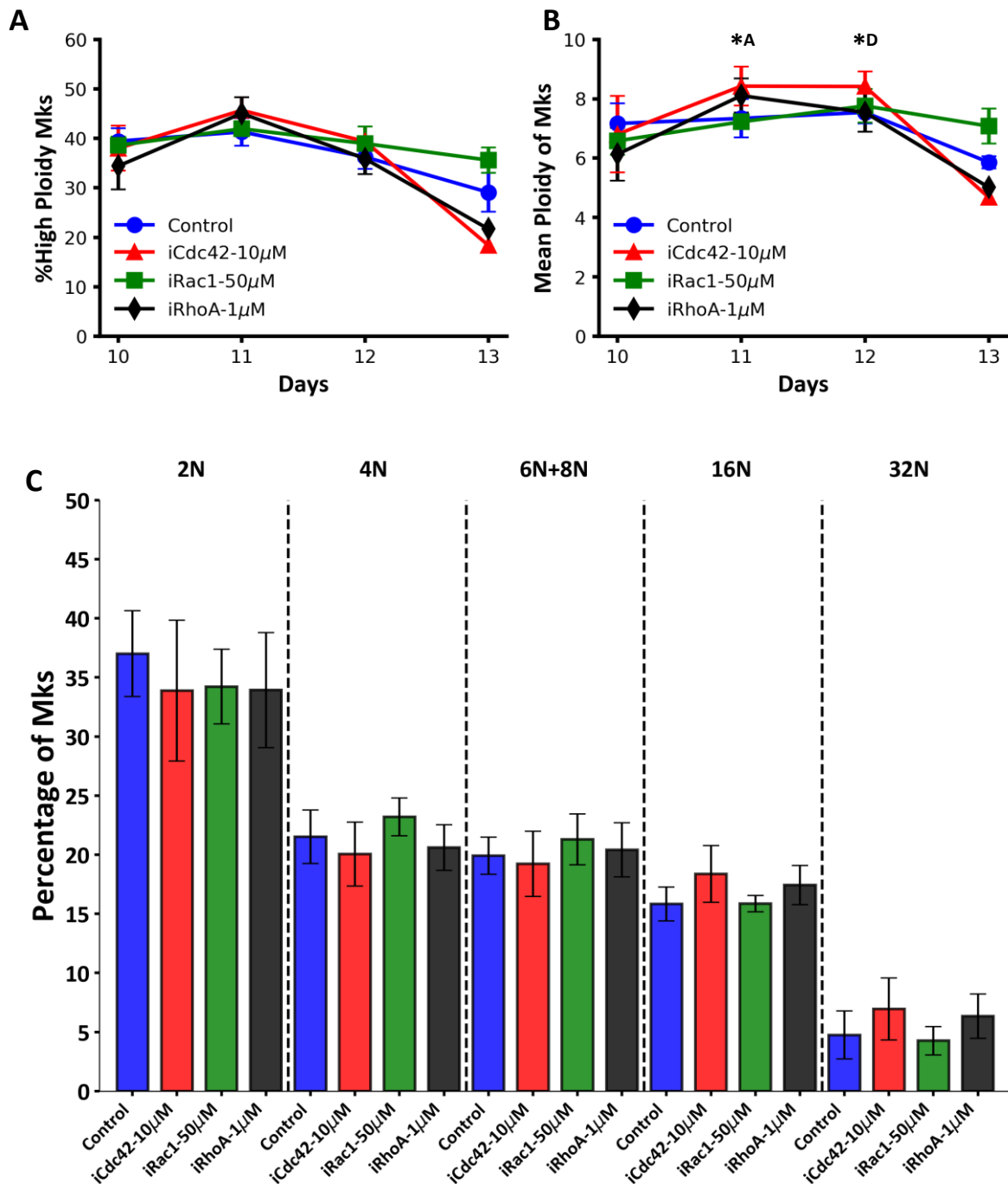


Figure 6.5 Ploidy analysis of inhibitor conditions. Time course profile of (A) %high-ploidy (> 4N) Mks and (B) mean ploidy. (C) Distribution of ploidy levels for Day 11 for all

the conditions. For Controls versus iRhoA-1 μ M: *A, $p < 0.05$. For Controls versus iCdc42-10 μ M: *D, $p < 0.05$. Day 10: Control n = 4, iCdc42 n = 3, iRac1 n = 3, iRhoA n = 4; Day 11: Control n = 5, iCdc42 n = 4, iRac1 n = 4, iRhoA n = 5; Day 12: Control n = 6, iCdc42 n = 5, iRac1 n = 5, iRhoA n = 6; Day 13: Control n = 1, iCdc42 n = 1, iRac1 n = 1, iRhoA n = 1. Points and bars = +/- SEM.

6.3.5 Combined inhibition of Rac1 and Cdc42 increases ploidy of Mks but with reduced proPLT formation

From previous results, inhibition of Rac1 significantly reduced proPLT formation and inhibition of Cdc42 improved the mean ploidy. Downstream of Rac1 and Cdc42 is Pak2 and inhibition of Pak2 led to higher ploidy mouse Mks but diminished proPLT formation.[74] We hypothesized that a dual inhibition (iRac1+iCdc42) approach may improve the ploidy of our human Mk cultures. Control cultures and iRac1+iCdc42 conditions had similar viability profiles (**Figure 6.6A**). For the same donor, iRac1+iCdc42 proPLT formation remained lower than control and iCdc42-10 μ M but was similar to iRac1-50 μ M up until Day 12 (**Figure 6.6B**) when characteristic proPLTs were observed (**Figure 6.6C, D**). Comparing individual inhibition of Rac1 and Cdc42 to iRac1+iCdc42 for the same donor, the %high-ploidy Mks was the highest on Day 11 for iRac1+iCdc42 indicating an additive effect (**Figure 6.6E**). For three donors, the %high-ploidy was significantly higher on Day 11 for iRac1+iCdc42 versus the controls and remained higher over time (**Figure 6.6F**). The mean ploidy was also highest at Day 11 (**Figure 6.6G**). Confocal images revealed large non-round polyploid Mks (**Figure 6.6H**). The ploidy distribution on Day 11 indicated that

iRac1+iCdc42 cultures had significantly lower percentages of 2N Mks and an increase in 16N Mks (**Figure 6.6I**). These experiments showed that dual inhibition was more efficient at increasing the ploidy of the cultures versus single inhibition conditions.

Effectors downstream from Rac1 and Cdc42 interact with the Arp2/3 complex and inhibition of Arp2/3 in mouse Mks has been shown to increase proPLT formation.[137] We were interested in understanding the impact of inhibition of Arp2/3 on human mPB Mks as well. Overall, viability of iArp2/3-0.5 μ M was similar to control (**Figure 6.7A**). There was an increase in the fraction of proPLT forming-Mks compared to controls (**Figure 6.7B**) and Mks displayed normal proPLT formation (**Figure 6.7C, D**). %High-ploidy Mks and mean ploidy on Day 11 was slightly higher for iArp2/3-0.5 μ M than controls (**Figure 6.7E, F**).

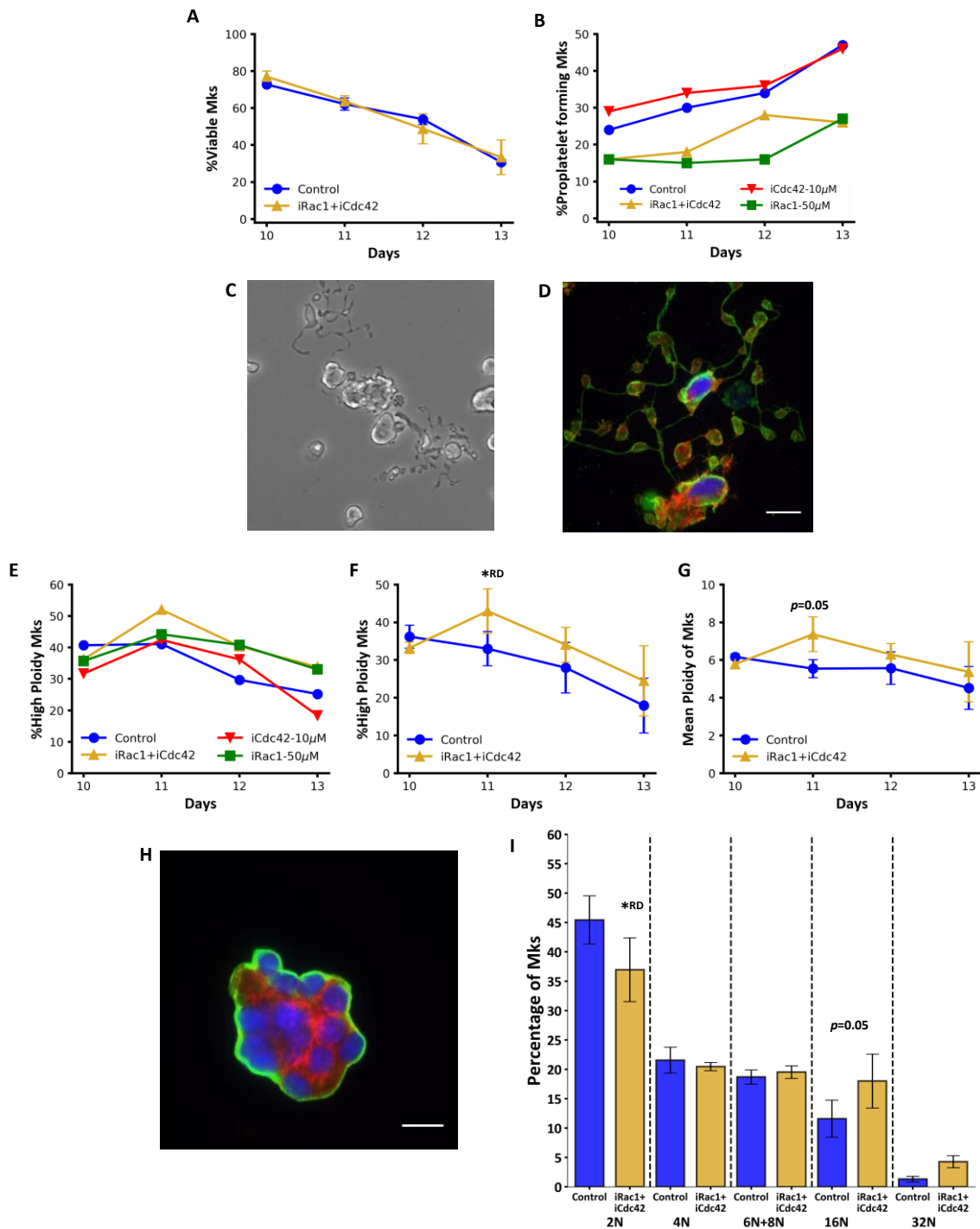


Figure 6.6 Dual inhibition of Rac1 and Cdc42 increased Mk ploidy. Time course profile of (A) viability and (B) percentage of Mks forming proPLTs. (C) Brightfield images of

iRac1+iCdc42 on Day 12. (D) Confocal images of proPLTs in iRac1+iCdc42. (E, F) Time course profile of %high-ploidy (> 4N) Mks. (G) Mean ploidy of Mks. (H) Confocal images of large Mk in iRac1+iCdc42. (I) Distribution of ploidy levels for Day 11. For confocal images, red = actin, green = beta-tubulin, blue = DNA. For Controls versus iRac1+iCdc42: *RD, $p < 0.05$. For (A, F, G, I) $n = 3$, (B, E) $n = 1$, (E) $n = 1$. Scale bars = 10 μm . Points and bars = +/- SEM.

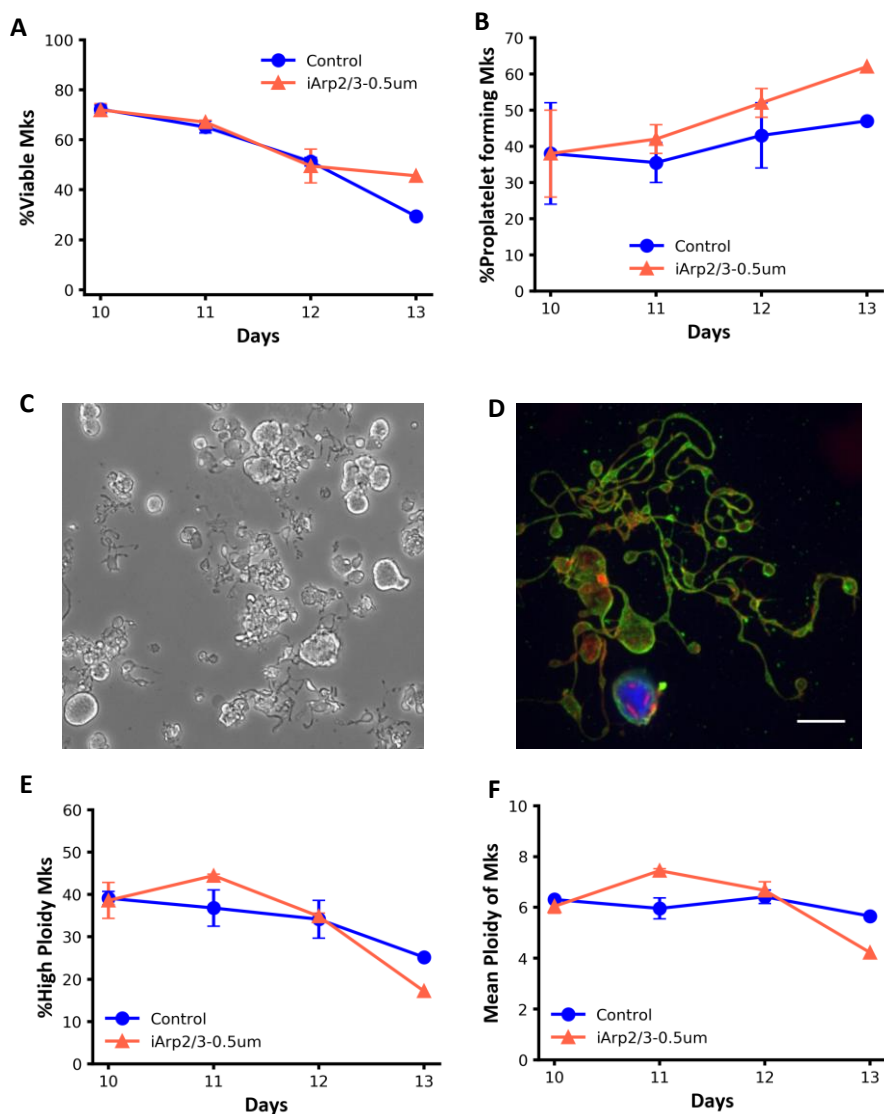


Figure 6.7 Analysis of inhibition of Arp2/3 on Mks. Time course profile of (A) viability and (B) percentage of Mks forming proPLTs. (C) Brightfield images of iArp2/3-0.5μM on Day 12. (D) Confocal images of proPLTs in iArp2/3-0.5μM, red = actin, green = beta-tubulin, blue = DNA. Time course profile of (E) %high-ploidy (> 4N) Mks and (F) mean ploidy of Mks. n = 2 for all points except n = 1 for Day 13. Scale bars = 10 μm. Points = +/- SEM.

6.3.6 Evaluating platelet-like-particle generation from inhibited conditions

Lastly, we were interested in evaluating the PLP generation from selected conditions: iRac1+iCdc42, iRhoA-1 μ M, iArp2/3-0.5 μ M and controls. As noted above, the dual iRac1+iCdc42 condition appeared to increase the %high-ploidy Mks and iArp2/3-0.5 μ M trended towards higher proPLT formation. iRhoA-1 μ M on average increased the mean ploidy of Mks. First, we subjected Mks to shear forces using our published uniform shear rate bioreactor, USB-7 μ m.[76] Mks are trapped at 7- μ m slits mimicking the endothelial cell gaps or fenestrations and extend proPLTs past the slits. Within the device, we observed Mks making proPLTs and releasing individual PLPs across all the conditions (**Figure 6.8**) as has been described in our published study.[76]

Next, we analyzed the bioreactor effluents for Calcein⁺CD41⁺CD42b⁺ PLPs (**Figure 6.9**). The control and iArp2/3-0.5 μ M had similar percentages of viable Calcein⁺CD41⁺CD42b⁺ PLPs at ~70% and iRhoA-1 μ M the highest at ~83%. Interestingly, the dual inhibition condition, iRac1+iCdc42, had the lowest percentage of viable particles at ~48%. Confocal analysis of the collected PLPs from all conditions showed a characteristic tubulin ring in the absence of thrombin and that upon activation with thrombin, particles spread over fibrinogen (**Figure 6.10**), similar to the behavior of blood platelets.[42]

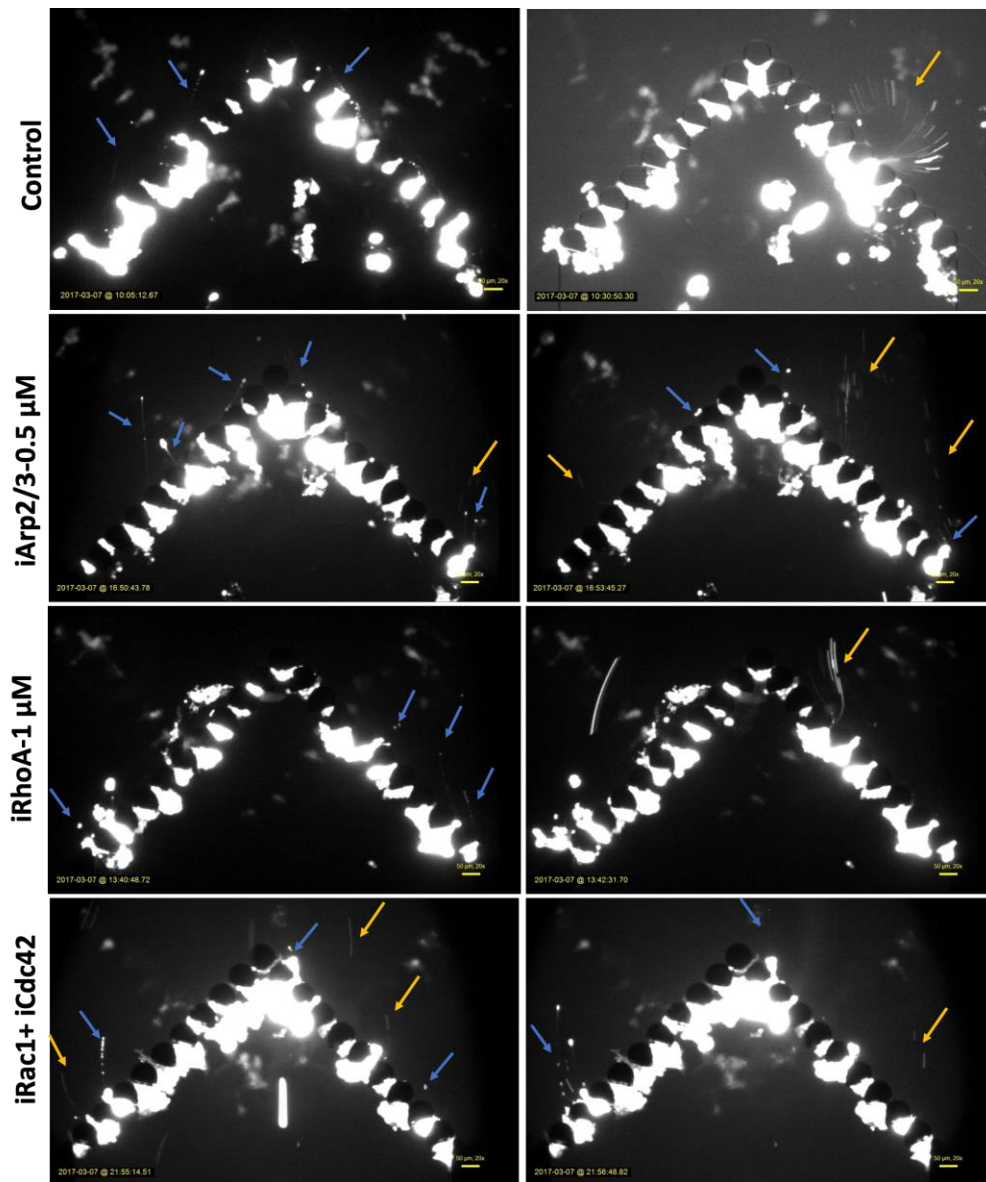


Figure 6.8 Analysis of proPLT and PLP generation from inhibitor conditions in bioreactor. Calcein stained Mks on Day 12 for control, iArap2/3-0.5 μM , iRhoA-1 μM and iRac1+iCdc42. (iRac at 50 μM and iCdc42 at 10 μM). Blue arrows = proPLTs and yellow arrows = PLPs. Center channel flow rate = 1.5 $\mu\text{L}/\text{min}$ and combined outside flow = 0 $\mu\text{L}/\text{min}$.

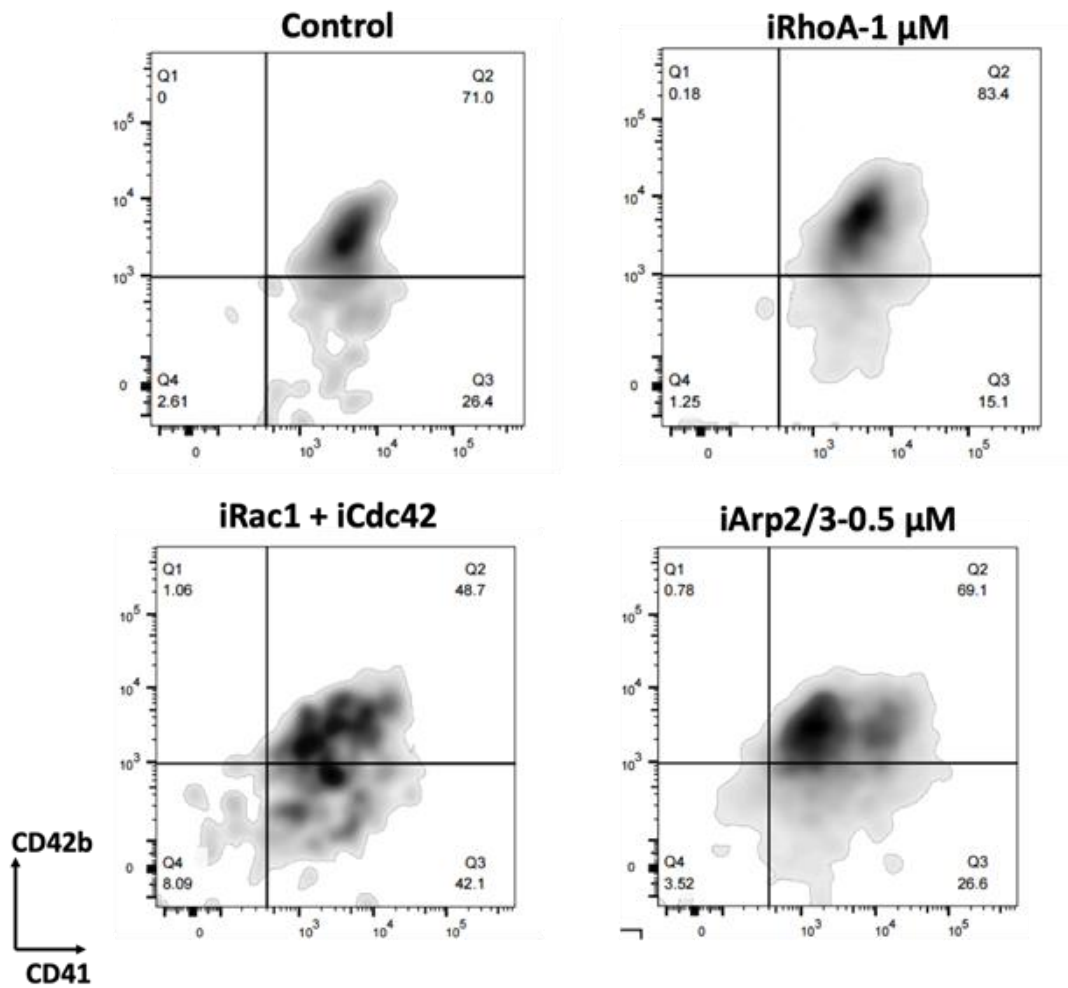


Figure 6.9 Analysis of PLPs collected from inhibitor conditions from bioreactor.

Calcein⁺PLPs were gated and then CD42b vs. CD41 flow plots were analyzed for Day 12 bioreactors for control, iArp2/3-0.5 μ M, iRhoA-1 μ M and iRac1+iCdc42. (iRac at 50 μ M and iCdc42 at 10 μ M).

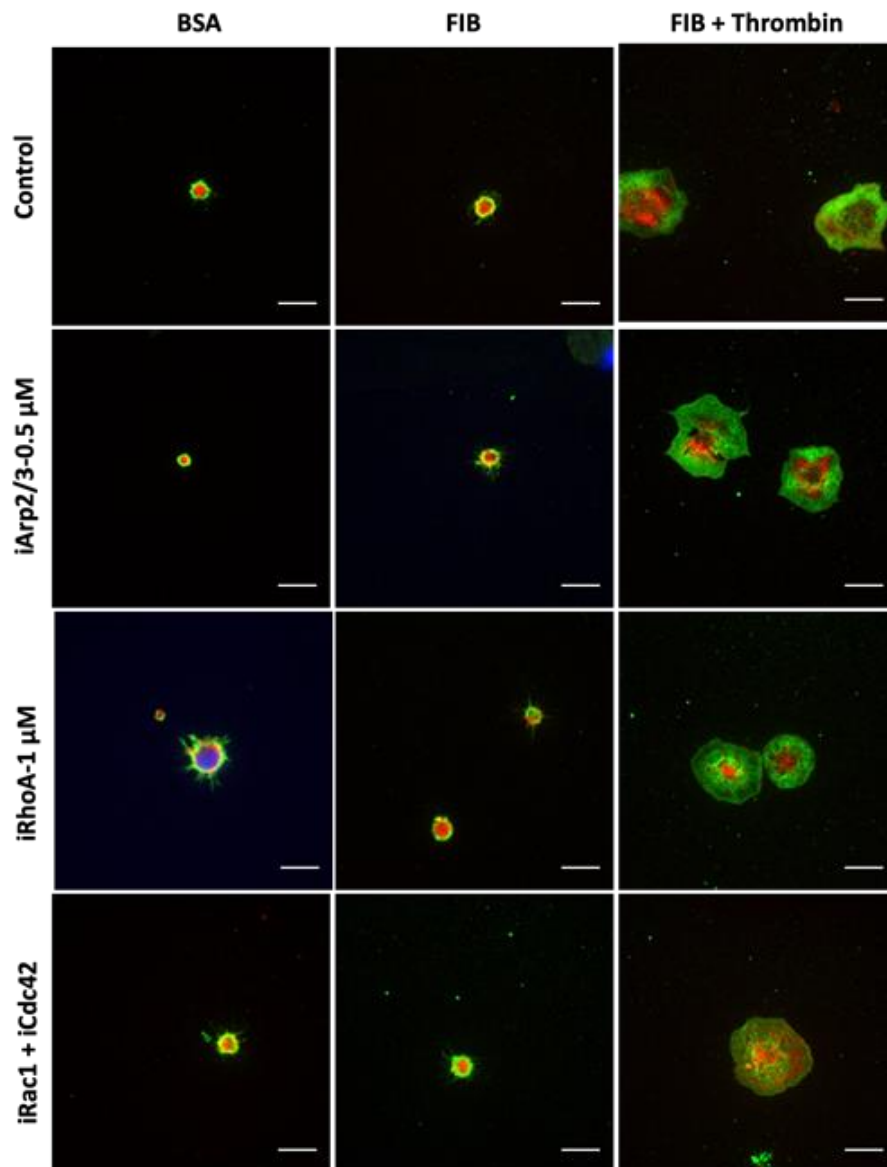


Figure 6.10 Confocal analysis of collected PLPs from inhibitor conditions from **bioreactor**. Images of PLPs on BSA, fibrinogen and fibrinogen + thrombin for collected bioreactor PLPs on Day 12 for control, iArp2/3-0.5μM, iRhoA-1μM and iRac1+iCdc42. (iRac at 50 μM and iCdc42 at 10 μM). Red = actin, green = beta-tubulin, blue = DNA. Scale bars = 10 μm.

Finally, to estimate PLP-yields, we used an orbital shaker to process a larger number of Mks. After the respective inhibitors were added on Day 9, the conditions were shaken and sampled on Day 12. For one donor, the %CD41⁺CD42b⁺ PLPs was ~25% for both control and iArp2/3-0.5 μ M. It was substantially lower for iRhoA-1 μ M and iRac1+iCdc42 at ~12% (**Figure 6.11A**). The estimated PLP-yield per seeded Mk was low for all conditions but iArp2/3-0.5 μ M and iRhoA-1 μ M were higher than the control and iRac1+iCdc42 had the lowest production (**Figure 6.11B**). We then decided to analyze iArp2/3-0.5 μ M and iRhoA-1 μ M for an additional three donors. These two conditions had similar %CD41⁺CD42b⁺ PLPs as the control (**Figure 6.12A**), however, PLPs produced per seeded Mk was on average higher in the controls (**Figure 6.12B**).

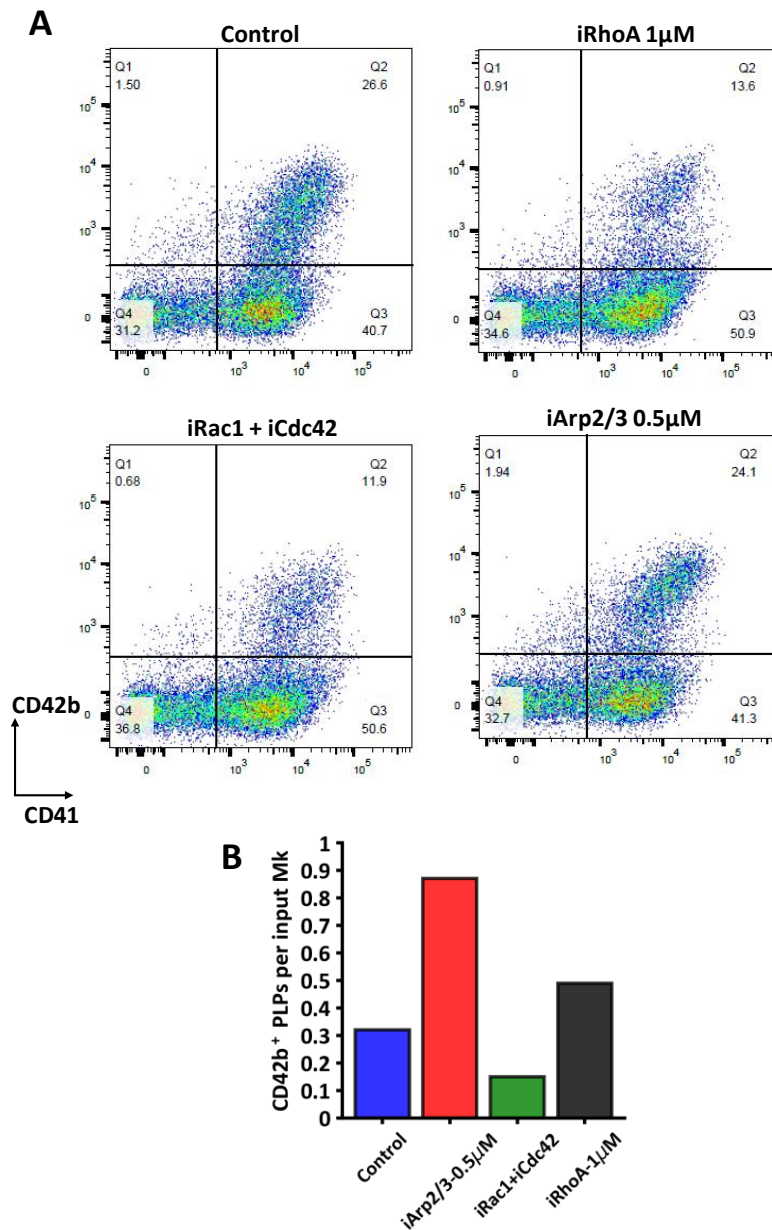


Figure 6.11 Analysis of PLPs collected from inhibitor conditions from orbital shaker.

(A) CD42b vs. CD41 flow plots of PLPs collected from orbital shaker. (B) Estimated PLP yields per seeded Mk for control, iArp2/3-0.5µM, iRhoA-1µM and iRac1+iCdc42. (iRac at 50 µM and iCdc42 at 10 µM). Results for single donor.

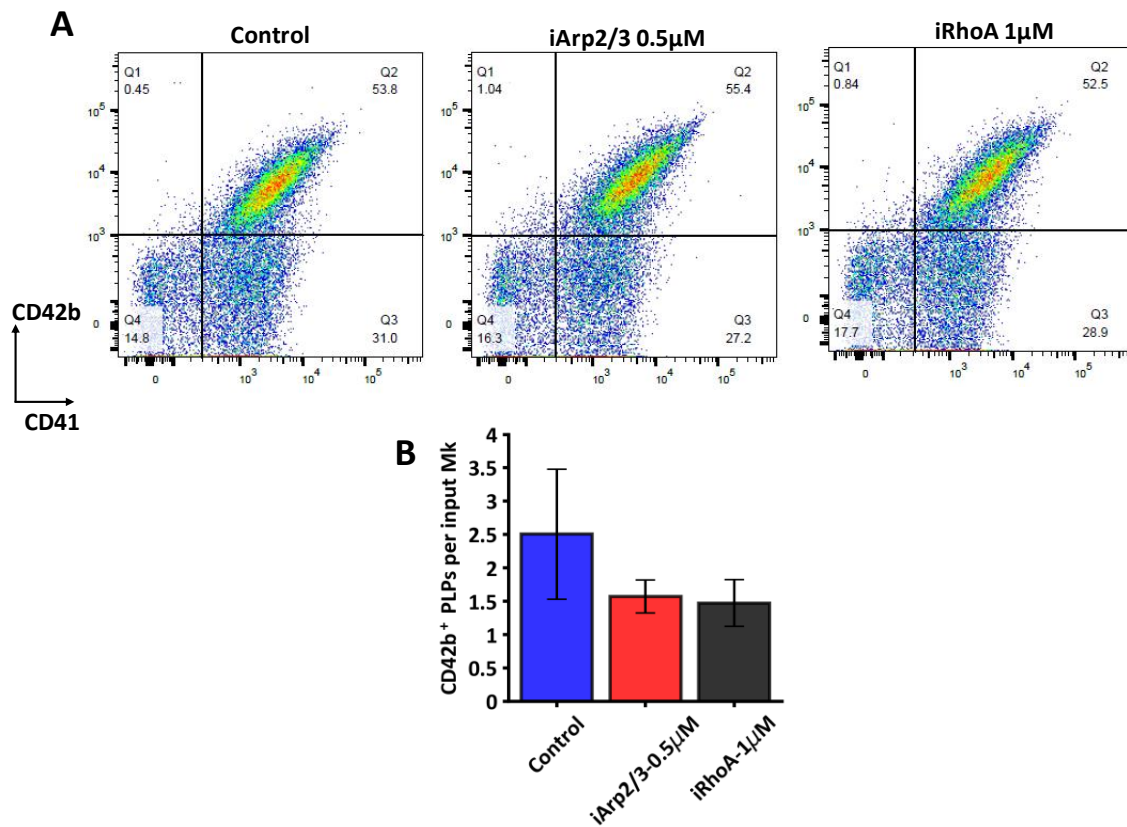


Figure 6.12 PLPs collected from inhibited Arp2/3 and RhoA conditions from orbital shaker. (A) CD42b vs. CD41 flow plots of PLPs collected from orbital shaker. (B) Estimated PLP yields per seeded Mk for control, iArp2/3-0.5µM and iRhoA-1µM. $n = 3$. Bars = +/- SEM.

6.4. Discussion

In these studies, we aimed to understand the impact of pharmacological inhibition of RhoA, Rac1 and Cdc42 GTPases with the goal of enhancing aspects of Mk culture to improve platelet yields. The selected inhibitors have been used before with mouse Mks and fresh blood platelets but not investigated *in vitro* with human Mks. After selecting inhibitor concentrations based on impact to Mk culture viability, we investigated exposure of Mks to these inhibitors and their effect on ploidy levels, proPLT formation and particle generation. The selected inhibitor concentrations were also within ranges tested *in vitro*. [29,135,136] An interesting observation from our viability studies was that Cdc42 inhibition with ML141 led to a shift in DAPI uptake for Mks while retaining Calcein and thus appearing as viable cells. We are not aware of other reported studies using ML141 with a similar observation on viability of cells. Since studies involving knockout of Cdc42 interacting protein, CIP4, which interacts with activated Cdc42, resulted in a more rigid plasma membrane and softer cell cortex [138], we speculate that changes to the Mk membrane might allow DAPI to enter the cell and/or not be pumped out of the cells efficiently.

Conditional knockout of Cdc42 in bone marrow(BM)-derived mouse Mks was reported to reduce proPLT formation *in vitro*. [65] In the same study, conditional knockout of Rac1 did not impact proPLT formation. In contrast, our results using human mPB-Mks showed that inhibition of Cdc42 with 10 μ M of ML141 did not impact proPLT formation, but inhibition of Rac1 with 50 μ M of NSC23766 nearly abolished proPLT formation. Our results are supported by reported low proPLT formation of mouse Mks in the presence of NSC23766

at 50 μM . [29] The removal of Rac1 inhibitor NSC23766 from treated Mks appeared to re-start proPLT formation, though removing the inhibitor too late in culture still led to low number of Mks making proPLTs. Interestingly, the use of ML141 on BM-mouse Mks showed a negative impact to proPLT formation that was not seen in our studies. [135] Differences between our results and published studies could be attributed to the cell-source, mice vs. human, and knockout models vs. pharmacological inhibition. Other studies have instead used the inhibitor CASIN for Cdc42 studies. [135,139] Notably, a recent study that used CASIN on mPB-derived Mks reported reduced proPLT formation. [140]

Using a conditional double knockout of Cdc42 and Rac1 significantly reduced proPLT formation compared to single knockouts in BM-mouse Mks. [65] Additionally, pharmacological inhibition of Pak2 (a downstream effector of both Rac1 and Cdc42) or a knockout model of Pak2 significantly reduced proPLT formation in BM-mouse Mks. Our double inhibition studies of Rac1 and Cdc42 had lower proPLT formation than single inhibition of Cdc42 and controls but was similar to Rac1 single inhibition. Another factor downstream of Rac1 and Cdc42 is the Arp2/3 complex and its inhibition with CK-636 in mouse Mks improved proPLT formation. [137] Though we did not observe a significant increase in proPLT formation with CK-636 on human mPB-Mks, these cultures tended to have higher proPLT formation than controls.

In our studies, RhoA inhibition with Rhosin did not increase proPLT formation. Previous studies of inhibition of RhoA with small molecule Tat-C3 slightly increased proPLT

formation but inhibition of RhoA's downstream effector ROCK with Y-27362 increased proPLT formation of mPB-Mks near 2-fold in static cultures.[58] Therefore, directly targeting RhoA activity with inhibitors may not be an effective way to improve proPLT formation and rather targeted downstream inhibition of effectors may be more productive.

Only dual inhibition of Rac1 and Cdc42 led to improved %high-ploidy Mks compared to control. Although single and double knockout of Rac1 and Cdc42 in mouse Mks did not change ploidy[65], inhibition of downstream effector Pak2 led to higher ploidy mouse Mks[74] supporting our observations. Based on previous studies, we expected RhoA inhibition to increase polyploidization but did not see a significant change to the treated Mks. Interestingly, one study delivered the RhoA inhibitor Tat-C3 through electroporation into Mks and reported a significant increase in Mk ploidy[16]. Additionally, the use of ROCK inhibitor Y-27362 on mPB-Mks and cord blood-derived Mks also increased ploidy levels.[16,19]

These Rho GTPases are also highly involved in platelet function.[141] Platelets generated from mouse Mks lacking RhoA spread normally on fibrinogen upon thrombin addition but had deficiency in clot formation.[142] Platelets from Cdc42 conditional knockout study in mice were able to normally spread on fibrinogen in the presence of thrombin [65] but other mouse studies showed limited spreading and reduced secretion of alpha and dense granules.[143] Conditional knockout of Rac1 in mouse Mks created platelets that were not able form lamellipodia or spread on fibrinogen after thrombin addition [65,69] and inhibition

with NSC23766 in mouse platelets also impacted secretion but had no impact on platelet counts.[144] Though our confocal analysis of PLPs collected from the bioreactor showed characteristic spreading on fibrinogen in the presence of thrombin, further studies should be conducted such as aggregation studies and flow cytometry activation assays to understand potentially negative impacts of exposure of Mks to these inhibitors prior to PLP generation. However, based on our experiments none of the inhibitor conditions tested improved PLP-yield per seeded Mk after shaking for numerous days.

It is important to note that most likely there is cross-talk between RhoA, Cdc42 and Rac1 and even some redundancy.[145] A recent study demonstrated that RhoA and Cdc42 activity is closely linked during terminal proPLT formation stages.[146] Future studies should also provide data on levels of GTP-bound GTPases to see if inhibition of a single GTPase is affecting the activity levels of the others. Additionally, measuring the GTP-bound levels of the targeted GTPase will allow one to understand if their activity in Mks can be substantially altered with pharmacological inhibition. Our studies indicate that the results between reported knockout models and pharmacological inhibitions at times do not agree. Even though we observed lower Mk viability at higher inhibitor concentrations, a more in-depth dose-response analysis may provide additional insight. Finally, differences in results between commercially available inhibitors and methods of delivery should also be considered moving forward.[16,135,147] The lack of PLP yield improvements through attempts to increase proPLT formation or ploidy in our Mk cultures with a targeted high-

level inhibition of cytoskeletal regulators further underlines our gaps in understanding platelet biogenesis.

6.5 Acknowledgements

This research was supported by NSF grant CBET-1265029. Andres Martinez was supported in part by NIH Predoctoral Training Grant T32 GM008449. We acknowledge the use of the Micro/Nano Fabrication Facility (NUFAB), Flow Cytometry Core Facility, and Biological Imaging Facility (BIF) at Northwestern University. We thank Kathleen Jenkins, Vasil Kukushliev and Damien Doser for assistance with several experiments.

CHAPTER 7: Conclusions and recommendations

7.1 CHAPTERS 2-4: Microfluidic bioreactors to study proPLT and PLP formation

In Chapters 2 and 3, I described our uniform shear rate bioreactor (USRB-7um), performed computational fluid dynamics modeling (CFD) and experimentally showed that environmental factors can influence Mk productivity. Using the findings from Chapters 2 and 3, we engineered the USRB-5um (Chapter 4) to improve the capture efficiency of cord blood-derived (CB) Mks and evaluated different cultures and their impact to PLP production. Additionally, we took steps to scale up the bioreactors to the lung-USRB (Chapter 4) and performed proof of concept studies to show the potential of the system.

The microfluidic systems presented in this work can serve as characterization tools but there are limitations and challenges in further scaling up these microfluidic systems. Improving the Lung-USRB microfluidic with numerical modeling and simulations and improved construction is crucial [91,92]. A re-designed network should mitigate non-uniform environments we observed. Best practices of microfluidic designs have led to increased cell number capacities nearing 10^7 cells, controlled environments with automation, stacking of multiple networks and incorporating temporal gradients.[148-150] Therefore, a focused strategy on developing techniques, designs and processes can deliver platelet microfluidic bioreactors with *in vivo* physiological attributes and I believe this is achievable.

We have seen that after the flow has stagnated using syringe pumps and Mk productivity is low, tapping the Lung-USRB jostled the Mks trapped at the slits and restarted PLP

generation (**Figure 7.2**). With these observations, we could use a peristaltic pump to oscillate the flow in the system when stagnation occurs. This would lead to controlled method of restarting PLP generation and a closed-loop system in which a reservoir of Mks are continuously processed.

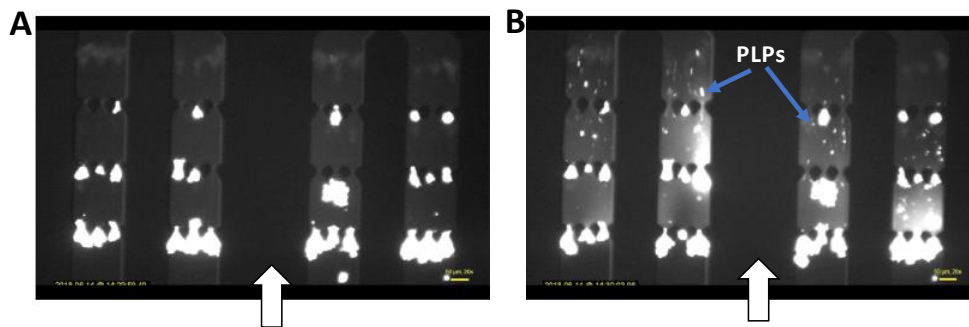


Figure 7.1 Restarting Mk productivity in stagnated environments in Lung-USRB. (A) Calcein-labeled Mks at the slits show little PLP activity. (B) After tapping the bioreactor, PLP generation restarts. White arrow = direction of flow. Scale bar = 50 μm . Flow rate = 40 $\mu\text{L}/\text{min}$.

There could still be a limitation on the number of cells that can be processed in microfluidic systems and so assessing other technologies to generate PLPs is necessary. A recent approach to generating large numbers of PLPs from iPSC-derived Mks used a reciprocating blade bioreactor to impart shear and turbulent energy on Mks.[51] This system could be explored with mPB or CB-Mks.

7.2 CHAPTER 5: Improving megakaryocyte yields with G-Rex surfaces and fed-batch dilutions

In Chapter 5, we developed a new culture process (G40D) that utilizes the G-Rex technology during the first phase of our culture as well as media dilutions to significantly improve Mk yield per input CD34⁺ cell.[97] This new process has great potential and there are numerous areas of optimization and understanding highlighted below.

We should focus on further increasing the number of Mk progenitors. As described in the chapter, higher G-Rex seeding densities led to greater Mk progenitor numbers by mid culture. Screening studies with high densities ($> 100 \times 10^3$ cells/cm²) also supported these results but retaining the cells too long in the G-Rex (until Day 7) at high densities led to lower Mk numbers. The new protocol retains the cells in the G-Rex until Day 5 only. Exploring the upper limit of seeding-cell densities is highly recommended. We could also use more hypoxic conditions during the first 5 days (near 0% O₂) to achieve lower oxygen tension near the cells resting on the silicon membrane in the G-Rex.

Re-visiting our cytokine strategy is recommended to take advantage of the expansion potential of increased Mk progenitors. We should perform a factorial analysis of cytokine concentrations as was executed by our lab previously.[42] Specifically, we should focus on IL-3 levels since IL-3 has been shown to promote expansion of Mk progenitors.[110,111] However, there have been studies that suggest IL-3 could impact Mk maturation.[98,151,152] G40D conditions showed ~50% more high-ploidy Mk numbers per

input CD34⁺ cell compared to controls. Therefore, polyploidization wasn't impacted, but other potential negative should be considered in the future.

Our culture generates a heterogenous population of Mks. Reports have indicated that there are two different populations of Mk progenitors and that one is responsive to IL-3 for proliferation.[153] Our experiments with late media removal or lack of IL-3 support this as the total number of Mks was diminished compared to media dilutions with IL-3. Thus, gathering additional information on these IL-3-dependent Mks, which may be immature, will be highly beneficial. A cell-sorting strategy would first use ploidy levels to isolate 2N/4N Mks since diluted conditions have higher numbers of these Mks. Then to isolate immature Mks, we could use the uptake of fluorescently labeled coagulation factor-V by mature Mks.[96] The two populations could be then be compared based on structural analysis through TEM, transcription factor analysis or proteomics.[154]

An observation from our G-Rex and dilutions studies was that lower %high-ploidy cultures were generated due to higher 2N and 4N Mk numbers. Interestingly, nicotinamide addition appeared to have minimal effect on these smaller Mks. Therefore, we could explore other factors that can promote polyploidization. Studies have already identified potential molecules to use such as Src kinase inhibitor (SU6656) and a Rho-associated kinase inhibitor (Y27632)[19,123]. Additionally, these studies could be carried out with the pharmacological inhibitors of the Rho GTPases described in Chapter 6.

Finally, mechanistic studies on the retention of CD34 on cells within G-Rex high density conditions are recommended. The concentration of secreted soluble factors could be measured using a Human Cytokine 30-Plex panel from Invitrogen or other ELISA kits as has been used in previous media dilution studies of HSPCs.[108] Thus, we could understand if the retention of CD34 is driven by an autocrine/paracrine response or if it is due to cell-cell contact. The concentration of these soluble factors could be measured at later stages of the process as well. This approach would also allow us to measure any inhibitory cytokines and factors secreted by the cells.

7.3 CHAPTER 6: Increasing ploidy, proPLTs and PLPs by targeting cytoskeletal signaling pathways of Rho GTPases

In this study, we focused on using reversible pharmacological inhibitors for RhoA (Rhosin), Cdc42 (ML141) and Rac1 (NSC23766) to improve Mk ploidy and/or proPLT formation that could lead to higher PLP yields. These Rho GTPases are implicated largely in the actin and tubulin cytoskeletal systems, however, have complicated signaling pathways.[75,132] Our results indicate that our high-level targeting approach was insufficient to improve Mk culture characteristics. Inhibition of downstream effectors of RhoA, Rac1 or Cdc42 could be explored in our primary cultures.

In our culture, we purified the Mk fraction via bead selections on Day 7 and then on Day 9 we added the different inhibitors to the culture. Nicotinamide was also added on Day 7 to our culture to promote polyploidization. Previous studies in the lab showed that adding

nicotinamide on Day 5 had similar positive effects on ploidy levels as Day 7 addition, but few changes occurred when it was added on Day 9.[42] Therefore, the addition of the inhibitors on Day 9 might be too late. Exploring the addition of the inhibitors on Day 7 along with nicotinamide may lead to a synergistic effect on ploidy.

Our results with the Rac1 inhibitor, NSC23766, showed largely diminished proPLT formation but removal of the inhibitor re-initiated proPLT formation. We've made observations in the past that Mks can retract proPLTs *in vitro* after a period of time yet it is not clear what the trigger is. To further understand the impact of Rac1 on proPLT formation and given the strong antagonistic effect of early inhibition, adding NSC23766 to late proPLT forming cultures and monitoring for larger numbers of retractions and reduced proPLT formation might further elucidate Rac1's role in PLP generation. This experiment could be conducted in the Nikon Biostation systems which integrate an incubator with microscopy for long term and multi-point live cell imaging.

As was described in Chapter 5, the use of media dilutions promoted the expansion of Mks in our non-selected cultures primarily due to the media retention/IL-3. Our data in Chapter 5 indicated that larger numbers of 2N and 4N Mks were generated, therefore, it is plausible that coupling the Rho GTPase inhibitors with the media dilution process could promote higher ploidy Mks by preventing the 2N/4N Mks from dividing.

Finally, developing novel mechanistic studies of the Rho GTPase pathways that can illuminate their transient behavior and improved imaging techniques to track localization will lead to greater understanding of platelet biogenesis and likely identify optimal targets for *ex vivo* in cultures.[56]

7.4 Towards a scalable *ex vivo* Mk and PLP production process

The limited understanding of the processes that govern HSPC expansion and commitment to Mks as well as the maturation of Mks into platelet-producing cells leads to the *ex vivo* challenges of (1) producing many Mks from each input CD34⁺ cell and (2) efficiently generating platelet-like-particles (PLPs) from Mks. The work I have completed (**Figure 7.2**) identified cell-culture process development approaches that improved Mk numbers (Chapter 5) and engineered bioreactors to further our understanding of *ex vivo* PLP generation (Chapter 2-4). Though these projects help further our goal of developing an *ex vivo* Mk and PLP production process and tackle the challenges of the field, we are still considerably short of clinically relevance. I believe that a combined effort between scientists – helping us understand fundamental biological mechanisms – and engineers – designing technologies that incorporate biological relevance – will lead to success in the field.

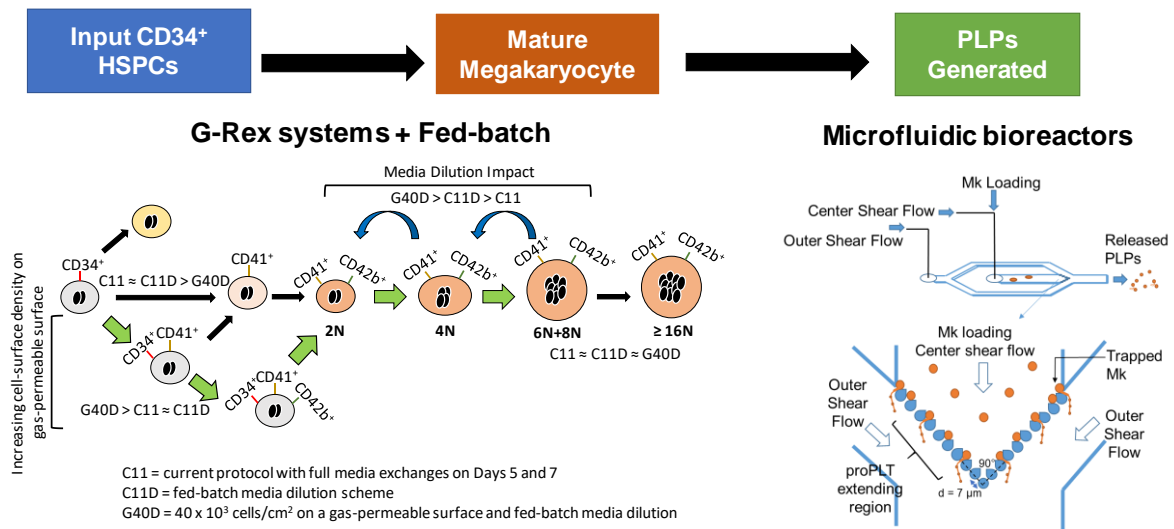


Figure 7.2 Towards a scalable *ex vivo* Mk and PLP production process.

References

1. Freireich EJ. Origins of platelet transfusion therapy. *Transfus Med Rev.* 2011;25(3):252-256.
2. Whitaker BI, Schlumpf, K., Schulman, J. Report of the US Department of Health and Human Services. The 2009 national blood collection and utilization survey report. Washington, DC: US Department of Health and Human Services, Office of the Assistant Secretary for Health; 2011.
3. Whitaker B, Rajbhandary S, Kleinman S, Harris A, Kamani N. Trends in United States blood collection and transfusion: results from the 2013 AABB Blood Collection, Utilization, and Patient Blood Management Survey. *Transfusion.* 2016;56(9):2173-2183.
4. Ellingson KD, Sapiano MR, Haass KA, Savinkina AA, Baker ML, Chung KW, Henry RA, Berger JJ, Kuehnert MJ, Basavaraju SV. Continued decline in blood collection and transfusion in the United States–2015. *Transfusion.* 2017;57(S2):1588-1598.
5. Hartwig J, Italiano J. The birth of the platelet. *J Thromb Haemost.* 2003;1(7):1580-1586.
6. Stasi R. How to approach thrombocytopenia. *ASH Education Program Book.* 2012;2012(1):191-197.
7. Stroncek DF, Rebulla P. Platelet transfusions. *The Lancet.* 2007;370(9585):427-438.
8. Ohto H, Nollet KE. Overview on platelet preservation: better controls over storage lesion. *Transfusion Apheresis Sci.* 2011;44(3):321-325.
9. Baigger A, Blasczyk R, Figueiredo C. Towards the manufacture of megakaryocytes and platelets for clinical application. *Transfusion Medicine and Hemotherapy.* 2017;44(3):165-173.
10. Avanzi MP, Mitchell WB. Ex vivo production of platelets from stem cells. *Br J Haematol.* 2014;165(2):237-247.

11. Gollomp K, Lambert MP, Poncz M. Current status of blood ‘pharming’: megakaryocyte transfusions as a source of platelets. *Curr Opin Hematol.* 2017;24(6):565-571.
12. Sim X, Poncz M, Gadue P, French DL. Understanding platelet generation from megakaryocytes: implications for in vitro–derived platelets. *Blood.* 2016;127(10):1227-1233.
13. Thon JN, Medvetz DA, Karlsson S, Italiano Jr JE. Road blocks in making platelets for transfusion. *J Thromb Haemost.* 2015;13:S55-S62.
14. Chow DC, Wenning LA, Miller WM, Papoutsakis ET. Modeling pO₂ distributions in the bone marrow hematopoietic compartment. II. Modified Kroghian models. *Biophys J.* 2001;81(2):685-696.
15. Jež M, Rožman P, Ivanović Z, Bas T. Concise review: the role of oxygen in hematopoietic stem cell physiology. *J Cell Physiol.* 2015;230(9):1999-2005.
16. Lordier L, Jalil A, Aurade F, Larbret F, Larghero J, Debili N, Vainchenker W, Chang Y. Megakaryocyte endomitosis is a failure of late cytokinesis related to defects in the contractile ring and Rho/Rock signaling. *Blood.* 2008;112(8):3164-3174.
17. Tomer A. Human marrow megakaryocyte differentiation: multiparameter correlative analysis identifies von Willebrand factor as a sensitive and distinctive marker for early (2N and 4N) megakaryocytes. *Blood.* 2004;104(9):2722-2727.
18. Mattia G, Vulcano F, Milazzo L, Barca A, Macioce G, Giampaolo A, Hassan HJ. Different ploidy levels of megakaryocytes generated from peripheral or cord blood CD34⁺ cells are correlated with different levels of platelet release. *Blood.* 2002;99(3):888-897.
19. Avanzi MP, Chen A, He W, Mitchell WB. Optimizing megakaryocyte polyploidization by targeting multiple pathways of cytokinesis. *Transfusion.* 2012;52(11):2406-2413.

20. Giammona LM, Fuhrken PG, Papoutsakis ET, Miller WM. Nicotinamide (vitamin B3) increases the polyploidisation and proplatelet formation of cultured primary human megakaryocytes. *Br J Haematol.* 2006;135(4):554-566.
21. Behnke O. An electron microscope study of the megakaryocyte of the rat bone marrow: I. The development of the demarcation membrane system and the platelet surface coat. *J Ultrastruct Res.* 1968;24(5):412-433.
22. Eckly A, Heijnen H, Pertuy F, Geerts W, Proamer F, Rinckel J-Y, Léon C, Lanza F, Gachet C. Biogenesis of the demarcation membrane system (DMS) in megakaryocytes. *Blood.* 2014;123(6):921-930.
23. Junt T, Schulze H, Chen Z, Massberg S, Goerge T, Krueger A, Wagner DD, Graf T, Italiano JE, Shivdasani RA, von Andrian UH. Dynamic visualization of thrombopoiesis within bone marrow. *Science.* 2007;317(5845):1767-1770.
24. Kaufman RM, Airo R, Pollack S, Crosby WH. Circulating megakaryocytes and platelet release in the lung. *Blood.* 1965;26(6):720-731.
25. Levine R, Eldor A, Shoff P, Kirwin S, Tenza D, Cramer E. Circulating megakaryocytes: delivery of large numbers of intact, mature megakaryocytes to the lungs. *Eur J Haematol.* 1993;51(4):233-246.
26. Fuentes R, Wang Y, Hirsch J, Wang C, Rauova L, Worthen GS, Kowalska MA, Poncz M. Infusion of mature megakaryocytes into mice yields functional platelets. *The Journal of clinical investigation.* 2010;120(11):3917-3922.
27. Lefrançois E, Ortiz-Muñoz G, Caudrillier A, Mallavia B, Liu F, Sayah DM, Thornton EE, Headley MB, David T, Coughlin SR, Krummel MF, Leavitt AD, Passequé E, Looney MR. The lung is a site of platelet biogenesis and a reservoir for haematopoietic progenitors. *Nature.* 2017;544(7648):105-109.
28. Hamada T, Möhle R, Hesselgesser J, Hoxie J, Nachman RL, Moore MA, Rafii S. Transendothelial migration of megakaryocytes in response to stromal cell-derived factor 1 (SDF-1) enhances platelet formation. *The Journal of experimental medicine.* 1998;188(3):539-548.

29. Zhang L, Orban M, Lorenz M, Barocke V, Braun D, Urtz N, Schulz C, von Brühl M-L, Tirniceriu A, Gaertner F, Proia RL, Graf T, Bolz S-S, Montanez E, Prinz M, Müller A, von Baumgarten L, Billich A, Sixt M, Fässler R, von Andrian UH, Junt T, Massberg S. A novel role of sphingosine 1-phosphate receptor S1pr1 in mouse thrombopoiesis. *The Journal of Experimental Medicine*. 2012;209(12):2165-2181.
30. Deutsch VR, Tomer A. Megakaryocyte development and platelet production. *Br J Haematol*. 2006;134(5):453-466.
31. Zucker-Franklin D, Petursson S. Thrombocytopoiesis--analysis by membrane tracer and freeze-fracture studies on fresh human and cultured mouse megakaryocytes. *The Journal of cell biology*. 1984;99(2):390-402.
32. Zucker-Franklin D, Philipp CS. Platelet production in the pulmonary capillary bed: new ultrastructural evidence for an old concept. *The American journal of pathology*. 2000;157(1):69-74.
33. Nishimura S, Nagasaki M, Kunishima S, Sawaguchi A, Sakata A, Sakaguchi H, Ohmori T, Manabe I, Italiano JE, Ryu T. IL-1 α induces thrombopoiesis through megakaryocyte rupture in response to acute platelet needs. *The Journal of cell biology*. 2015;209(3):453-466.
34. Lambert MP, Sullivan SK, Fuentes R, French DL, Poncz M. Challenges and promises for the development of donor-independent platelet transfusions. *Blood*. 2013;121(17):3319-3324.
35. Mostafa SS, Miller WM, Papoutsakis ET. Oxygen tension influences the differentiation, maturation and apoptosis of human megakaryocytes. *Br J Haematol*. 2000;111(3):879-889.
36. Yang H, Miller W, Papoutsakis E. Higher pH promotes megakaryocytic maturation and apoptosis. *Stem Cells*. 2002;20(4):320-328.
37. Pineault N, Boucher J-F, Cayer M-P, Palmqvist L, Boyer L, Lemieux R, Proulx C. Characterization of the effects and potential mechanisms leading to increased megakaryocytic differentiation under mild hyperthermia. *Stem cells and development*. 2008;17(3):483-494.

38. Proulx C, Dupuis N, St-Amour I, Boyer L, Lemieux R. Increased megakaryopoiesis in cultures of CD34-enriched cord blood cells maintained at 39° C. *Biotechnol Bioeng.* 2004;88(6):675-680.
39. Bruyn CD, Delforge A, Martiat P, Bron D. Ex vivo expansion of megakaryocyte progenitor cells: cord blood versus mobilized peripheral blood. *Stem cells and development.* 2005;14(4):415-424.
40. Matsunaga T, Tanaka I, Kobune M, Kawano Y, Tanaka M, Kuribayashi K, Iyama S, Sato T, Sato Y, Takimoto R. Ex vivo large-scale generation of human platelets from cord blood CD34+ cells. *Stem Cells.* 2006;24(12):2877-2887.
41. Panuganti S, Papoutsakis ET, Miller WM. Bone marrow niche-inspired, multiphase expansion of megakaryocytic progenitors with high polyploidization potential. *Cytotherapy.* 2010;12(6):767-782.
42. Panuganti S, Schlinker AC, Lindholm PF, Papoutsakis ET, Miller WM. Three-stage ex vivo expansion of high-ploidy megakaryocytic cells: toward large-scale platelet production. *Tissue engineering Part A.* 2013;19(7-8):998-1014.
43. Nakamura S, Takayama N, Hirata S, Seo H, Endo H, Ochi K, Fujita K-i, Koike T, Harimoto K-i, Dohda T, Watanabe A, Okita K, Takahashi N, Sawaguchi A, Yamanaka S, Nakauchi H, Nishimura S, Eto K. Expandable megakaryocyte cell lines enable clinically applicable generation of platelets from human induced pluripotent stem cells. *Cell Stem Cell.* 2014;14(4):535-548.
44. Cabrita GJ, Ferreira BS, Da Silva CL, Goncalves R, Almeida-Porada G, Cabral JM. Hematopoietic stem cells: from the bone to the bioreactor. *Trends Biotechnol.* 2003;21(5):233-240.
45. Rodrigues CA, Fernandes TG, Diogo MM, da Silva CL, Cabral JM. Stem cell cultivation in bioreactors. *Biotechnol Adv.* 2011;29(6):815-829.
46. Yang Y, Liu C, Lei X, Wang H, Su P, Ru Y, Ruan X, Duan E, Feng S, Han M, Xu Y, Shi L, Jiang E, Zhou J. Integrated Biophysical and Biochemical Signals Augment Megakaryopoiesis and Thrombopoiesis in a Three-Dimensional Rotary Culture System. *Stem cells translational medicine.* 2016;5(2):175-185.

47. Sullenbarger B, Bahng JH, Gruner R, Kotov N, Lasky LC. Prolonged continuous in vitro human platelet production using three-dimensional scaffolds. *Exp Hematol*. 2009;37(1):101-110.
48. Blin A, Le Goff A, Magniez A, Poirault-Chassac S, Teste B, Sicot G, Nguyen KA, Hamdi FS, Reyssat M, Baruch D. Microfluidic model of the platelet-generating organ: beyond bone marrow biomimetics. *Sci Rep*. 2016;6:21700.
49. Di Buduo CA, Wray LS, Tozzi L, Malara A, Chen Y, Ghezzi CE, Smoot D, Sfara C, Antonelli A, Spedden E, Bruni G, Staii C, De Marco L, Magnani M, Kaplan DL, Balduini A. Programmable 3D silk bone marrow niche for platelet generation ex vivo and modeling of megakaryopoiesis pathologies. *Blood*. 2015;125(14):2254-2264.
50. Thon JN, Mazutis L, Wu S, Sylman JL, Ehrlicher A, Machlus KR, Feng Q, Lu S, Lanza R, Neeves KB, Weitz DA, Italiano JE. Platelet bioreactor-on-a-chip. *Blood*. 2014;124(12):1857-1867.
51. Ito Y, Nakamura S, Sugimoto N, Shigemori T, Kato Y, Ohno M, Sakuma S, Ito K, Kumon H, Hirose H. Turbulence activates platelet biogenesis to enable clinical scale ex vivo production. *Cell*. 2018;174(3):636-648. e618.
52. Schlinker AC, Radwanski K, Wegener C, Min K, Miller WM. Separation of in-vitro-derived megakaryocytes and platelets using spinning-membrane filtration. *Biotechnol Bioeng*. 2015;112(4):788-800.
53. Italiano JE, Lecine P, Shivdasani RA, Hartwig JH. Blood platelets are assembled principally at the ends of proplatelet processes produced by differentiated megakaryocytes. *The Journal of cell biology*. 1999;147(6):1299-1312.
54. Patel SR, Richardson JL, Schulze H, Kahle E, Galjart N, Drabek K, Shivdasani RA, Hartwig JH, Italiano JE. Differential roles of microtubule assembly and sliding in proplatelet formation by megakaryocytes. *Blood*. 2005;106(13):4076-4085.
55. Bender M, Thon JN, Ehrlicher AJ, Wu S, Mazutis L, Deschmann E, Sola-Visner M, Italiano JE, Hartwig JH. Microtubule sliding drives proplatelet elongation and is dependent on cytoplasmic dynein. *Blood*. 2015;125(5):860-868.

56. Pleines I, Cherpokova D, Bender M. Rho GTPases and their downstream effectors in megakaryocyte biology. *Platelets*. 2019;30(1):9-16.
57. Ridley AJ, Hall A. The small GTP-binding protein rho regulates the assembly of focal adhesions and actin stress fibers in response to growth factors. *Cell*. 1992;70(3):389-399.
58. Chang Y, Auradé F, Larbret F, Zhang Y, Le Couedic J-P, Momeux L, Larghero J, Bertoglio J, Louache F, Cramer E. Proplatelet formation is regulated by the Rho/ROCK pathway. *Blood*. 2007;109(10):4229-4236.
59. Sabri S, Jandrot-Perrus M, Bertoglio J, Farndale RW, Mansat-De Mas V, Debili N, Vainchenker W. Differential regulation of actin stress fiber assembly and proplatelet formation by $\alpha 2\beta 1$ integrin and GPVI in human megakaryocytes. *Blood*. 2004;104(10):3117-3125.
60. Pan J, Lordier L, Meyran D, Rameau P, Lecluse Y, Kitchen-Goosen S, Badirou I, Mokrani H, Narumiya S, Alberts AS. The formin DIAPH1 (mDia1) regulates megakaryocyte proplatelet formation by remodeling the actin and microtubule cytoskeletons. *Blood*. 2014;124(26):3967-3977.
61. Gao Y, Smith E, Ker E, Campbell P, Cheng E-c, Zou S, Lin S, Wang L, Halene S, Krause DS. Role of RhoA-specific guanine exchange factors in regulation of endomitosis in megakaryocytes. *Dev Cell*. 2012;22(3):573-584.
62. Suzuki A, Shin J-W, Wang Y, Min SH, Poncz M, Choi JK, Discher DE, Carpenter CL, Lian L, Zhao L. RhoA is essential for maintaining normal megakaryocyte ploidy and platelet generation. *PLoS One*. 2013;8(7):e69315.
63. Kozma R, Ahmed S, Best A, Lim L. The Ras-related protein Cdc42Hs and bradykinin promote formation of peripheral actin microspikes and filopodia in Swiss 3T3 fibroblasts. *Mol Cell Biol*. 1995;15(4):1942-1952.
64. Millard TH, Sharp SJ, Machesky LM. Signalling to actin assembly via the WASP (Wiskott-Aldrich syndrome protein)-family proteins and the Arp2/3 complex. *Biochem J*. 2004;380(1):1-17.

65. Pleines I, Dütting S, Cherpokova D, Eckly A, Meyer I, Morowski M, Krohne G, Schulze H, Gachet C, Debili N. Defective tubulin organization and proplatelet formation in murine megakaryocytes lacking Rac1 and Cdc42. *Blood*. 2013;122(18):3178-3187.
66. Ridley AJ, Paterson HF, Johnston CL, Diekmann D, Hall A. The small GTP-binding protein rac regulates growth factor-induced membrane ruffling. *Cell*. 1992;70(3):401-410.
67. Miki H, Suetsugu S, Takenawa T. WAVE, a novel WASP-family protein involved in actin reorganization induced by Rac. *The EMBO journal*. 1998;17(23):6932-6941.
68. Takenawa T, Miki H. WASP and WAVE family proteins: key molecules for rapid rearrangement of cortical actin filaments and cell movement. *J Cell Sci*. 2001;114(10):1801-1809.
69. Pleines I, Elvers M, Strehl A, Pozgajova M, Varga-Szabo D, May F, Chrostek-Grashoff A, Brakebusch C, Nieswandt B. Rac1 is essential for phospholipase C- γ 2 activation in platelets. *Pflügers Archiv-European Journal of Physiology*. 2009;457(5):1173-1185.
70. Gao Y, Dickerson JB, Guo F, Zheng J, Zheng Y. Rational design and characterization of a Rac GTPase-specific small molecule inhibitor. *Proc Natl Acad Sci U S A*. 2004;101(20):7618-7623.
71. Michaelson D, Abidi W, Guardavaccaro D, Zhou M, Ahearn I, Pagano M, Philips MR. Rac1 accumulates in the nucleus during the G2 phase of the cell cycle and promotes cell division. *The Journal of cell biology*. 2008;181(3):485-496.
72. Moore KA, Sethi R, Doanes AM, Johnson TM, Pracyk JB, Kirby M, Irani K, GOLDSCHMIDT-CLERMONT PJ, Finkel T. Rac1 is required for cell proliferation and G2/M progression. *Biochem J*. 1997;326(1):17-20.
73. Yoshida T, Zhang Y, Rosado LAR, Chen J, Khan T, Moon SY, Zhang B. Blockade of Rac1 activity induces G1 cell cycle arrest or apoptosis in breast cancer cells through downregulation of cyclin D1, survivin, and X-linked inhibitor of apoptosis protein. *Mol Cancer Ther*. 2010;9(6):1657-1668.

74. Kosoff RE, Aslan JE, Kostyak JC, Dulaimi E, Chow HY, Prudnikova TY, Radu M, Kunapuli SP, McCarty OJ, Chernoff J. Pak2 restrains endomitosis during megakaryopoiesis and alters cytoskeleton organization. *Blood*. 2015;125(19):2995-3005.
75. Poulter NS, Thomas SG. Cytoskeletal regulation of platelet formation: Coordination of F-actin and microtubules. *The international journal of biochemistry & cell biology*. 2015;66:69-74.
76. Martinez AF, McMahon RD, Horner M, Miller WM. A uniform-shear rate microfluidic bioreactor for real-time study of proplatelet formation and rapidly-released platelets. *Biotechnol Progr*. 2017;33(6):1614-1629.
77. Thon JN, Dykstra BJ, Beaulieu LM. Platelet bioreactor: accelerated evolution of design and manufacture. *Platelets*. 2017;28(5):472-477.
78. Dunois-Lardé C, Capron C, Fichelson S, Bauer T, Cramer-Bordé E, Baruch D. Exposure of human megakaryocytes to high shear rates accelerates platelet production. *Blood*. 2009;114(9):1875-1883.
79. Jiang J, Woulfe DS, Papoutsakis ET. Shear enhances thrombopoiesis and formation of microparticles that induce megakaryocytic differentiation of stem cells. *Blood*. 2014;124(13):2094-2103.
80. Pallotta I, Lovett M, Kaplan DL, Balduini A. Three-dimensional system for the in vitro study of megakaryocytes and functional platelet production using silk-based vascular tubes. *Tissue Engineering Part C: Methods*. 2011;17(12):1223-1232.
81. Avanzi MP, Oluwadara OE, Cushing MM, Mitchell ML, Fischer S, Mitchell WB. A novel bioreactor and culture method drives high yields of platelets from stem cells. *Transfusion*. 2016;56(1):170-178.
82. Nakagawa Y, Nakamura S, Nakajima M, Endo H, Dohda T, Takayama N, Nakauchi H, Arai F, Fukuda T, Eto K. Two differential flows in a bioreactor promoted platelet generation from human pluripotent stem cell-derived megakaryocytes. *Exp Hematol*. 2013;41(8):742-748.

83. Mazo IB, von Andrian UH. Adhesion and homing of blood-borne cells in bone marrow microvessels. *J Leukocyte Biol.* 1999;66(1):25-32.
84. Hathcock JJ. Flow effects on coagulation and thrombosis. *Arterio Thromb Vasc Biol.* 2006;26(8):1729-1737.
85. Sharma C, Malhotra D, Rathore A. Review of computational fluid dynamics applications in biotechnology processes. *Biotechnol Progr.* 2011;27(6):1497-1510.
86. Huang M, Fan S, Xing W, Liu C. Microfluidic cell culture system studies and computational fluid dynamics. *Mathematical and Computer Modelling.* 2010;52(11):2036-2042.
87. Wu JJ. Data-driven strategies for optimization of human megakaryocyte differentiation. PhD Dissertation. Northwestern University; 2019.
88. Hoganson DM, Pryor II HI, Bassett EK, Spool ID, Vacanti JP. Lung assist device technology with physiologic blood flow developed on a tissue engineered scaffold platform. *Lab on a Chip.* 2011;11(4):700-707.
89. Oh KW, Lee K, Ahn B, Furlani EP. Design of pressure-driven microfluidic networks using electric circuit analogy. *Lab on a Chip.* 2012;12(3):515-545.
90. Potkay JA. The promise of microfluidic artificial lungs. *Lab on a Chip.* 2014;14(21):4122-4138.
91. Emerson DR, Cieřlicki K, Gu X, Barber RW. Biomimetic design of microfluidic manifolds based on a generalised Murray's law. *Lab on a Chip.* 2006;6(3):447-454.
92. Domachuk P, Tsioris K, Omenetto FG, Kaplan DL. Bio-microfluidics: biomaterials and biomimetic designs. *Adv Mater.* 2010;22(2):249-260.
93. Chen Z, Mondal NK, Ding J, Gao J, Griffith BP, Wu ZJ. Shear-induced platelet receptor shedding by non-physiological high shear stress with short exposure time: glycoprotein Iba and glycoprotein VI. *Thromb Res.* 2015;135(4):692-698.

94. Bergmeier W, Burger PC, Piffath CL, Hoffmeister KM, Hartwig JH, Nieswandt B, Wagner DD. Metalloproteinase inhibitors improve the recovery and hemostatic function of in vitro–aged or–injured mouse platelets. *Blood*. 2003;102(12):4229-4235.
95. Feng Q, Shabrani N, Thon JN, Huo H, Thiel A, Machlus KR, Kim K, Brooks J, Li F, Luo C. Scalable generation of universal platelets from human induced pluripotent stem cells. *Stem cell reports*. 2014;3(5):817-831.
96. Sim X, Jarocha D, Hayes V, Hanby HA, Marks MS, Camire RM, French DL, Poncz M, Gadue P. Identifying and enriching platelet-producing human stem cell–derived megakaryocytes using factor V uptake. *Blood*. 2017;130(2):192-204.
97. Martinez AF, Miller WM. Enabling Large-Scale ex vivo Production of Megakaryocytes from CD34+ Cells Using Gas-Permeable Surfaces. *STEM CELLS Translational Medicine*. 2019;10.1002/sctm.18-0160.
98. Reems J-A, Pineault N, Sun S. In vitro megakaryocyte production and platelet biogenesis: state of the art. *Transfus Med Rev*. 2010;24(1):33-43.
99. Borst S, Sim X, Poncz M, French DL, Gadue P. Induced Pluripotent Stem Cell–Derived Megakaryocytes and Platelets for Disease Modeling and Future Clinical Applications. *Arterio Thromb Vasc Biol*. 2017;37(11):2007-2013.
100. Moreau T, Evans AL, Vasquez L, Tijssen MR, Yan Y, Trotter MW, Howard D, Colzani M, Arumugam M, Wu WH, Dalby A, Lampela R, Bouet G, Hobbs CM, Pask DC, Payne H, Ponomaryov T, Brill A, Soranzo N, Ouwehand WH, Pedersen RA, Ghevaert C. Large-scale production of megakaryocytes from human pluripotent stem cells by chemically defined forward programming. *Nature communications*. 2016;7:11208.
101. Sugimoto N, Eto K. Platelet production from induced pluripotent stem cells. *J Thromb Haemost*. 2017;15(9):1717-1727.
102. Bird GA, Polsky A, Estes P, Hanlon T, Hamilton H, Morton JJ, Gutman J, Jimeno A, Turner BC, Refaeli Y. Expansion of human and murine hematopoietic stem and progenitor cells ex vivo without genetic modification using MYC and Bcl-2 fusion proteins. *PLoS One*. 2014;9(8):e105525.

103. Dave H, Luo M, Blaney J, Patel S, Barese C, Cruz CR, Shpall EJ, Bollard CM, Hanley PJ. Toward a rapid production of multivirus-specific T cells targeting BKV, adenovirus, CMV, and EBV from umbilical cord blood. *Molecular Therapy - Methods & Clinical Development*. 2017;5:13-21.
104. Forget M-A, Haymaker C, Dennison JB, Toth C, Maiti S, Fulbright OJ, Cooper LJ, Hwu P, Radvanyi LG, Bernatchez C. The beneficial effects of a gas-permeable flask for expansion of Tumor-Infiltrating lymphocytes as reflected in their mitochondrial function and respiration capacity. *Oncoimmunology*. 2016;5(2):e1057386.
105. Lapteva N, Durett AG, Sun J, Rollins LA, Huye LL, Fang J, Dandekar V, Mei Z, Jackson K, Vera J, Ando J, Ngo MC, Coustan-Smith E, Campana D, Szmania S, Garg T, Moreno-Bost A, Vanrhee F, Gee AP, Rooney CM. Large-scale ex vivo expansion and characterization of natural killer cells for clinical applications. *Cytotherapy*. 2012;14(9):1131-1143.
106. Vera JF, Brenner LJ, Gerdemann U, Ngo MC, Sili U, Liu H, Wilson J, Dotti G, Heslop HE, Leen AM, Rooney CM. Accelerated production of antigen-specific T-cells for pre-clinical and clinical applications using Gas-permeable Rapid Expansion cultureware (G-Rex). *Journal of immunotherapy (Hagerstown, Md: 1997)*. 2010;33(3):305-315.
107. Gerdemann U, Katari UL, Papadopoulou A, Keirnan JM, Craddock JA, Liu H, Martinez CA, Kennedy-Nasser A, Leung KS, Gottschalk SM, Krance RA, Brenner MK, Rooney CM, Heslop HE, Leen AM. Safety and clinical efficacy of rapidly-generated trivirus-directed T cells as treatment for adenovirus, EBV, and CMV infections after allogeneic hematopoietic stem cell transplant. *Mol Ther*. 2013;21(11):2113-2121.
108. Csaszar E, Kirouac DC, Yu M, Wang W, Qiao W, Cooke MP, Boitano AE, Ito C, Zandstra PW. Rapid expansion of human hematopoietic stem cells by automated control of inhibitory feedback signaling. *Cell stem cell*. 2012;10(2):218-229.
109. Bajgain P, Mucharla R, Wilson J, Welch D, Anurathapan U, Liang B, Lu X, Ripple K, Centanni JM, Hall C, Hsu D, Couture LA, Gupta S, Gee AP, Heslop HE, Leen AM, Rooney CM, Vera JF. Optimizing the production of suspension cells using the G-Rex "M" series. *Molecular Therapy - Methods & Clinical Development*. 2014;1:14015.

110. Debili N, Hegyi E, Navarro S, Katz A, Mouthon M, Breton-Gorius J, Vainchenker W. In vitro effects of hematopoietic growth factors on the proliferation, endoreplication, and maturation of human megakaryocytes. *Blood*. 1991;77(11):2326-2338.
111. Broudy VC, Lin N, Kaushansky K. Thrombopoietin (c-mpl ligand) acts synergistically with erythropoietin, stem cell factor, and interleukin-11 to enhance murine megakaryocyte colony growth and increases megakaryocyte ploidy in vitro. *Blood*. 1995;85(7):1719-1726.
112. Wang X, Rivière I. Manufacture of tumor-and virus-specific T lymphocytes for adoptive cell therapies. *Cancer Gene Ther*. 2015;22(2):85-94.
113. Ivetic N, Nazi I, Karim N, Clare R, Smith JW, Moore JC, Hope KJ, Kelton JG, Arnold DM. Producing megakaryocytes from a human peripheral blood source. *Transfusion*. 2016;56(5):1066-1074.
114. Choi JS, Mahadik BP, Harley BA. Engineering the hematopoietic stem cell niche: Frontiers in biomaterial science. *Biotechnology journal*. 2015;10(10):1529-1545.
115. Holst J, Watson S, Lord MS, Eamegdool SS, Bax DV, Nivison-Smith LB, Kondyurin A, Ma L, Oberhauser AF, Weiss AS, Rasko JEJ. Substrate elasticity provides mechanical signals for the expansion of hemopoietic stem and progenitor cells. *Nat Biotechnol*. 2010;28(10):1123-1128.
116. Lefebvre P, Winter JN, Meng Y, Cohen I. Ex vivo expansion of early and late megakaryocyte progenitors. *J Hematother Stem Cell Res*. 2000;9(6):913-921.
117. Majka M, Janowska-Wieczorek A, Ratajczak J, Ehrenman K, Pietrkowski Z, Kowalska MA, Gewirtz AM, Emerson SG, Ratajczak MZ. Numerous growth factors, cytokines, and chemokines are secreted by human CD34+ cells, myeloblasts, erythroblasts, and megakaryoblasts and regulate normal hematopoiesis in an autocrine/paracrine manner: Presented at the 41st Annual Meeting of the American Society of Hematology, New Orleans, LA, December 3-7, 1999, and published in abstract form in *Blood*. 1999; 94 (suppl 1): 465a. *Blood*. 2001;97(10):3075-3085.

118. Heazlewood SY, Neaves RJ, Williams B, Haylock DN, Adams TE, Nilsson SK. Megakaryocytes co-localise with hemopoietic stem cells and release cytokines that up-regulate stem cell proliferation. *Stem cell research*. 2013;11(2):782-792.
119. Wickenhauser C, Lorenzen J, Thiele J, Hillienhof A, Jungheim K, Schmitz B, Hansmann M-L, Fischer R. Secretion of cytokines (interleukins-1 alpha,-3, and-6 and granulocyte-macrophage colony-stimulating factor) by normal human bone marrow megakaryocytes. *Blood*. 1995;85(3):685-691.
120. Cid J, Lozano M. Platelet dose for prophylactic platelet transfusions. *Expert Rev Hematol*. 2010;3(4):397-400.
121. An HH, Poncz M, Chou ST. Induced Pluripotent Stem Cell-Derived Red Blood Cells, Megakaryocytes, and Platelets: Progress and Challenges. *Current Stem Cell Reports*. 2018;4(4):310-317.
122. Hölig K. G-CSF in healthy allogeneic stem cell donors. *Transfusion Medicine and Hemotherapy*. 2013;40(4):225-235.
123. Jarocha D, Vo KK, Lyde RB, Hayes V, Camire RM, Poncz M. Enhancing functional platelet release in vivo from in vitro-grown megakaryocytes using small molecule inhibitors. *Blood advances*. 2018;2(6):597-606.
124. Wang H, Ge W, Zhuang Y, Fu J, Li D, Ju X. Fast recovery of platelet production in NOD/SCID mice after transplantation with ex vivo expansion of megakaryocyte from cord blood CD34+ cells. *J Cancer Res Ther*. 2018;14(1):233-239.
125. Wang Y, Hayes V, Jarocha D, Sim X, Harper DC, Fuentes R, Sullivan SK, Gadue P, Chou ST, Torok-Storb BJ, Marks MS, French DL, Poncz M. Comparative analysis of human ex vivo-generated platelets vs megakaryocyte-generated platelets in mice: a cautionary tale. *Blood*. 2015;125(23):3627-3636.
126. Decaudin D, Vantelon J, Bourhis J, Farace F, Bonnet M, Guillier M, Greissenger N, Marracho M, Assari S, Bennaceur A. Ex vivo expansion of megakaryocyte precursor cells in autologous stem cell transplantation for relapsed malignant lymphoma. *Bone Marrow Transplant*. 2004;34(12):1089.

127. Xi J, Zhu H, Liu D, Nan X, Zheng W, Liu K, Shi W, Chen L, Lv Y, Yan F. Infusion of megakaryocytic progenitor products generated from cord blood hematopoietic stem/progenitor cells: results of the phase 1 study. *PLoS One*. 2013;8(2):e54941.
128. Scheding S, Bergmann M, Rathke G, Vogel W, Brugger W, Kanz L. Additional transplantation of ex vivo generated megakaryocytic cells after high-dose chemotherapy. *Haematologica*. 2004;89(5):630-631.
129. Bertolini F, Battaglia M, Pedrazzoli P, Da Prada GA, Lanza A, Soligo D, Caneva L, Sarina B, Murphy S, Thomas T. Megakaryocytic progenitors can be generated ex vivo and safely administered to autologous peripheral blood progenitor cell transplant recipients. *Blood*. 1997;89(8):2679-2688.
130. Begemann P, Hassan H, Kröger N, Krüger W, Kabisch H, Zander A. Correlation of time to platelet engraftment with amount of transplanted CD34+ CD41+ cells after allogeneic bone marrow transplantation. *J Hematother Stem Cell Res*. 2002;11(2):321-326.
131. Eicke D, Baigger A, Schulze K, Latham SL, Halloin C, Zweigerdt R, Guzman CA, Blasczyk R, Figueiredo C. Large-scale production of megakaryocytes in microcarrier-supported stirred suspension bioreactors. *Sci Rep*. 2018;8(1):10146.
132. Etienne-Manneville S, Hall A. Rho GTPases in cell biology. *Nature*. 2002;420(6916):629-635.
133. Shang X, Marchioni F, Sipes N, Evelyn CR, Jerabek-Willemsen M, Duhr S, Seibel W, Wortman M, Zheng Y. Rational design of small molecule inhibitors targeting RhoA subfamily Rho GTPases. *Chem Biol*. 2012;19(6):699-710.
134. Surviladze Z, Waller A, Strouse JJ, Bologna C, Ursu O, Salas V, Parkinson JF, Phillips GK, Romero E, Wandinger-Ness A. A potent and selective inhibitor of Cdc42 GTPase. 2010.
135. Antkowiak A, Viaud J, Severin S, Zanoun M, Ceccato L, Chicanne G, Strassel C, Eckly A, Leon C, Gachet C. Cdc42-dependent F-actin dynamics drive structuration of the demarcation membrane system in megakaryocytes. *J Thromb Haemost*. 2016.

136. Akbar H, Duan X, Saleem S, Davis AK, Zheng Y. RhoA and Rac1 GTPases differentially regulate agonist-receptor mediated reactive oxygen species generation in platelets. *PLoS One*. 2016;11(9):e0163227.
137. Machlus KR, Wu SK, Stumpo DJ, Soussou TS, Paul DS, Campbell RA, Kalwa H, Michel T, Bergmeier W, Weyrich AS. Synthesis and dephosphorylation of MARCKS in the late stages of megakaryocyte maturation drive proplatelet formation. *Blood*. 2016;127(11):1468-1480.
138. Chen Y, Aardema J, Kale S, Whichard ZL, Awomolo A, Blanchard E, Chang B, Myers DR, Ju L, Tran R. Loss of the F-BAR protein CIP4 reduces platelet production by impairing membrane-cytoskeleton remodeling. *Blood*. 2013;122(10):1695-1706.
139. Liu W, Du W, Shang X, Wang L, Evelyn C, Florian MC, Ryan MA, Rayes A, Zhao X, Setchell K. Rational identification of a Cdc42 inhibitor presents a new regimen for long-term hematopoietic stem cell mobilization. *Leukemia*. 2018;1.
140. Palazzo A, Bluteau O, Messaoudi K, Marangoni F, Chang Y, Souquere S, Pierron G, Lapiere V, Zheng Y, Vainchenker W. The cell division control protein 42–Src family kinase–neural Wiskott–Aldrich syndrome protein pathway regulates human proplatelet formation. *J Thromb Haemost*. 2016;14(12):2524-2535.
141. Aslan JE, McCarty OJ. Rho GTPases in platelet function. *J Thromb Haemost*. 2013;11(1):35-46.
142. Pleines I, Hagedorn I, Gupta S, May F, Chakarova L, van Hengel J, Offermanns S, Krohne G, Kleinschnitz C, Brakebusch C. Megakaryocyte-specific RhoA deficiency causes macrothrombocytopenia and defective platelet activation in hemostasis and thrombosis. *Blood*. 2012;119(4):1054-1063.
143. Akbar H, Shang X, Perveen R, Berryman M, Funk K, Johnson JF, Tandon NN, Zheng Y. Gene targeting implicates Cdc42 GTPase in GPVI and non-GPVI mediated platelet filopodia formation, secretion and aggregation. *PLoS One*. 2011;6(7):e22117.
144. Akbar H, Kim J, Funk K, Cancelas J, Shang X, Chen L, Johnson J, Williams D, Zheng Y. Genetic and pharmacologic evidence that Rac1 GTPase is involved in

- regulation of platelet secretion and aggregation. *J Thromb Haemost.* 2007;5(8):1747-1755.
145. Iden S, Collard JG. Crosstalk between small GTPases and polarity proteins in cell polarization. *Nature reviews Molecular cell biology.* 2008;9(11):846.
 146. Dütting S, Gaits-Iacovoni F, Stegner D, Popp M, Antkowiak A, Van Eeuwijk JM, Nurden P, Stritt S, Heib T, Aurbach K. A Cdc42/RhoA regulatory circuit downstream of glycoprotein Ib guides transendothelial platelet biogenesis. *Nature communications.* 2017;8:15838.
 147. Dütting S, Heidenreich J, Cherpokova D, Amin E, Zhang SC, Ahmadian MR, Brakebusch C, Nieswandt B. Critical off-target effects of the widely used Rac1 inhibitors NSC 23766 and EHT 1864 in mouse platelets. *J Thromb Haemost.* 2015;13(5):827-838.
 148. Leclerc E, Sakai Y, Fujii T. Microfluidic PDMS (polydimethylsiloxane) bioreactor for large-scale culture of hepatocytes. *Biotechnol Progr.* 2004;20(3):750-755.
 149. Mehling M, Tay S. Microfluidic cell culture. *Curr Opin Biotechnol.* 2014;25:95-102.
 150. Halldorsson S, Lucumi E, Gómez-Sjöberg R, Fleming RM. Advantages and challenges of microfluidic cell culture in polydimethylsiloxane devices. *Biosens Bioelectron.* 2015;63:218-231.
 151. Dolzhanskiy A, Basch RS, Karpatkin S. The development of human megakaryocytes: III. Development of mature megakaryocytes from highly purified committed progenitors in synthetic culture media and inhibition of thrombopoietin-induced polyploidization by interleukin-3. *Blood.* 1997;89(2):426-434.
 152. Norol F, Vitrat N, Cramer E, Guichard J, Burstein SA, Vainchenker W, Debili N. Effects of cytokines on platelet production from blood and marrow CD34+ cells. *Blood.* 1998;91(3):830-843.
 153. Kaushansky K, Broudy VC, Lin N, Jorgensen MJ, McCarty J, Fox N, Zucker-Franklin D, Lofton-Day C. Thrombopoietin, the Mp1 ligand, is essential for full

megakaryocyte development. *Proceedings of the National Academy of Sciences*. 1995;92(8):3234-3238.

154. Haas S, Hansson J, Klimmeck D, Loeffler D, Velten L, Uckelmann H, Wurzer S, Prendergast ÁM, Schnell A, Hexel K. Inflammation-induced emergency megakaryopoiesis driven by hematopoietic stem cell-like megakaryocyte progenitors. *Cell stem cell*. 2015;17(4):422-434.